COMPUTATIONAL INVESTIGATION OF SEPARATED FLOW AND STALL EVENTS ON ROTATING SYSTEMS

A Dissertation
Presented to
The Academic Faculty

By

Amanda Grubb

In Partial Fulfillment
of the Requirements for the Degree
Doctor of Philosophy in the
School of Aerospace Engineering

Georgia Institute of Technology

May 2022

COMPUTATIONAL INVESTIGATION OF SEPARATED FLOW AND STALL EVENTS ON ROTATING SYSTEMS

Approved by:

Dr. Marilyn Smith, Advisor
School of Aerospace Engineering
Georgia Institute of Technology

Mr. Rohit Jain
Aviation & Missile Center
US Army AvMC

Dr. Juergen Rauleder
School of Aerospace Engineering
Georgia Institute of Technology

Dr. Cristina Riso
School of Aerospace Engineering
Georgia Institute of Technology

Dr. Daniel Schrage
School of Aerospace Engineering
Georgia Institute of Technology

Date Approved: April 13, 2022

ACKNOWLEDGMENTS

Funding for this project was supported through the Army Research Office (ARO) under grant number W911NF-13-1-0244 by technical monitor, Matthew Munson. Computational time was provided by the Department of Defense (DoD) High Performance Computing Modernization Program (HPCMP) from the DoD HPC Center. Roger Strawn is the HPCMP S/AAA. Without financial support from ARO and access to DoD HPCMP resources, my graduate education and research would not have been possible.

I would like to acknowledge the research collaborators in the US/French Partnership Agreement for Helicopter Aeromechanics: the U.S. Army Combat Capabilities Development Command Aviation and Missile Center (AvMC) and Onera, the French Aerospace Lab. Specifically, I would like to thank the rotorcraft aeromechanics experts from these entities: Rohit Jain of the U.S. Army AvMC and Francois Richez and Arnaud Le Pape of Onera. They have provided guidance and insight throughout my graduate career. Success in my research endeavors would not have been possible without their collaboration.

I would like to thank my advisor, Dr. Marilyn Smith. My graduate education would not have been possible without her expertise and guidance. I'd like to thank the entire Nonlinear Computational Aeroelasticity Lab for their support throughout my graduate career, especially Kevin Jacobson, who was always willing to help even if he didn't have the time; Isaac Wilbur who was always up for a mid-afternoon hot tea or coffee break; Robert Bauman whose outgoing personality was the foundation for a group of wonderful friends; and Jan Kiviaho for making long Friday nights at work in the lab strangely fun. I'd like to thank all of my fellow graduate students who made this journey possible: Shane Lympany, Nick Breen, and Mohit Gupta who made studying for and passing qualifying exams a reality; and Kate Gunderson for running out our stress together and becoming lifelong friends. A huge thank you as well to Katie Richardson, who still checks in on me weekly, over a decade after sharing a tiny freshman dorm room together.

I would like to thank my parents for their support during my time at Georgia Tech. From providing financial support, to answering desperate middle of the night phone calls, to convincing me not to give up, they were always there for me. They believed in me even when I didn't believe in myself, and I would not be where I am today without them.

Lastly I'd like to thank my husband, Andy. He made a career change, leaving medical device engineering for a software engineering role, to move to Atlanta so that he could support my academic endeavors. His incredible work ethic inspires me to do my best work. His kindness, patience, compassion, and generosity are a model of how I strive to treat others. His raw unconditional love is truly a reflection of his faith and God's love for humankind.

TABLE OF CONTENTS

LIST OF TABLES

LIST OF FIGURES

SUMMARY

Helicopters have traditionally been largely associated with military use. Over the past decade, new and diverse commercial applications have been discovered for vehicles that can take-off/land vertically and achieve mid-flight hover. The need for a new military rotorcraft fleet, coupled with the explosion of potential commercial applications, has created a sense of urgency in developing next generation rotorcraft with improved speed, range, and agility.

Rotorcraft are highly complex, dynamic vehicles with aeromechanics that are conducive to challenging problems. Many problems encountered by rotorcraft are a result of flow separation on the rotor. Increased speed, range, and agility requirements will only exacerbate these effects. Understanding flow separation on the rotor plane and the effects it has on the vehicle is fundamental to solving problems facing the next generation of rotorcraft development. The best approach to fully understand flow separation on the rotor plane is through a combination of experimentation and computational fluid dynamics (CFD).

This dissertation couples high-fidelity CFD with trusted experimental data sets to create a complete picture of rotorcraft flowfields for study. State-of-the-art CFD modeling techniques, many of which have not been addressed recently, are evaluated to identify and quantify their capabilities and limitations. This includes grid refinement approach, numerical approach, turbulence model effectiveness, and aeroelastic coupling bias. Rich flowfield data from CFD, coupled with experimental data, are explored to further understand separated flow on the rotor and its effects on rotorcraft performance. Separated flow is classified by separation mechanism via isolation of blade motion from shed tip vortices. Dominant flowfield vortices are studied to understand their impact on rotor performance using the Biot-Savart Law.

NOMENCLATURE

Abbreviations

c_l	Sectional Lift
c_m	Sectional Moment
$c_{l_{max}}$	Maximum Sectional Lift
$c_{m_{max}}$	Maximum Sectional Moment
SDP_l	Standard Deviation Percent of Sectional Moment
SDP_m	Standard Deviation Percent of Sectional Lift
ARO	Army Research Office
AvMC	U.S. Army Combat Capabilities Development Command Aviation & Missile Center
CFD	Computational Fluid Dynamics
CSD	Computational Structural Dynamics
DDES	Delayed Detached Eddy Simulation
DES	Detached Eddy Simulation
DNS	Direct Numerical Simulation
DoD	Department of Defense
FVL	Future Vertical Lift

LDV	Laser Doppler Velocimetry
LES	Large Eddy Simulation
MPI	Message Passing Interface
PIV	Particle Image Velocimetry
SA	Spalart-Allamaras
SDP	Standard Deviation Percent
SGS	sub-grid scale
UAS	Unmanned Aerial Systems
URANS	Unsteady Reynolds-Averaged Navier-Stokes
VTOL	Vertical Takeoff and Landing

CHAPTER 1

BACKGROUND

1.1 Motivation

Rotorcraft are invaluable assets to the aerospace sector because of their unique abilities to take off/land vertically and to achieve in-flight hover. These two capabilities permit rotorcraft to perform a diverse range of missions, far beyond the capabilities of fixed-wing aircraft. Prior to the early 2000s, rotorcraft development was largely military-specific. The current fleet of U.S. Army helicopters was completed with the Boeing AH-64 Apache, whose development began in 1975. In the years following completion of the Apache program, the majority of rotorcraft work was focused on upgrading existing platforms, therefore novel rotorcraft design was largely stagnant from the 1980s to the early 2000s.

During the early 2000s, much of the U.S. Army helicopter fleet was deployed overseas into combat environments. These environments included not only adversarial threats but also volatile weather conditions and hazardous terrain. This combination of environmental factors proved to be deadly, as many helicopters and their crews were lost. It became apparent that the aging helicopter fleet did not meet the needs of U.S. troops in these dangerous environments and upgrades to the existing platforms would not be sufficient to address the many issues. In 2009, the U.S. Army launched its Future Vertical Lift (FVL) program to develop a fleet of next-generation rotorcraft designed to perform more tactical missions and survive in hostile environments [1].

Over the past decade, the unique abilities of rotorcraft have also been realized for their versatility and range of applicability outside military operations. Modern applications of small unmanned aerial systems (UAS) range from commercial package delivery to recreational drone flying. Urban vertical lift initiatives, such as the CityAirbus, are working to integrate air mobility in cities around the world [2]. Other initiatives, such as the Boeing-sponsored GoFly challenge, have been established for the purpose of developing “personal flying devices” [3]. Commercial air

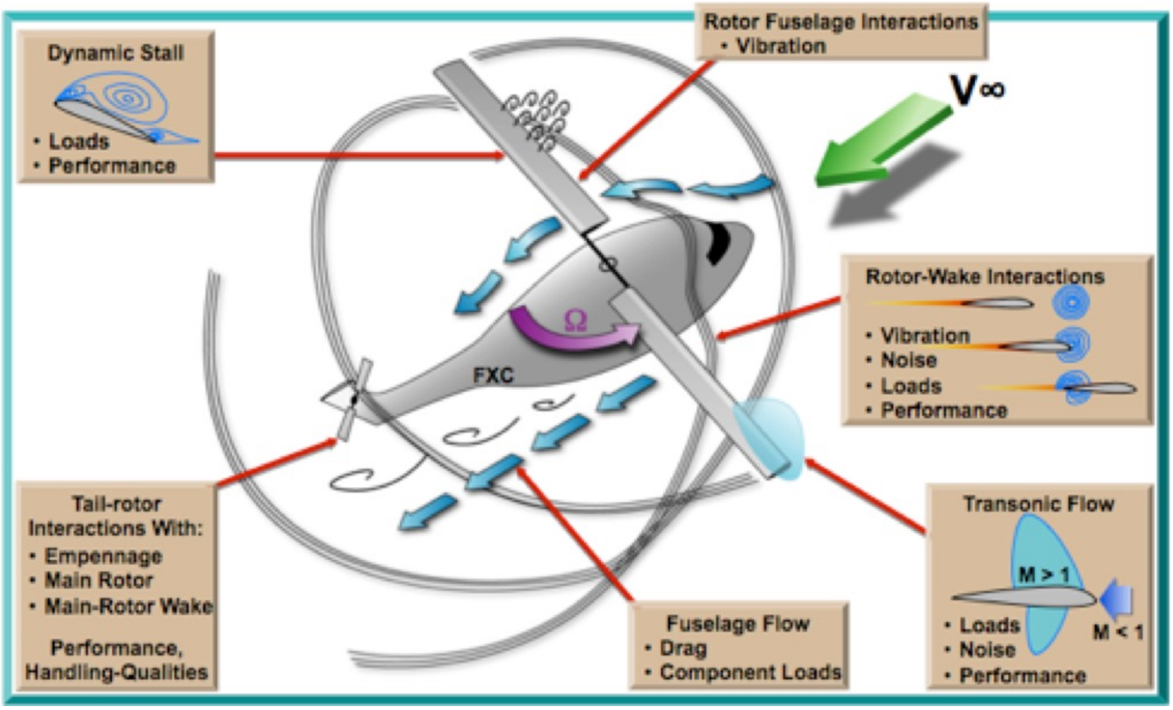

Figure 1.1: Complexities of rotorcraft aeromechanics (courtesy of Frank Caradonna, US Army ADD-A)

travel is on the rise, and the incorporation of vertical takeoff and landing (VTOL) vehicles into the commercial transportation sector has been an ever-growing topic of discussion [4–6].

The realization of new and diverse rotorcraft applications, in both the military and commercial sectors, has created an explosion in demand for next-generation vehicles with advanced capabilities. However, rotorcraft are highly complex, dynamic vehicles subject to aeromechanics phenomena not experienced by traditional fixed-wing aircraft. The complexities of and problems associated with these phenomena are highlighted in Figure 1.1. Many of these problems are not completely understood, even on traditional helicopter configurations. The integration of advanced capabilities into innovative rotary-wing-based designs exacerbates these already complex issues.

A number of the problems highlighted in Figure 1.1 can be related to flow separation on the rotor. Flow separation on the rotor is not uncommon and can be predicted with robust analysis tools; however, the associated physics are highly complex and not fully understood as they are inherently aeroelastic in nature. Current design tools lack the capability to accurately predict separation in a timely manner, as summarized in Table 1.1. CREATE™-AV Helios [7] is a high-fidelity, multidisciplinary rotorcraft modeling framework developed under the sponsorship from the High Performance Computing Modernization Program Computational Research and Engineering Acquisition Tools and Environments – Air Vehicles (HPCMP CREATE™-AV) program and the US Army. Its rotorcraft-specific environment, Helios, provides robust physics-based analyses that couple CFD with other analysis tools within a single framework. With its high-fidelity CFD solvers, Helios can predict separated flow but solution convergence requires too much computational time for use in the vehicle design phase. Lower fidelity CFD for rotorcraft design is available using Sukra-Helitec's RotCFD. Its URANS-based CFD on Cartesian grids coupled with a a momentum based rotor model provides quick predictions of rotor performance quantities such as thrust, torque, and Figure of Merit but lacks the robustness to predict separation [8]. Semi-empirical dynamic stall models can predict rotor blade stall, and thus separation, based on static airfoil data [9]. These models are based on traditional helicopter configurations and may not be applicable to innovative rotary wing designs. Additionally, they cannot predict separation induced by mechanisms other than classic dynamic stall. A gap in prediction capabilities exists between high-fidelity analysis that requires significant computational time and low-fidelity analysis that can be used in the design phase. Additional insight into the physics of separated flow on the rotor is essential to develop predictive reduced order models to fill this gap. Such models can help address and eliminate many of the aeromechanics problems that must be overcome to produce a next-generation rotorcraft fleet during the design phase. This research seeks to advance the understanding of and explore the capabilities of various solvers in capturing separated flow on the rotor by evaluating high thrust and high speed flight conditions.

Table 1.1: Summary of rotorcraft performance prediction tools

Code	CREATE-AV Helios	RotCFD	Dynamic Stall Models
Solution Method	Hybrid URANS-DDES CFD	URANS CFD	Semi-Empirical
Grid Type	Body-Fitted	Cartesian	N/A
Separation Prediction	Yes	No	Classic DS Only
Solution Time Order of Magnitude	Days	Minutes	Seconds

1.2 Dynamic Stall

One of the complex problems that rotorcraft frequently encounter in high thrust or high speed flight is dynamic stall. Classic dynamic stall is an unsteady aerodynamic phenomenon dominated by massively separated flows. It is characterized by a strong vortex core that convects along the upper surface of the rotor blade in the chordwise direction until it is shed from the trailing edge. Motion of the vortex core causes rapidly changing induced velocities and pressure fluctuations in the near-body flowfield that impinge on the blade surface. As the vortex approaches the trailing edge, the blade will experience large losses in lift and large negative pitching moments [10]. This behavior can produce undesirable vibratory loading, excessive noise, loss of structural integrity, and degradation of aircraft controls [11].

Traditionally, the term “dynamic stall” referred only to “classic dynamic stall” where the vortex formation is a product of lifting surface kinematics. Extensive experimentation spanning several decades has led to an accepted sequence of events which comprise this “classic” dynamic stall [10]. Figure 1.2 outlines this sequence of events and relates those events to typical lift and moment trends.

A lifting surface undergoing rapid pitching motion can maintain attached flow past its static stall angle. However, at some angle of attack beyond its static stall angle, the boundary layer begins to separate, and one or several large eddies form in the separated boundary layer regions.

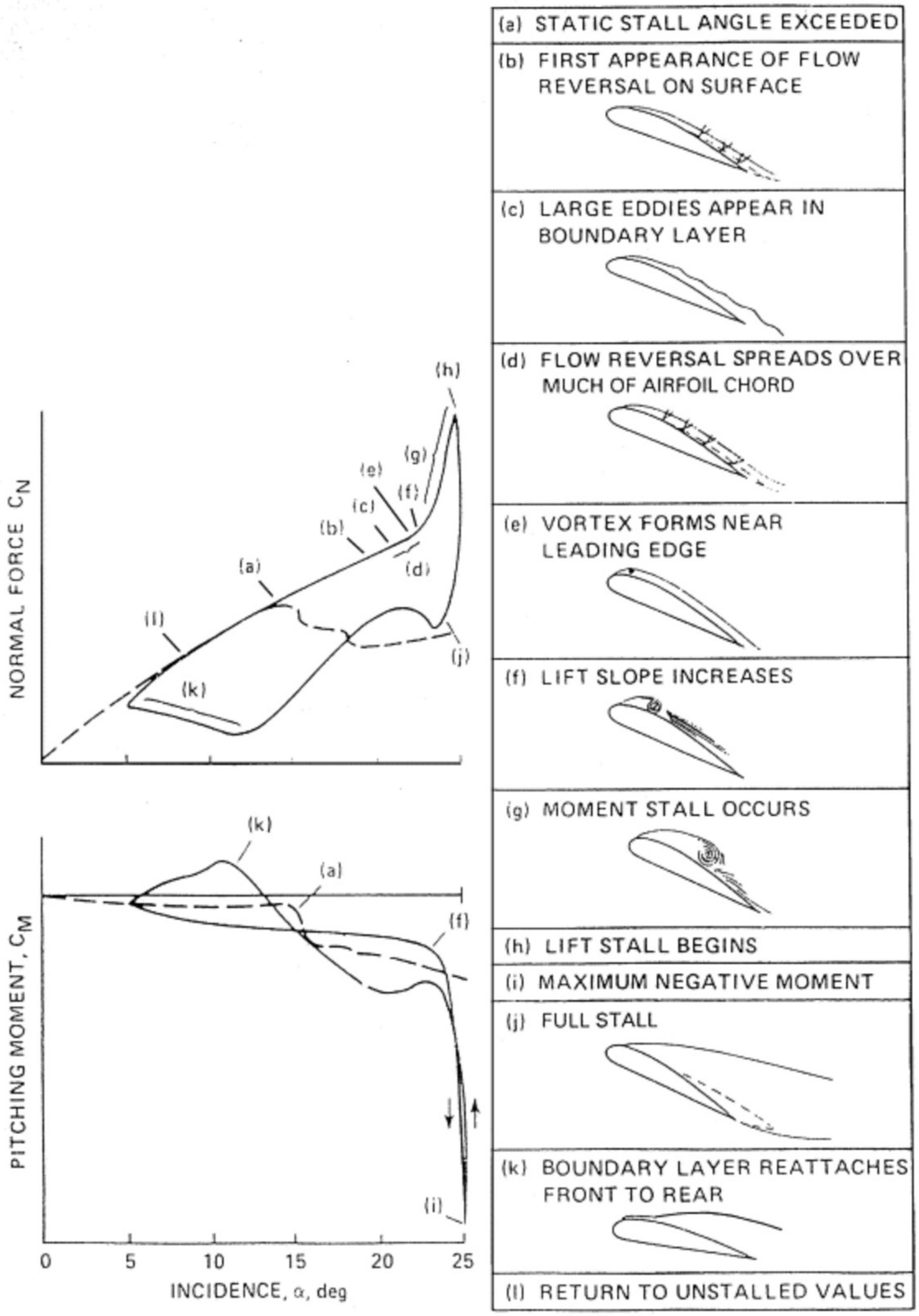

Figure 1.2: Progression of classic dynamic stall events (from Ref. [12])

These eddies, which may occur anywhere along the chord, roll up through the boundary layer to the leading edge. At this point the vortex begins to convect downstream along the upper surface. The presence of the low-pressure vortex core on the upper surface permits the blade to exceed its static stall angle without loss of lift or moment. Once the vortex is shed from the trailing edge, improved blade performance due to the low pressure vortex core is lost, producing significant lift and moment stalls. Classic dynamic stall is primarily a concern for rotorcraft applications due to the rapid pitching motion of the blades throughout a single rotor revolution. However, it can also be a concern for fixed-wing aircraft undergoing rapid maneuvers, such as a fighter jet pull-up [10] and wind turbines [13].

Classic dynamic stall has traditionally been associated with flight vehicles, such as helicopters and fighter jets, where three-dimensional finite wing and/or rotational effects play a significant role in performance. The large majority of dynamic stall research has focused on two-dimensional dynamic stall experimentation and computational approaches [10, 14–16]. However, research over the past decade has shown that two-dimensional experimentation and computations tend to overpredict lift and moment trends (Refs. [17, 18]) and are therefore insufficient analyses to fully understand dynamic stall [19–22].

Only recently have dynamic stall investigations moved towards three-dimensional finite wings [20, 23–27] and rotating systems [19, 28–33]. Initial investigations have demonstrated that the inclusion of these additional effects significantly alters dynamic stall behavior [19, 25, 34]. However, because three-dimensional dynamic stall investigations are a relatively new research focus, the physics associated with these behaviors are not well understood. Recent advancements in computing capabilities now permit the application of high-fidelity CFD to full rotor configurations under the influence of complex aeromechanics phenomena. These tools can be leveraged in conjunction with experimental data to provide the means for furthering the understanding of flow separation and stall events on rotors.

1.3 Importance of Computational Analyses

Rotorcraft are highly complex, dynamic vehicles subject to aeromechanics phenomena not experienced by traditional fixed-wing aircraft. Experimentation has provided some level of insight into the complexities of rotorcraft aeromechanics, however it does not permit the full understanding of the entire flowfield due to physical limitations on data acquisition capability [23, 28, 30, 32]. High-fidelity analyses, such as CFD, can be leveraged to fill this knowledge gap. CFD has been a rapidly changing field over the past several decades. At its inception, CFD was widely considered a purely academic endeavor. Advanced algorithm development coupled with the rapid advancement of modern computing capabilities has resulted in accelerations of up to six orders of magnitude over the past 20 years [35]. This permits CFD to be used for high-fidelity simulations of full rotor configurations. Because of the massive computational requirements, only recent advances in high performance computing capabilities have enabled such high-fidelity computations. Only a few researchers throughout the international community have begun pursuit of investigating separated flows on three-dimensional rotor systems, so there is still much to be learned [19, 21, 22, 31].

Efforts to understand the capabilities and limitations of current state-of-the-art approaches have been the focus of a multi-year joint research effort under the US/French Partnership Agreement for Helicopter Aeromechanics. Collaboration with experts in the international community permitted a broad range of analysis techniques to be compared and evaluated. Together the research partners were able to identify the unknowns of complex aeromechanics prediction capabilities that are investigated in this work.

1.4 Thesis Goals

- Goal 1: To identify and quantify capabilities and limitations of state-of-the-art CFD modeling approach for capturing massively separated flows on three-dimensional rotors

- Goal 2: To advance the knowledge of the physics of separated flows on rotors using a combination of state-of-the-art CFD modeling and high-quality experimental data

- Goal 3: To explore the application of the Biot-Savart Law to the entire rotor plane to evaluate the effects of trailing tip vortices on the rotor plane aerodynamics

1.4.1 Goal 1: Identify/Quantify Capabilities and Limitations of State-of-the-Art Modeling

CFD, when leveraged correctly, can be a very powerful assessment tool. When leveraged incorrectly, however, CFD wastes significant computational resources and can lead to erroneous conclusions. Understanding how to produce accurate, usable data is fundamental to any CFD analysis and becomes increasingly more important with increasing aerodynamic complexity such as unsteady flow separation. Helicopters present some of the most complex aerodynamic problems in the aerospace industry today as the flowfields are dominated by nonlinear flow features. CFD simulations must be performed so that underlying models accurately capture the physics. This often requires an expert user to predict the physical features that will dominate the flowfield, and for non-experts, this is an overwhelming task. This thesis details the analysis process including grid generation techniques, choice of turbulence models and numerical schemes, verifying solution accuracy, and understanding discrepancies between computational and experimental data. Together, this serves the aerospace community as a complete guide on accurately modeling the aerodynamics of rotating systems with massively separated flow.

Questions to Answer:

- Grid generation techniques for finite wing and rotating blade dynamic stall analyses are largely based on infinite wing grid generation techniques, where spanwise/radial spacing is quite large.
  - **Is spanwise/radial grid density important in capturing separated flow?**
  - **Can radial spacing requirements be quantified for general use?**
- Flowfield resolution is dependent not only on grid refinement but also turbulence model and numerical scheme robustness. Three-dimensional separated flows have been evalu-

ated across several government and academia entities using a number of turbulence model-numerical scheme combinations. Comparisons, however, are often drawn between results synthesized from different flow solvers and grids, introducing many factors that could contribute to varying behaviors. Understanding the direct impact of flow solver options requires variation of a single input keeping all other variables constant.

  - **Which popular turbulence models most accurately capture separated flows when applied within the same flow solver on the same grid?**
  - **Are there coupled effects between grid refinement and turbulence model in separated flow regimes?**

- Prediction of classic dynamic stall is highly dependent on blade kinematics when aeroelastics are in play. Computational approaches often ignore aeroelastics via rigid blade simulations or include the effects using only prescribed motions to avoid complexity in simulation setup.
  - **How important are aeroelastic effects in capturing separated flows?**
  - **What bias, if any, is introduced when prescribed motions are applied versus coupled CFD-CSD?**

1.4.2 Goal 2: Advance the Knowledge of the Physics of Separated Flows on Rotors

A state-of-the-art CFD modeling approach will evaluate multiple scenarios with separated flow on rotating systems where high-quality experimental data are also available. Experiments and computations, when leveraged in parallel, have the potential to yield a wealth of information. Access to high-quality, trusted experimental data is crucial for validation of computational approaches and results. Once validated, computations can be exploited to gather data that are not restricted by data acquisition capability, feasibility of sensor placement, and other physical limitations. This gives aerodynamicists access to data that fully define the entire flowfield which cannot be achieved via experimentation. These large data sets permit the exploration of complex flowfields that hold the potential to significantly advance understanding of flowfield physics and associated aeromechanics phenomena. Advancement from this work can be leveraged for enhancements to model-based design, improvements in aeromechanics predictions, and mitigation of undesirable aeromechanics phenomena.

Enhancements to Model-Based Design

Traditional approaches to rotorcraft design rely largely on empirical methods derived from historical helicopter data [36–38]. Many next-generation rotorcraft designs propose leveraging non-conventional design features to meet advanced performance requirements. Traditional empirical approaches do not work well for evaluating these modern VTOL designs [39]. Experts have called for a shift from purely empirical design methods to model-based design [40–42]. Rapid early design phase assessments rely on reduced-order models, which are computationally cheaper but still accurate, for evaluation. Deeper understanding of flowfield physics, using CFD data, not only permits the refinement of current empirical models to achieve increased robustness but also permits the development of new models that have a basis in physics and are not purely empirical functions based on obsolete technology. Current efforts to develop physics-based reduced-order models target aeromechanics phenomena such as dynamic stall, a common cause of separated flow on the rotor [43]. CFD has the potential to play an important role in guiding the development of these reduced-order models.

Improvements in Aeromechanics Prediction

Accurate predictions of complex aeromechanics phenomena require high-fidelity analyses as problems are highly coupled and the underlying physics are highly nonlinear. Many prediction methods rely on the accurate identification and classification of dominant flowfield features, such as tip vortices. Blade-vortex interactions (BVI), as an example, are partially responsible for flow separation on the rotor [44–46]. Knowledge of the strength and location of the vortices with respect to the blade for all azimuth positions permits application of the three-dimensional Biot-Savart Law over the entire rotor plane, advancing the understanding that individual flow features have on separated flow on the rotor. Even state-of-the art experimental facilities do not have the capability to capture such data, thus high-fidelity computations must fill that gap.

Mitigation of Undesirable Aeromechanics Phenomena

A portion of current rotorcraft research targets the reduction and/or mitigation of complex aeromechanics phenomena. Active flow control efforts seek to alter flow separation dynamics to diminish the negative effects that these phenomena can have on the rotor, such as fatigue due to vibratory loading. These efforts require detailed knowledge of the flowfield physics, and furthering the current understanding of flowfield physics will guide future active flow control research. Proposed noise reduction techniques rely on identification of acoustic source points on the rotor so that aerodynamics in the vicinity of the rotor can be altered [47–49]. Both identifying these source points and effectively altering the local aerodynamics also requires extensive knowledge of the flowfield physics.

Questions to Answer:

Both classic dynamic stall and blade vortex interactions are responsible for flow separation on the rotor. Experimental data used to identify stall on a rotating system is often limited to pressure sensors on the blades as particle image velocimetry (PIV) and laser doppler velocimetry (LDV) placement are extremely difficult for a rotating system. Pressure integration along the blade surface yields sectional airloads that can be used to identify regions of flow separation. However, with limited visual and flowfield data it is impossible to classify flow separation mechanism based on experimentation alone.

- **How can classic dynamic stall be isolated from BVI and other mechanisms of separation on a rotating system?**
- **Can flowfield data from CFD simulations be used to classify flow separation mechanisms on a rotating system?**
- **How do isolation methods affect rotor downwash, and what is effect does that have on**

airloads predictions?

1.4.3 Goal 3: Explore Application of the Biot-Savart Law to Rotor Plane Vortex Filaments

Blade vortex interactions are a common aeromechanic phenomena experienced by rotorcraft and are known to cause flow separation on the rotor. However, little research has been performed to understand what vortex characteristics are linked to flow separation. What little research has been done has remained focused on two-dimensional simulations where rotation is not considered [50]. Understanding the behavior of trailing tip vortices in the rotor plane and their effect on subsequent blade passes is crucial to further advancement of rotorcraft design.

Questions to Answer:

The Biot-Savart Law can predict induced velocities at a point due to a vortex filament by integrating over the entire length of the filament. CFD provides entire flowfield data where vortex filaments can be identified and tracked throughout an entire rotor revolution, providing aerodynamicists with sufficient data to use the Biot-Savart Law on real data.

- **Can the Biot-Savart Law be applied to accurately predict induced velocities in a complex rotor plane?**
- **What modifications, if any, are required to apply the Biot-Savart Law to a viscous flowfield?**
- **What are the extents of BVI influence over the advancing and retreating rotor blades?**

CHAPTER 2

METHODOLOGY

Separated flows are highly nonlinear and require high-fidelity modeling techniques such as CFD. However, there are an abundance of CFD solvers used in the modern aerospace industry. Each solver is equipped with a variety of turbulence models and solves the Navier-Stokes equations using a number of different techniques. Prior to a CFD study that will be dominated by separated flows and their associated nonlinearities, it is important to understand the consequences that different models, numerical schemes, overall code formulations, and meshes have on the solution accuracy to ensure informed decisions are made. The most important features required for accurately capturing separated flow physics are discussed here and explored through computations to identify best practices for at a state-of-the-art CFD approach for massively separated flows in a three-dimensional rotating system.

2.1 Turbulence Modeling

The most accurate turbulence predictions are achieved using direct numerical simulation (DNS). DNS requires that grid resolution is refined to capture all of the scales of turbulence. It has the ability to accurately capture massively separated flows; however, it is prohibitively expensive for application outside of basic turbulence research. Therefore, for engineering applications, turbulence must be at least partially modeled [51].

As CFD has evolved over the years, a number of turbulence models have been developed, implemented, and widely applied throughout academia, government, and industry. The models vary in fidelity and associated computational cost. The capabilities and limitations of various turbulence and transition models with respect to engineering applications are addressed here, in order of decreasing fidelity.

2.1.1 Large Eddy Simulation

A large eddy simulation (LES) is the most robust turbulence modeling technique below DNS. Like DNS, LES methods are able to capture massively separated flows. LES methods resolve large scale eddies that dominate the flowfield physics. These large eddies are responsible for the majority of momentum transport, contain most of the flow's kinetic energy, and comprise a large majority of the contributions to the Reynolds stress tensor. Smaller sub-grid scale (SGS) eddies that are not resolved are modeled via the SGS stress tensor, shown in Equation 2.1 [52].

$$\tau_{ij} = \left(\rho\overline{\overline{u_i}\,\overline{u_j}} - \overline{u_i}\,\overline{u_j}\right) + \left(\overline{u'_i\overline{u_j}} + \overline{\overline{u_i}u'_j}\right) + \left(u'_i u'_j\right) \tag{2.1}$$

LES requires highly refined grids. Thus, statistical data can be leveraged to model the sub-grid scale eddies accurately with relatively simplistic models. Because sub-grid scale turbulence is modeled, the grids can be much coarser than those required for DNS, which requires grid scales to be on the same order of magnitude as the Kolmogorov length scale. This results in reduced computational time. However, the grids must still be refined so that all non-isotropic turbulence is captured, not modeled. Because highly refined grids are still required to resolve non-isotropic turbulence, the reduction in computational time is not sufficient for practical engineering applications. LES computations were prohibitively expensive and were not considered in this study [51].

2.1.2 Reynolds-Averaged Navier-Stokes

For most engineering applications, turbulence is modeled explicitly in the unsteady Reynolds-Averaged Navier-Stokes (URANS) equations. The URANS equations are achieved by applying Reynolds averaging to the Navier-Stokes equations, separating each variable into mean and fluctuating components and then time-averaging the result. The resulting URANS equations contain a symmetric tensor known as the Reynolds stress tensor: =

$$\tau_{ij} = \overline{u_i u_j} \tag{2.2}$$

The components of the Reynolds stress tensor are unknown and can not be precisely determined, adding six additional unknowns to the system. This is known as the turbulence closure problem [51]. Most URANS models make use of the Boussinesq approximation

$$\tau_{ij} = 2\nu_T S_{ij} - \frac{2}{3}k\delta_{ij} \tag{2.3}$$

to estimate the components of the Reynolds stress tensor, where ν_T is the eddy viscosity and k is the turbulent kinetic energy.

These methods range in fidelity from algebraic models, where no additional differential equations are added to the system up to two-equation models, where two additional differential equations are added to the system to estimate turbulent kinetic energy, eddy viscosity, and length scales. [51].

Algebraic models are the simplest of the URANS methods and are quite easy to implement. However, algebraic models are incomplete. Their formulations contain empirical coefficients which have been determined from a subset of cases. Their application is thus limited to cases that demonstrate similar physics to the cases from which the model was developed. As flight vehicle designs become more and more complex, a priori knowledge of the flowfield physics can not be assumed when complex geometries come into play. Because of their limited application to complex aerodynamics, algebraic models were not investigated in this study.

One-equation models incorporate one additional differential equation into the system of equations to determine the value of the turbulent eddy viscosity. Most one-equation models truncate the Boussinesq approximation after the first term[53]:

$$\tau_{ij} = 2\nu_T S_{ij} \tag{2.4}$$

This eliminates the contributions of turbulent kinetic energy to the Reynolds stress tensor. While eliminating the need for a second equation, truncation of the second term significantly reduces the fidelity of the one-equation models [51].

The most robust and commonly used one-equation model in modern engineering applications is the Spalart-Allmaras (SA) model [54], which is included as port of this study. Unlike some other one-equation models, the SA model is complete, meaning an a priori knowledge of the turbulent mixing length is not required. It introduces a differential equation for the turbulent molecular viscosity which is used to calculate the eddy viscosity. A modified version of the SA model includes a trip term for transition modeling; however, the standard SA model utilized for this study is a fully turbulent model. Details on the standard SA formulation as well as the trip modification, can be found in References [53, 54].

The SA model fills a specific niche for engineering applications. It has been shown to provide accurate force, moment, and performance predictions in when the flow is attached [55]. However, it must be applied with caution. Outside of the linear aerodynamic regime, it has shown to have insufficient complexity to capture massively separated flows [56]. In addition, when laminar flows exist for moderate Reynolds numbers, transition must be taken into account in order to get accurate lift over drag (L/D) predictions [55]. Thus, when flow separation and transition come into play, a more robust model is required. Two-equation models are some of the most commonly used turbulence modeling techniques for modern engineering applications. Unlike one-equation models, the entire Boussinesq approximation is retained, leading to a more complex and higher fidelity solution. Thus, the addition of two differential equations instead of one is required to determine both the eddy viscosity and kinetic energy. All two-equation turbulence models are complete, thus a priori knowledge of the turbulent mixing length is not required.

A common two-equation model that is evaluated here is the Menter $k\omega$ shear-stress transport ($k\omega$-SST) model which introduces equations for turbulent kinetic energy specific dissipation into the system. Additional details of the model can be found in Reference [57].

Two-equation models have their place in engineering applications as well. They provide improved performance over the one-equation models due to retention of the full Boussinesq approximation. They have demonstrated the ability to provide accurate boundary layer predictions; however, for time-accurate simulations of separated flows, they do not accurately capture separated flow physics [58]. This drawback can significantly affect performance predictions on complex aircraft [55]. Thus, a more robust equation is still required for future aircraft design applications.

2.1.3 Hybrid URANS-LES

A hybrid URANS-LES model serves as a compromise between URANS and LES [59]. Hybrid models are able to accurately capture separated flows while keeping computational costs relatively low compared to LES and DNS by combining them into a unified turbulence model. LES calculations are used to resolve large eddies away from the body. This allows separated regions of the flowfield to be resolved instead of modeled. In the boundary layer where turbulence scales are very small and not isotropic, hybrid methods switch to URANS turbulence closures. LES methods would required extreme refinement in these regions, while URANS methods can provide similar accuracy on a much coarser grid for significantly reduced computational cost.

A detached eddy simulation (DES) is one of the most commonly used hybrid URANS-LES methods. In its original formulation, DES was intended for thin boundary layers. Depending on the mesh cell size in the near-body grid, the model would switch from URANS to LES too close to the body. To correct this, a modification, was made in 2006 to delay the switch from URANS to LES and made the updated model, known as delayed detached eddy simulation (DDES) less susceptible to variable grid spacing. In most simulations with massively separated flows, DDES is preferable to DES [60].

2.1.4 Turbulence Modeling Approach

A turbulence model study comparing both URANS and DDES methods is first performed on a finite wing. The finite wing at post-stall angles of attack produces large regions of separated flow but does not require the computational resources of a three-dimensional rotating system. This permits the evaluation of many turbulence models on a number of grids with separated flows while minimizing computational expenditures. The most effective turbulence models are then applied to the full three-dimensional rotating simulations to achieve the highest-fidelity state-of-the-art solution.

2.2 Solution Refinement

CFD error arises from the discretization of continuum flow into discrete spatial elements via the computational grid and discrete temporal elements via the computational timestep. Solution accuracy is highly dependent on using appropriate grid and timestep refinement. Thus, it is important for any CFD user to understand how to determine what defines appropriate grid and timestep refinement for a state-of-the-art CFD simulation.

Grid refinement is an important factor in achieving accurate high-fidelity CFD simulations. In numerical simulations, as grid spacing is refined, error associated with spatial discretization should asymptote to a minimum value. While increased grid refinement reduces discretization error, it also impacts the accuracy of turbulence models. Increasingly refined grids capture a wider range of eddy scales and reduce the levels of turbulence that must be modeled.

To verify that appropriate grid refinement has been achieved for any CFD simulation, grid refinement studies must be performed. Grid refinement studies involve generating a set of grids for the same model with increasing levels of refinement. CFD solutions are obtained for all grid levels and key variables are analyzed for solution convergence across the grid levels. For fixed wing applications, common variables used to evaluate grid convergence are lift, drag, and skin friction. For rotorcraft applications, these variables are often thrust, power, and Figure of Merit. For each of the configurations evaluated here, grids are developed in accordance with the results of a refinement study performed in Section 5.1. When performing any CFD simulation it is important for the user to follow similar grid refinement studies or grid generation best practices to ensure the complete CFD model is accurate.

Timestep refinement has been the topic of previous research and is another important factor in achieving an accurate unsteady numerical simulation, as separated flows are often dominated by time-varying nonlinear flow features. Significant prior research has explored timestep refinement for dynamic stall (Refs. [61–63]) and rotor simulations ([21, 64]). State-of-the-art best practices are applied in this thesis with respect to timestep.

2.3 Numerical Schemes

Structured CFD solvers often have number of spatial discretization schemes, or stencils, that can yield anywhere from first-order accurate to sixth-order accurate data. Research has shown that leveraging high-order accurate numerical schemes for rotor simulations can improve solution accuracy without significantly increasing run time [65, 66]. Unlike structured solvers, unstructured solvers typically do not have high-order spatial discretization schemes. The finite volume methods typically applied to unstructured stencils make spatial discretization algorithms much more difficult to develop. Thus, with current technological and computing advances, unstructured solvers are only second-order accurate in space.

Understanding the details and impacts of various numerical schemes and how they compare to each other is important. This study analyzes results obtained using various differencing schemes in OVERFLOW. Details of each numerical scheme used in this study are provided in Section 2.4.1. Results of the numerical scheme investigation can be found in Chapters 5 and 6.

2.4 Computational Tools

2.4.1 OVERFLOW

OVERFLOW [67] is a state-of-the-art full Navier-Stokes CFD solver developed at NASA Langley Research Center in Hampton, Virginia. It is a compressible, structured solver with two-dimensional, three-dimensional, and axisymmetric operational modes. The solver has up to fourth-order temporal accuracy and sixth-order spatial accuracy, employing node-based finite differencing [68]. OVERFLOW also employs a number of turbulence models, ranging in fidelity from large algebraic models to large eddy simulations, as discussed in Section 2.1.

OVERFLOW implements a number of high-order spatial flux differencing schemes. The second-, fourth-, and sixth-order central differencing schemes are given for a flux, F, in Equations 2.5-2.7 [68].

$$\frac{\partial F}{\partial x} = \frac{F_{i+1} - F_{i-1}}{2\Delta x} \tag{2.5}$$

$$\frac{\partial F}{\partial x} = \frac{-F_{i+2} + 8F_{i+1} - 8F_{i-1} + F_{i-2}}{12\Delta x} \tag{2.6}$$

$$\frac{\partial F}{\partial x} = \frac{F_{i+3} - 9F_{i+2} + 45F_{i+1} - 45F_{i-1} + 9F_{i-2} - F_{i-3}}{60\Delta x} \tag{2.7}$$

OVERFLOW has message passing interface (MPI) and domain splitting capabilities so that it can be used on massively parallel computing systems. This is important as it permits the use of large, dense grids to resolve complex flowfield physics while still achieving reasonable solution times.

2.4.2 Dymore

Dymore is a multi-body dynamics code, developed by Prof. Olivier A. Bauchau, that is used to model the structure of complex vehicles such as multi-body rotorcraft [69]. It is a finite element-based code that can model both rigid and elastic components. Rigid bodies are modeled as localized masses while elastic components, such as wings or rotor blades, are modeled as discretized beams with axial, bending, torsional, and shearing stiffness. Rigid and elastic components are connected via joint models, including revolute, prismatic, screw, cylindrical, planar, and spherical joints. Elastomeric properties of the connections can be included in the joint model via torsional springs and dampers. Dymore can compute both static and dynamic analyses. Static analyses solve the system's equations of motion by eliminating all time derivatives, providing initial conditions for dynamic analyses. Dynamic analyses solve the system's complete equations of motion as perturbed by airloads.

For analyses here, Dymore is coupled with OVERFLOW to achieve a loosely-coupled CFD/CSD solution, which has been proven for a number of CFD and CSD solvers [31, 70–74].

Airloads are obtained from CFD analyses in OVERFLOW and passed to Dymore through an external aerodynamics plugin. Airloads are used within Dymore to perturb the dynamic solution to obtain updated blade deformations. Blade deformations are passed back to OVERFLOW and applied to the CFD simulation. This loose coupling procedure is continued until both the structural and CFD solutions converge.

CHAPTER 3

EXPERIMENTAL DATA SETS

A large majority of experimental dynamic stall research has focused efforts on semi-infinite pitching wings [10, 12, 14]. Three-dimensional finite wing [23, 75] and rotating effects [28] were first investigated via experimentation in the 1990s. Since then, only a handful of other high-quality, trusted experiments that can be used for CFD validation have been completed due to the complexity of gathering experimental data in a moving frame [26, 30, 32]. It is important that experimental data used for validation of CFD be performed in controlled wind tunnel environments, where CFD simulations can be designed to match the experimental conditions as closely as possible. Attempting to model flight test scenarios, such as those from the UH-60 Airloads program, introduces significantly more unknowns. Discrepancies between experimental data and CFD results can be identified when experimentation is isolated to a controlled wind tunnel environment. This research leverages experimental wind tunnel data sets for a finite wing and a rotor configuration.

3.1 OA209 Finite Wing

Wind tunnel tests were performed in the ONERA F2 wind tunnel specifically to study the three-dimensional effects of dynamic stall [23]. The facility has a test section with a length of 5.0 meters, a width of 1.4 meters and a height of 1.8 meters in which wind speeds are capable of reaching 100 m/s.

Three wall-mounted models were constructed for the OA209 airfoil for these tests. The OA209 airfoil, shown in Figure 3.1, is a slightly cambered airfoil with a 9% maximum thickness at 29.3% chord and a 1.6% maximum camber at 17.1% chord. Two of the models were infinite wings, spanning the entire width of the test section (1.4 m) with no twist. One (model C300) was constructed with a chord length of 0.3m and the other (model C500) with a chord length of 0.5m.

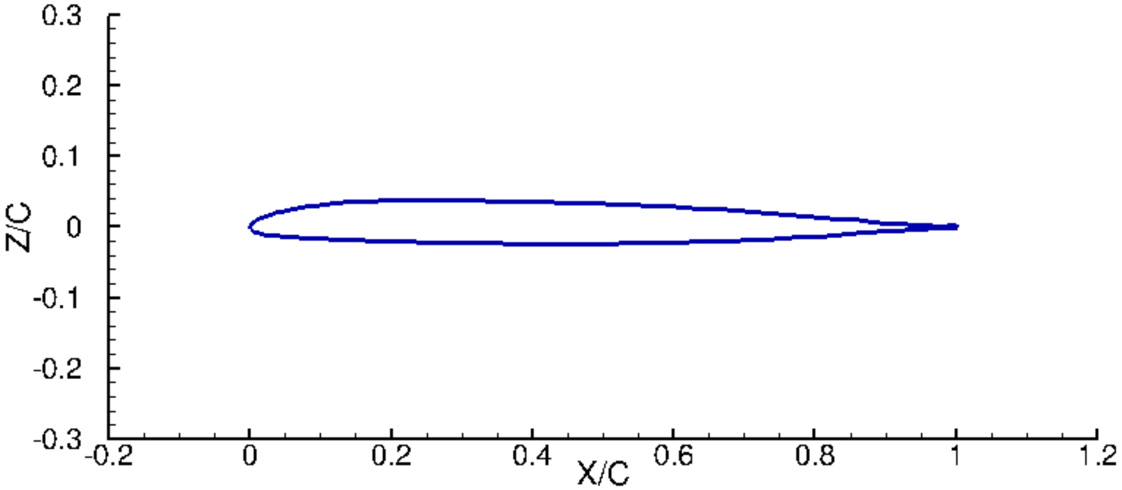

Figure 3.1: OA209 airfoil geometry

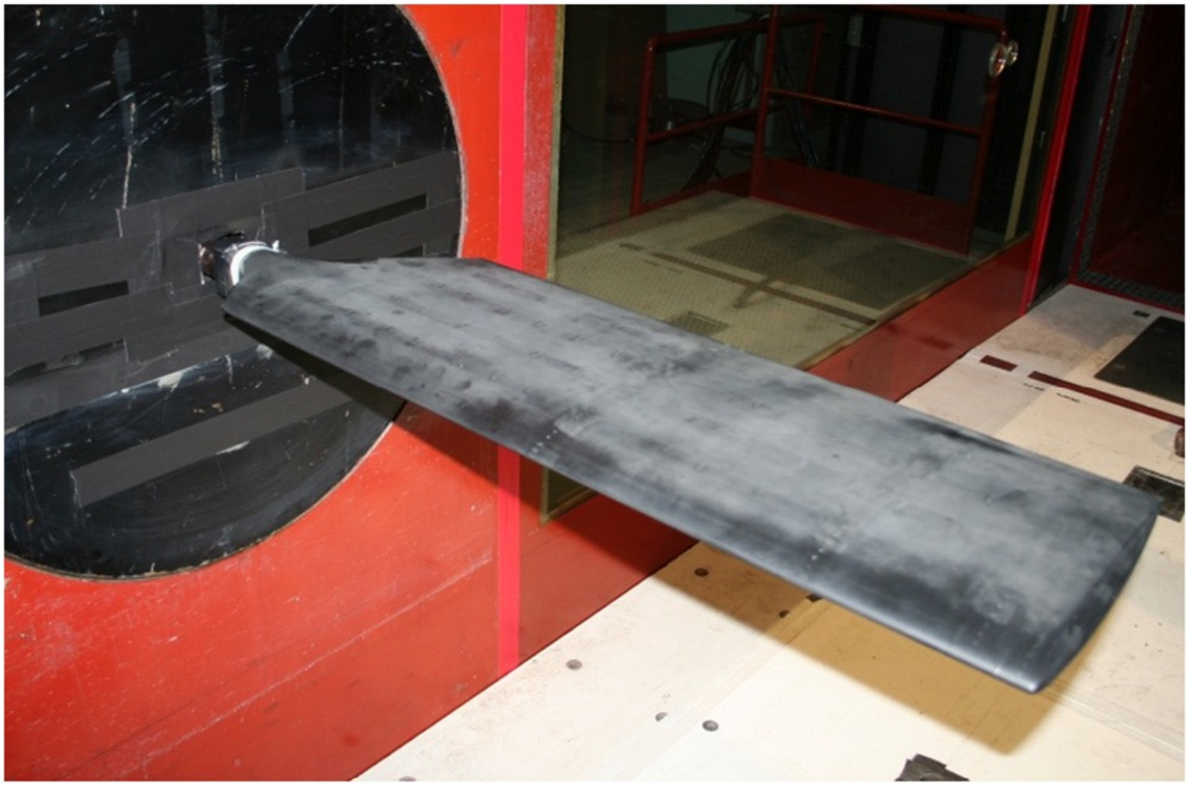

Figure 3.2: Finite OA209 wing (C300-3D model) mounted in the ONERA F2 wind tunnel (from Ref. [23])

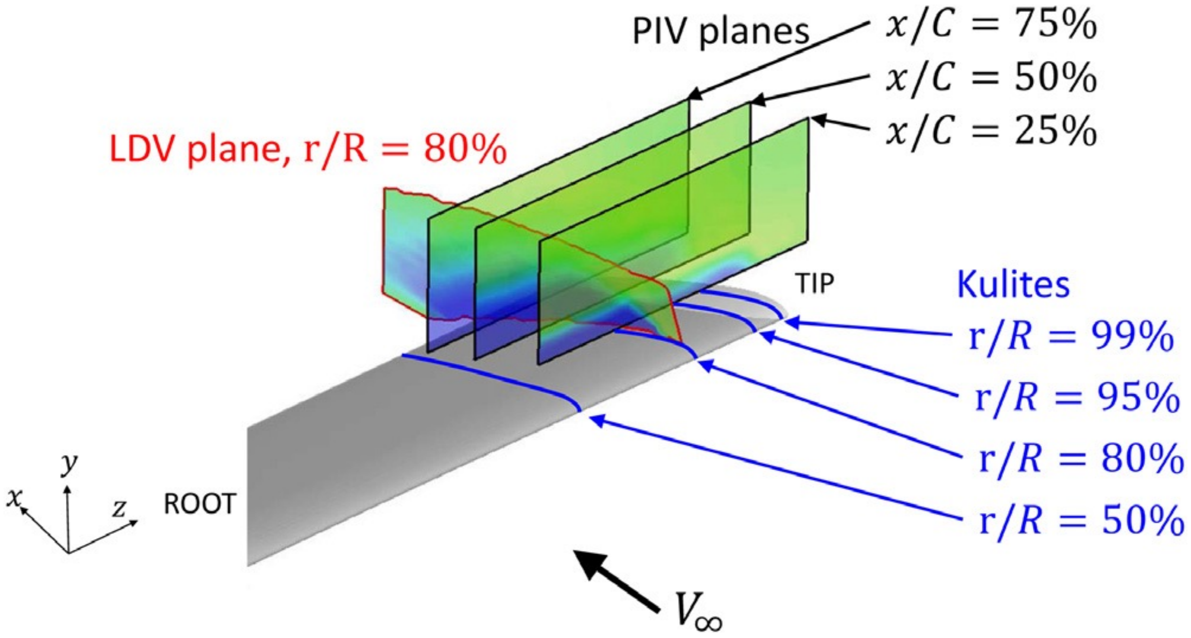

Figure 3.3: PIV and LDV plane locations on finite OA209 wing (from Ref. [23])

The third model (C300-3D) was a finite wing with a span of 0.9m and chord length of 0.3m. As the purpose of this study is to evaluate and further understand the complete physics of dynamic stall, computational efforts are focused solely on the finite C300-3D wing [24].

The finite C300-3D wing model, shown in Figure 3.3, was equipped with various instrumentation to permit correlation with CFD data. Four spanwise locations ($r/R = 50\%$, 80%, 95%, and 99%) were equipped with 28 Kulite pressure transducers each for a total of 112 simultaneous static pressure measurements. Integration of these static pressures at each pitch angle permits comparison between experimental and computational aerodynamic forces and moments at the four aforementioned spanwise stations. Mean flow velocities and turbulent quantities were gathered via an LDV system, installed to capture data at the spanwise r/R=80% spanwise station. These LDV data not only permit comparison between experimental and computationally derived flowfields but also allow for more in-depth analyses of the spanwise forces and moments at that spanwise location. Force and moment data can be mapped to and further explained by specific flowfield features. Similarly, flowfield data were acquired via a PIV system at three different chordwise locations ($x/c = 25\%$, 50%, and 75%) to allow further investigation of crossflow and three-dimensional ef-

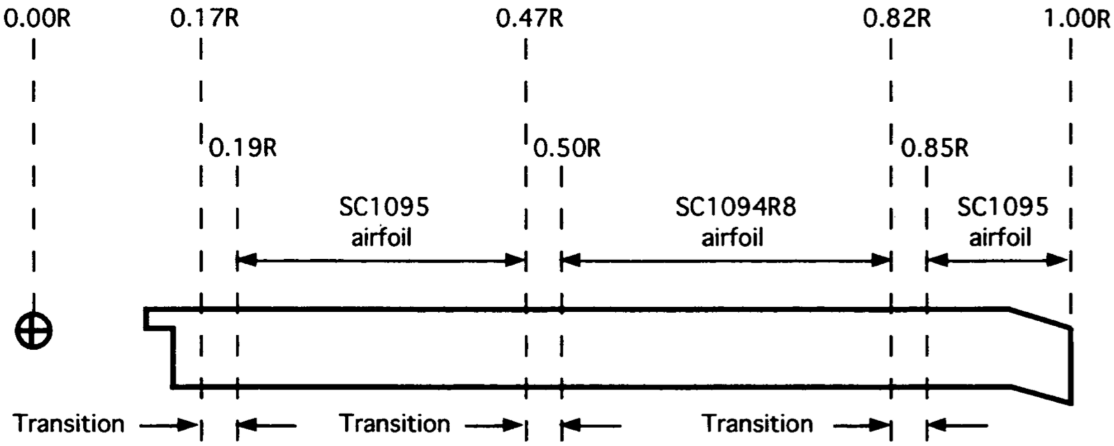

Figure 3.4: UH-60A blade airfoil distribution (from Ref. [76])

fects near the wingtip. The instrumentation setup is summarized in Figure 3.3. Additional details on the experimental setup and data acquisition can be found in Ref. [23]. Static stall data were acquired for the finite wing in flow defined by a Mach number of 0.16 and a chord-length Reynolds number of 1.0×10^6 for pitch angles ranging from $4°$ to $24°$.

3.2 UH-60A

In 2010, NASA and the United States Army jointly completed extensive wind tunnel testing on the Sikorsky UH-60A rotor [30]. Testing was conducted in the United States Air Force (USAF) National Full-Scale Aerodynamics Complex (NFAC) 40-by-80 foot wind tunnel at NASA Ames Research Center (ARC) in Moffett Field, California. The dimensions of the test section measure 39 feet high by 79 feet wide by 80 feet long. This is a closed-circuit wind tunnel that can reach maximum test section velocities of approximately 300 knots.

The UH-60A rotor is a four-bladed rotor with a radius of 26.83 feet, a chord length of 20.76 inches, and solidity of 0.0826. Blades are constructed out of SC1095 and SC1094R8 airfoil sections, as shown in Figure 3.4 and have an equivalent twist of -18 degrees. The SC1095 airfoil, shown in Figure 3.5 has a maximum thickness 9.5% at 26.9% chord and a maximum camber 0.8% at 26.9% chord. The SC1094R8 airfoil, shown in Figure 3.6 has a maximum thickness 9.4% at

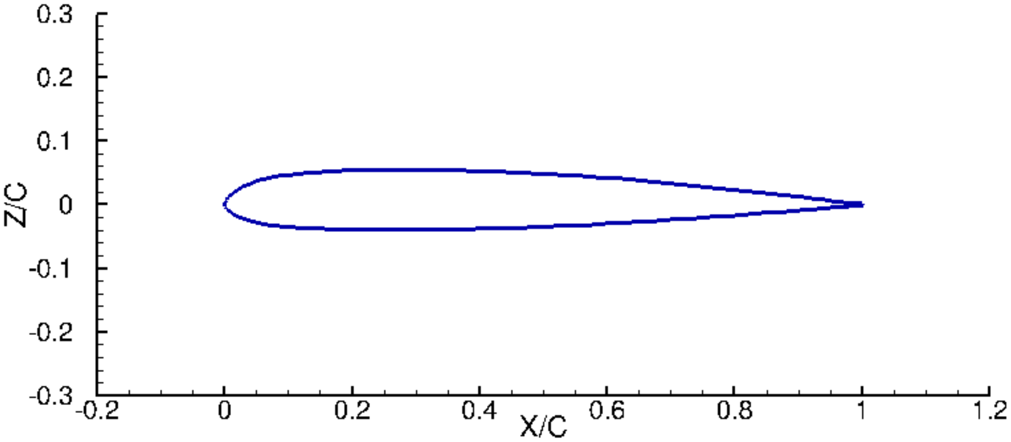

Figure 3.5: SC1095 airfoil geometry

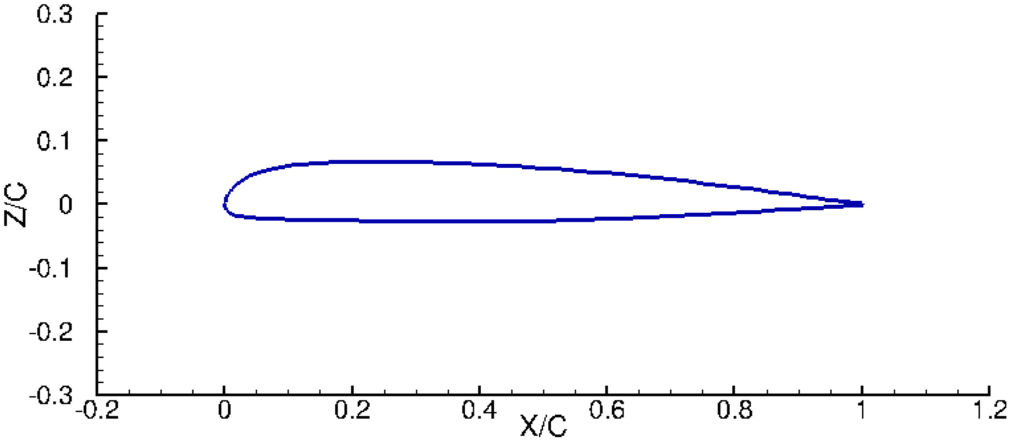

Figure 3.6: SC1094R8 airfoil geometry

Figure 3.7: UH-60A rotor mounted on the LRTA in the NFAC 40-by-80 ft. wind tunnel at NASA Ames Research Center in Moffett Field, California (from Ref. [30])

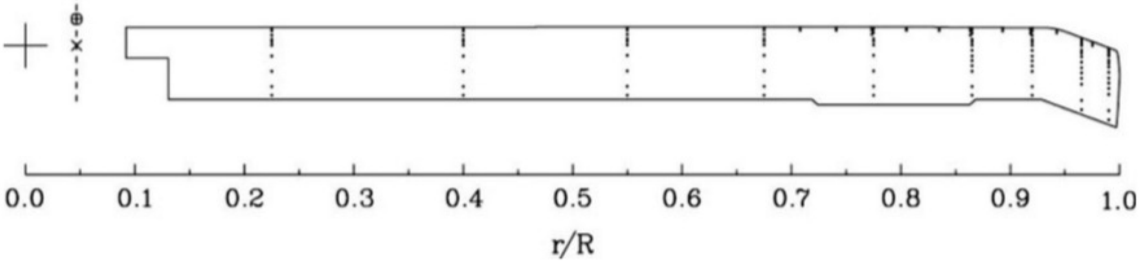

Figure 3.8: UH-60A rotor blade pressure transducer locations (from Ref. [30])

27.8% chord and a maximum camber 2.1% at 21.7% chord. It is an articulated rotor that allows lead/lag and flapping motion while the blade pitch is controlled by adjustable pitch links that move with the swash plate. For testing, the rotor was mounted on the NFAC Large Rotor Test Apparatus (LRTA) as shown in Figure 3.7 [30].

The UH-60A rotor blade was instrumented with 215 working pressure transducers, mainly placed along nine radial stations with a few additional leading edge locations, shown in Figure 3.8. PIV data were collected for one of the dynamic stall cases, however the PIV plane was spatially fixed at an azimuth angle of $\psi = 90°$. Because separated flow primarily occurs on the retreating blade, the PIV data from this experiment do not enhance the current study [30].

The experimental data set is extensive and contains six different collective sweeps where dynamic stall develops with increasing thrust. Six data points from a single collective sweep are leveraged to understand the development of separated flow on the rotor with increasing thrust, summarized in Table 3.1.

Table 3.1: Flow conditions for UH-60 rotor test points 4530, 4533-4537 in Ames NFAC 40-by-80 foot wind tunnel.

$Parameter$	TP 4530	TP 4533	TP 4534	TP 4535	TP 4536	TP 4537
α_q	$0.167°$	$0.703°$	$0.782°$	$0.858°$	$0.940°$	$0.975°$
θ_0	$4.115°$	$6.895°$	$7.956°$	$9.080°$	$10.418°$	$11.932°$
θ_{1C}	$0.326°$	$1.345°$	$1.773°$	$2.126°$	$2.760°$	$3.617°$
θ_{1S}	$-2.886°$	$-4.972°$	$-5.843°$	$-6.928°$	$-8.424°$	$-10.190°$
M_{tip}	0.625	0.625	0.625	0.625	0.625	0.625
$\frac{C_T}{\sigma}$	0.040	0.090	0.100	0.110	0.120	0.125

CHAPTER 4

COMPUTATIONAL MODELS

Computational models used in this study are constructed to represent as closely as possible the experimental setups described in Chapter 3. Details of each computational model are described in the following sections.

4.1 OA209 Finite Wing

The first configuration evaluated in this research is the three-dimensional OA209 C300-D finite pitching wing. The OA209 C300-D wing is modeled as a rigid, wall-mounted finite wing using structured grids. An extensive structured grid refinement study was performed to assess the effects of both chordwise and spanwise refinement on static stall prediction capabilities. A total of nine near-body grids were evaluated to achieve three levels of chordwise refinement as well as three levels of spanwise refinement. The nine OA-209 grid systems are constructed to mimic the experimental wind tunnel test section setup (Fig. 4.1) detailed in Section 3.1. The near-body wing grids, represented in black, are constructed of a main wing grid, a root grid, and tip grid (Figure 4.2). For all near-body grids, the leading edge spacing is 0.05% of the chord, and the trailing edge spacing is 0.02% of the chord. The near-body grids extend 0.5 chord lengths from the wing surface with $y^+ < 1.0$ and approximately 50 normal points in the boundary layer. Grid sizes for each near-body main wing grid are detailed in Table 4.1. The root and tip grids are equivalent across all nine grid systems and are detailed in Table 4.2.

Three superimposed background grids of varying refinement surround the wing and are equivalent across all nine grid systems. The level 1 background grid, represented in blue, extends 1 chord length upstream of the wing, 4 chord lengths downstream of the wing, and 2 chord lengths above and below the wing. The average spacing on the level 1 background grid for all is 1.6% of the chord length for a total of 23,688,376 points. The level 2 background grid, represented in red

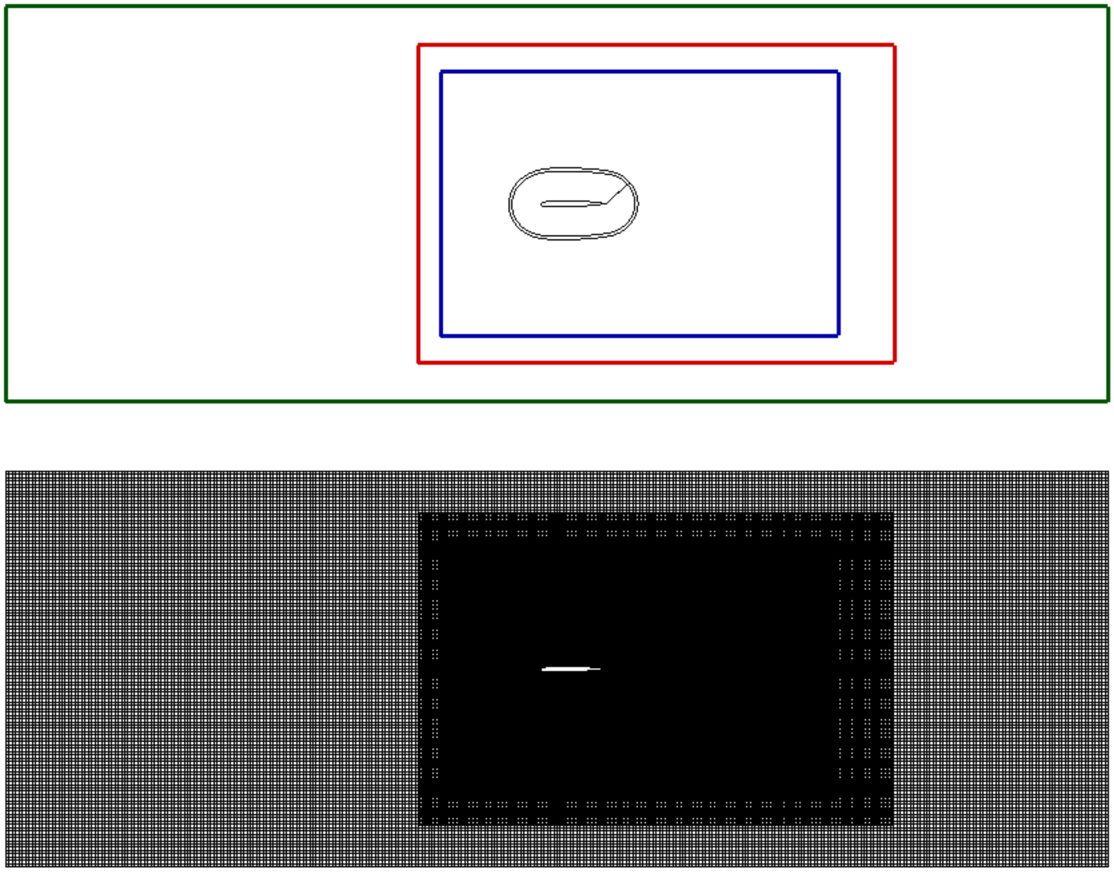

Figure 4.1: Finite OA209 wing (C300-3D model) grid overview

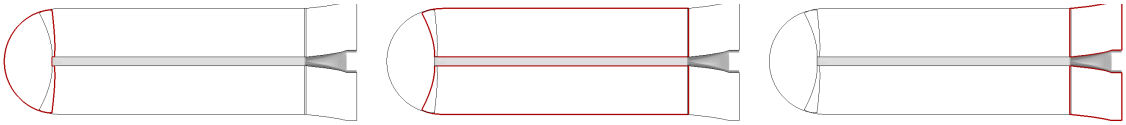
(a) Tip Grid (b) Main wing grid (c) Root grid

Figure 4.2: OA-209 near-body grid components

Table 4.1: Main wing grid sizes for OA209 C300-3D wing refinement study

Grid Level	Spanwise Points	Chordwise Points	Normal Points	Total Structured Grid Points
1A	200	278	159	8,840,400
1B	200	518	159	16,472,400
1C	200	998	159	31,736,400
2A	400	278	159	17,680,800
2B	400	518	159	32,944,800
2C	400	998	159	63,472,800
3A	800	278	159	35,361,600
3B	800	518	159	65,889,600
3C	800	998	159	126,945,600

extends 1.35 chords upstream of the wing, 4.85 chords downstream of the wing and 2.4 chords above and below the wing. The average spacing on the level 2 background grids is 3.0% of the chord length for a total of 5,626,145 points. The level 3 background grid, represented in green, matches the extents of the wind tunnel detailed in Section 3.1. The average spacing on the level 3 background grid is 5.0% of the chord length for a total of 3,850,825 points. Background grid parameters are summarized in Table 4.3.

Each of the wind tunnel walls are modeled as inviscid, adiabatic walls while the test section inlet and outlet are modeled using the characteristic condition based on Riemann invariants. Inflow is assumed constant across the inlent; no wind tunnel boundary layer is added.

Table 4.2: Root and tip grid parameters for OA209 C300-3D wing

Grid Level	Spanwise Points	Chordwise Points	Normal Points	Total Structured Grid Points
Root Grid	118	167	159	3,133,254
Tip Grid	201	81	159	2,588,679

Table 4.3: Background grid parameters for OA209 C300-3D wing

Grid Level	X Points	Y Points	Z Points	Total Structured Grid Points
Background 1	376	251	251	23,688,376
Background 2	241	145	161	5,626,145
Background 3	335	95	121	3,850,825

4.2 UH-60A Rotor

The UH-60A rotor is modeled as an aeroelastic rotor, using a loosely coupled CFD-CSD approach. Details of both CFD and CSD models are described in the following sections.

4.2.1 OVERFLOW Grids

Two different grid systems were leveraged to investigate separated flows on the UH-60A rotor in OVERFLOW: a moderate engineering grid and a refined physics grid. Both near-body grid systems model four UH-60A rotor blades and the LRTA (Fig. 4.3). The near-body wing grids are constructed of a main wing grid, a root grid, and a tip grid (Fig. 4.4). The root and tip grids, along with the LRTA grids, are equivalent between the two grid systems. All near-body grids in both systems have $y^+ \leq 1.0$ with approximately 35-50 normal points in the boundary layer. Refinement is limited to the main wing grid on each of the four blades as well as the off-body grids.

For the engineering grid, the blade is modeled by a C-grid that consists of approximately 3 million grid points. There are 302 total points in the flow direction (198 on the body and 104 in the wake), 100 spanwise points, and 77 normal points. Both the leading and trailing edge spacing values are 0.1% of the chord. Two near-body refined blocks, consisting of 20 million and 4 million

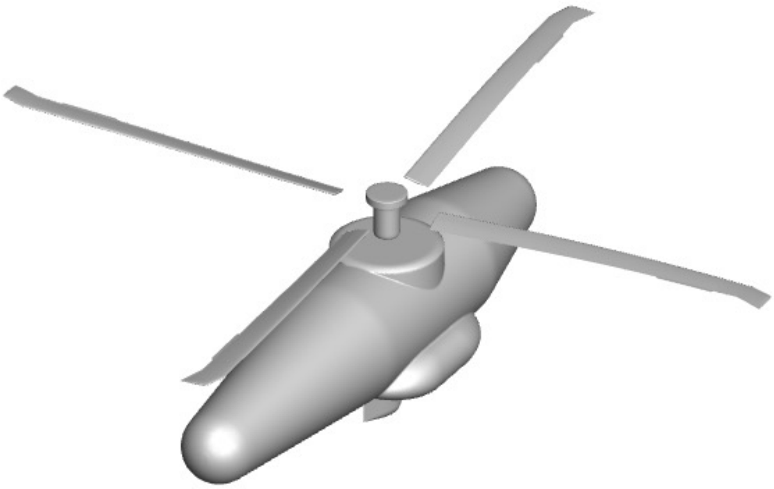

Figure 4.3: UH-60A model

points respectively, were used ensure sufficient refinement in the near wake. Seven levels of off-body grids generated by OVERFLOW extend 6.25 rotor radii in all directions and consists of 42.6 million points. The engineering grid is summarized in Table 4.4.

Blade grids for the refined UH-60A were constructed using the findings from the grid study in Section 5.1. Each blade consists of approximately 49 million grid points with 500 chordwise points to sufficiently define the characteristic length, 697 spanwise points to achieve a maximum mid-chord aspect ratio less than 5, and 140 normal points. The leading edge spacing is 0.04% of the chord and the trailing edge spacing is 0.01% of the chord. Seven levels of off-body grids generated by OVERFLOW extend 10 rotor radii in all directions and total 71 million points. The refined physics grid size is summarized in Table 4.5.

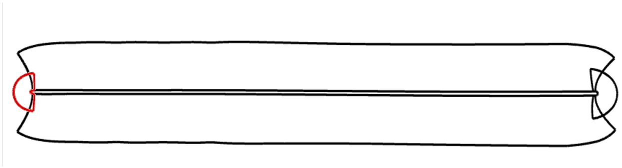

(a) Tip Grid

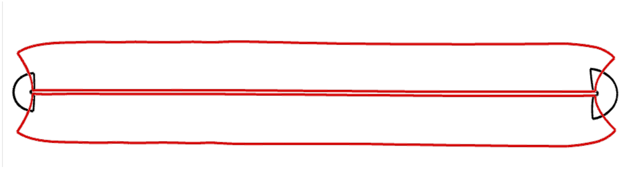

(b) Main wing grid

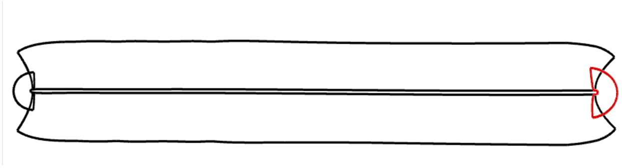

(c) Root grid

Figure 4.4: UH-60A wing grid components

4.2.2 Dymore Model

The UH-60A structural model used in this investigation is a multi-body dynamics model, developed in part by The Improved Prediction of Rotor Loads TAJI project, funded by the Vertical Lift Consortium, that accurately captures the motion of the entire rotor head (Ref. [77]). A sketch of the model is provided in Figure 4.7. Each blade is modeled as a elastic beam with 11 elements: ten elements on the main blade with one additional element to capture the swept tip, that permits blade deflection and torsion but not deformation in the blade cross section. When coupled with the moderate grid, 99 aerodynamic stations are used. When coupled with the refined grid, 499 aerodynamic stations are used. Each blade is rigidly connected to the pitch horn and damper horn, both modeled as rigid bodies. Each pitch horn is attached to its pitch link, also modeled as a rigid body, via a spherical joint. Each pitch link is connected to the swashplate, modeled as four rigid swashplate spokes, via a universal joint. Each root retention structure is modeled as three rigid body segments, as shown in Figure 4.7. Segment 3 is rigidly connected to the blade and damper horn. Segments 2 and 3 are rigidly joined to each other as well as the pitch horn. Segments 1 and

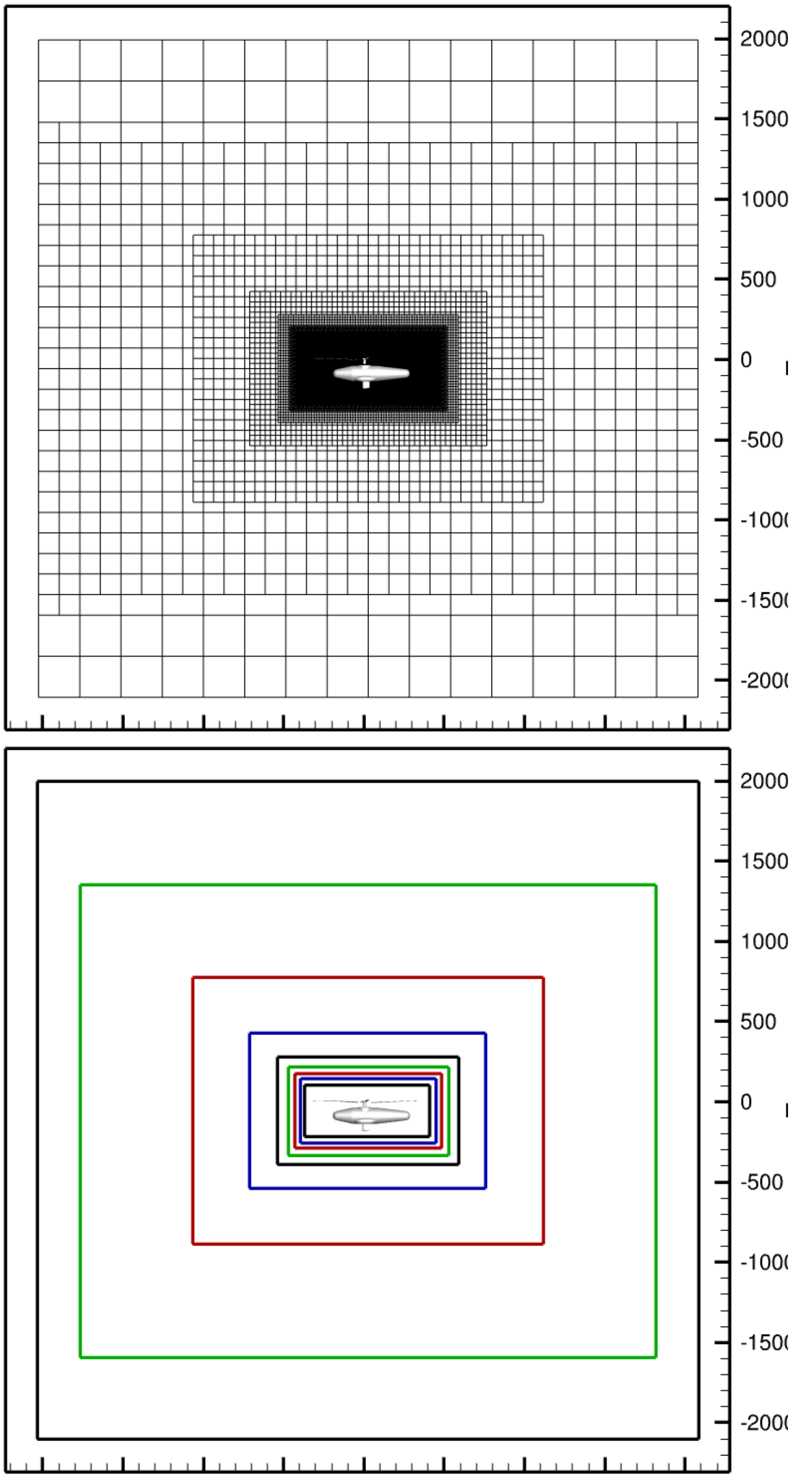

Figure 4.5: UH-60A grid overview

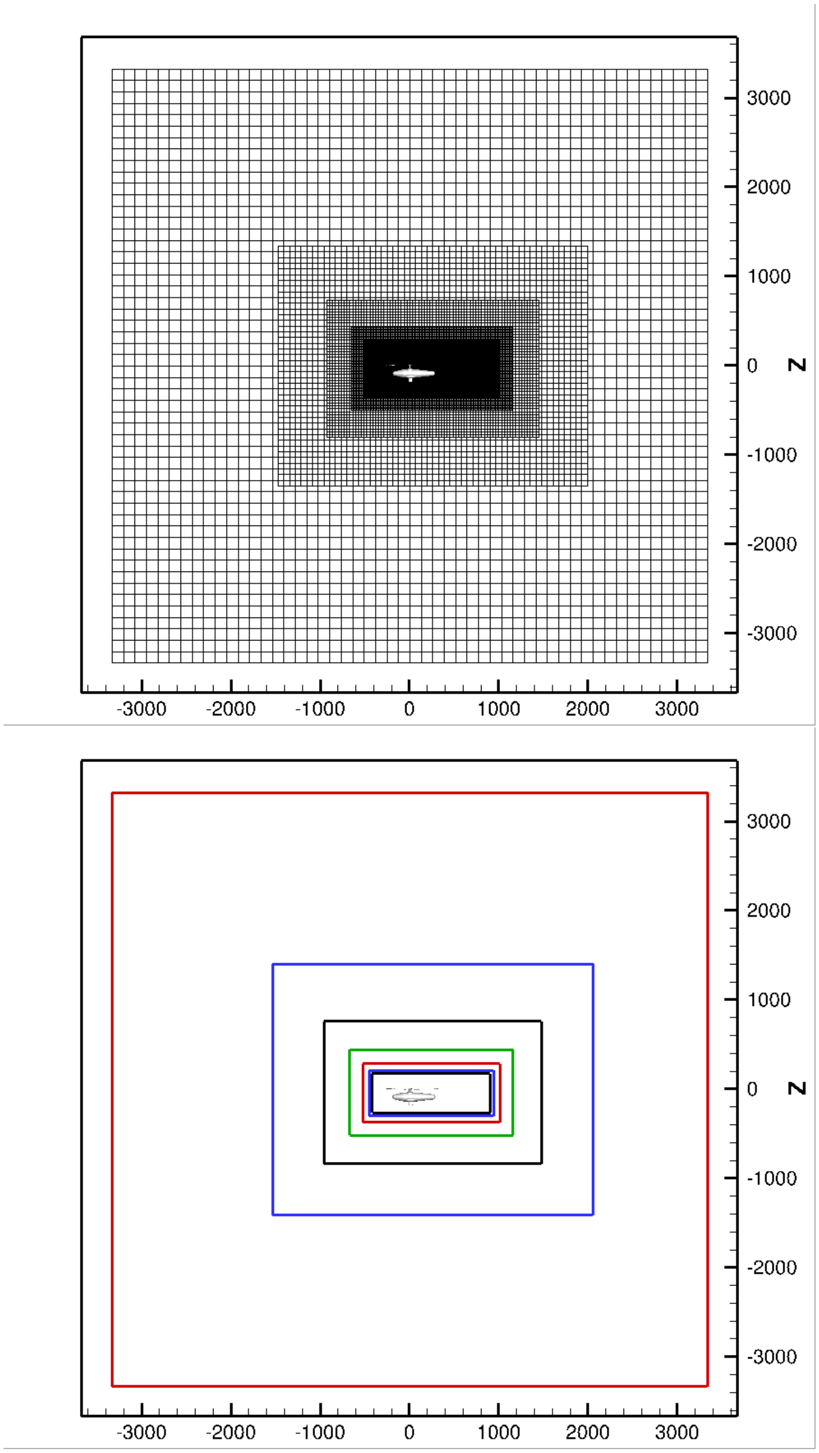

Figure 4.6: UH-60A grid overview

Table 4.4: UH-60 Engineering Grid Information

Component	Grid Size
Blade (x4)	3,009,050 (x4)
LRTA	8,127,242
Near-Body Level 1	20,416,500
Near-Body Level 2	3,898,440
Off-Body Level 1	6,269,562
Off-Body Level 2	546,966
Off-Body Level 3	187,830
Off-Body Level 4	85,458
Off-Body Level 5	51,700
Off-Body Level 6	37,638
Off-Body Level 7	3,468
Total	33,286,154

Table 4.5: UH-60 Optimized Grid Information

Component	Grid Size
Blade (x4)	49,361,357 (x4)
LRTA	8,127,242
Off-Body Level 1	65,082,576
Off-Body Level 2	3,729,102
Off-Body Level 3	1,207,414
Off-Body Level 4	476,261
Off-Body Level 5	239,157
Off-Body Level 6	141,831
Off-Body Level 7	180,842
Total	276,629,863

2 are attached via an elastomeric bearing. Lag, flap, and pitch rotations are modeled by coincident revolute joints while the elastomeric properties are simulated using torsional springs and dampers. Segment 1 is rigidly attached to the hub. The damper arm is modeled by a rigid body and rigidly connected to the hub. The lead-lag damper is modeled as a prismatic joint connected to the damper arm and damper horn. The hub and swashplate are connected via the upper rotor shaft (not shown in Fig. 4.7), modeled as a one element elastic beam. The lower shaft (not shown in Fig. 4.7), modeled as a rigid body, connects the rotor head to the turbine.

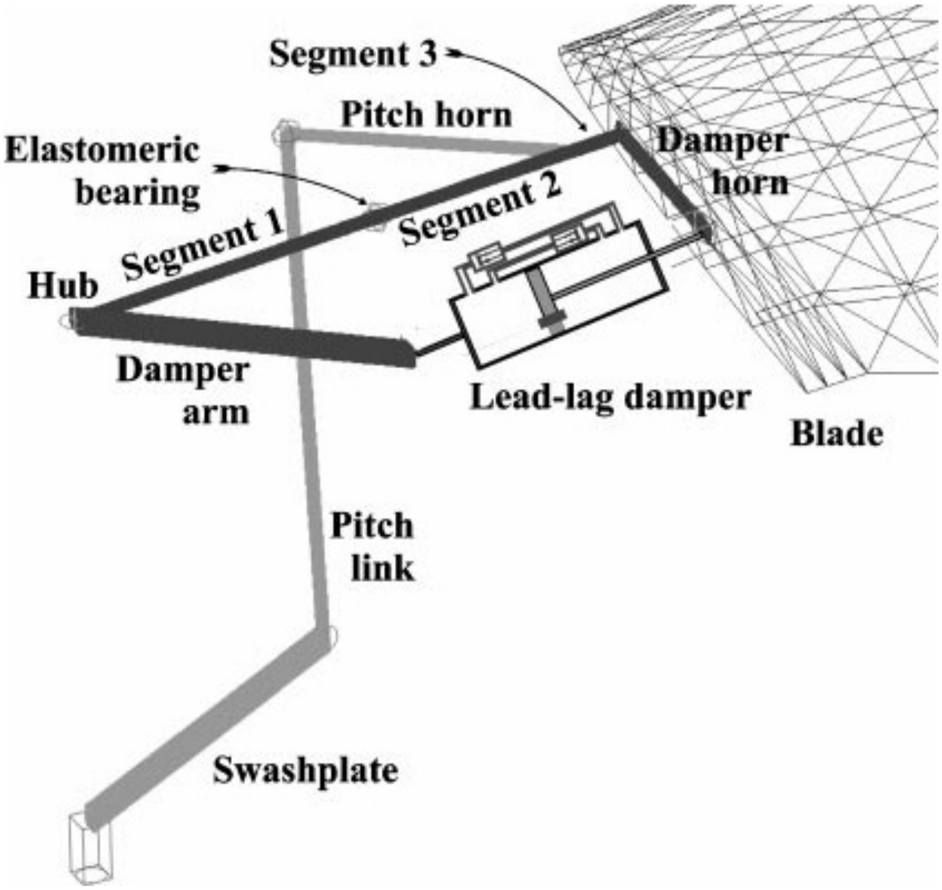

Figure 4.7: UH-60A rotor configuration (from Ref. [78])

CHAPTER 5

SEPARATED FLOW ON A THREE-DIMENSIONAL FINITE WING

The first configuration evaluated in this study is the three-dimensional OA209 C300-D finite wing. While the focus of this thesis is to further the understanding of separated flows on three-dimensional rotating systems, it can be instructive to first evaluate separated flows on a wing without rotation to distinguish effects of rotation and interactions between blades and wakes. That knowledge can then be leveraged in decision making when developing computational models for three-dimensional rotating systems, which is an expensive undertaking.

The OA209 wing was extensively tested in the ONERA F2 wind tunnel, as described in Chapter 3 Section 3.1. The available data sets from these experiments are high quality and can be used to validate methodologies of massively separated flows for translating and pitching wings. Data from numerous OA209 wing computations are evaluated to determine the most effective approach to accurately capture massively separated flows.

The OA209 C300-3D was evaluated experimentally for twenty different static configurations with varying angle of attack values that captured pre-stall and post-stall behavior. Pre-stall, stall, and post-stall configurations are simulated to evaluate the effects of mesh sizing and turbulence model on solution accuracy. The best practices determined here with static stall are then applied to dynamic stall for the UH-60A rotor.

5.1 Grid Refinement Study

In this grid refinement study, nine near body grids, detailed in Section 4.1 are evaluated for their ability to predict flow field physics on a static configuration in both attached and separated flows. Each grid was analyzed at angles of attack of $10°$, $15°$, $20°$, $21°$, and $22°$ with four popular turbulence models. The turbulence models leveraged for this study are SA RANS, SA DDES, $k\omega$-SST RANS, and $k\omega$-SST DDES. Some grid/turbulence model combinations were additionally evaluated at $19°$ based on initial results to confirm mixed results. Turbulence model selection was varied along with grid refinement to fully understand the coupling of mesh and turbulence model requirements.

Sectional lift and moment data were extracted at four spanwise stations ($r/R = 0.5$, $r/R = 0.8$, $r/R = 0.95$, and $r/R = 0.99$) corresponding to pressure tap locations on the experimental blade. Standard deviation percent (SDP) of sectional lift (c_l) and sectional moment (c_m) is used to examine solution sensitivity for pre-stall ($\alpha = 10°, 15°$), stall onset ($\alpha = 20°$), and post-stall ($\alpha = 21°, 22°$) angles of attack.

The SDP of the sectional lift (SDP_l) is the population standard deviation of sectional lift (σ_l) as a percentage of maximum magnitude of sectional lift ($c_{l_{max}}$):

$$SDP_l = \frac{\sigma_l}{|c_{l_{max}}|}. \tag{5.1}$$

where the population standard deviation of lift is the calculated using individual c_l values (c_{l_i}), the average c_l value ($c_{l_{avg}}$), and the total number of data points in the population (N).

$$\sigma_l = \sqrt{\frac{\Sigma\left(c_{l_i} - c_{l_{avg}}\right)}{N}} \tag{5.2}$$

The SDP of the sectional moment (SDP_m) is the population standard deviation of sectional moment (σ_m) as a percentage of maximum sectional moment magnitude ($c_{m_{max}}$):

$$SDP_m = \frac{\sigma_m}{|c_{m_{max}}|} \tag{5.3}$$

where the population standard deviation of moment is the calculated using individual c_m values (c_{m_i}), the average c_m value ($c_{m_{avg}}$), and the total number of data points in the population (N).

$$\sigma_m = \sqrt{\frac{\Sigma\left(c_{m_i} - c_{m_{avg}}\right)}{N}} \tag{5.4}$$

Previous studies of airfoils and wings in separated flows have provided best practices for the normal mesh cell requirements (Refs, [79],[80]). Best practices to accurately capture separated flow behavior are 30-50 normal direction boundary layer points with $y^+ \leq 1.0$ and average normal growth rate of no more than 15%. Those best practices are applied here so that deeper insights could be evaluated for the wing planar meshes. This mesh refinement study not only considered grid spacing in the wing planar directions, but also the cell aspect ratios. Combinations of mesh refinement were evaluated for three sequentially refined meshes in both the chordwise and spanwise directions, using the same hyperbolic equation with fixed 1D grid spacing at the root, tip, and leading and trailing edges. The mesh cell count around the airfoil section chord (upper and lower surfaces) was increased from 250 points to 500 points to 1000 points, while the mesh refinement along the span (each surface) doubled from 200 points to 400 points to 800 points. All meshes were analyzed at the five angles of attack and for each turbulence model for completeness. Lift and moment predictions using the four turbulence models are provided in Figures. Each figure demonstrates variation in predictions for a single turbulence model due to either chordwise or spanwise refinement. To quantify solution independence, each mesh-turbulence model-angle of attack combination was analyzed using the SDP of the sectional lift and moment. Variation is considered significant when maximum SDP values exceed the 5.0% threshold or when averages exceed the 2.0% threshold. The SDP data for each modeling combination at each of the four span locations are provided for lift and moment with varying chordwise refinement in Appendices A.1 and A.2, respectively and for lift and moment with varying spanwise refinement in Appendices A.3 and A.4, respectively. Average and maximum SDP values for each flow regime are provided for lift and moment in Appendix A.5.

Grid refinement requirements obtained from this study for each turbulence model-flow regime combination are summarized in Table 5.1. This chapter details the approach taken to determine optimized grid parameters. Those parameters are then generalized with respect to characteristic length and aspect ratio to achieve similar refinement on other finite wing geometries.

Table 5.1: Grid requirements (radial x chordwise) for each turbulence model in three flow regimes

	SA RANS	SA DDES	$k\omega$-SST RANS	$k\omega$-SST DDES
Pre-Stall	200R x 250C	200R x 250C	200R x 250C	200R x 250C
Stall	200R x 250C	800R x 500C	800R x 500C	800R x 500C
Post-Stall	800R x 500C	800R x 500C	800R x 500C	800R x 500C

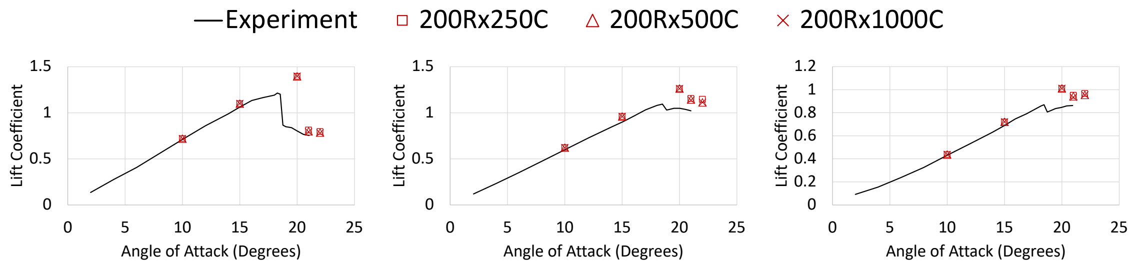

(a) r/R=0.5 (b) r/R=0.8 (c) r/R=0.95

Figure 5.1: Variation in sectional lift with 200 radial points and increasing chordwise refinement using SA-RANS turbulence model

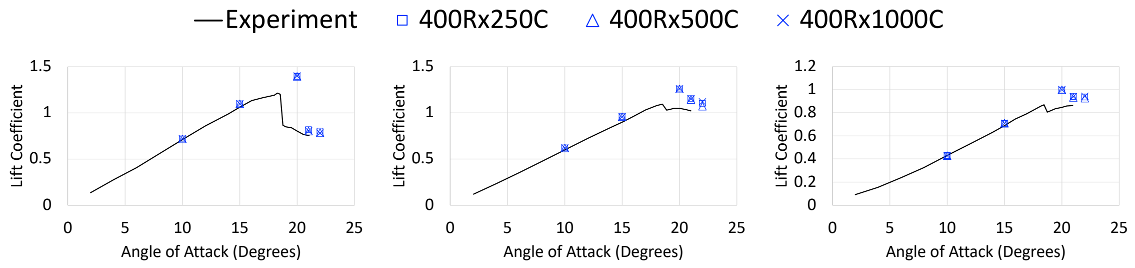

(a) r/R=0.5 (b) r/R=0.8 (c) r/R=0.95

Figure 5.2: Variation in sectional lift with 400 radial points and increasing chordwise refinement using SA-RANS turbulence model

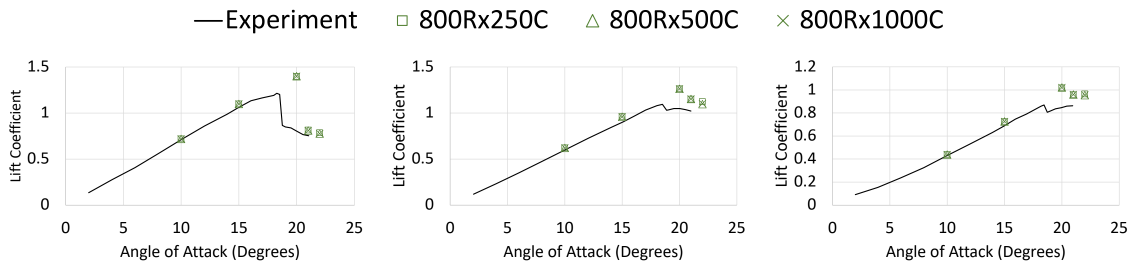

(a) r/R=0.5 (b) r/R=0.8 (c) r/R=0.95

Figure 5.3: Variation in sectional lift with 800 radial points and increasing chordwise refinement using SA-RANS turbulence model

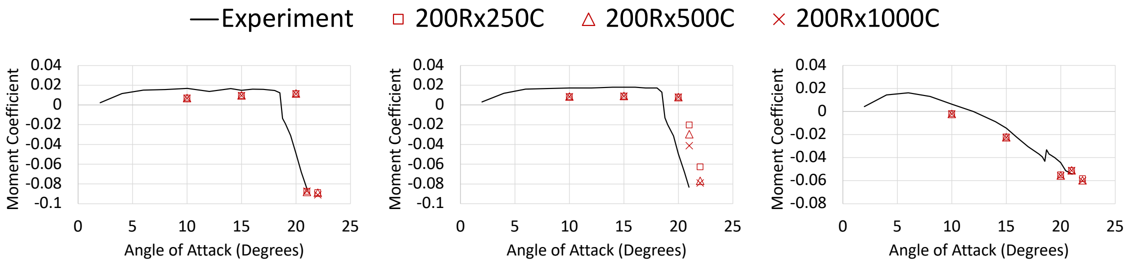

(a) r/R=0.5 (b) r/R=0.8 (c) r/R=0.95

Figure 5.4: Variation in sectional moment with 200 radial points and increasing chordwise refinement using SA-RANS turbulence model

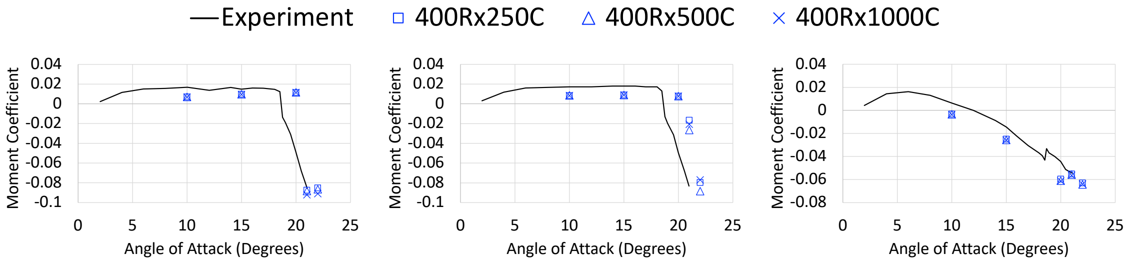

(a) r/R=0.5 (b) r/R=0.8 (c) r/R=0.95

Figure 5.5: Variation in sectional moment with 400 radial points and increasing chordwise refinement using SA-RANS turbulence model

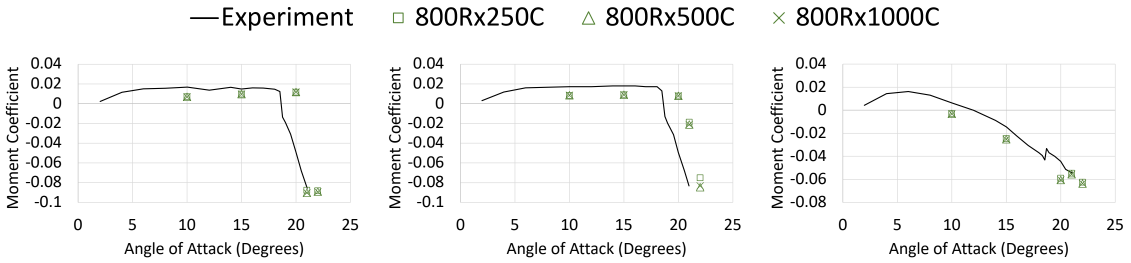

(a) r/R=0.5 (b) r/R=0.8 (c) r/R=0.95

Figure 5.6: Variation in sectional moment with 800 radial points and increasing chordwise refinement using SA-RANS turbulence model

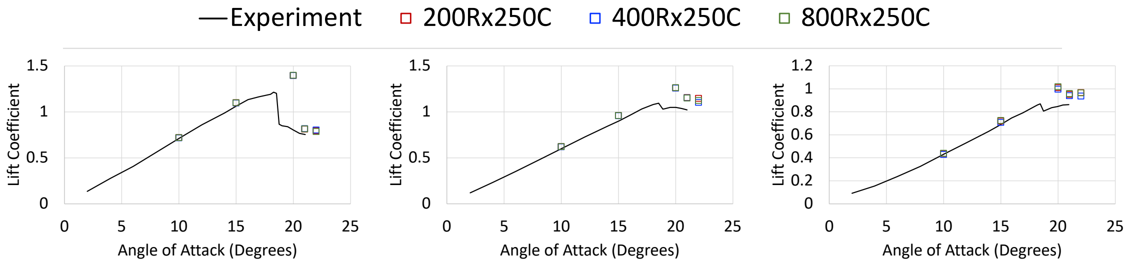

(a) r/R=0.5 (b) r/R=0.8 (c) r/R=0.95

Figure 5.7: Variation in sectional lift with 250 chordwise points and increasing spanwise refinement using SA-RANS turbulence model

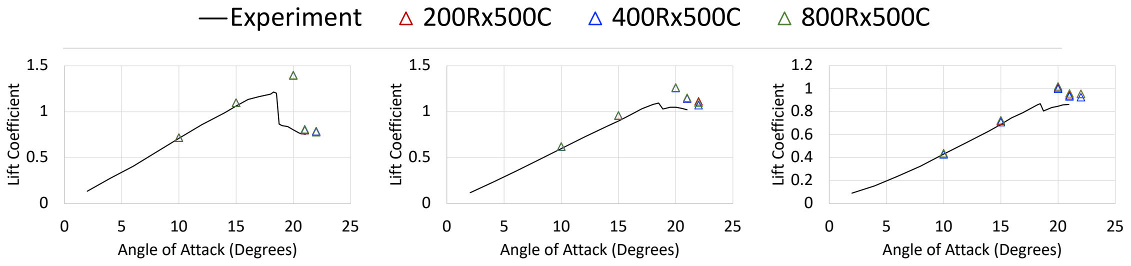

(a) r/R=0.5 (b) r/R=0.8 (c) r/R=0.95

Figure 5.8: Variation in sectional lift with increasing 500 chordwise points and varying spanwise refinement using SA-RANS turbulence model

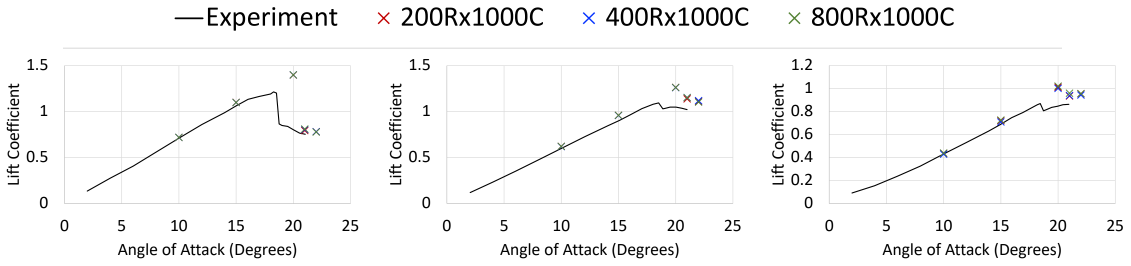

(a) r/R=0.5 (b) r/R=0.8 (c) r/R=0.95

Figure 5.9: Variation in sectional lift with increasing 1000 chordwise points and varying spanwise refinement using SA-RANS turbulence model

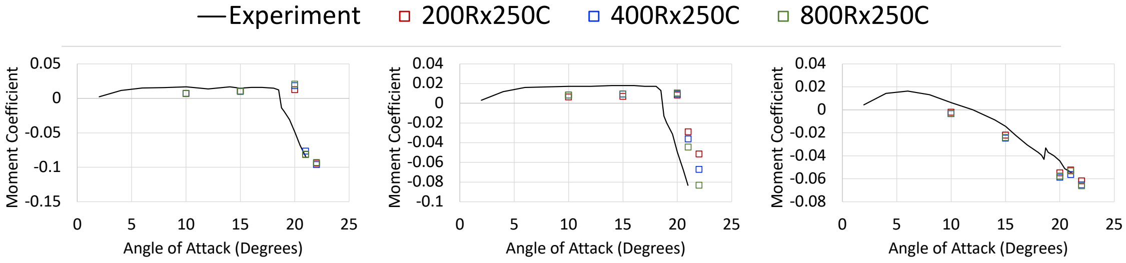

(a) r/R=0.5 (b) r/R=0.8 (c) r/R=0.95

Figure 5.10: Variation in sectional moment with 250 chordwise points increasing spanwise refinement using SA-RANS turbulence model

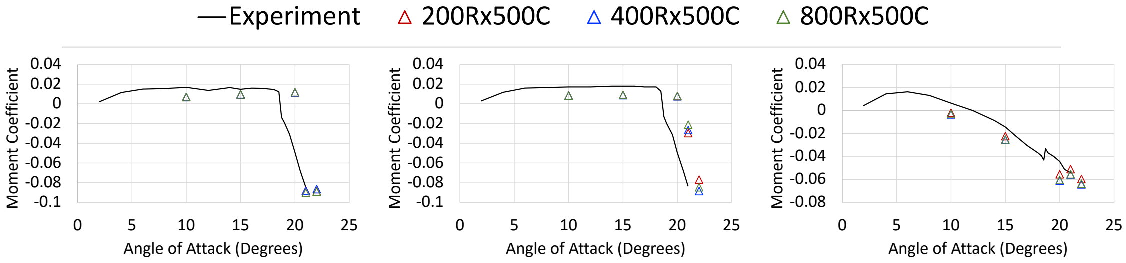

(a) r/R=0.5 (b) r/R=0.8 (c) r/R=0.95

Figure 5.11: Variation in sectional moment with 500 chordwise points increasing spanwise refinement using SA-RANS turbulence model

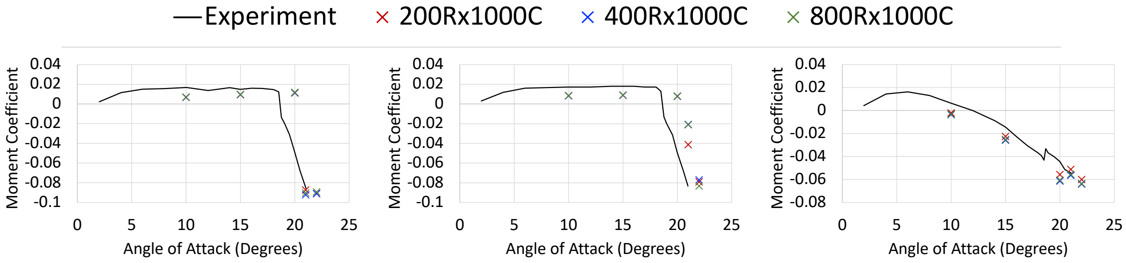

(a) r/R=0.5 (b) r/R=0.8 (c) r/R=0.95

Figure 5.12: Variation in sectional moment with 1000 chordwise points increasing spanwise refinement using SA-RANS turbulence model

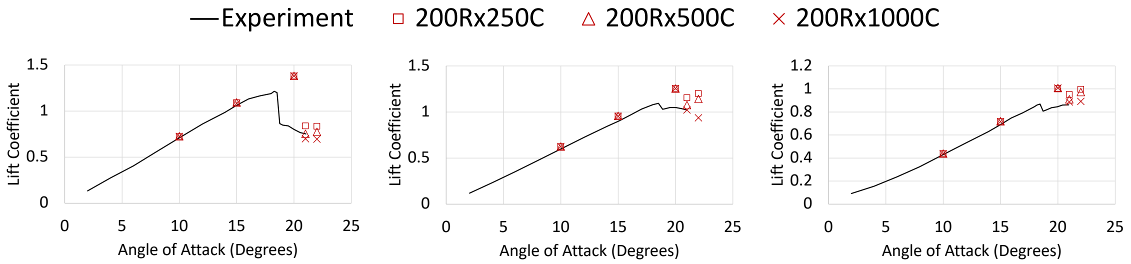

(a) r/R=0.5 (b) r/R=0.8 (c) r/R=0.95

Figure 5.13: Variation in sectional lift with 200 radial points and increasing chordwise refinement using SA-DDES turbulence model

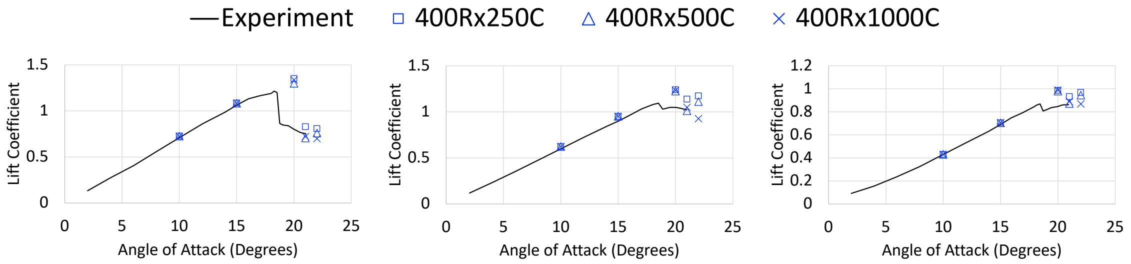

(a) r/R=0.5 (b) r/R=0.8 (c) r/R=0.95

Figure 5.14: Variation in sectional lift with 400 radial points and increasing chordwise refinement using SA-DDES turbulence model

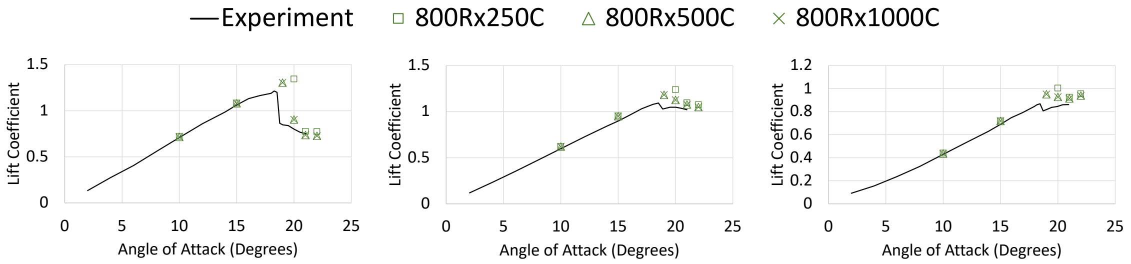

(a) r/R=0.5 (b) r/R=0.8 (c) r/R=0.95

Figure 5.15: Variation in sectional lift with 800 radial points and increasing chordwise refinement using SA-DDES turbulence model

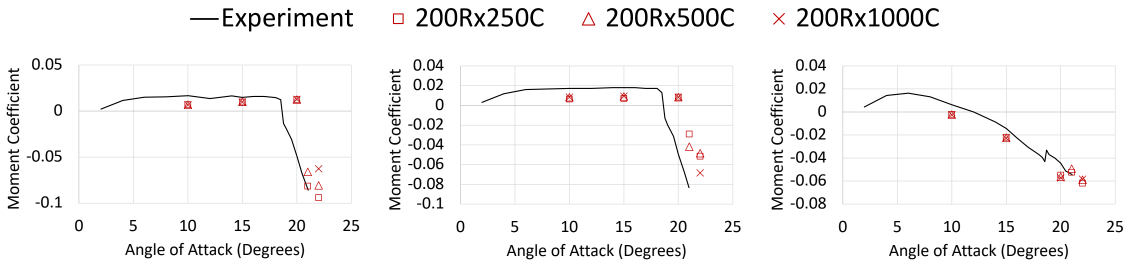

(a) r/R=0.5 (b) r/R=0.8 (c) r/R=0.95

Figure 5.16: Variation in sectional moment with 200 radial points and increasing chordwise refinement using SA-DDES turbulence model

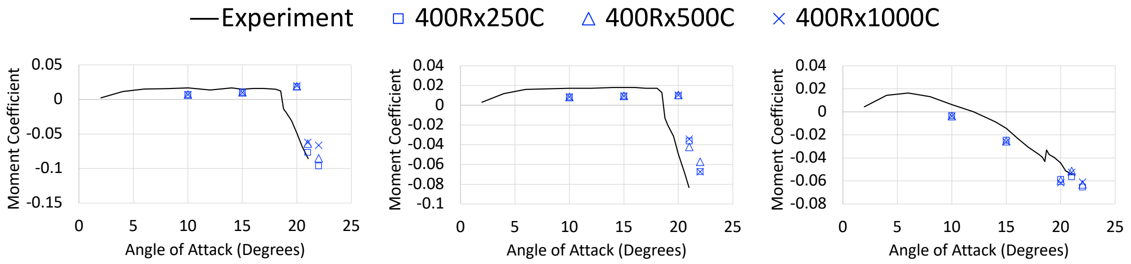

(a) r/R=0.5 (b) r/R=0.8 (c) r/R=0.95

Figure 5.17: Variation in sectional moment with 400 radial points and increasing chordwise refinement using SA-DDES turbulence model

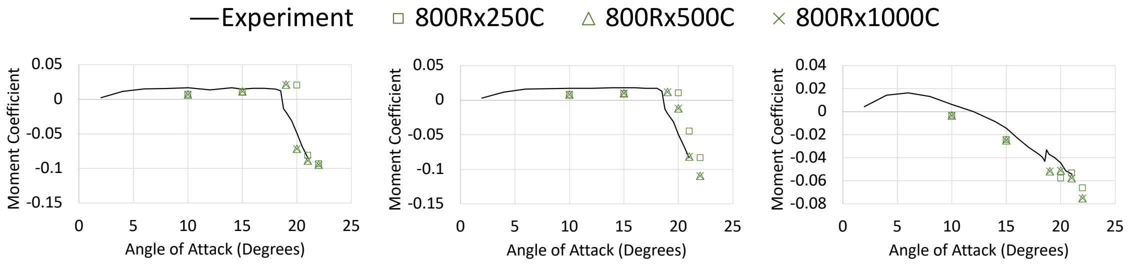

(a) r/R=0.5 (b) r/R=0.8 (c) r/R=0.95

Figure 5.18: Variation in sectional moment with 800 radial points and increasing chordwise refinement using SA-DDES turbulence model

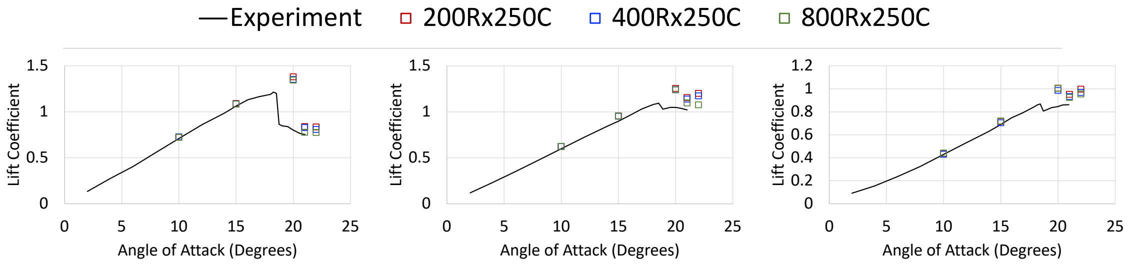

(a) r/R=0.5 (b) r/R=0.8 (c) r/R=0.95

Figure 5.19: Variation in sectional lift with 250 chordwise points and increasing spanwise refinement using SA-DDES turbulence model

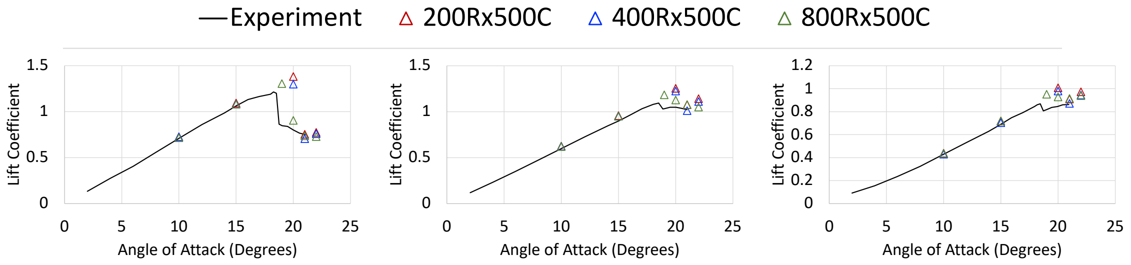

(a) r/R=0.5 (b) r/R=0.8 (c) r/R=0.95

Figure 5.20: Variation in sectional lift with 500 chordwise points and increasing spanwise refinement using SA-DDES turbulence model

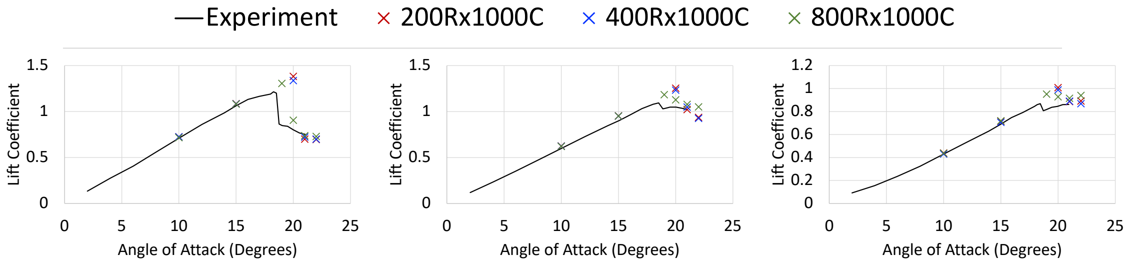

(a) r/R=0.5 (b) r/R=0.8 (c) r/R=0.95

Figure 5.21: Variation in sectional lift with 1000 chordwise points and increasing spanwise refinement using SA-DDES turbulence model

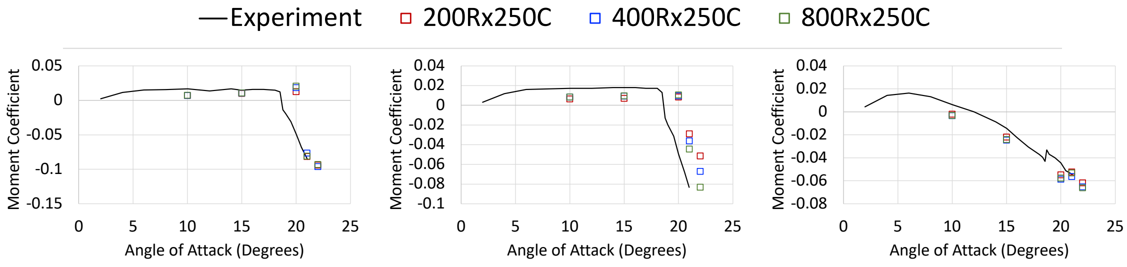

(a) r/R=0.5 (b) r/R=0.8 (c) r/R=0.95

Figure 5.22: Variation in sectional moment with 250 chordwise points and increasing spanwise refinement using SA-DDES turbulence model

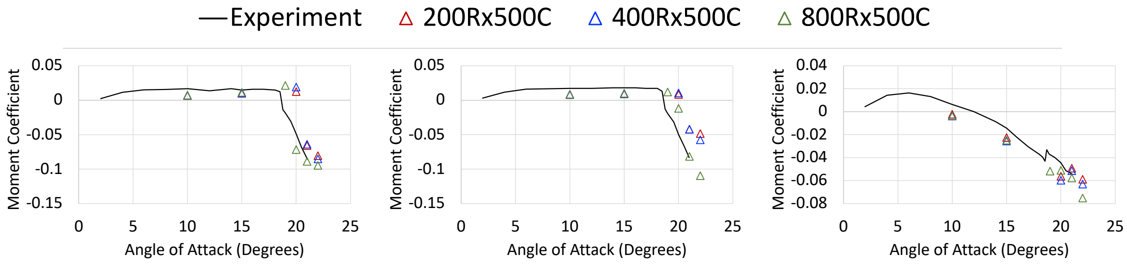

(a) r/R=0.5 (b) r/R=0.8 (c) r/R=0.95

Figure 5.23: Variation in sectional moment with 500 chordwise points and increasing spanwise refinement using SA-DDES turbulence model

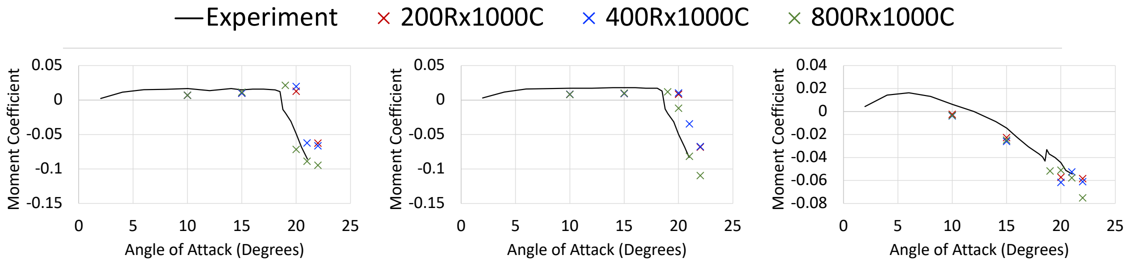

(a) r/R=0.5 (b) r/R=0.8 (c) r/R=0.95

Figure 5.24: Variation in sectional moment with 1000 chordwise points and increasing spanwise refinement using SA-DDES turbulence model

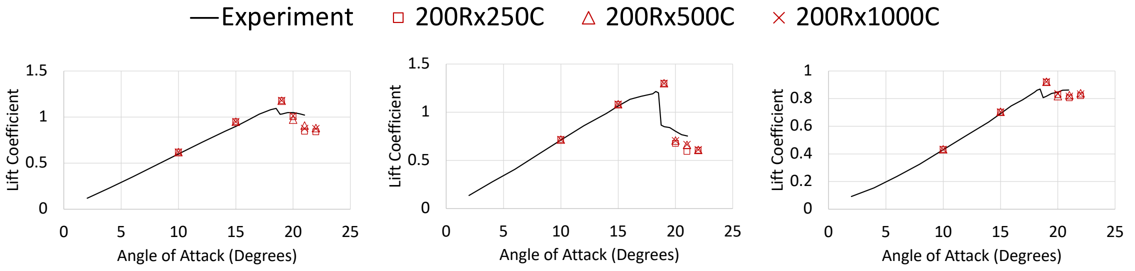

(a) r/R=0.8 (b) r/R=0.5 (c) r/R=0.95

Figure 5.25: Variation in sectional lift with 200 radial points and increasing chordwise refinement using $k\omega$-RANS turbulence model

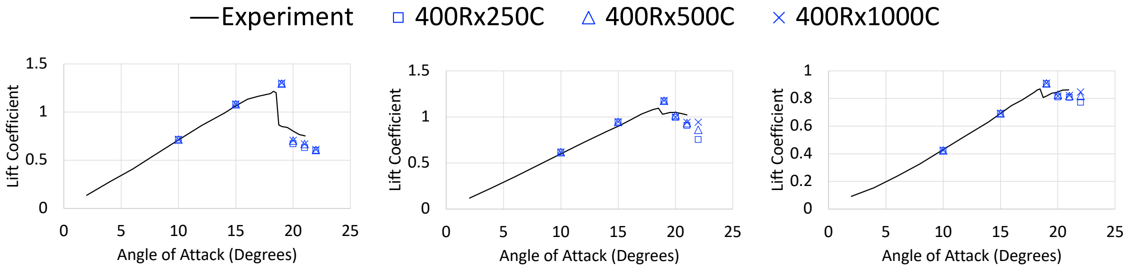

(a) r/R=0.5 (b) r/R=0.8 (c) r/R=0.95

Figure 5.26: Variation in sectional lift with 400 radial points and increasing chordwise refinement using $k\omega$-RANS turbulence model

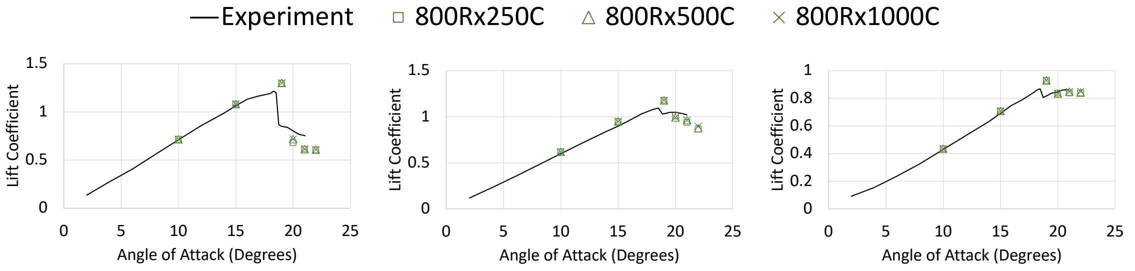

(a) r/R=0.5 (b) r/R=0.8 (c) r/R=0.95

Figure 5.27: Variation in sectional lift with 800 radial points and increasing chordwise refinement using $k\omega$-RANS turbulence model

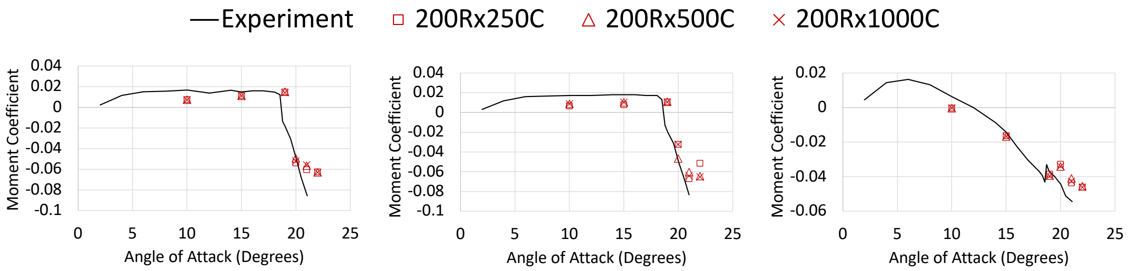

(a) r/R=0.5 (b) r/R=0.8 (c) r/R=0.95

Figure 5.28: Variation in sectional moment with 200 radial points and increasing chordwise refinement using $k\omega$-RANS turbulence model

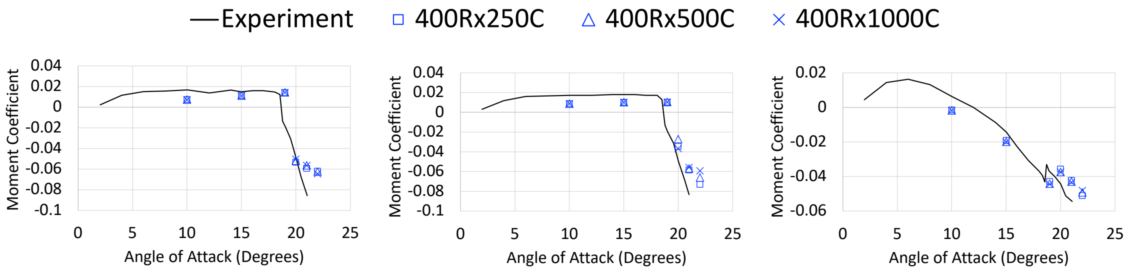

(a) r/R=0.5 (b) r/R=0.8 (c) r/R=0.95

Figure 5.29: Variation in sectional moment with 400 radial points and increasing chordwise refinement using $k\omega$-RANS turbulence model

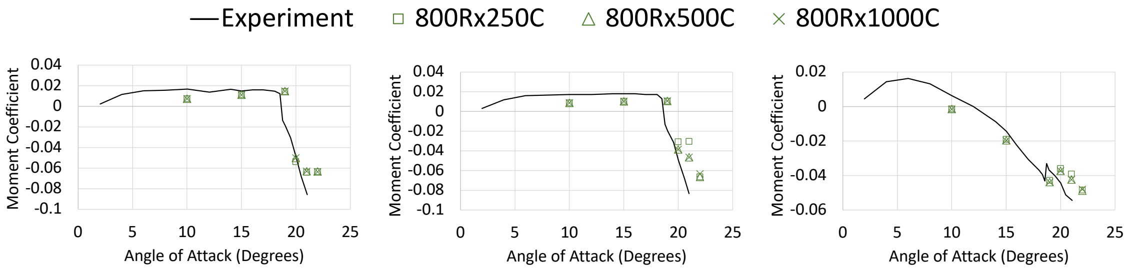

(a) r/R=0.5 (b) r/R=0.8 (c) r/R=0.95

Figure 5.30: Variation in sectional moment with 800 radial points and increasing chordwise refinement using $k\omega$-RANS turbulence model

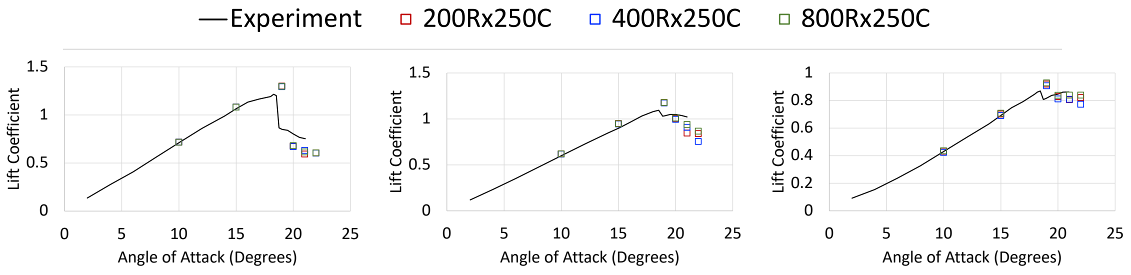

(a) r/R=0.5 (b) r/R=0.8 (c) r/R=0.95

Figure 5.31: Variation in sectional lift with 250 chordwise points and increasing spanwise refinement using $k\omega$-RANS turbulence model

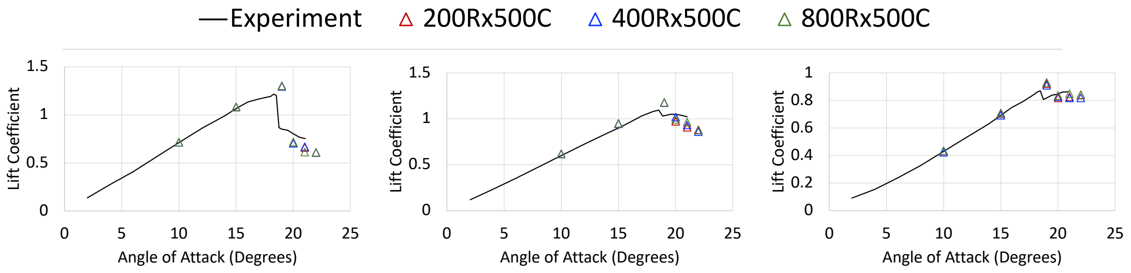

(a) r/R=0.5 (b) r/R=0.8 (c) r/R=0.95

Figure 5.32: Variation in sectional lift with 500 chordwise points and increasing spanwise refinement using $k\omega$-RANS turbulence model

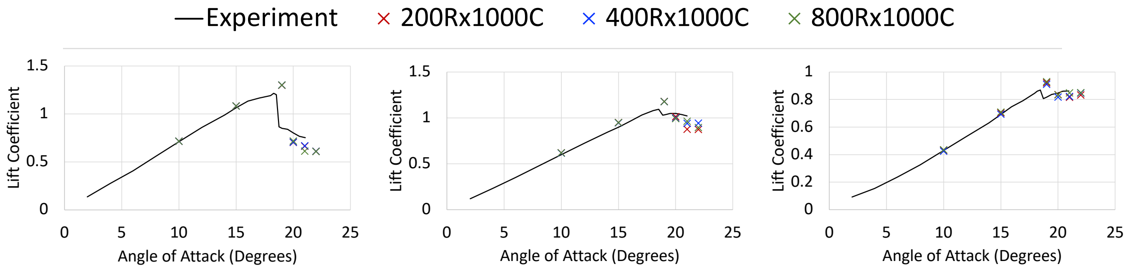

(a) r/R=0.5 (b) r/R=0.8 (c) r/R=0.95

Figure 5.33: Variation in sectional lift with 1000 chordwise points and increasing spanwise refinement using $k\omega$-RANS turbulence model

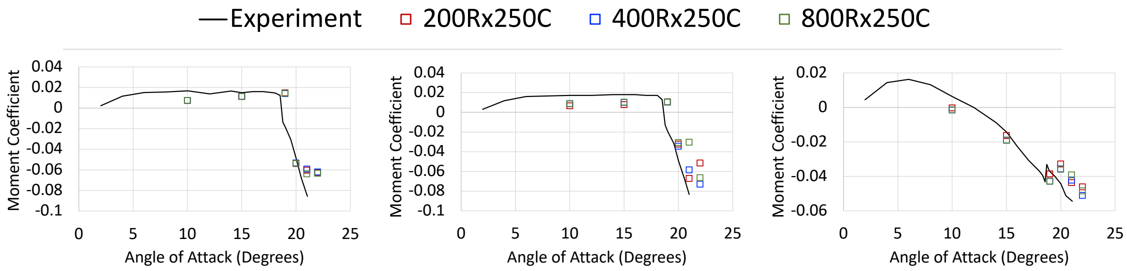

(a) r/R=0.5 (b) r/R=0.8 (c) r/R=0.95

Figure 5.34: Variation in sectional moment with 250 chordwise points and increasing spanwise refinement using $k\omega$-RANS turbulence model

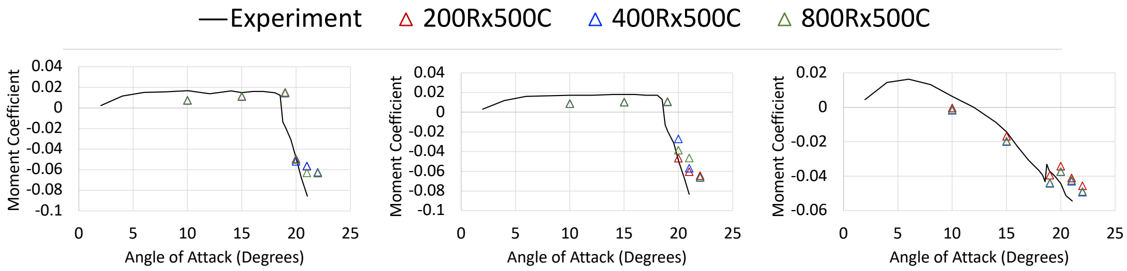

(a) r/R=0.5 (b) r/R=0.8 (c) r/R=0.95

Figure 5.35: Variation in sectional moment with 500 chordwise points and increasing spanwise refinement using $k\omega$-RANS turbulence model

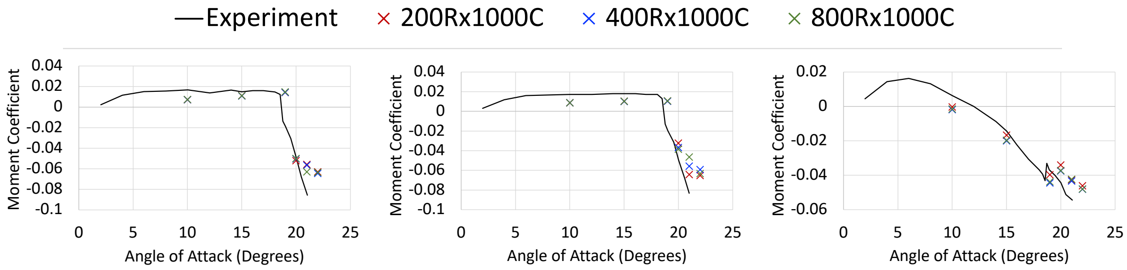

(a) r/R=0.5 (b) r/R=0.8 (c) r/R=0.95

Figure 5.36: Variation in sectional moment with 1000 chordwise points and increasing spanwise refinement using $k\omega$-RANS turbulence model

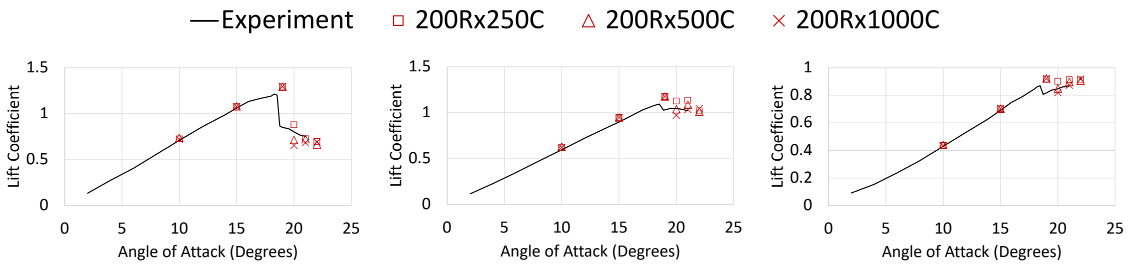

(a) r/R=0.5
200 spanwise points

(b) r/R=0.8
200 spanwise points

(c) r/R=0.95
200 spanwise points

Figure 5.37: Variation in sectional lift with 200 radial points and increasing chordwise refinement using $k\omega$-DDES turbulence model

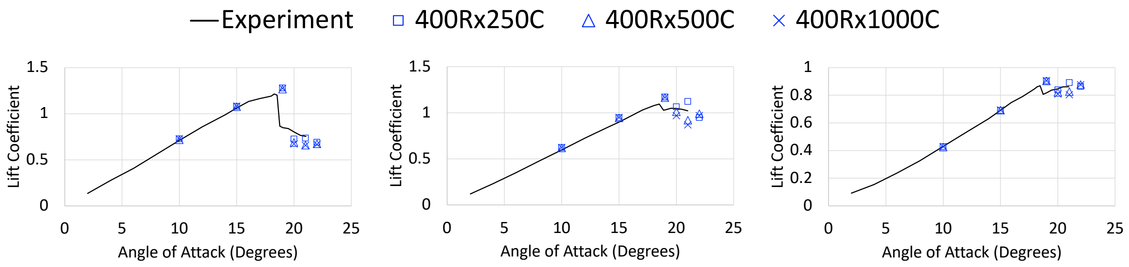

(a) r/R=0.5
400 spanwise pointts

(b) r/R=0.8
400 spanwise points

(c) r/R=0.95
400 spanwise pointts

Figure 5.38: Variation in sectional lift with 400 radial points and increasing chordwise refinement using $k\omega$-DDES turbulence model

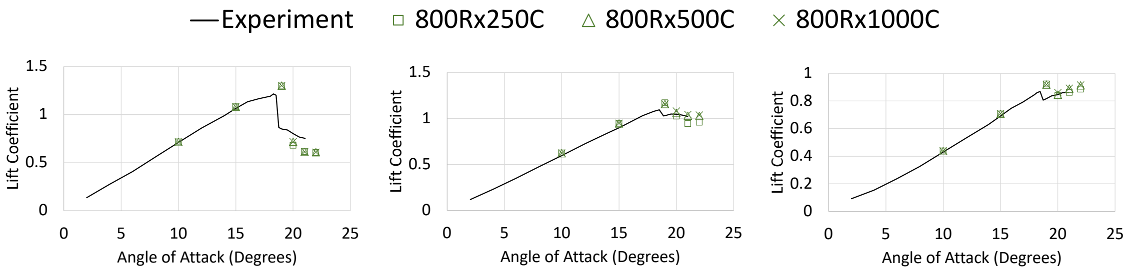

(a) r/R=0.5
800 spanwise points

(b) r/R=0.8
800 spanwise points

(c) r/R=0.95
800 spanwise points

Figure 5.39: Variation in sectional lift with 800 radial points and increasing chordwise refinement using $k\omega$-DDES turbulence model

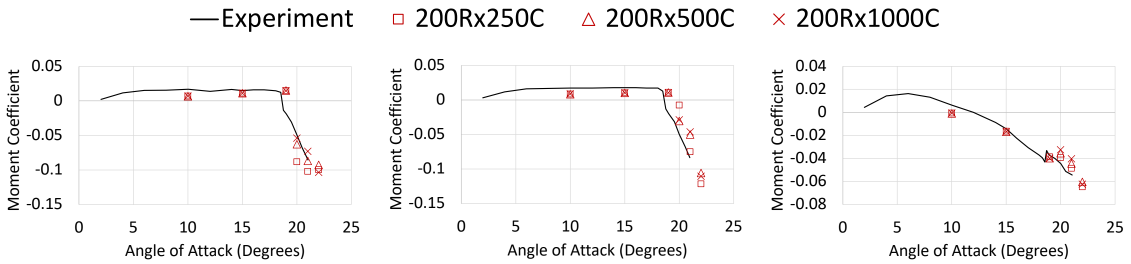

(a) r/R=0.5
200 spanwise points

(b) r/R=0.8
200 spanwise points

(c) r/R=0.95
200 spanwise points

Figure 5.40: Variation in sectional moment with 200 radial points and increasing chordwise refinement using $k\omega$-DDES turbulence model

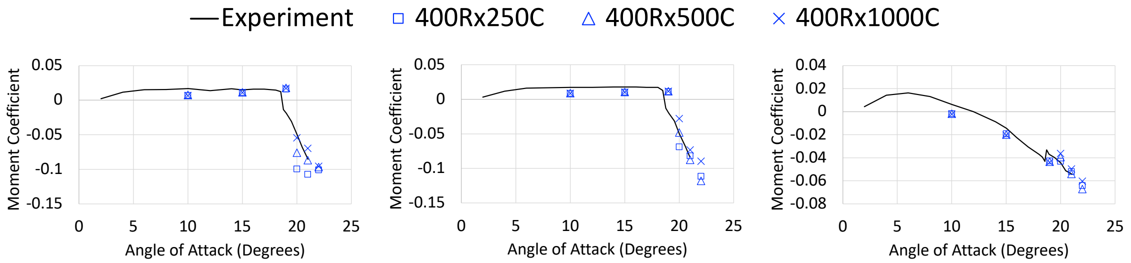

(a) r/R=0.5
400 spanwise pointts

(b) r/R=0.8
400 spanwise pointts

(c) r/R=0.95
400 spanwise pointts

Figure 5.41: Variation in sectional moment with 400 radial points and increasing chordwise refinement using $k\omega$-DDES turbulence model

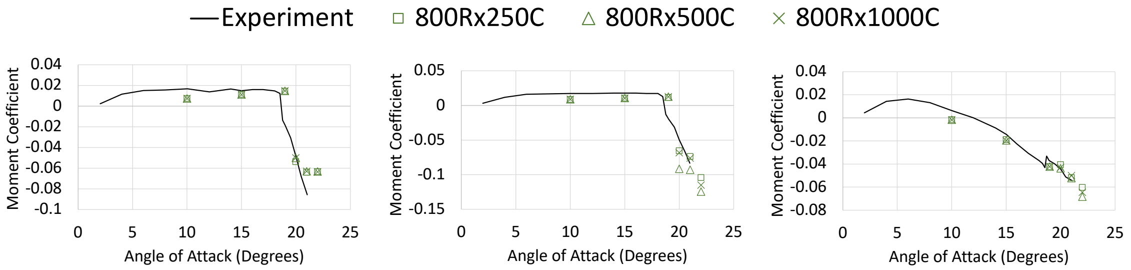

(a) r/R=0.5
800 spanwise points

(b) r/R=0.8
800 spanwise points

(c) r/R=0.95
800 spanwise points

Figure 5.42: Variation in sectional moment with 800 radial points and increasing chordwise refinement using $k\omega$-DDES turbulence model

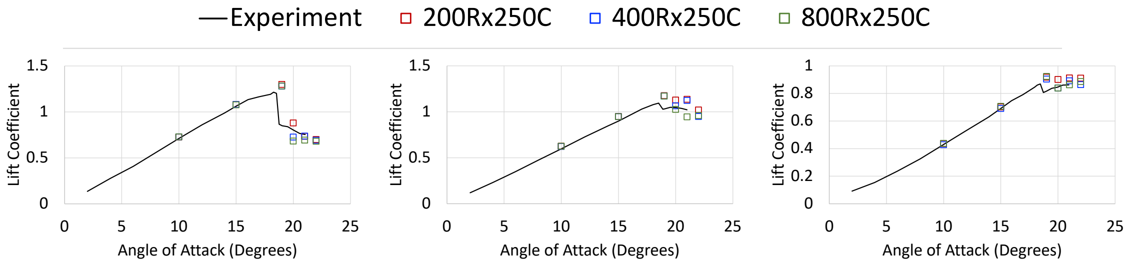

(a) r/R=0.5 (b) r/R=0.8 (c) r/R=0.95

Figure 5.43: Variation in sectional lift with 250 chordwise points and increasing spanwise refinement using $k\omega$-DDES turbulence model

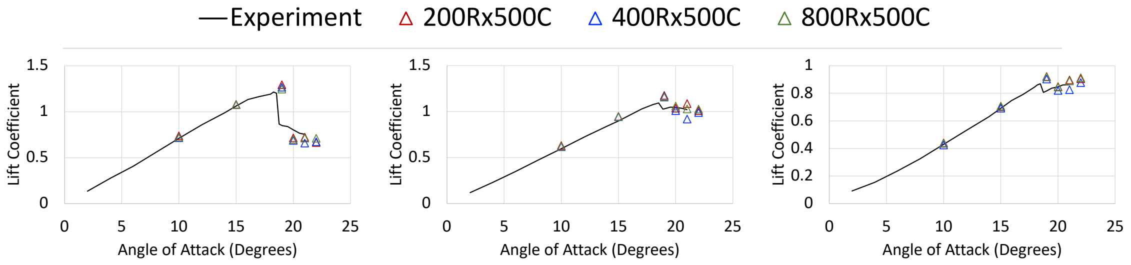

(a) r/R=0.5 (b) r/R=0.8 (c) r/R=0.95

Figure 5.44: Variation in sectional lift with 500 chordwise points and increasing spanwise refinement using $k\omega$-DDES turbulence model

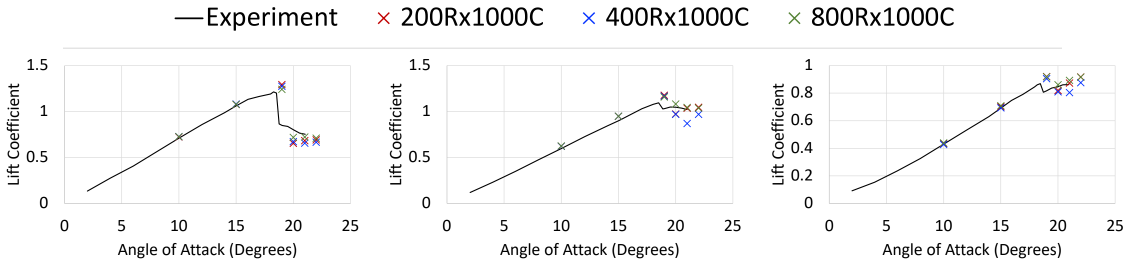

(a) r/R=0.5 (b) r/R=0.8 (c) r/R=0.95

Figure 5.45: Variation in sectional lift with 1000 chordwise points and increasing spanwise refinement using $k\omega$-DDES turbulence model

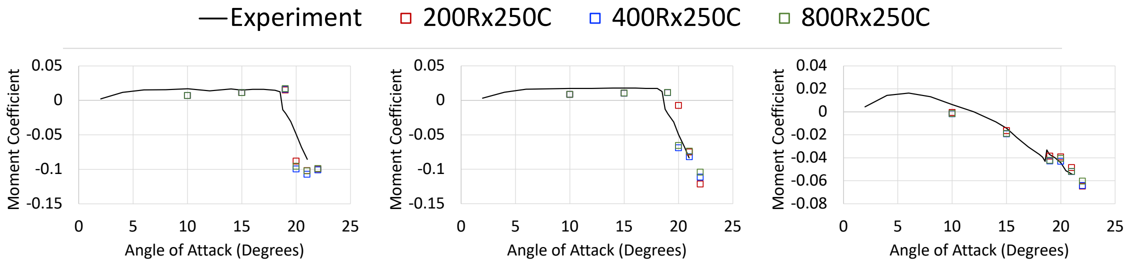

(a) r/R=0.5 (b) r/R=0.8 (c) r/R=0.95

Figure 5.46: Variation in sectional moment with 250 chordwise points and increasing spanwise refinement using $k\omega$-DDES turbulence model

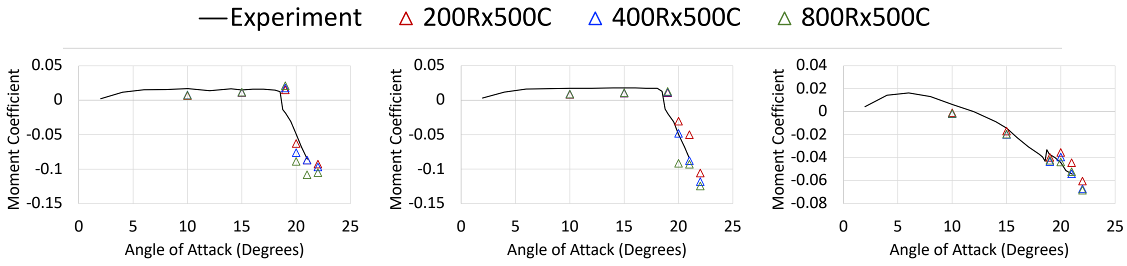

(a) r/R=0.5 (b) r/R=0.8 (c) r/R=0.95

Figure 5.47: Variation in sectional moment with 500 chordwise points and increasing spanwise refinement using $k\omega$-DDES turbulence model

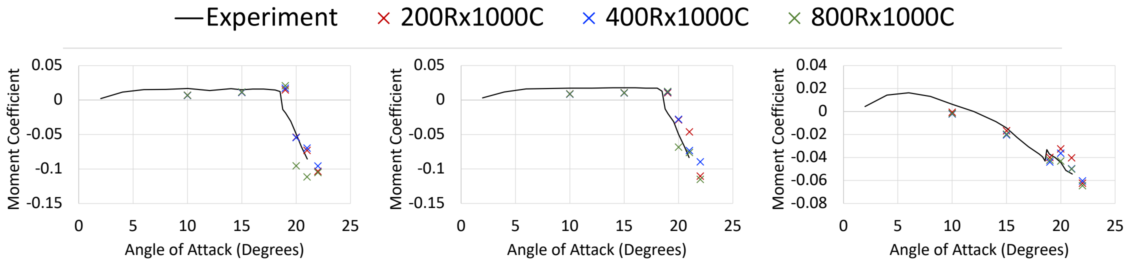

(a) r/R=0.5 (b) r/R=0.8 (c) r/R=0.95

Figure 5.48: Variation in sectional moment with increasing spanwise refinement using $k\omega$-DDES turbulence model

Planar Mesh Requirements at Pre-Stall Angles of Attack

Sectional lift and moment predictions using the SA RANS turbulence model are provided in Figures 5.1-5.12. At pre-stall angles of attack ($\alpha = 10°$, $15°$), both lift and moment predictions exhibit little variation with mesh refinement in both the chordwise and spanwise directions. The maximum and average SDP data are provided in Tables A.49-A.52, for chordwise refinement and in Tables A.53-A.56 for spanwise refinement. The SDP maximum and averages fall within the 5.0% and 2.0% threshold values, respectively for all cell variations, indicating little variation across all refinement levels.

The SA DDES, $k\omega$-SST RANS, and $k\omega$ DDES turbulence models demonstrated similar behavior at pre-stall angles of attack, all exhibiting little variation across both chordwise and spanwise directions, as illustrated in Figures 5.1-5.48. Variation analyses prove minimal variation as maximum and average SDP values, provided in Appendix A.5, all fall within the 5.0% and 2.0% threshold values. Based on these findings, mesh requirements are considered sufficient with a 250 × 200 (chord × span) planar mesh, for all turbulence models at pre-stall angles of attack. Pressure coefficient contours at $r/R = 0.5$ overlaid with streamtraces demonstrate attached flow behavior using all four turbulence models on the 250 × 200 (chord × span) planar mesh (Figs. 5.50 and 5.49).

Planar Mesh Requirements During Stall Onset

During the onset of stall (20°), the turbulence models exhibited a range of variations, resulting in differing grid requirements for each turbulence model. The SA RANS turbulence model exhibited little variation in both lift and moment with mesh refinement in both the chordwise and spanwise directions. The maximum and average SDP data, provided in Tables A.57-A.60, for chordwise refinement and in Tables A.53-A.56 for spanwise refinement, fall within threshold values, respectively for all cell variations, indicating little variation across all refinement levels. Mesh requirements are considered sufficient to achieve solution independence with a 250 × 200 (chord × span) planar mesh, for the SA RANS turbulence model near the onset of stall. However,

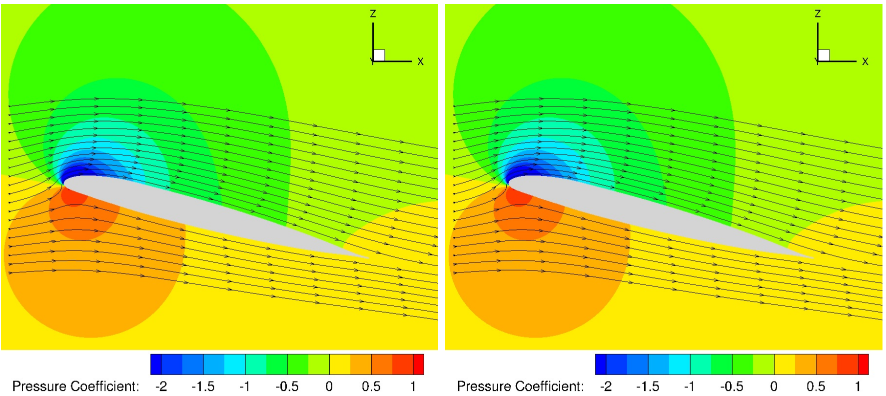

(a) SA RANS (b) SA DDES

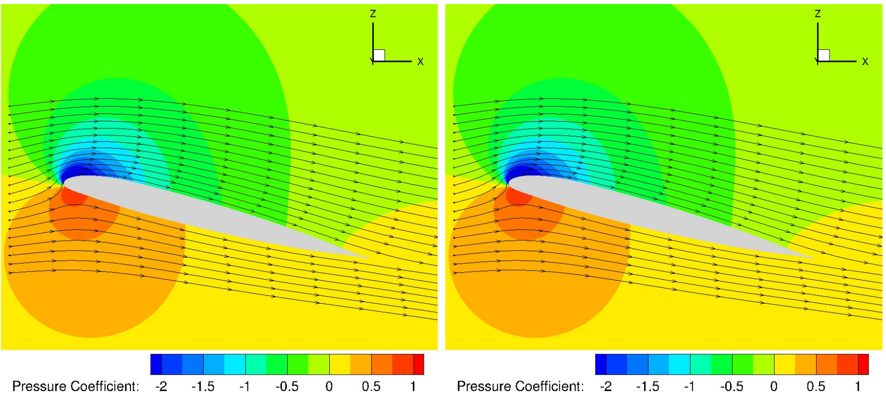

(c) $k\omega$-SST RANS (d) $k\omega$-SST DDES

Figure 5.49: Pressure coefficient contours overlaid with streamtraces at $r/R = 0.5$ slices at $\alpha = 15^\circ$ using all four turbulence models.

it is important to note that while solution independence from grid refinement is achieved, the SA RANS model is unable to predict separation at this angle of attack with any level of grid refinement as demonstrated by lift and moment predictions (Figs. 5.1-5.48) as well as pressure coefficient contour overlaid with streamtraces in Figure for the coarsest and finest grids.

The additional turbulence models all exhibit elevated levels of variation, indicating solution independence from grid refinement at the onset of stall requires a more highly refined grid than at pre-stall angles of attack. Using the $k\omega$-SST RANS turbulence model, lift predictions exhibit little variation with mesh refinement in both the chordwise and spanwise directions. The maximum and average SDP data are provided in Tables A.57-A.60, for chordwise refinement and in Tables A.61-A.64 for spanwise refinement. The lift SDP maximum and averages fall within the 5.0% and 2.0% threshold values, respectively for all cell variations, indicating little variation across all

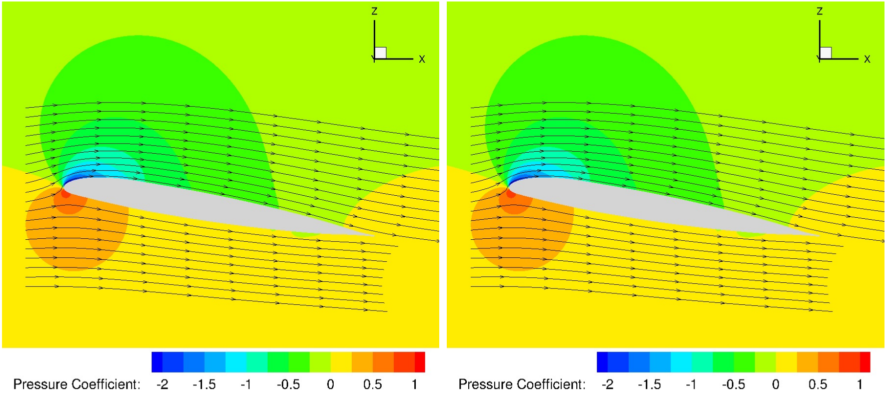

(a) SA RANS (b) SA DDES

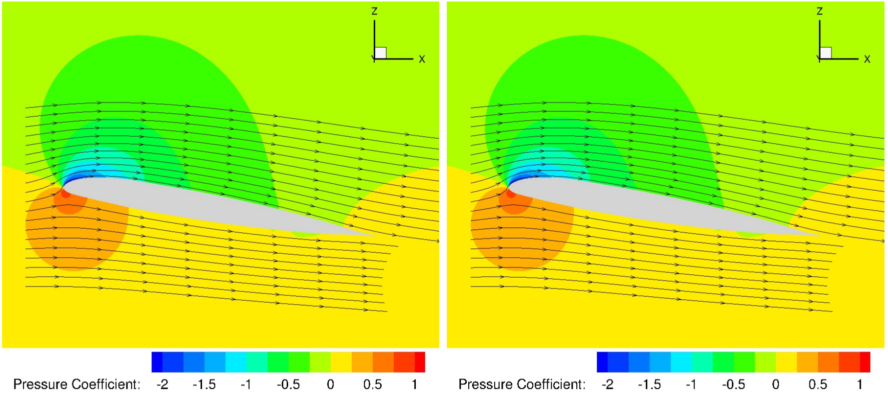

(c) $k\omega$-SST RANS (d) $k\omega$-SST DDES

Figure 5.50: Pressure coefficient contours overlaid with streamtraces at $r/R = 0.5$ slices at $\alpha = 10°$ using all four turbulence models.

refinement levels. The moment SDP maximum and averages fall within the 5.0% and 2.0% threshold values at three spanwise locations ($r/R = 0.5, 0.9, 0.99$). However, moment predictions at the $r/R = 0.8$ spanwise station display significant variation across chordwise and spanwise refinement, with average and maximum SDP values exceeding the 2.0% and 5.0% threshold values, respectively, indicating the solution is not fully independent of the entire chordwise and spanwise refinement sweeps. With 200 and 400 spanwise points, moment predictions do not exhibit convergent behavior with increasing chordwise refinement, (red and blue respectively in Fig. 5.52). Only with 800 radial points is convergent behavior towards a final value realized (green in Fig. 5.52).

Pressure coefficient contours of the blade surface in Figure 5.53 show that the $r/R = 0.8$ radial station coincides with a low pressure bubble while $r/R = 0.5$, $r/R = 0.95$, and $r/R = 0.99$ do not. As chordwise refinement is assessed on grids with 200 and 400 radial points the

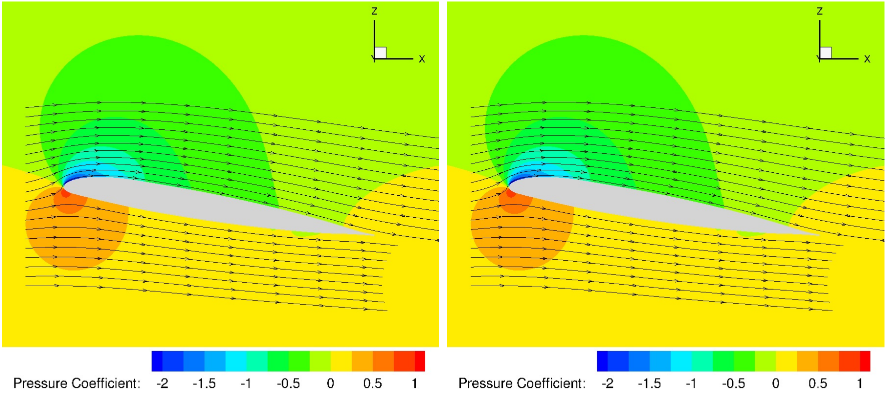

(a) 250 × 200 (chord × span) (b) 1000 × 800 (chord × span)

Figure 5.51: Pressure coefficient contours overlaid with streamtraces at $r/R = 0.5$ slices at $\alpha = 20^\circ$ using SA RANS turbulence model.

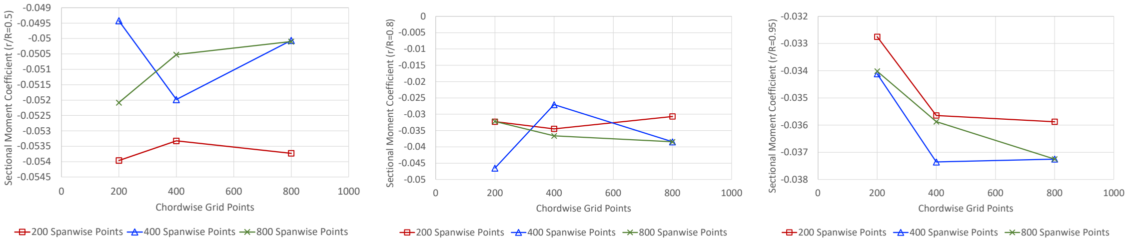

(a) r/R=0.5 (b) r/R=0.8 (c) r/R=0.95

Figure 5.52: Stall moment convergence with increasing chordwise refinement at $\alpha = 20^\circ$ with $k\omega$-SST RANS turbulence model

low pressure bubble shifts in size and shape, exposing varying percentages of the chord to lower pressure. This affects moment predictions at $r/R = 0.8$ while moment predictions at the other radial stations which are subjected to constant pressure regions throughout refinement sweeps are relatively unaffected. With 800 radial points, movement of the low pressure bubble does not occur with increased chordwise refinement, indicating convergence of the solution. Unlike the SA RANS turbulence model, the $k\omega$-SST turbulence model predicts separation at $\alpha = 20^\circ$, as illustrated in Figure 5.54.

The SA DDES turbulence model exhibits variation in both lift and moment with refinement chordwise and spanwise directions. Average and maximum SDP values of lift and moment exceed the 2.0% and 5.0% variation thresholds for both chordwise (Tab.A.57-A.60) and spanwise (Tab.A.61-A.64) refinement. Variation in lift and moment predictions using the SA DDES model, is largely due to the ability of DDES models to capture flow physics more accurately with higher refinement. As shown in Figures 5.37-5.38, meshes with 200 and 400 radial stations predict equivalent lift and moment values at $\alpha = 20°$, that do not predict stall. However, when spanwise refinement is increased to 800 radial stations, the solution captures both lift and moment stall with 500 and 1000 chordwise points (5.39). This behavior is illustrated in Figure 5.55. The coarsest chordwise refinement level of 250 points is not sufficient to capture this stall. With 800 spanwise points, variation in chordwise refinement from 500 to 1000 points produces maximum and average SDP values less than 1.0%. This indicates that solution independence from grid refinement for the SA DDES turbulence model is achieved with 800Rx500C points.

The $k\omega$-SST model produces variation in lift and moment predictions with mesh refinement in both the chordwise and spanwise directions. The maximum and average SDP data are provided in Tables A.57-A.60, for chordwise refinement and in Tables A.61-A.64 for spanwise refinement. The lift SDP maximum and averages exceed the 5.0% and 2.0% threshold values, respectively for all cell variations, indicating variation across refinement levels.

Like predictions from the the SA DDES model, the increased variation in lift and moment predictions using the $k\omega$-SST DDES turbulence model, is largely due to the ability of DDES solvers to capture flow physics more accurately with higher refinement. However, unlike the SA DDES model, the $k\omega$-SST DDES turbulence model captures stall at $\alpha = 20°$ on all grid refinement levels, not just with 800 spanwise points. Thus, the choice of appropriate chordwise and spanwise spacing is not as clearly identified. In Figures 5.37 - 5.42, there is drastic jump in both lift and moment predictions when chordwise refinement is increased from 250 to 500 points at all spanwise stations. This indicates that once again, the $k\omega$-SST DDES solution is not independent of chordwise refinement from 250 to 500 points. Further chordwise refinement, yields slight changes in lift and moment predictions, however the max SDP of lift over this refinement level is 2.96% with an average of 1.46%. The significant reduction in SDP to values under 3.0% indicates 500 chordwise points are sufficient for lift predictions using the $k\omega$-SST DDES turbulence model. However, over the same refinement range from 500 to 1000 chordwise points, the max SDP of moment is

10.43% with an average of 4.08%, indicating the solution still lacks independence from grid refinement. Taking a second look at Figures 5.37-5.39 and 5.40-5.42, it is apparent that changes in lift and moment predictions due to chordwise refinement are reduced as spanwise refinement is increased, suggesting that chordwise solution independence is coupled to the spanwise refinement (i.e. the solution is sensitive to aspect ratio). Based on those findings, 800R x 500C is sufficient grid refinement to capture stall using the $k\omega$-SST DDES turbulence model.

Planar Mesh Requirements at Post-Stall Angles of Attack

At post-stall angles of attack (21° and 22°), lift predictions at all spanwise stations and moment predictions at three of the four spanwise stations ($r/R = 0.5, 0.95, 0.99$) exhibit little variation with mesh refinement in both the chordwise and spanwise directions. The maximum and average SDP data are provided in Tables A.57-A.60, for chordwise refinement and in Tables A.53-A.56 for spanwise refinement. The SDP maximum and averages fall within the 5.0% and 2.0% threshold values, respectively, for all cell variations, except at the $r/R = 0.8$ station. Here, significant moment variation is present with maximum chordwise and spanwise SDP values exceeding the 5.0% variation threshold. At post-stall angles of attack, the $r/R = 0.8$ radial station once again coincides with a low pressure bubble (Fig. 5.56), causing elevated levels of variation compared to other radial stations and requiring increased radial refinement. To determine appropriate grid size, convergence was further assessed.

First, the $\alpha = 21°$ post-stall angle was evaluated. With 200 spanwise points, moment predictions increase in magnitude but do not indicate convergence (red in Fig. 5.57). With 400 spanwise points, moment predictions increase in magnitude from 250 to 500 chordwise points and then decrease in magnitude from 500 to 1000 chordwise points. This, once again demonstrates no convergence with increasing refinement (blue in Fig. 5.57). Only with 800 spanwise points is asymptotic progression towards a final value realized (green in Fig. 5.57).

Next the $\alpha = 22°$ post-stall angle of attack was considered. With 200 spanwise points, moment predictions increase in magnitude with increased refinement, illustrating some convergence (red in Fig. 5.58). With 400 spanwise points, however, moment predictions increase in magnitude from 250 to 500 chordwise points while decreasing in magnitude from 500 to 1000 chordwise points, exhibiting no convergence (blue in Fig. 5.58). Once again with 800 spanwise points, asymptotic progression towards a final value is realized (green in Fig. 5.58).

For both post-stall angles of attack, only with 800 spanwise points is there moment convergence at $r/R = 0.8$ with increasing chordwise refinement. Based on the chordwise refinement using 800 spanwise stations, variation from 500 to 1000 chordwise points exhibits little to no variation, verifying the 800Rx500C grid is sufficient for post-stall moment predictions using the SA RANS turbulence model.

The SA DDES, $k\omega$-SST RANS, and $k\omega$-SST DDES turbulence models all produce significant variation lift and moment predictions at post-stall angles of attack ($\alpha = 21°$, $22°$). Average and maximum SDP values of both quantities exceed the 2.0% and 5.0% variation thresholds for both chordwise and spanwise refinement at all radial stations, requiring additional convergence studies for all three turbulence models.

SA DDES

Chordwise refinement does not result in lift convergence when only 200 and 400 spanwise points are used at both $\alpha = 21°$ (Fig. 5.59) and $\alpha = 22°$ (Fig. 5.60). Similarly, chordwise refinement does not result in moment convergence with increasing chordwise refinement when only 200 and 400 spanwise points are used at $\alpha = 21°$ (Fig. 5.61) and $\alpha = 21°$ (Fig. 5.62). Only with 800 spanwise points does moment convergence correspond with increasing chordwise refinement.

With 800 spanwise points, increased chordwise refinement beyond 500 points yields no change in lift and moment predictions, verifying 800Rx500C is sufficient for post-stall force and moment predictions using the SA DDES turbulence model.

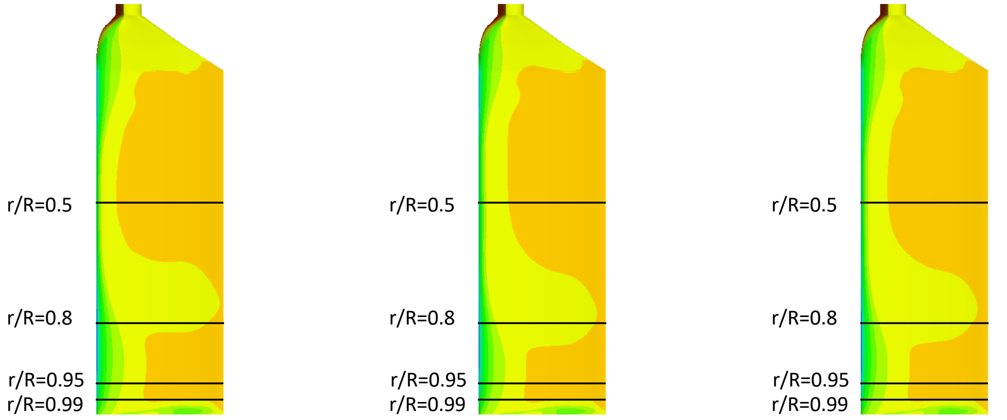

(a) 200Rx250C (b) 200Rx500C (c) 200Rx1000C

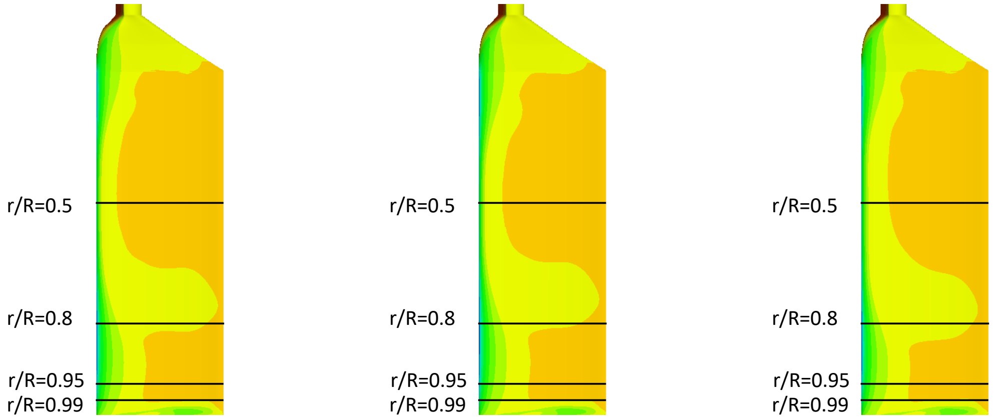

(d) 400Rx250C (e) 400Rx500C (f) 400Rx1000C

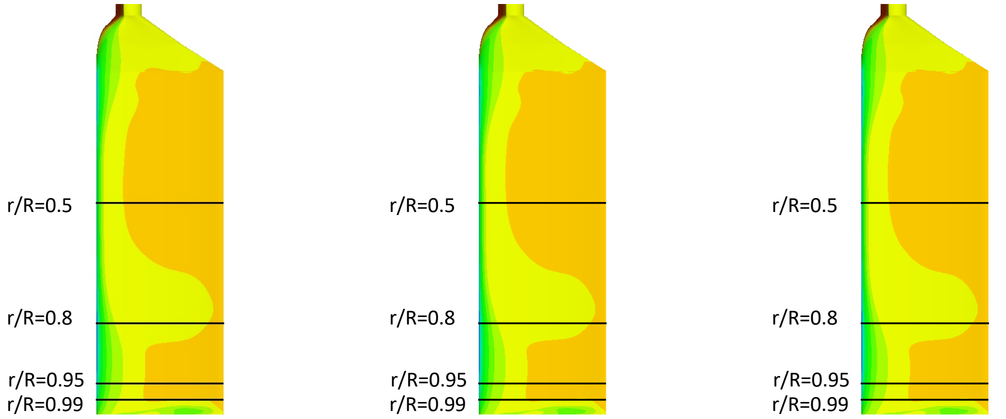

(g) 800Rx250C (h) 800Rx500C (i) 800Rx1000C

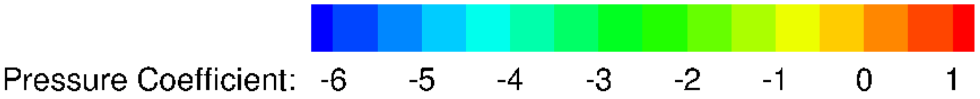

Figure 5.53: Pressure coefficient contours on blade surface at the onset of stall ($\alpha - 20°$) with $k\omega$-SST RANS turbulence model

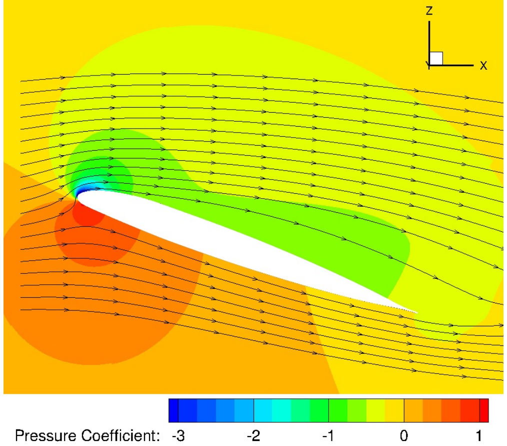

Figure 5.54: Separated flow at onset of stall ($\alpha = 20°$) with $k\omega$-SST RANS turbulence model

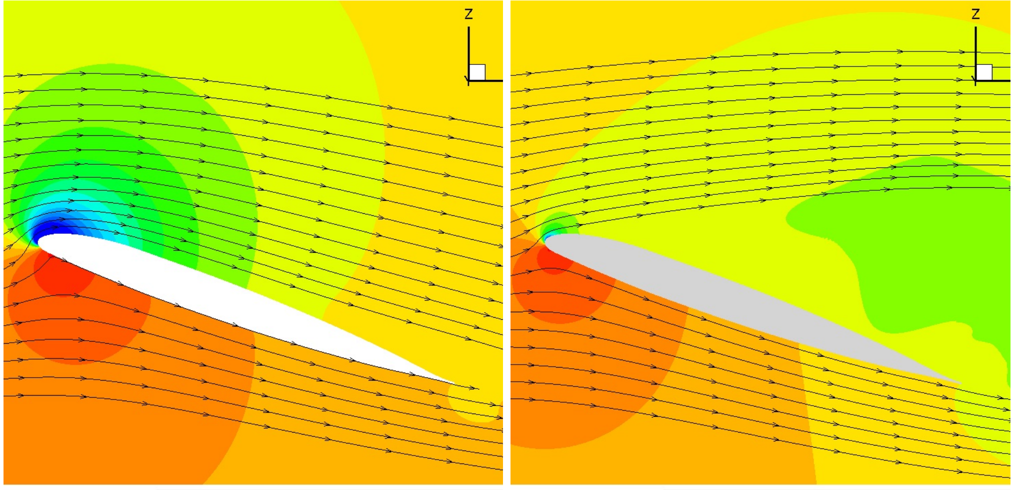

(a) 800Rx250C (b) 800Rx500C

Figure 5.55: Separated flow predicted at stall onset ($\alpha = 20°$) with increased refinement using SA DDES turbulence model

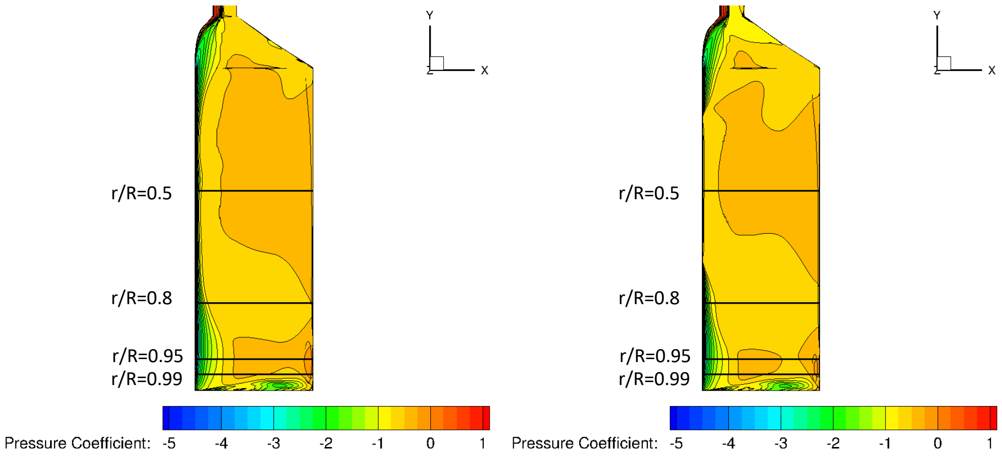

(a) $\alpha = 21°$ (b) $\alpha = 22°$

Figure 5.56: Pressure coefficient contours on blade surface at post-stall angles of attack ($\alpha = 21°$, $\alpha = 22°$) with SA RANS turbulence model.

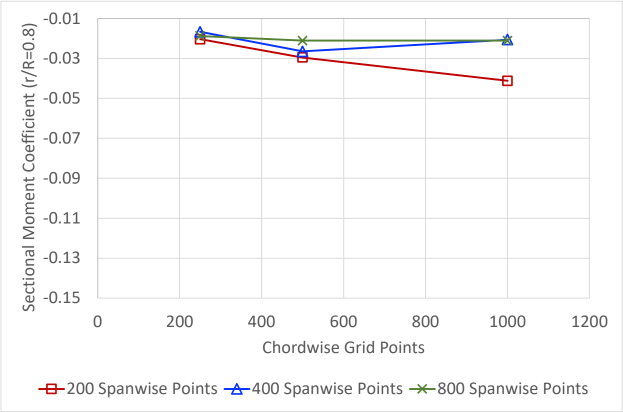

Figure 5.57: Chordwise convergence of sectional moment coefficient at r/R=0.8 for each spanwise refinement level

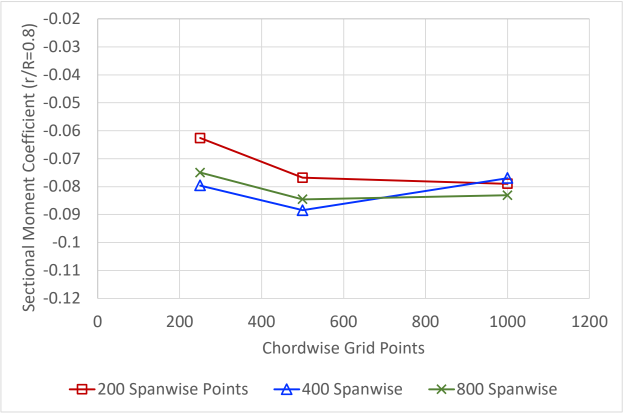

Figure 5.58: Chordwise convergence of sectional moment coefficient at r/R=0.8 for each spanwise refinement level

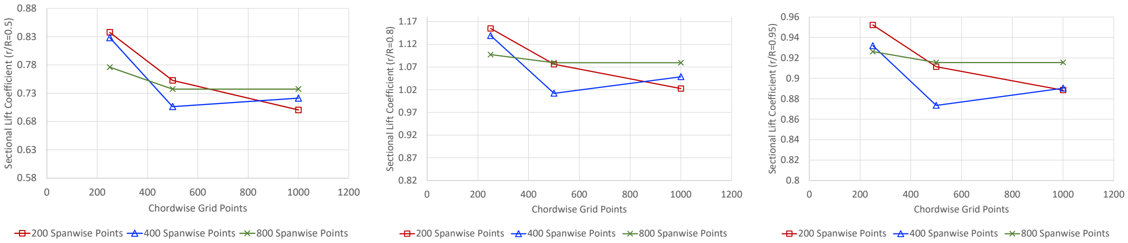

(a) r/R=0.5 (b) r/R=0.8 (c) r/R=0.95

Figure 5.59: Post-stall lift convergence with increasing chordwise refinement at $\alpha = 21°$ with SA DDES turbulence model

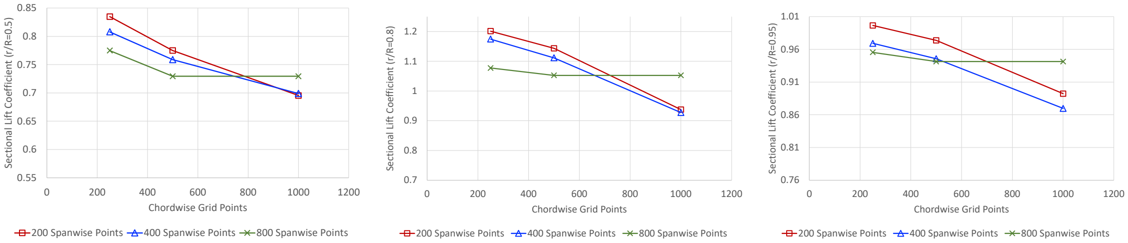

(a) r/R=0.5 (b) r/R=0.8 (c) r/R=0.95

Figure 5.60: Post-stall lift convergence with increasing chordwise refinement at $\alpha = 22°$ with SA DDES turbulence model

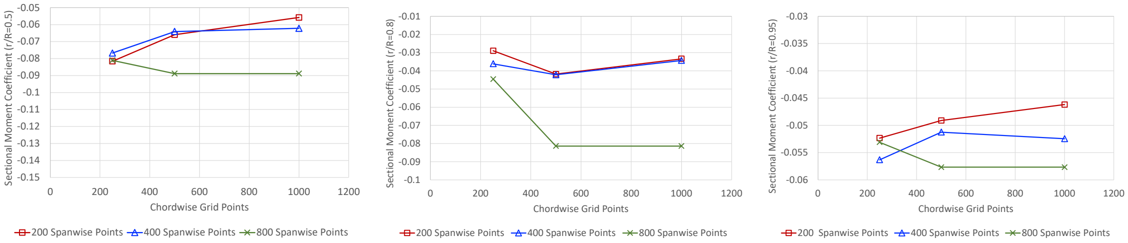

(a) r/R=0.5 (b) r/R=0.8 (c) r/R=0.95

Figure 5.61: Post-stall moment convergence with increasing chordwise refinement at $\alpha = 21°$ with SA DDES turbulence model

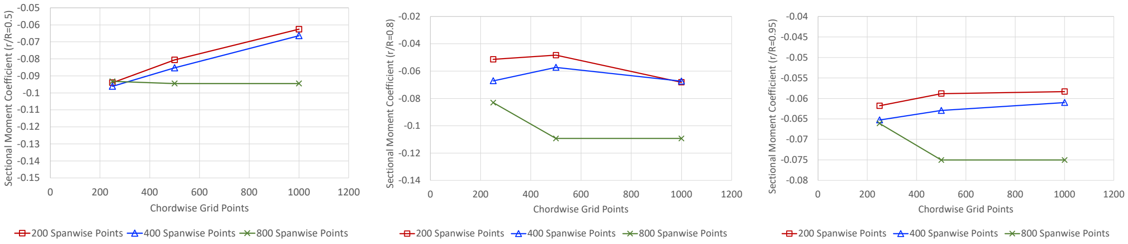

(a) r/R=0.5 (b) r/R=0.8 (c) r/R=0.95

Figure 5.62: Post-stall moment convergence with increasing chordwise refinement at $\alpha = 22°$ with SA DDES turbulence model

$k\omega$-SST RANS

Post-stall lift convergence is shown for $\alpha = 21°$ in Figure 5.63 and $\alpha = 22°$ in Figure 5.64. While lift predictions using 200 spanwise points do not exhibit convergent behavior with increasing chordwise refinement, lift predictions using 400 and 800 spanwise points do converge. The majority of variation in lift prediction is due to an increase from 250 to 500 chordwise points. Further increase in chordwise refinement from 500 to 1000 results in minimal change in prediction capabilities. The maximum SDP of lift when increasing from 500 to 1000 chordwise points is 4.10%, a far outlier, with all other SDP values well under the 3.0% mark. The average SDP of lift over the same range is 0.70%, suggesting very small variation as chordwise refinement is increased past 500 points. Thus, 500 chordwise points is sufficient to capture post-stall lift using the $k\omega$-SST RANS turbulence model, when sufficient spanwise refinement is chosen.

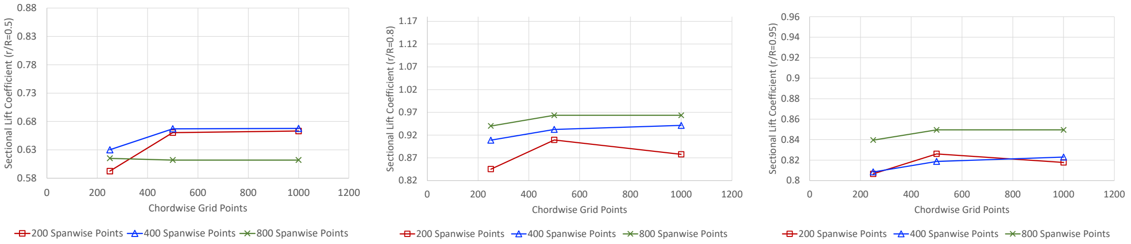

(a) r/R=0.5 (b) r/R=0.8 (c) r/R=0.95

Figure 5.63: Post-stall lift convergence with increasing chordwise refinement at $\alpha = 21°$ with $k\omega$-SST RANS turbulence model

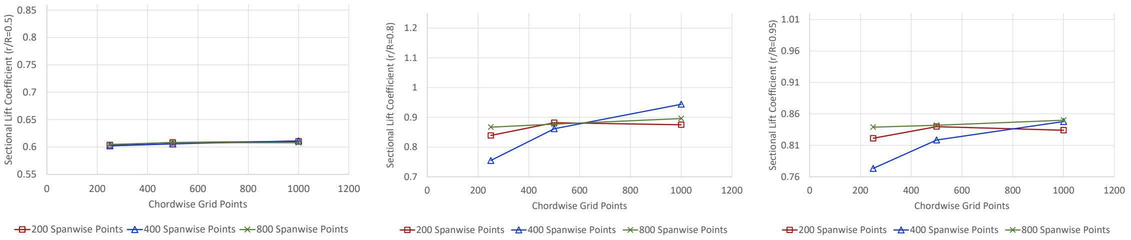

(a) r/R=0.5 (b) r/R=0.8 (c) r/R=0.95

Figure 5.64: Post-stall lift convergence with increasing chordwise refinement at $\alpha = 22°$ with $k\omega$-SST RANS turbulence model

Post-stall moment convergence is shown for $\alpha = 21°$ in Figure 5.65 and $\alpha = 22°$ in

Figure 5.66. Moment predictions using 200 and 400 spanwise points do not exhibit convergent behavior with increasing chordwise refinement. However, moment predictions using 800 spanwise points do converge. As Figures 5.65 and 5.66 illustrate, the majority of variation in moment prediction using 800 spanwise points is due to an increase from 250 to 500 chordwise points. Further increase in chordwise refinement from 500 to 1000 results in minimal change in prediction capabilities. Thus, 800R x 500C is sufficient grid refinement to capture post-stall behavior using the $k\omega$-SST RANS turbulence model.

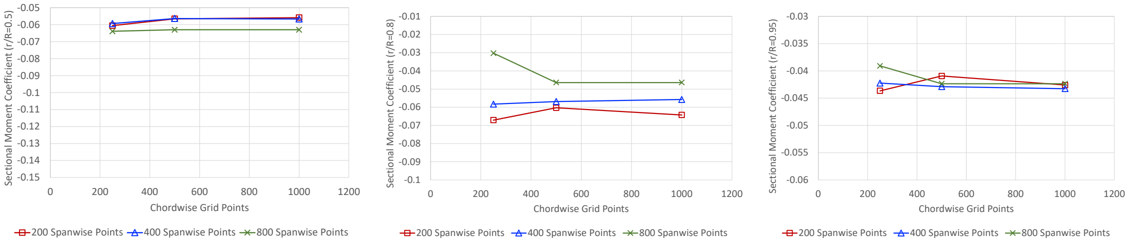

(a) r/R=0.5

(b) r/R=0.8

(c) r/R=0.95

Figure 5.65: Post-stall moment convergence with increasing chordwise refinement at $\alpha = 21°$ with $k\omega$-SST RANS turbulence model

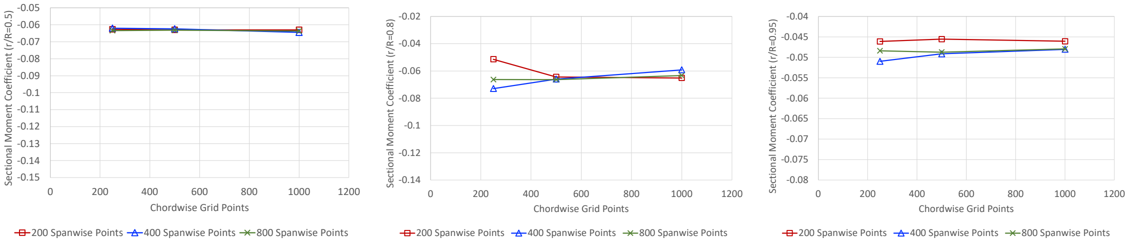

(a) r/R=0.5

(b) r/R=0.8

(c) r/R=0.95

Figure 5.66: Post-stall moment convergence with increasing chordwise refinement at $\alpha = 22°$ with $k\omega$-SST RANS turbulence model

$k\omega$-SST DDES

Lift convergence at $\alpha = 21°$ and $\alpha = 22°$ is displayed in Figures 5.67 and 5.68, respectively. With 200 and 400 spanwise points, lift does not exhibit convergent behavior with increasing chordwise refinement. Similar to behavior noticed with other turbulence models, the only convergent behavior occurs when there are 800 spanwise points. With 800 spanwise points, there is little change in lift prediction values when chordwise refinement is increased from 500 to 1000 points.

Moment convergence at $\alpha = 21°$ and $\alpha = 22°$ is illustrated in Figures 5.69 and 5.70. The solution does not converge when 200 and 400 spanwise points are used, confirming once again that the solution is sensitive to aspect ratio. Visually, the solution does not converge for 800 spanwise points, however chordwise variation from 500 to 1000 points is minimized with 800 spanwise points. Thus 800R x 500C is sufficient grid refinement to capture post-stall behavior using the $k\omega$-SST RANS turbulence model.

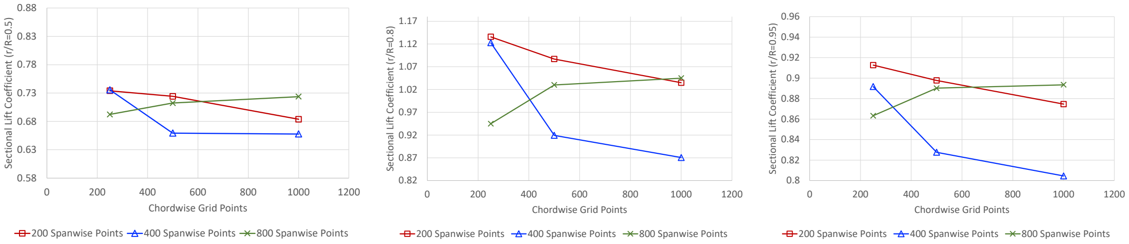

(a) r/R=0.5 (b) r/R=0.8 (c) r/R=0.95

Figure 5.67: Post-stall lift convergence with increasing chordwise refinement at $\alpha = 21°$ with $k\omega$-SST DDES turbulence model

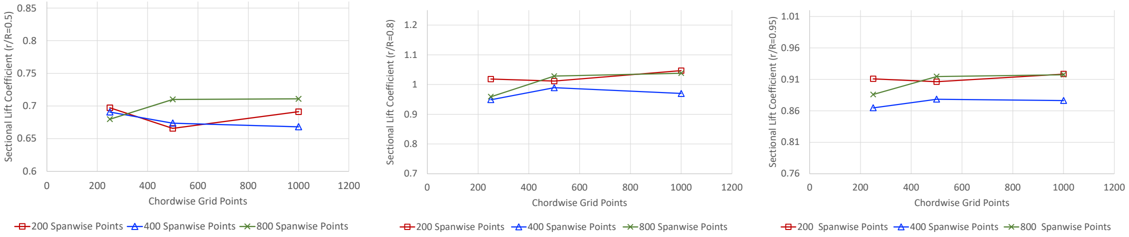

(a) r/R=0.5 (b) r/R=0.8 (c) r/R=0.95

Figure 5.68: Post-stall lift convergence with increasing chordwise refinement at $\alpha = 22°$ with $k\omega$-SST DDES turbulence model

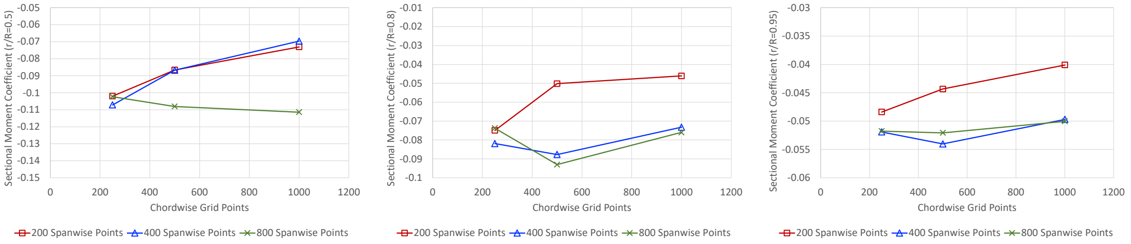

(a) r/R=0.5 (b) r/R=0.8 (c) r/R=0.95

Figure 5.69: Post-stall moment convergence with increasing chordwise refinement at $\alpha = 21°$ with $k\omega$-SST DDES turbulence model

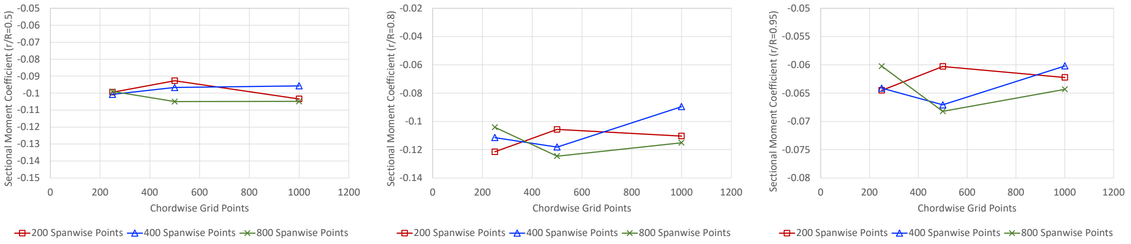

(a) r/R=0.5 (b) r/R=0.8 (c) r/R=0.95

Figure 5.70: Post-stall moment convergence with increasing chordwise refinement at $\alpha = 22°$ with $k\omega$-SST DDES turbulence model

Mesh Dependence on Aspect Ratio

In addition to cell refinement, predictions also affected by mid-chord cell aspect ratio. With 200 and 400 spanwise points, evenly distributed aspect ratio along the wing is not achieved with chordwise refinement. As indicated in Figure 5.71, increases in chordwise refinement result in an aspect ratio maximum at $r/R = 0.5$.

Figure 5.71a, shows that with 200 spanwise points, the mid-chord aspect ratio increases with each chordwise refinement level and each of the grids have a local aspect ratio maximum. Only near the root and tip ($r/R < 0.15$ and $r/R > 0.95$) does mid-chord aspect ratio decrease with increasing chordwise refinement.

Similar behavior is observed for 400 spanwise points grid, as demonstrated in Figure 5.71b. With 250 chordwise points, an aspect ratio minimum is achieved at the mid-span. However, increasing chordwise refinement to 500 and 1000 points creates local aspect ratio maxima and aspect ratio distributions that are not consistent with refinement level. Additionally, the aspect ratio near $r/R = 0.4$ and $r/R = 0.8$ is equivalent between the grids with 250 and 1000 chordwise points while the grid with 500 chordwise points has a smaller aspect ratio.

This behavior occurs when spanwise refinement is required at the root and tip but is allowed to coarsen significantly in the mid-span, resulting in large mid-span aspect ratios at all chordwise stations. This is standard engineering practice for finite wings, however this study proves it is not sufficient for finite wing grid independence studies where spanwise flow gradients are present.

From the onset of stall through post-stall angles of attack, moment predictions at $r/R = 0.8$ had consistently high variation across turbulence models and chordwise refinement for 200 and 400 spanwise points. At $r/R = 0.8$, a low pressure bubble was prone to unpredictable movement and growth when grids with 200 and 400 spanwise points were leveraged, resulting in non-convergent force and moment behavior, indicating solution dependence on aspect ratio. The non-convergent behavior of moment with chordwise refinement at $r/R = 0.8$ mimics the changes in aspect ratio at $r/R = 0.8$ for both 200 and 400 spanwise points, indicating once again that compatibility between grid spacing and distribution is fundamental to performing grid independence studies on a finite wing using any standard turbulence model.

With 800 spanwise points, an increase in chordwise refinement creates a grid with much more evenly distributed aspect ratio that is consistent with refinement level across all spanwise locations, as shown in Figure 5.71c. The low pressure bubble maintains its shape and size with increasing chordwise refinement, and the resulting behavior is convergence towards a single moment values at $r/R = 0.8$ across all turbulence models.

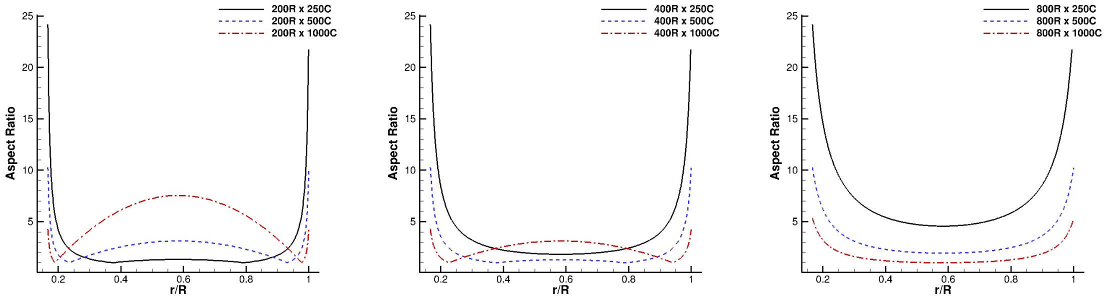

(a) 200 spanwise points (b) 400 spanwise points (c) 800 spanwise points

Figure 5.71: Variation in aspect ratio with increasing chordwise refinement for various spanwise refinement levels

Grid refinement sensitivity was analyzed for three different levels of chordwise as well as spanwise grid refinement. Each grid was used to obtain solutions using four different turbulence models, to understand grid refinement requirements when using varying fidelity turbulence models. Thorough analysis of this data has demonstrated that an 500 x 800 (chord x span) grid is sufficient to capture pre-stall, stall, and post-stall behavior using all four turbulence models on the finite OA-209 wing. To achieve similar refinement on other geometries, chordwise spacing and distribution should be equivalent, with 500 surface points, leading and trailing edge spacings of 0.04% and 0.01% chord, respectively, and a hyperbolic distribution to achieve equivalent mesh parameters along the characteristic length. In the spanwise direction, root and tip spacing should be chosen to accurately capture the geometry. Using a hyperbolic distribution, the spanwise connector dimension should be chosen to minimize mid-chord aspect ratio at the mid-span, as demonstrated in Figure 5.71c.

5.2 Turbulence Model Study

As discussed in Section 2.1.4, the first of two turbulence model studies was performed on the finite wing. The study uses the OA209 grid with 800 spanwise and 500 chordwise points to ensure a grid independent solution for all turbulence models, based on the findings from the grid study in Section 5.1. Four turbulence models (SA RANS, SA DDES, $k\omega$-SST RANS, and $k\omega$-

SST DDES) were leveraged to determine the effectiveness of each turbulence model at predicting pre-stall, stall and post-stall behavior. Figures 5.72 and 5.73 contain lift and moment predictions, respectively, for all four turbulence models and are referenced throughout the turbulence model discussion.

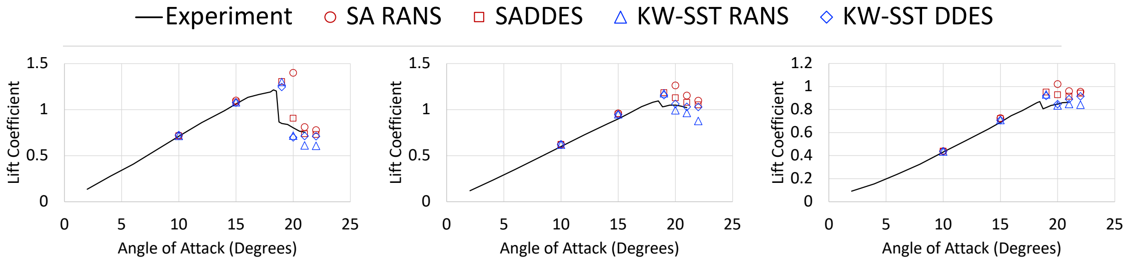

(a) r/R=0.5 (b) r/R=0.8 (c) r/R=0.95

Figure 5.72: Lift predictions using 800Rx500C grid using four turbulence models

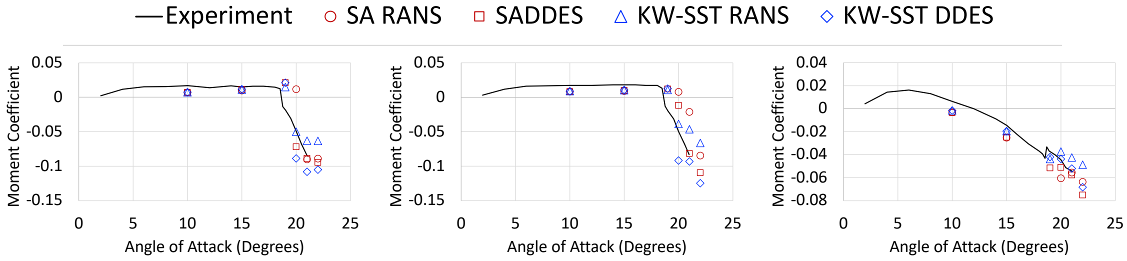

(a) r/R=0.5 (b) r/R=0.8 (c) r/R=0.95

Figure 5.73: Moment predictions using 800Rx500C grid using four turbulence models

Pre-Stall

At pre-stall angles of attack ($alpha = 10^\circ$, $\alpha = 15^\circ$), all four turbulence models predict similar lift and moment values. In Figure 5.72, lift predictions at pre-stall angles of attack are equivalent for all four turbulence models. Similarly in Figure 5.73, moment predictions are equivalent for all four turbulence models. Thus, for pre-stall predictions, all four turbulence models are sufficiently robust to capture the flowfield physics.

Stall

During stall ($\alpha = 20°$) the flowfield is much more complex than at pre-stall angles of attack. Varying levels of turbulence model fidelity are distinguishable. At $\alpha = 20°$, we can see that the SA DDES, $k\omega$-SST RANS, and $k\omega$-SST DDES models capture both lift (Fig. 5.72) and moment (Fig. 5.73) stall. The SA RANS model does not capture stall, and instead predicts an increase in both lift and moment values consistent with the linear lift curve slope. The SA RANS model does not predict stall until $\alpha = 21°$. While the SA RANS model is simple and fast, it does not have the robustness to capture separation as accurately as the other three models and is not considered past point.

The SA DDES and both $k\omega$-SST models have slightly different lift predictions at $\alpha = 20°$ that all all hover around the experimental value as shown in Figure 5.72. The moment predictions at $\alpha = 20°$ are highly variant across turbulence models (Fig. 5.73), however the moment curve is steep at that angle of attack and predictions are thus extremely sensitive to the flowfield. The three models predict stall at varying degrees and provide sufficient robustness to be further considered.

Post-Stall

During post-stall ($\alpha = 21°$, $22°$) the flowfield is similarly complex to the flowfield complexity during stall at $\alpha = 20°$. The SA DDES and $k\omega$-SST DDES models provide highly accurate post-stall lift (Fig. 5.72) and moment (Fig. 5.73) predictions. The $k\omega$-SST RANS model tends to overpredict lift stall magnitude and underpredict moment stall magnitude in these post-stall configurations. While the $k\omega$-SST RANS predictions predict stall, they do not provide the accuracy of DDES models. Any additional turbulence modeling studies will not consider RANS models.

CHAPTER 6

IDENTIFICATION AND CLASSIFICATION SEPARATED FLOW ON THREE-DIMENSIONAL ROTORS

6.1 Identification of Separated Flow on Rotating Systems

The availability of high quality wind tunnel data for the UH-60A rotor permit development and assessment of state-of-the-art computational methods to capture flow separation on the rotor for the more critical high speed and high thrust operational conditions. In this effort, flow separation on the rotor is identified by computing the tangential component of the skin friction vector, $\hat{t}$:

$$\tau_t = \hat{\tau} \cdot \hat{t}. \tag{6.1}$$

The tangent ($\hat{t}$) and normal unit vector($\hat{n}$) can be computed with respect to the blade surface at every grid point, as in Fig. 6.1. The radial unit vector ($\hat{r}$) is aligned with the radial component of the blade, neglecting flapping and lagging, and is defined using the azimuth position of the blade:

$$\overline{r} = \begin{bmatrix} \cos\psi \\ \sin\psi \\ 0 \end{bmatrix} \tag{6.2}$$

The tangential unit vector ($\hat{t}$) is tangential to the surface and defined as the cross product of the normal and radial vectors:

$$\hat{t} = \hat{n} \times \hat{r}. \tag{6.3}$$

Separated flow is identified when the tangential component of skin friction is negative. For each

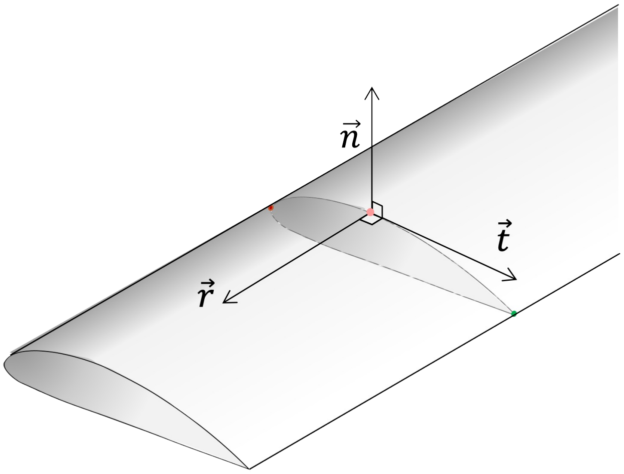

Figure 6.1: Definition of separated flow

azimuth station, the tangential component of skin friction is computed over the entire blade surface, as shown in Figure 6.2a, where blue indicates attached flow and red indicates separated flow. To quantify the degree of separation, the tangential component of skin friction is evaluated along spanwise slices to determine the separation length, or chordwise percentage of the blade experiencing separated flow, at each spanwise station. This data is best visualized for the entire rotor plane in the form of a separation length rotor map (Fig. 6.2b). A value of 0.0 indicates fully attached flow and a value of 1.0 indicates fully separated flow. An intermediate value, for example 0.4, indicates that 40% of the blade surface at a particular spanwise location and azimuth position is experiencing separated flow.

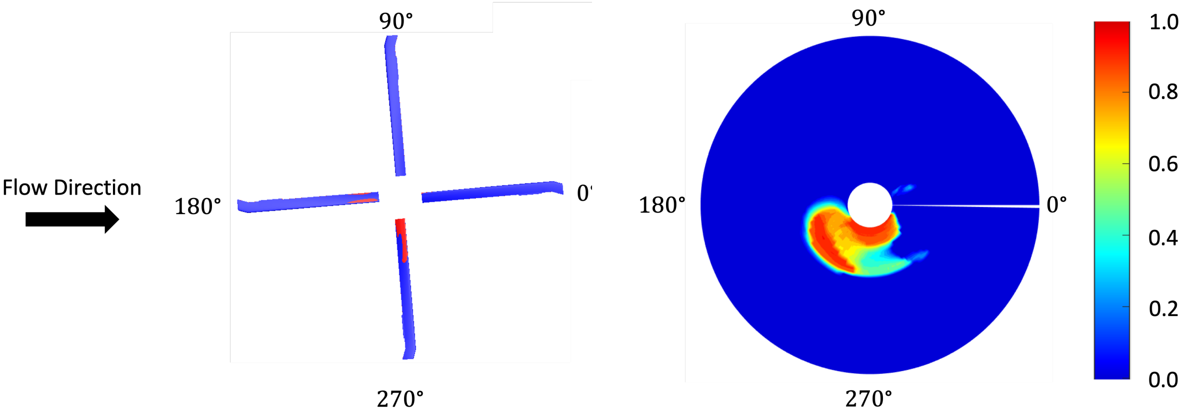

(a) Regions of separated flow (red) (b) Rotor map of separation length

Figure 6.2: Separated flow on a four-bladed articulated rotor in forward flight, where 0.0 indicates fully attached flow and 1.0 indicates fully separated flow

In 2018, Richez identified five flow separation regions (FS) on a four-bladed, articulated 7A rotor applying this criterion [31]. The various flow separation regions, shown in Figure 6.3, appear and develop with increasing thrust and may not be present for all test points. For example, Figure 6.4 shows separation length rotor maps for the UH-60A through a thrust sweep from $C_T/\sigma = 0.040 - 0.120$. Initially, one small flow separation region is present for the low thrust condition. It is observed to increase in size and strength with increasing thrust, as indicated by expanding regions of non-zero values and higher magnitudes in those regions, respectively, on the separation rotor map. For the high thrust conditions ($C_T/\sigma = 0.120$,0.125), additional flow separation regions begin to appear and develop on the outboard blade between $\psi = 270°$ and $\psi = 360°$. Identification and visualization of these flow separation regions using rotor maps is an important piece in understanding the physics of separated flow on the rotor and will be referenced throughout this study.

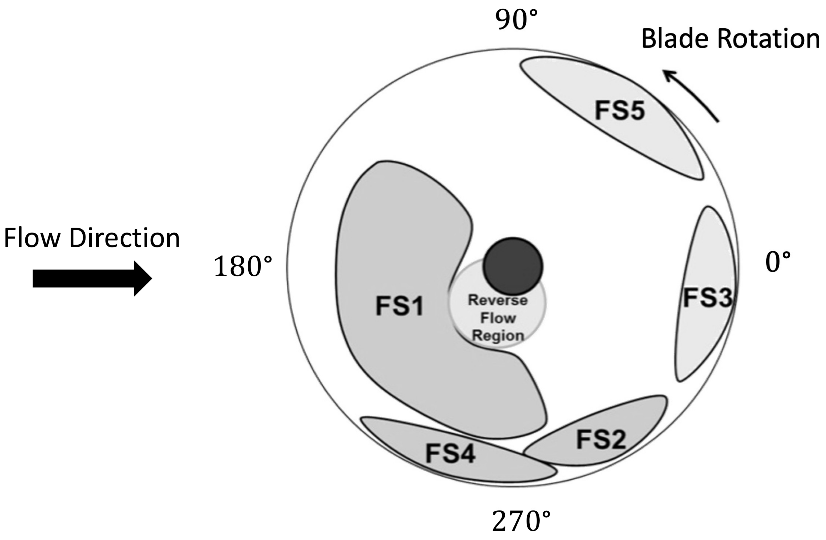

Figure 6.3: Separation regions on a four-bladed, articulated rotor, Ref. [31]

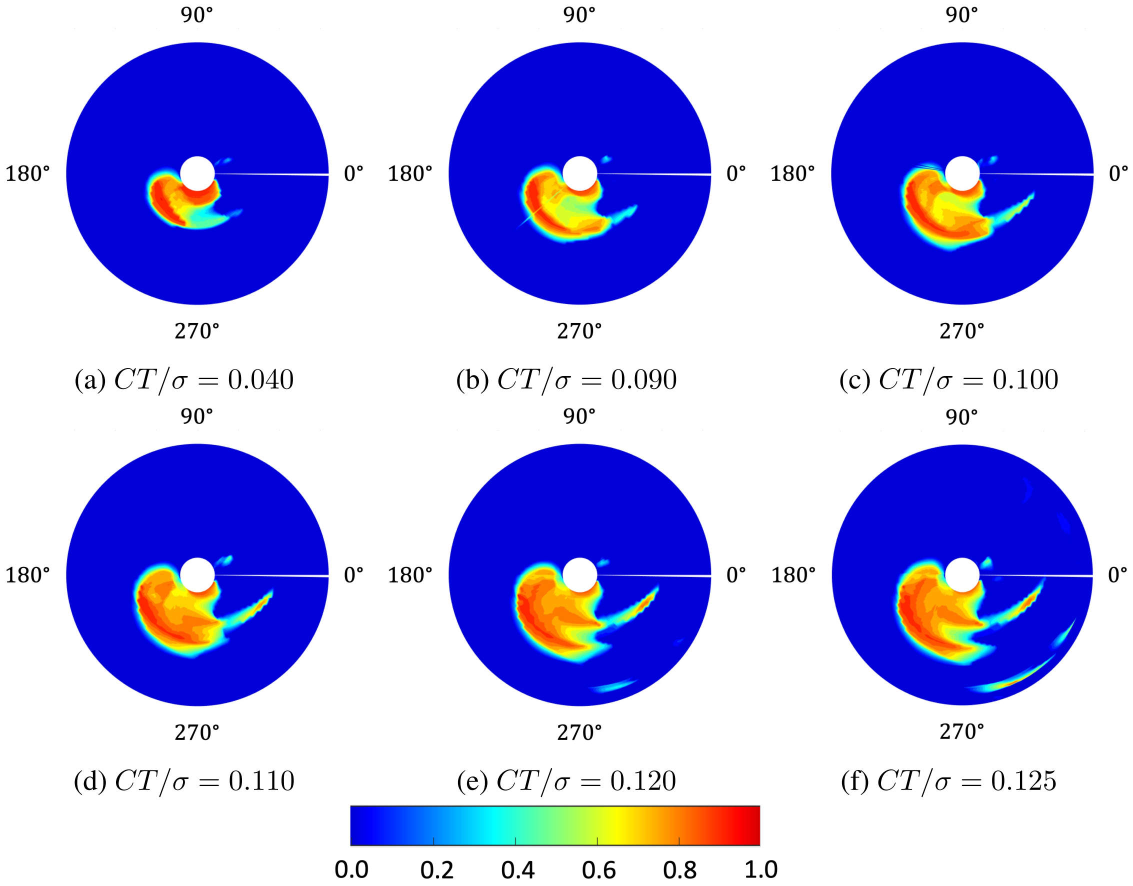

(a) $CT/\sigma = 0.040$ (b) $CT/\sigma = 0.090$ (c) $CT/\sigma = 0.100$

(d) $CT/\sigma = 0.110$ (e) $CT/\sigma = 0.120$ (f) $CT/\sigma = 0.125$

Figure 6.4: Development of flow separation on UH-60A rotor plane with increasing thrust where 0.0 indicates fully attached flow and 1.0 indicates fully separated flow. Flow direction is from left to right.

6.1.1 Effects of Grid Refinement

In Chapter, 5, a detailed grid refinement study was performed to understand the effects of grid refinement on predicting separated flow on a static wing in pre-stall, stall, and post-stall configurations. Results from this refinement study provide the optimized mesh characteristics for predicting separated flow on finite wings in translation.

Prediction of separated flow in the rotor plane is much more complex than a finite wing due to the nature of the flowfield. It is not possible to perform a robust grid refinement study on a three-dimensional, rotating system due to constraints of computational resources. However, a smaller-scale investigation is performed on two grid systems, a moderate engineering grid (baseline) and an optimized grid (based on Chapter 5 findings), to confirm that grid refinement based on best-practices from Chapter 5 translates to a rotating frame. Details of both grids can be found in Chapter 4. The baseline grid, detailed in Section 4.2, was developed and used by Boeing for engineering applications. Its planar mesh refinement is based on infinite wing best-practices that were shown in Chapter 5 to be insufficient for finite wings in separated flow. The optimized mesh was generated to achieve similar refinement to the finite wing in Chapter 5. The chordwise connector was dimensioned to 500 points with leading and trailing edge spacings of 0.04% and 0.01% chord, respectively, and a hyperbolic distribution to achieve equivalent mesh parameters along the characteristic length. In the spanwise direction, root and tip spacing were chosen to accurately capture the geometry. Using a hyperbolic distribution, the spanwise connector dimension was chosen to minimize mid-chord aspect ratio at the mid-span, as detailed in Chapter 4.

Figure 6.5 shows rotor maps from both mesh results. The fine grid predicts a larger separation area on the rotor disk than the coarse grid. However, the coarse grid predicts stronger separation than the fine grid. Two-dimensional CFD simulations of three-dimensional dynamic stall are well known to overpredict normal force and pitching moments, for example see Spentzos (Ref. [17]), Zanotti (Ref. [81]), and Kaufman (Ref. [25]). By limiting the simulation to two dimensions, three-dimensional relief effects during separation are not realized. Velocities and pressures are much higher, and flow features are much stronger in the two-dimensional simulations.

A similar phenomenon is observed with the baseline rotor blade. The baseline rotor blade has very large radial spacing, that has been typical of engineering grade CFD models. The large radial spacing is coincident with high radial velocity and pressure gradients. The resulting radial spatial differencing lengths are so large that two-dimensional behavior begins to emerge. Three-dimensional features are not captured due to radial grid coarseness, and large mid-chord aspect ratios. In this case, the flow features causing separation on the inboard blade do not experience radial relief, resulting in stronger separation over a smaller region, much like the two-dimensional dynamic stall simulations. In Figure 6.5a, the behavior can be visualized where the strong separation (dark red) is seen around $r/R \approx 50\%$ at the edge of the separation region in the bottom left quadrant of the rotor map between $\psi = 180°$ and $\psi = 270°$. When increased radial refinement is considered, three-dimensional relief effects are realized and a larger, weaker separation region is predicted from $\psi = 180°$ to $\psi = 270°$, as per Figure 6.5b, where a weaker separation region extends beyond $r/R \approx 50\%$.

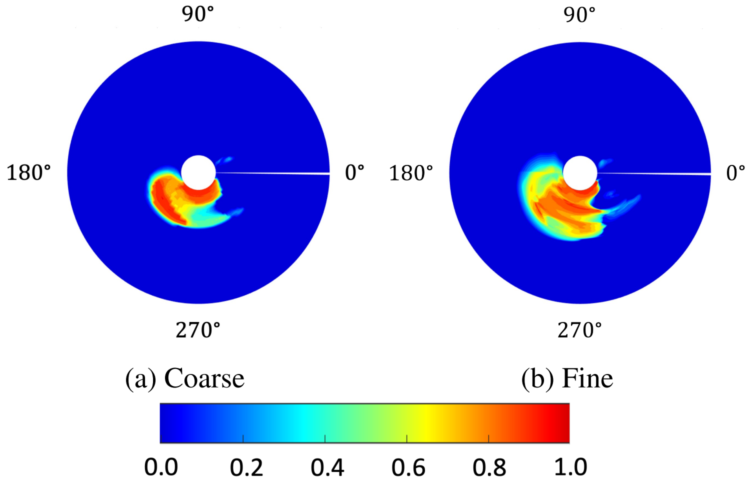

(a) Coarse (b) Fine

Figure 6.5: Rotor separation map at $CT/\sigma = 0.040$ where 0.0 indicates fully attached flow and 1.0 indicates fully separated flow. Flow direction is from left to right

This behavior also appears in airloads data, where Figure 6.6 shows normal force predictions at various radial stations using both the baseline and optimized grids for a light stall case. Both the grids exhibit similar behavior, however the optimized grid more accurately predicts the magnitude of peaks and drops in normal force. The baseline grid tends to overpredict the magnitude of both peaks and drops, which is caused by lack of three-dimensional relief. This further supports conclusions in Section 5.1 that radial refinement and aspect ratio is an important consideration.

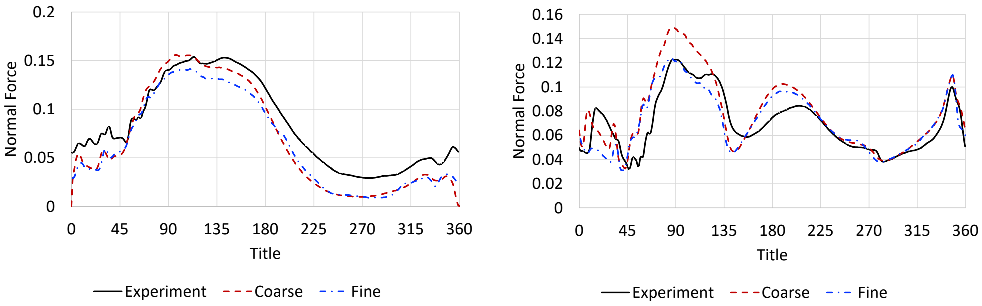

(a) $r/R = 0.400$ (b) $r/R = 0.675$

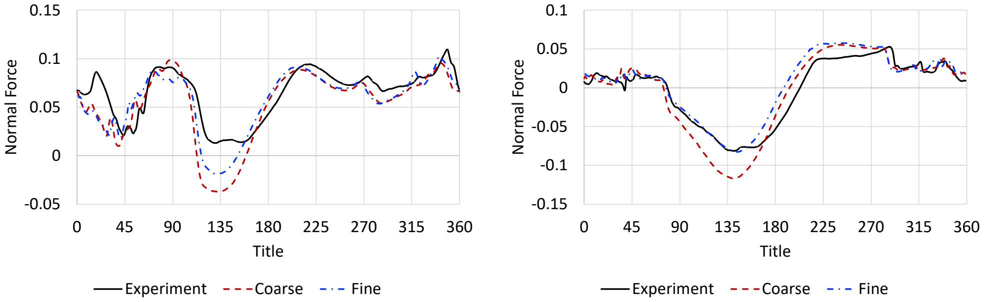

(c) $r/R = 0.775$ (d) $r/R = 0.990$

Figure 6.6: Normal force comparisons between coarse and fine grids. Experimental data from Ref. [30]

Figure 6.7 depicts the pitching moment predictions at various radial stations using both the grids for the same light stall case. As with the normal force predictions, both the grids exhibit similar behavior. At 40% and 67.5% radial stations, there is a clear offset between the experimental data and computational predictions. Differences between experimental and CFD-predicted pitching moment data are sometimes attributed to experimental pressure tap integration versus CFD surface pressure integration where many more data points are used. To determine pitching moment sensitivity to pressure tap versus CFD integration, pressure is extracted from the CFD data along the blade at the experimental pressure tap locations at the 40% and 67.5% radial stations for a different light stall case ($C_T/\sigma = 0.090$). The same procedure is applied to the CFD data that was applied to the experimental data to extract pitching moment distributions. While there are minor differences in predictions, the clear offset from experimental data still exists (Fig. 6.8), indicating integration method is not the root cause. Inboard moment predictions for the UH-60A using other CFD and CSD solvers, some of which have also included transition effects, have produced similar results (Refs. [74, 82]), suggesting that the offset from experimental data is due to the inboard blade structural properties, which is not the focus of this investigation. Moment predictions at 40% and 67.5% radial stations exhibit the same behavior where shape of the curve is captured but there is an offset in magnitude between the experimental and computational data for the remainder of the thrust sweep (Fig. 6.7).

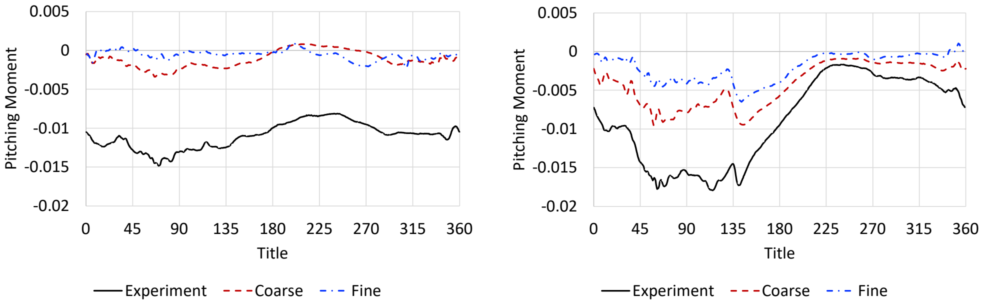

(a) $r/R = 0.400$ (b) $r/R = 0.675$

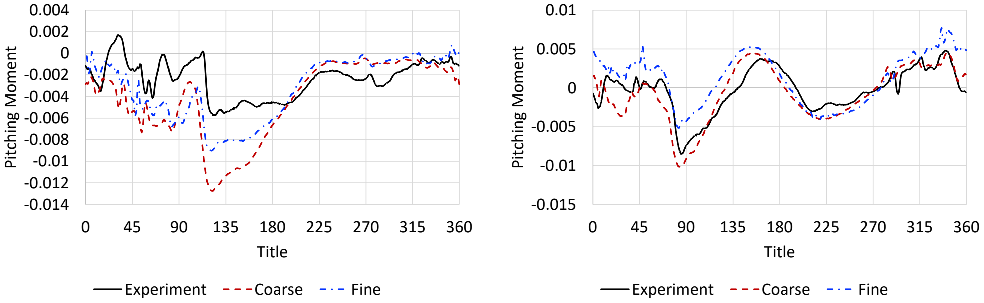

(c) $r/R = 0.775$ (d) $r/R = 0.990$

Figure 6.7: Pitching moment comparisons between baseline and optimized grids.

At higher thrust values, overall mesh refinement becomes important for capturing highly sensitive pitching moments. Figure 6.9 illustrates pitching moment predictions for the two deep stall cases, $C_T/\sigma = 0.120$ and $C_T/\sigma = 0.125$, at $r/R = 0.865$. Results using the baseline grid predict no moment stall at either thrust value, demonstrating that the mesh is insufficient to capture the onset of stall. The optimized grid predicts two moment stalls at both thrust values. The first moment stall is predicted around $\psi = 285°$ and the second is predicted around $\psi = 345°$. The

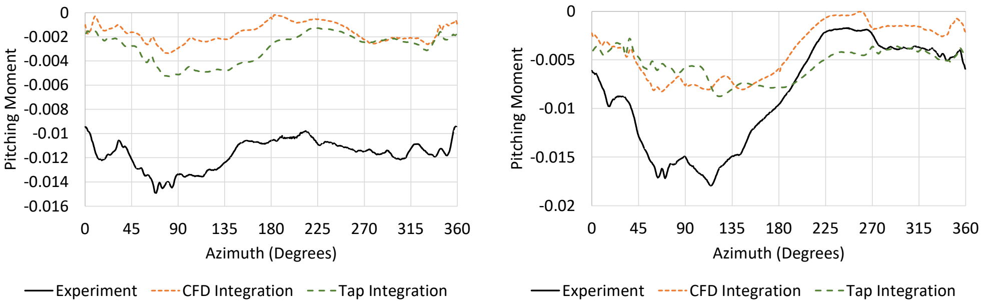

(a) $r/R = 0.400$ (b) $r/R = 0.675$

Figure 6.8: Pitching moment comparisons using pressure tap and CFD surface pressure integration.

experimental data show that stall at $\psi = 285°$ is present at both thrust values. However, the stall at $\psi = 345°$ is only present for $C_T/\sigma = 0.125$. At $\psi = 345°$, the OVERFLOW simulation predicts stall at a slightly lower C_T value than experiment, which is due to trim angle sensitivity at the tip near stall, as shown in Ref. [33]. An important takeaway is that the optimized mesh is able to predict the onset of the outboard stall within 5% of the actual thrust value. In a 2020 assessment of dynamic stall research state-of-the-art, Smith et al. (Ref. [18]) state "The goal of computational studies over the past few decades has been to be able to capture the onset of dynamic stall so that future vehicle designs can avoid this condition and upgrades to existing vehicles can be analyzed to see if the vehicle will encounter dynamic stall." Developing grid best practices that ensure the ability to predict dynamic stall onset within 5% of the thrust value is a significant advance towards using high-fidelity computations to avoid stall in vehicle design.

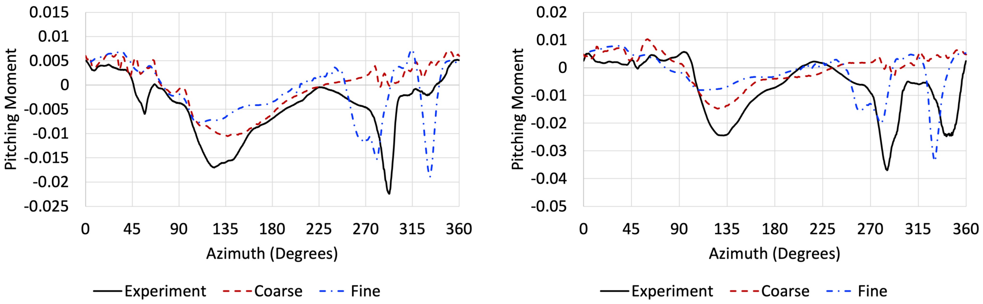

(a) $C_T/\sigma = 0.120$ (b) $C_T/\sigma = 0.125$

Figure 6.9: Deep stall pitching moment comparisons between baseline and fine grids at $r/R = 0.865$.

Coupled Effects of Grid Refinement and Turbulence Model

Chapter 5 considered not only grid refinement, but the integrated effect of grid refinement and turbulence model. Use of a higher-fidelity turbulence model is often leveraged in hopes of achieving a more accurate solution. In Chapter 5, analysis demonstrated that turbulence model does play an important role in prediction accuracy but only when grids were sufficiently refined. The coupled effects of grid refinement and turbulence model are explored in this section using prescribed motion from the coupled CFD-CSD case SA DDES case to isolate differences due to turbulence model from differences in blade motion and deformation that arise in coupled CFD-CSD cases.

Figures 6.10-6.11 and 6.13-6.14 depict normal force and pitching moment distributions for light and moderate stall cases, respectively, using the baseline grid. Comparisons of normal force, chord force, and pitching moment predictions for all test points and turbulence models can be found in Appendix B.

In the light stall case, normal force (Fig. 6.10) and pitching moment (Fig. 6.11) predictions are equivalent between all three turbulence models. The rotor maps in Figure 6.12 confirm that all three turbulence models predict equivalent separation regions, with the SA model predicting slightly stronger separation between $r/R = 0.6$ and $r/R = 0.7$ than the $k\omega$-SST models. However, the stronger separation predicted by the SA-DDES model has no effect on the airloads for the light stall case.

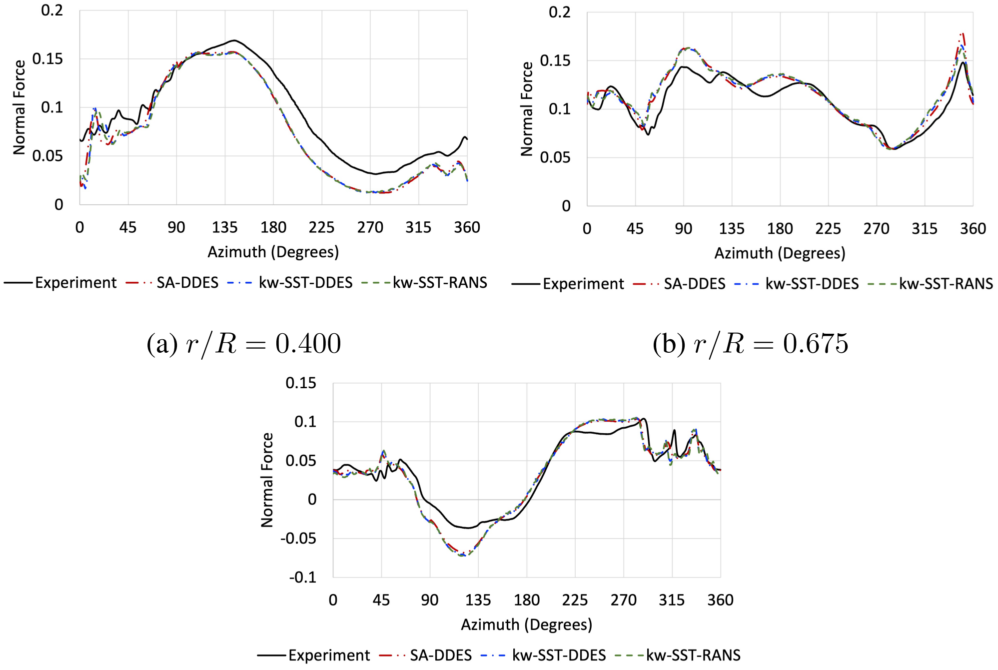

(a) $r/R = 0.400$

(b) $r/R = 0.675$

(c) $r/R = 0.990$

Figure 6.10: Normal force comparisons between turbulence models on coarse grids TP 4533 (Light Stall)

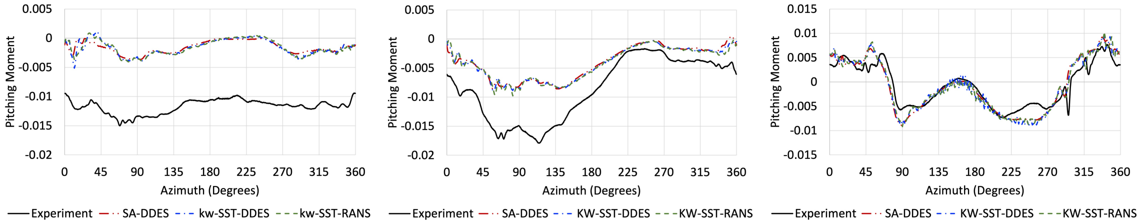

(a) $r/R = 0.400$

(b) $r/R = 0.675$

(c) $r/R = 0.990$

Figure 6.11: Pitching moment comparisons between turbulence models on coarse grids TP 4533 (Light Stall)

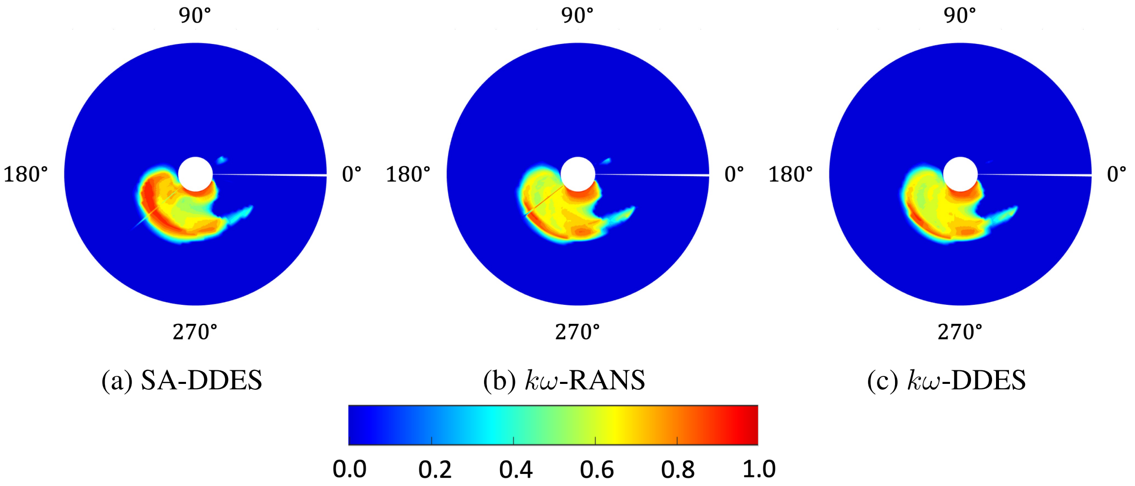

(a) SA-DDES (b) $k\omega$-RANS (c) $k\omega$-DDES

Figure 6.12: Rotor separation maps at $CT/\sigma = 0.09$ where 0.0 indicates fully attached flow and 1.0 indicates fully separated flow. Flow direction is from left to right

In the moderate stall case, normal force (Fig. 6.13) and pitching moment (Fig. 6.14) predictions are equivalent between the $k\omega$-SST RANS and DDES models but differ from the SA model. The rotor maps in Figure 6.15 indicate that, once again, all three turbulence models predict equivalent separation regions. The SA model predicts stronger separation over the entire region than the $k\omega$-SST models, which may attribute to the variation in airloads.

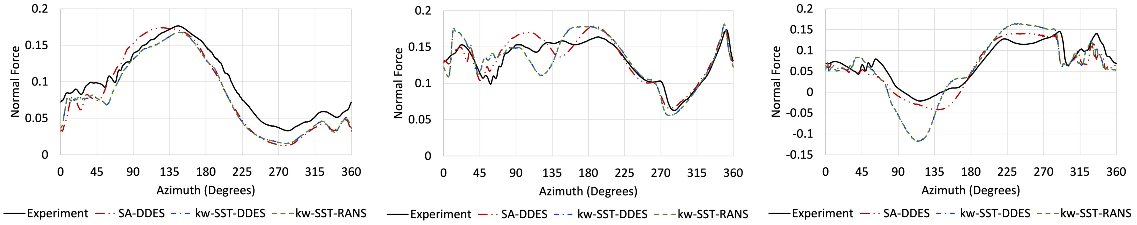

(a) $r/R = 0.400$ (b) $r/R = 0.675$ (c) $r/R = 0.990$

Figure 6.13: Normal force comparisons between turbulence models on baseline grids $C_T/\sigma = 0.110$

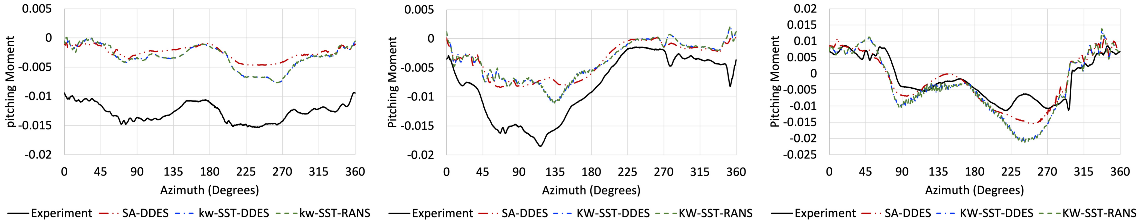

(a) $r/R = 0.400$ (b) $r/R = 0.675$ (c) $r/R = 0.990$

Figure 6.14: Pitching moment comparisons between turbulence models on baseline grids $C_T/\sigma = 0.110$

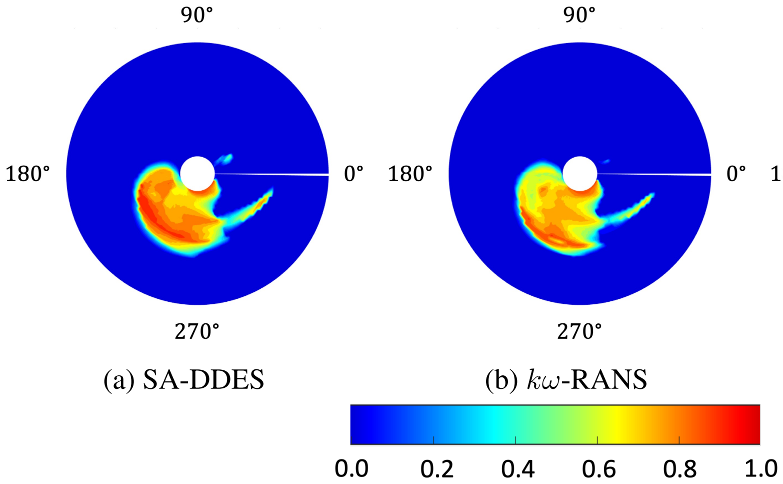

(a) SA-DDES

(b) $k\omega$-RANS

(c) $k\omega$-DDES

Figure 6.15: Rotor separation maps at $CT/\sigma = 0.11$ where 0.0 indicates fully attached flow and 1.0 indicates fully separated flow. Flow direction is from left to right

The $k\omega$-SST URANS and $k\omega$-SST DDES models predict equivalent separation location and strength as well as airloads across the the entire rotor plane. The $k\omega$-SST DDES model should produce different predictions than the $k\omega$-SST URANS model in separated flow if grid refinement is sufficient. In this case the grid is not sufficiently refined to capture the smallest scales of interest in separated flows and as a result, the DDES model is behaving like the URANS turbulence model. The baseline grid is too coarse to realize the improved effects of using a hybrid URANS-LES turbulence model.

Normal force and pitching moment predictions at various radial stations from the optimized grid are shown in Figures 6.16 and 6.17 for the light stall case and in Figures 6.18 and 6.19 for the moderate stall case. For both thrust values, the predicted airloads differ between all three turbulence models. This indicates that the grid has been refined sufficiently to support the smallest scales of interest in separated flow and the hybrid URANS-LES simulation is not reduced to a standard URANS model.

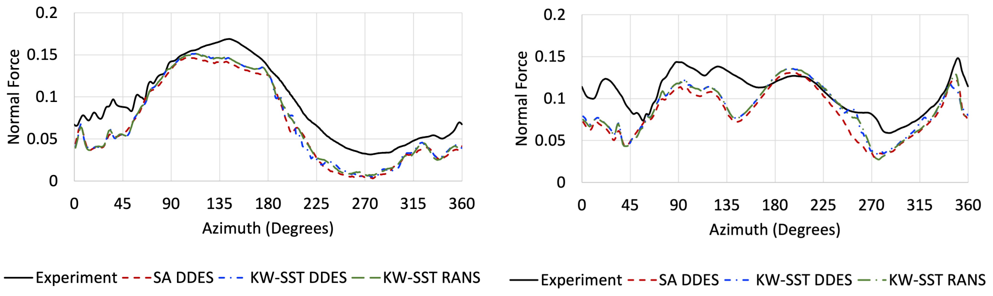

(a) $r/R = 0.400$ (b) $r/R = 0.675$

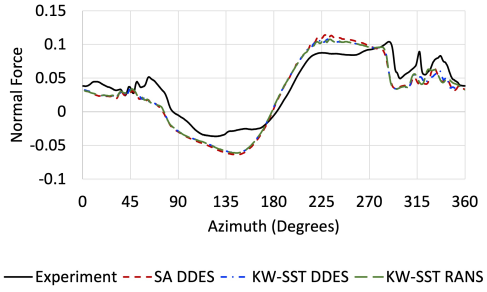

(c) $r/R = 0.990$

Figure 6.16: Normal force comparisons between turbulence models on optimized grids $C_T/\sigma = 0.090$

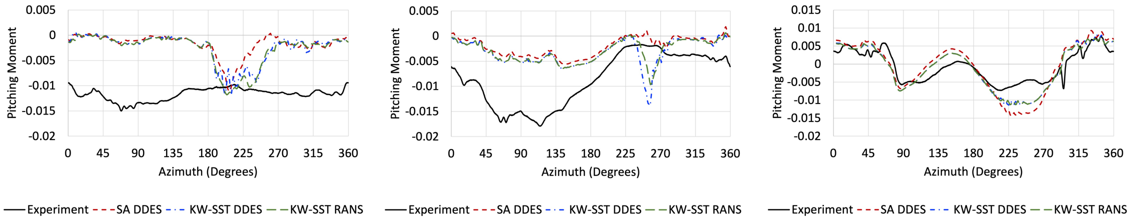

(a) $r/R = 0.400$ (b) $r/R = 0.675$ (c) $r/R = 0.990$

Figure 6.17: Pitching moment comparisons between turbulence models on optimized grids $C_T/\sigma = 0.090$

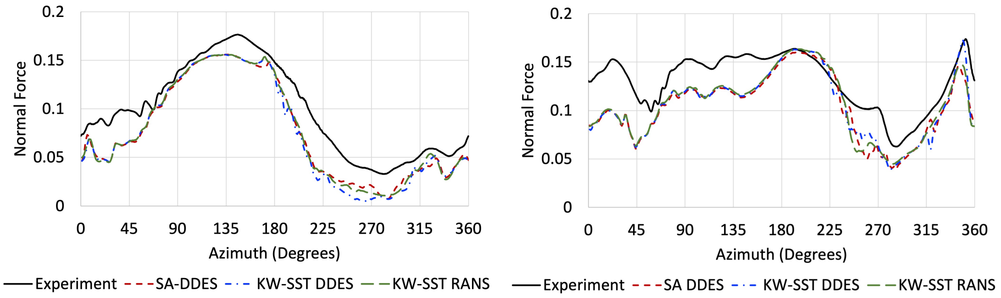

(a) $r/R = 0.400$ (b) $r/R = 0.675$

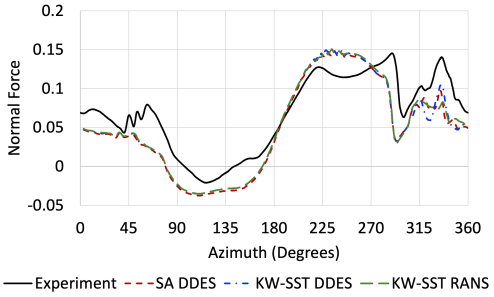

(c) $r/R = 0.990$

Figure 6.18: Normal force comparisons between turbulence models on optimized grids $C_T/\sigma = 0.011$

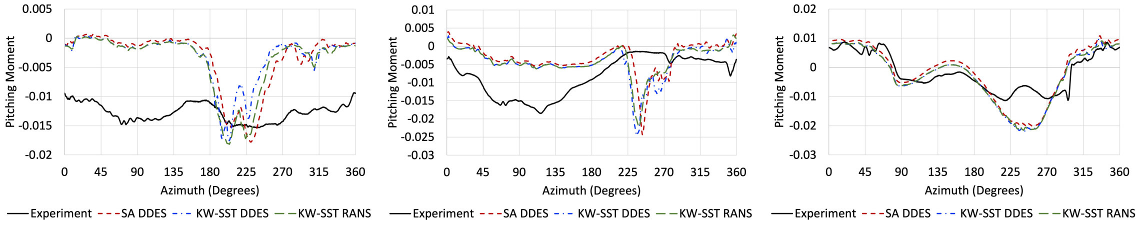

(a) $r/R = 0.400$ (b) $r/R = 0.675$ (c) $r/R = 0.990$

Figure 6.19: Pitching moment comparisons between turbulence models on optimized grids $C_T/\sigma = 0.110$

6.1.2 Effects of Turbulence Model

In Section 5.2 a turbulence model study was performed on a finite wing in various pre-stall, stall, and post-stall configurations. Results from this study demonstrated that the SA DDES and $k\omega$-SST DDES models most accurately predicted airloads consistently across all three regimes. The $k\omega$-SST RANS model did not predict airload magnitudes as accurately as the hybrid URANS-LES methods at post-stall angles of attack; however, it did accurately predict the onset of separation. The SA-RANS model failed to accurately capture separated flows for stall and post stall angles of attack. Rotorcraft experience all three regimes throughout a single rotor revolution with additional complexities from BVI and rotational effects. Only the hybrid URANS-LES models and the $k\omega$-SST RANS are considered in this section.

For this turbulence model study, blade motion and deformation for each test point are prescribed from the baseline coupled CFD-CSD simulations. The SA DDES, $k\omega$-SST RANS, and $k\omega$-SST DDES turbulence models are evaluated at each test point using the fine grid. Airload comparisons between each turbulence model at each radial station using the fine grid can be found in Appendix B.2.

Normal force and pitching moment predictions from each turbulence model are illustrated in Figures 6.20 and 6.21for a light stall case ($C_T/\sigma = 0.090$). All three turbulence models predict nearly equivalent behavior, as is expected in the light stall regime. Any of the three turbulence models used are sufficient to capture light stall on the refined grid.

Normal force and pitching moment predictions from each turbulence model are shown in Figures 6.22 and 6.23 for a moderate stall case ($C_T/\sigma = 0.110$). There are small but visually apparent differences in magnitude between the three models, however all once again predict very similar behavior, including inboard moment stalls that are not present in the experimental data. On this optimized grid, all three turbulence models capture the same behavior, and thus all are equally capable of capturing the physics in this moderate stall regime.

Normal force and pitching moment predictions from each turbulence model are shown in Figures 6.24 and 6.25 for a deep stall case ($C_T/\sigma = 0.125$). Like the light and moderate

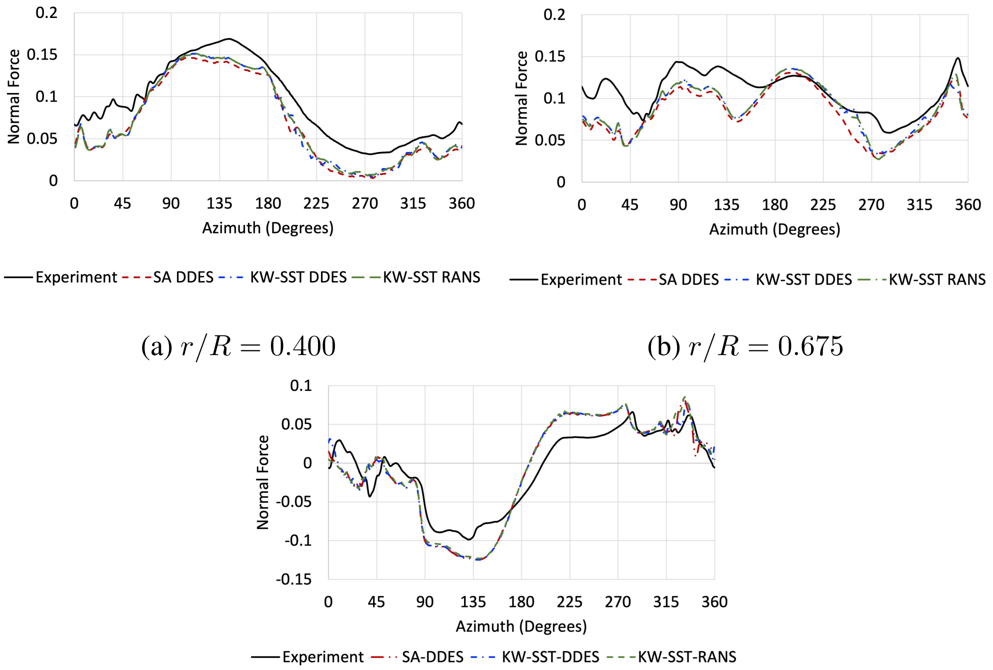

(a) $r/R = 0.400$

(b) $r/R = 0.675$

(c) $r/R = 0.920$

Figure 6.20: Normal force comparisons between turbulence models with the optimized grid C_T/σ=0.090

cases, all three turbulence models considered capture the same physical behavior with only minor differences in the magnitude of losses due to stall.

On this refined grid, all three turbulence models are considered are equally capable of capturing light, moderate and deep stall when run identically using the same fourth-order central differencing scheme and 60 subiterations with no residual cutoff. Across all test points, the SA-DDES model requires on average 7760 core-hours per quarter revolution on the HPCMP SGI ICE XA Centennial machine compared to 15,600 core-hours per quarter revolution using the $k\omega$-SST models. The SA-DDES model requires approximately 50% of the computational time required by the $k\omega$-SST models. Due to cost savings without loss of accuracy, the SA-DDES model will be applied in additional computations for this study.

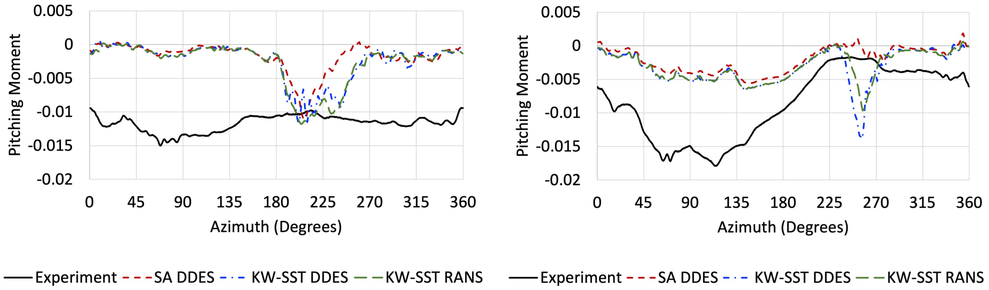

(a) $r/R = 0.400$ (b) $r/R = 0.675$

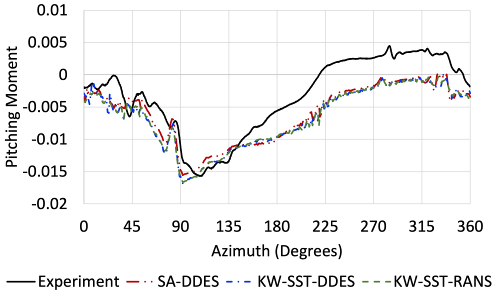

(c) $r/R = 0.920$

Figure 6.21: Pitching moment comparisons between turbulence models with the optimized grid C_T/σ=0.090

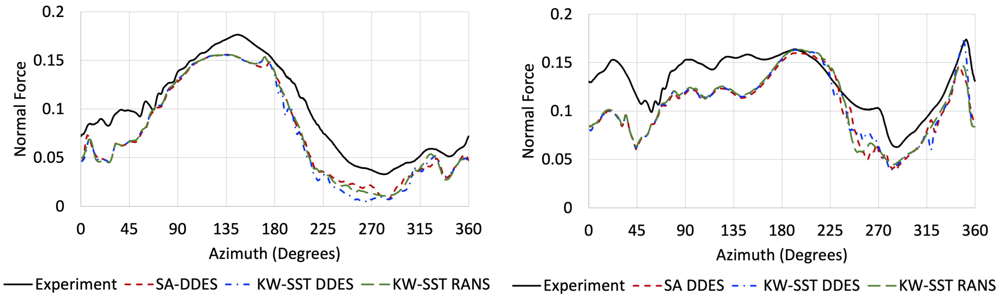

(a) $r/R = 0.400$ (b) $r/R = 0.675$

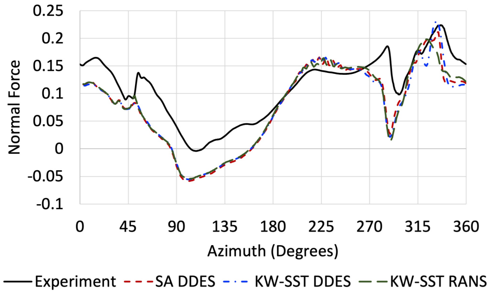

(c) $r/R = 0.920$

Figure 6.22: Normal force comparisons between turbulence models with the optimized grid C_T/σ=0.110

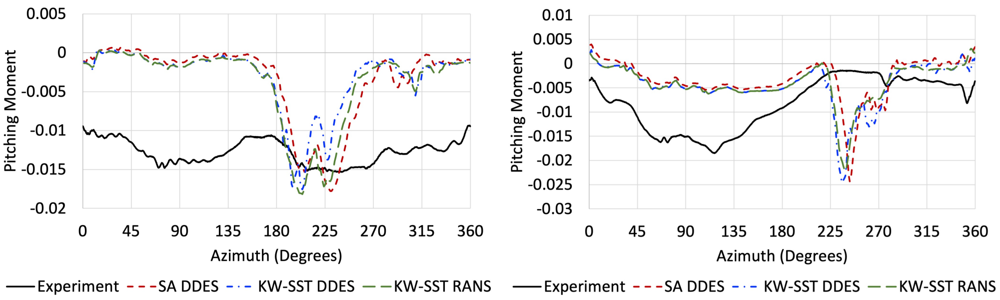

(a) $r/R = 0.400$

(b) $r/R = 0.675$

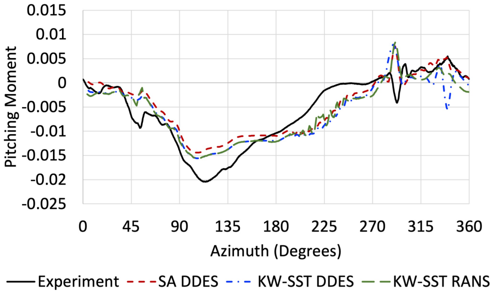

(c) $r/R = 0.920$

Figure 6.23: Pitching moment comparisons between turbulence models on fine grids C_T/σ=0.1100

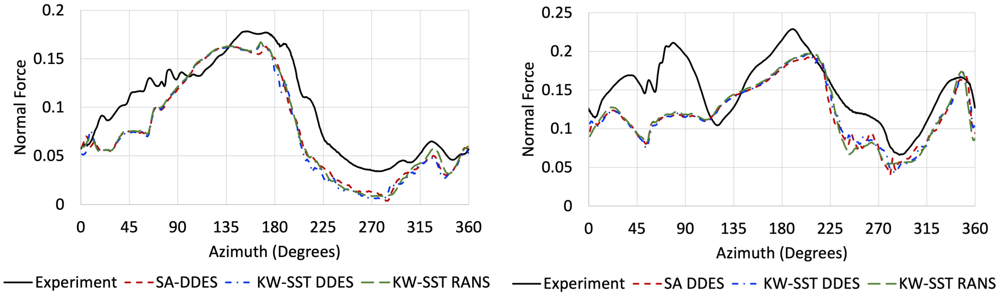

(a) $r/R = 0.400$

(b) $r/R = 0.675$

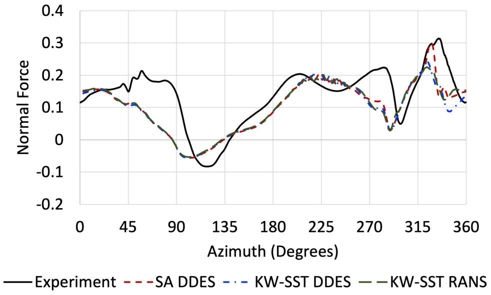

(c) $r/R = 0.990$

Figure 6.24: Normal force comparisons between turbulence models on fine grids C_T/σ=0.125

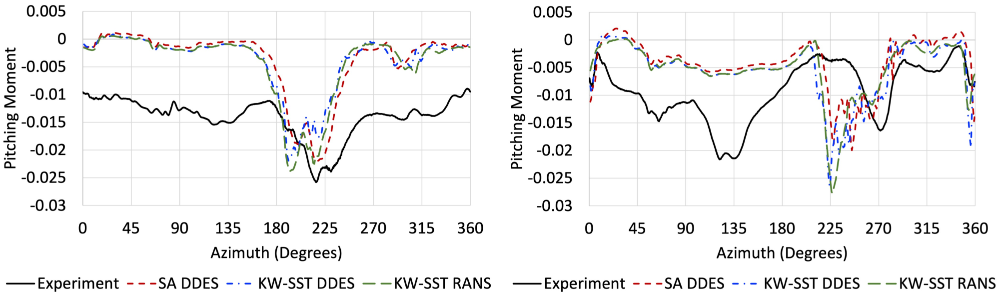

(a) $r/R = 0.400$ (b) $r/R = 0.675$

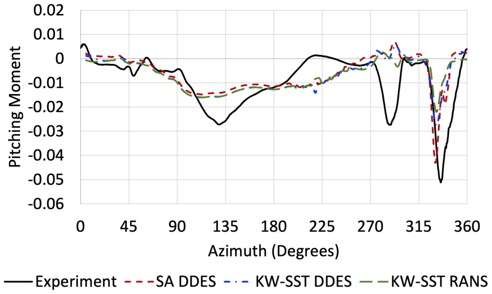

(c) $r/R = 0.920$

Figure 6.25: Pitching moment comparisons between turbulence models on fine grids C_T/σ=0.125

6.1.3 Effects of Aeroelastic Coupling

Full-scale rotors are highly elastic structures subjected to intense, repeated loading. Accurate CFD analyses must consider blade motion and deformation that occurs throughout a rotor revolution to achieve accurate predictions. Rotor blade motion and deformation can be accounted for in two different ways for an aeroelastic rotor: prescribed motion and coupled CFD-CSD. Prescribed motion applies blade motion and deformation from either another computation or experiment to deform the CFD grid. Loosely-coupled CFD-CSD uses an iterative process of developing rotor plane airloads in a CFD solver and using those airloads to calculate structural loading and corresponding CFD grid deformation in a CSD solver. The iterative process is continued until the airloads and blade deformation values converge to constants.

Prescribed motion is a simpler and faster approach than coupled CFD-CSD. Iteration between CFD and CSD solvers, which makes computations much more complex, is not required, and the solution needs only to run until subsequent rotor revolutions predict the same airloads values. Motion can either be taken from experiments if available or achieved via coupled CFD-CSD on a coarse grid to save the significant computational time coupled CFD-CSD requires on a refined physics grid.

Loosely-coupled CFD-CSD on a refined grid, however, can achieve more accurate airloads and resulting blade motions than prescribed motion from a coarse grid simulation. This yields not only better airloads predictions but overall thrust, power, and control angle predictions as well.

Figures 6.26 and 6.27 show normal force and pitching moment predictions for a light stall case ($C_T/\sigma = 0.090$) for several different aeroelastic approaches, all using the SA DDES turbulence model. Initially, loosely-coupled CFD-CSD was performed using the coarse grid (red). Converged motions from coarse grid simulation were then prescribed to a fine grid (blue). Finally, a loosely-coupled CFD-CSD simulation was performed using the fine grid (orange).

Normal force predictions (Fig. 6.26 are similar between the coarse CFD-CSD and fine prescribed motion cases, with the coarse CFD-CSD predicting inboard normal force stall magnitudes more accurately than the fine prescribed motion case. Coupled CFD-CSD results using the fine grid, however, predict normal force more accurately than either the coarse CFD-CSD or fine prescribed simulations. As shown in Figure 6.26, the predictions are by far the closest to experimental data of the three aeroelastic approaches.

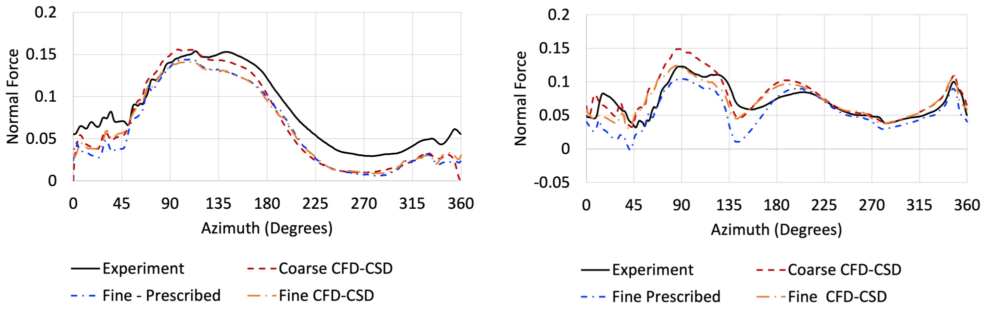

(a) $r/R = 0.400$ (b) $r/R = 0.675$

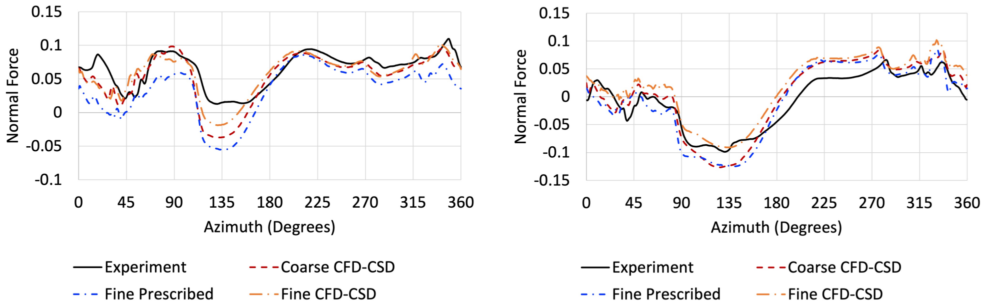

(c) $r/R = 0.775$ (d) $r/R = 0.920$

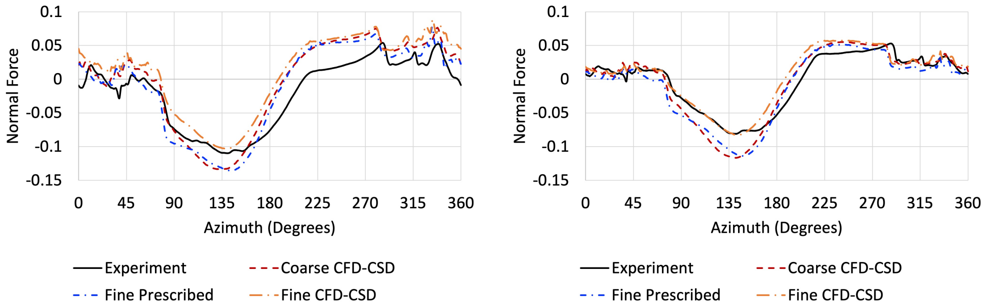

(e) $r/R = 0.965$ (f) $r/R = 0.990$

Figure 6.26: Normal force comparisons between aeroelastic approaches $C_T/\sigma = 0.090$

Inboard pitching moment predictions (Fig. 6.27) are similar between the fine CFD-CSD and fine prescribed motion cases, both of which are more accurate than the coarse CFD-CSD case. This is a result of the underlying motions. On the inboard region of the blade, the translational

(Fig. 6.28) and rotational (Fig. 6.29) deformations between the coarse CFD-CSD and fine CFD-CSD cases are similar as little deformation takes place near the root due to the blade structure. Differences in inboard predictions are then differentiated by how well the flowfield is resolved. At outboard stations the fine CFD-CSD produces the most accurate predictions with the prescribed motion case trending more towards the coarse CFD-CSD results. This is also a result of the underlying motions. Differences in the blade deformation from the coarse CFD-CSD and fine CFD-CSD become apparent near the blade tip, where the blade is most flexible and the most deformation occurs, as shown in Figures 6.28 and 6.29. The fine prescribed motion case tends towards the coarse results, as they are based on the same blade deformations. The fine CFD-CSD results are closer to experimental values as the underlying blade deformation is more accurate.

The most robust aeroelastic approach is a coupled CFD-CSD approach using a sufficiently refined grid. The refined grid produces a flowfield that more accurately depicts the strength and location of important physical features than a coarse grid. Resolving those physical features with a refined grid permits highly accurate rotor airloads to be used when coupled with a CSD solver. The resulting blade motion and deformation values can not be achieved with a coarse grid. When motions are prescribed from a coarse grid simulation, the resulting flowfield can be accurately resolved, however blade motions are still based on a less robust flowfield. Capturing the coupling between a flowfield and blade deformations eliminates any bias that may be introduced via prescribed motions.

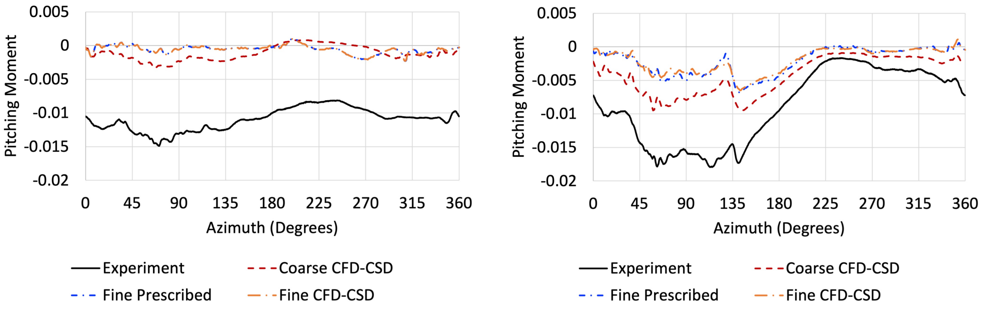

(a) $r/R = 0.400$ (b) $r/R = 0.675$

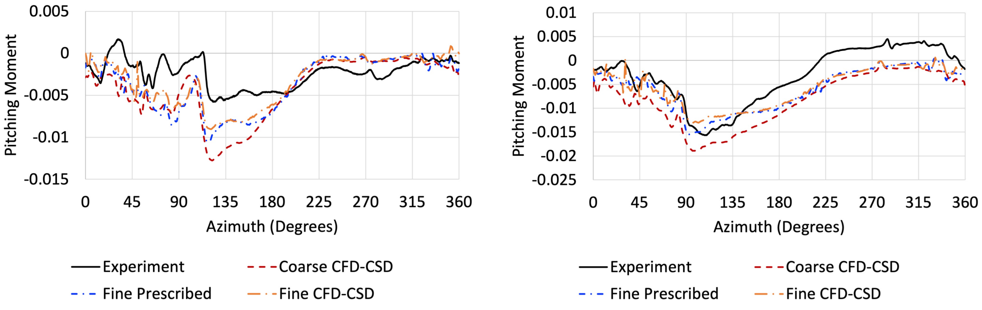

(c) $r/R = 0.775$ (d) $r/R = 0.920$

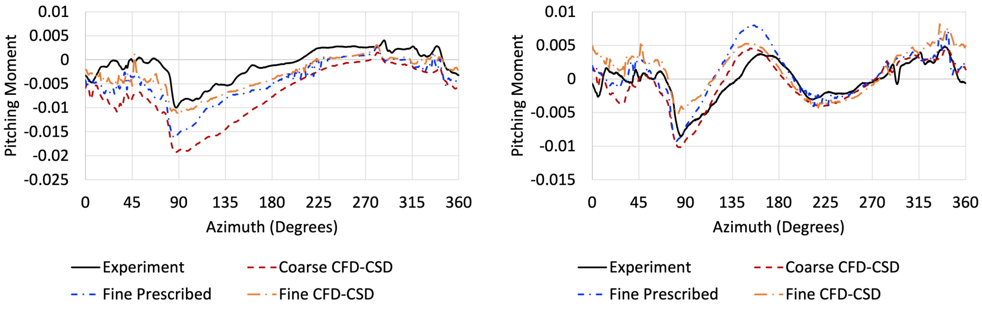

(e) $r/R = 0.965$ (f) $r/R = 0.990$

Figure 6.27: Pitching moment comparisons between aeroelastic approaches $C_T/\sigma = 0.040$

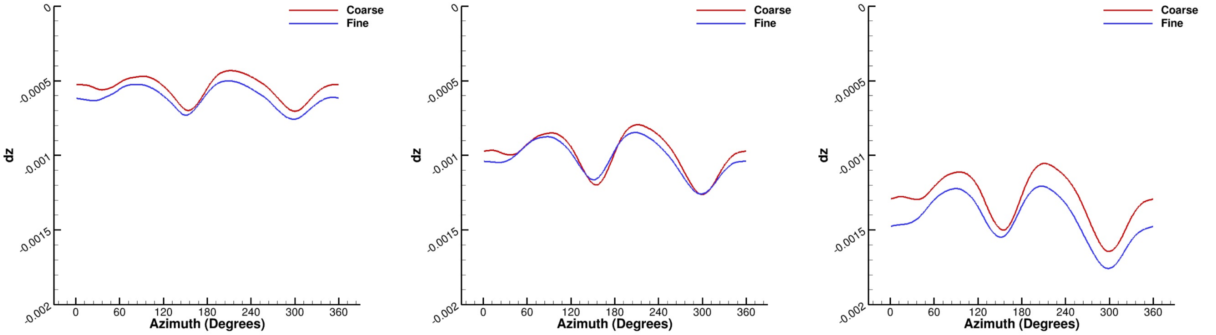

(a) $r/R = 0.200$ (b) $r/R = 0.300$ (c) $r/R = 0.400$

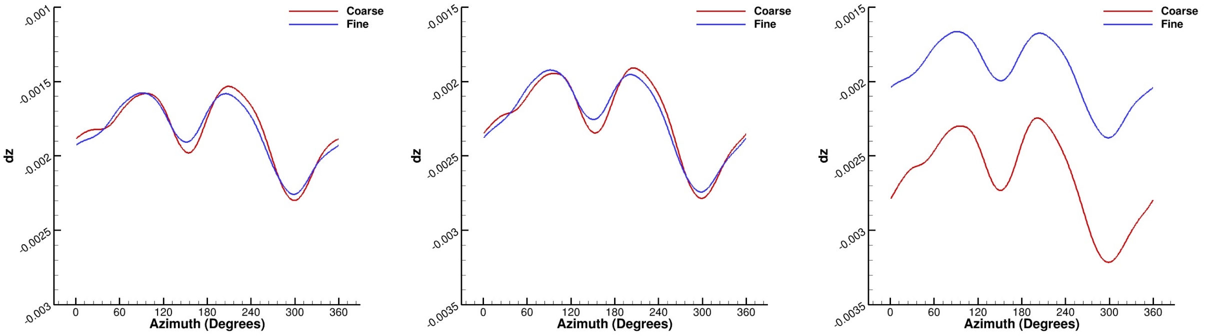

(d) $r/R = 0.500$ (e) $r/R = 0.600$ (f) $r/R = 0.700$

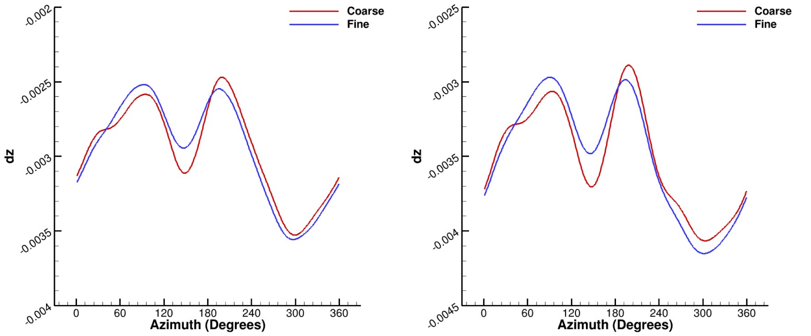

(g) $r/R = 0.800$ (h) $r/R = 0.900$

Figure 6.28: Comparison of z-direction blade deformations at various radial stations for coarse and fine CFD-CSD coupling

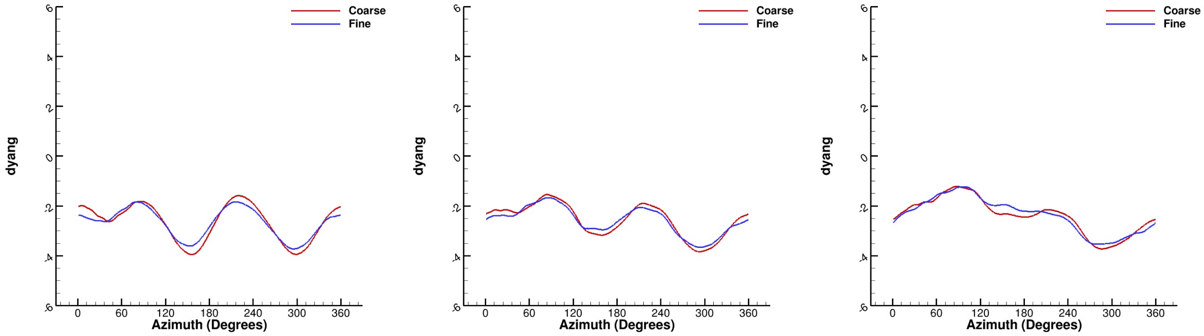

(a) $r/R = 0.200$ (b) $r/R = 0.300$ (c) $r/R = 0.400$

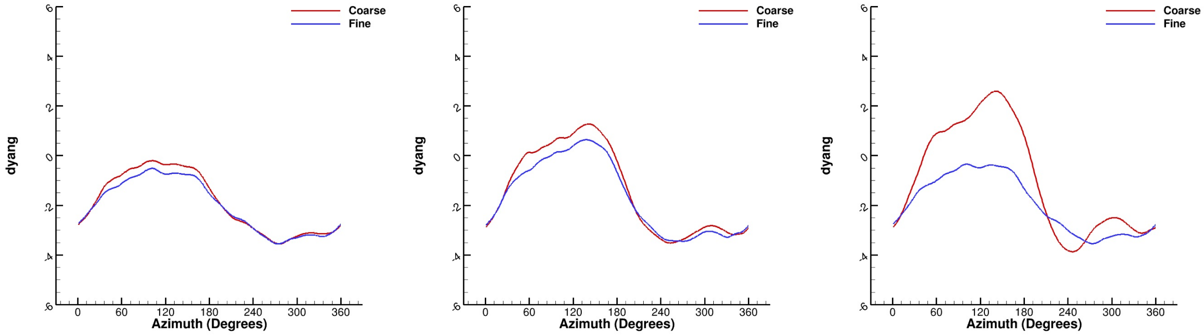

(d) $r/R = 0.500$ (e) $r/R = 0.600$ (f) $r/R = 0.700$

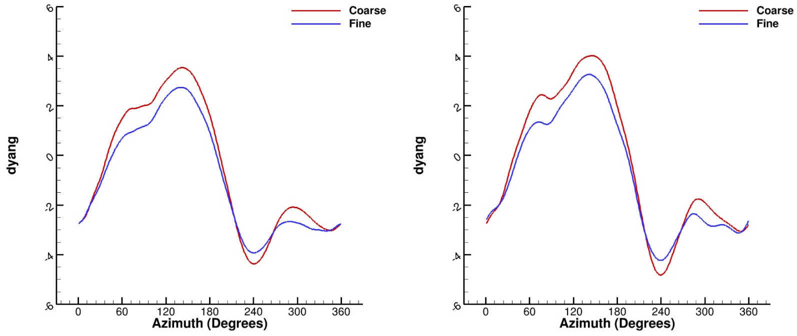

(g) $r/R = 0.800$ (h) $r/R = 0.900$

Figure 6.29: Comparison of y-axis rotational deformations at various radial stations for coarse and fine CFD-CSD coupling

6.2 Classification of Separated Flow on Rotating Systems

High-fidelity coupled CFD-CSD simulations can accurately predict flow separation on the rotor, as shown in Section 6.1. Further investigation of the flow fields, made possible by rich computational data sets, is now possible and may be used to identify flow separation mechanisms for each flow separation region on the rotor. Regions where flow separation is captured exhibit separation and reattachment that are consistent with dynamic stall behavior. For some of those regions, pitching motions of the retreating blade are consistent with classic dynamic stall. However, some of flow separation regions do not occur on the retreating blade where classic dynamic stall is expected and instead coincide with trailing tip vortices, indicating stall may be induced by blade vortex interactions.

6.2.1 Flowfield Inspection

A baseline method used to identify possible BVI-induced flow separation requires visual inspection of Q-criterion isosurfaces colored by vorticity magnitude. Q-criterion is a scalar quantity defined in Equation 6.4 as the second invariant of the velocity gradient tensor, where $\overline{\Omega}$ is the vorticity tensor and $\overline{S}$ is the strain rate tensor. This scalar quantity is useful in identifying vortex structures in the flowfield as it highlights regions with high vorticity and low strain rate, eliminating many boundary layer structures that are dominated by both high vorticity and high strain rate. These vortex structures are colored with vorticity magnitude to illustrate the vortex strength across the isosurface.

$$Q = \frac{1}{2}\left(||\overline{\Omega}||^2 - ||\overline{S}||^2\right) \tag{6.4}$$

As the rotor completes a revolution, the rotor blades pass through remnant vortices shed from the previous blade pass, as shown by the isocontours in Figure 6.30. The rotor blade can be visually tracked throughout a rotor revolution starting at $\psi = 40°$ azimuth (Fig. 6.30a). At this position, the advancing blade is parallel to trailing tip vortices, highlighted by the oval, and there is only a slight impingement of a trailing tip vortex impingement at the blade tip, identified by the arrow. As the blade advances to the $\psi = 90°$ azimuth position (Fig. 6.30b), normal vortex impingement begins to occur as the trailing tip vortices from the previous two blade passes interact with the advancing blade, identified by the two arrows in the figure. Normal vortex impingement from the previous two blade passes continues through $\psi = 130°$ (Fig. 6.30c), once again identified by the two arrows. As the blade advances beyond $\psi = 130°$, the tip vortex from the blade leading by $180°$ has convected far enough downstream that it no longer interacts with the blade in consideration. Normal impingement is reduced to a single shed vortex from the blade leading by $90°$, highlighted by the arrow in Figure 6.30d. As the blade begins to retreat, it continues to interact with the single tip vortex, however the impingement locations moves from inboard stations at $\psi = 180°$ (Fig. 6.30d) to outboard stations at $\psi = 270°$ (Fig. 6.30e), once again highlighted by the arrow. Between $\psi = 270°$ and $\psi = 310°$ (Fig. 6.30f) the blade retreats beyond the path of the vortex from the blade leading by $90°$ and the blade tip re-enters the path of the vortex from the blade leading by $180°$. The blade continues to interact with this vortex until it enters the hub wake and the rotor revolution is complete.

Potential locations for BVI-induced separation have been identified visually for a single test point. However, the effects of vortex impingement on the blade are dependent on vortex strength and location, which will be different for every test point. With increasing thrust throughout the UH-60A thrust sweep in this study, separation regions can appear and develop as Richez showed in Ref. [31]. For each test point, it is necessary to track each flow feature visually as described above while cross-referencing separation regions for the test point against sectional airloads and vortex impingement.

These visual inspections are important to identify flow separation regions which potentially have a BVI mechanism. However, this method relies purely on visual inspection of separate elements and there is no way to definitively prove mathematically or physically that the separation mechanism for flow separation regions in Sections is BVI, not blade motion. To do this would require isolation of the blade motion and BVI, which is discussed in Section 6.2.2.

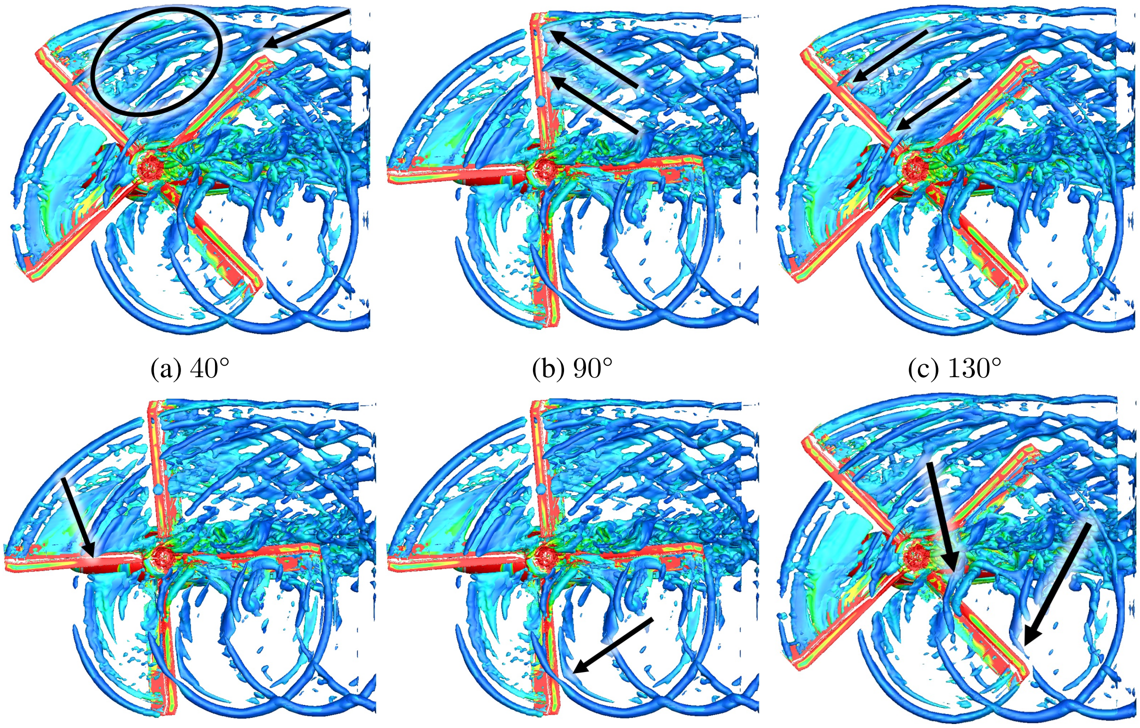

(a) 40° (b) 90° (c) 130°

(d) 180° (e) 270° (f) 310°

Figure 6.30: Q-Criterion isocontours colored with vorticity magnitude at various azimuth stations. Flow is from left to right.

6.2.2 One-Bladed Isolation

In Section 6.2.1, inspection of isocontours cross-referenced with blade airloads and rotor separation maps identified flow separation regions that possibly have a BVI mechanism. However, without decoupling blade motion from BVI, it is impossible to definitively classify the separation mechanism. In Ref. [22], Chaderjian proposed a method to isolate blade motion from BVI. Within the confines of a much larger study, he ran a four-bladed baseline loosely-coupled CFD-CSD simulation to match flight test conditions conducive to dynamic stall. He then computationally configured the rotor to run with only one blade while blade motion and deformation were prescribed to match motion and deformation from the four-bladed CFD-CSD results. While he briefly addresses results of a one-bladed simulation at a single azimuth he only employs visual inspection methods and does not investigate the entire rotor plane.

The one-bladed and four-bladed UH-60A configurations used in this study are shown in Figure

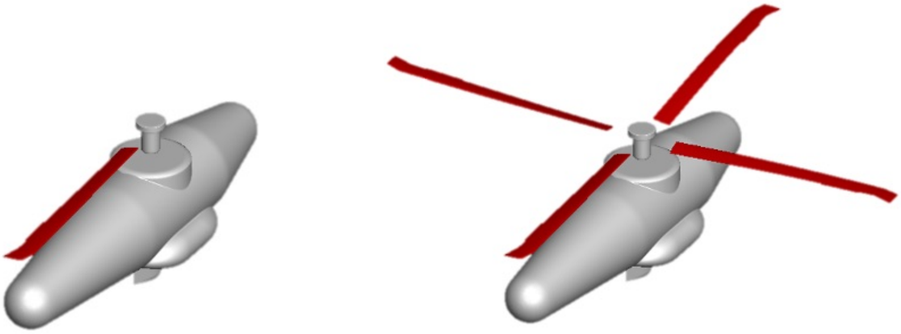

Figure 6.31: One-bladed and four-bladed UH-60A configurations

6.31. This investigation (also explored by the author in Ref. [83]) expands on Chaderjian's original one-bladed run in a number of ways:

- The effects of differential downwash between one-bladed and four-bladed configurations on airloads is investigated.
- An alternative isolation technique is explored to best capture equivalent one-bladed and four-bladed rotors.
- Multiple CFD simulations are performed to capture an entire thrust sweep with cases exhibiting light, moderate, and deep stall.
- The entire rotor plane is studied instead of a single azimuth position.
- Visual inspection of isocontours and blade surface separation plots are used along with full rotor separation maps, blade airloads, and rotor performance values to fully understand the differences between the one-bladed and four-bladed simulations.

The first study explores an alternative isolation technique to best capture equivalent one-bladed and four-bladed rotors. Two methods are evaluated:

- Prescribed Motion
- Coupled CFD-CSD

Prescribed Motion

The prescribed motion case mimics Chaderjian's setup [22]. A baseline four-bladed loosely-coupled CFD-CSD simulation is performed to obtain blade motions and deformations. The rotor is then computationally configured to have one blade. Motion and deformation from the four-bladed computation are applied to the single blade in a prescribed motion case to exactly mimic blade motions from the four-bladed run.

Normal force and pitching moment data provide useful insights into performance variations between the one-bladed and four-bladed rotors. For some azimuth angles, normal force and pitching moment data from the one-bladed and four-bladed rotors are nearly coincident. For those azimuth angles, normal force and pitching moment values are largely based on blade movement. For other azimuth angles, normal force and pitching moment data from the one-bladed and four-bladed rotors do not coincide. Because the blades in both the one-bladed and four-bladed configuration have the same motion, a difference in airloads data must be attributed to aerodynamic interactions. Normal force and pitching moment data for all cases are provided in Appendix B.3.

For a light-stall condition ($C_T/\sigma = 0.040$), only one of the flow separation regions discussed in Section 6.1, FS1, is present (Fig. 6.32). Even though the flow field associated with this light stall case does not include flow separation regions FS2-FS5, it is still subjected to the nonlinear flowfield features, such as tip vortices, in those regions that may trigger dynamic stall at higher thrust values. Signatures of those complex flowfield features appear in normal force (Fig. B.31) and pitching moment (Fig. B.32) data.

There are two main regions where there is significant difference between the one- and four-bladed predictions: from $\psi = 0°$ to $\psi = 135°$ from and $\psi = 270°$ to $\psi = 360°$. Near these regions, the data suggest the presence of a dominant flowfield feature in one configuration that is not in the other, resulting in different airloads behavior for the same blade motion and deformation.

Between $\psi = 0°$ and $\psi = 135°$, normal force predictions from the four-bladed CFD simulation are nearly coincident with experimental normal force data. However, the one-bladed CFD simulation overpredicts normal force throughout the entire quarter revolution and does not capture the slight normal force stall experienced in the four-bladed simulation at $\psi = 45°$.

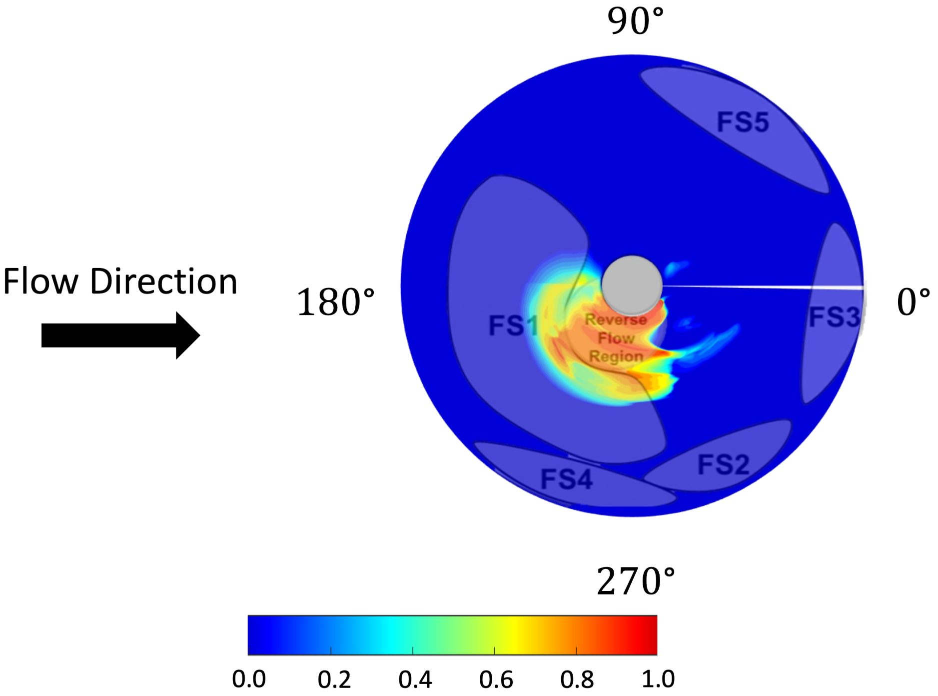

Figure 6.32: Rotor map for light stall case ($C_T/\sigma = 0.040$) overlaid with four-bladed articulated rotor separation regions, where 0.0 indicates fully attached flow and 1.0 indicates fully separated flow.

Figure 6.33 compares Q-criterion isocontours colored with vorticity magnitude for the one-bladed and four-bladed rotors. In both configurations, the blade in consideration is located at an azimuth station of $\psi = 40°$. As the blade advances from $\psi = 0°$ to $\psi = 90°$, the four-bladed rotor blade interacts with trailing vortices from the three previous blades, as highlighted in Figure 6.33a. From $\psi = 0°$ to $\psi = 90°$, the one-bladed rotor encounters only one trailing vortex from it's previous pass, as shown in Figure, 6.33b.

Figure 6.34 shows a volume slice along the blade at $\psi = 40°$. The one-bladed vorticity slice shows two distinct vortices. One vortex is in close proximity to the tip and one is in close proximity to the root. Both vortex cores are above the rotor plane, connected via a vortex sheet. There is no direct impingement of these features on the advancing blade. The four-bladed vorticity slice shows one distinct vortex in close proximity to the tip and a continuous vortex sheet that runs beneath the blade at inboard radial stations and impinges on the blade at outboard stations.

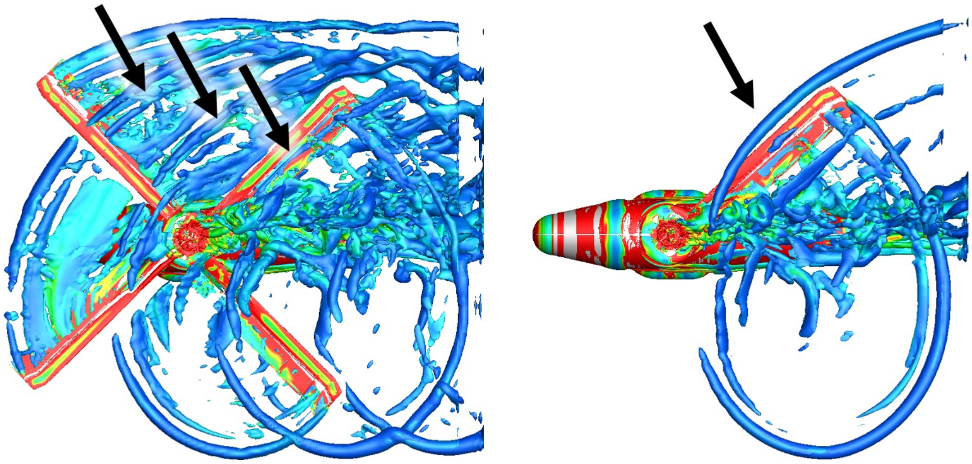

(a) Four-Bladed (b) One-Bladed

Figure 6.33: Q-criterion isocontours for four-bladed and one-bladed configurations in light stall ($C_T/\sigma = 0.040$) at $\psi = 40°$. Flow is from left to right.

The vortex sheet in both configurations is a roll-up of vorticity from previous blade passes. The four-bladed configuration includes roll-up from four previous blade passes compared to one for the one-blade configuration, resulting in stronger vorticity magnitude. The four-bladed rotor generates significantly more downwash than the one-bladed rotor, both above (Fig. 6.35) and at the rotor plane (Fig. 6.36). The downwash generated by the four-bladed configuration is strong enough to pull the vortex sheet into the rotor plane. Interaction with the vortex sheet, limits lift production on the four-bladed advancing blade. The one-bladed rotor produces significantly weaker downwash that does not pull the vortex sheet into the rotor plane, eliminating blade interaction with the vortex sheet. Without those interactions, the one-bladed advancing blade rotor does not experience normal force stall.

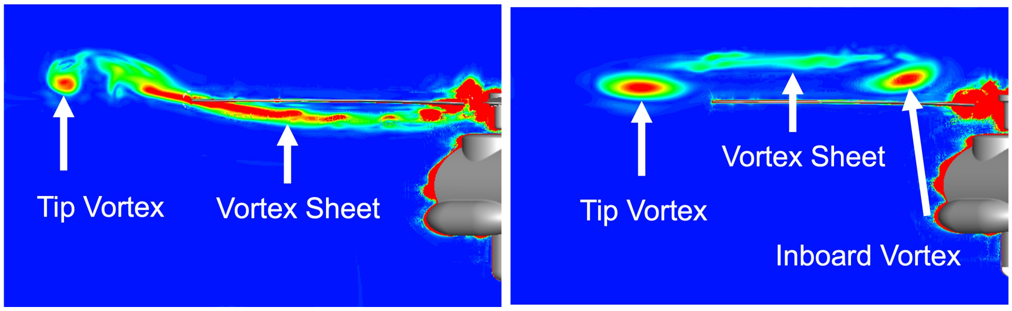

(a) Four-Bladed (b) One-Bladed

Figure 6.34: Volume slices of vorticity magnitude along blade at $\psi = 40°$ for four-bladed and one-bladed configurations in light stall ($C_T/\sigma = 0.040$). Flow is from left to right.

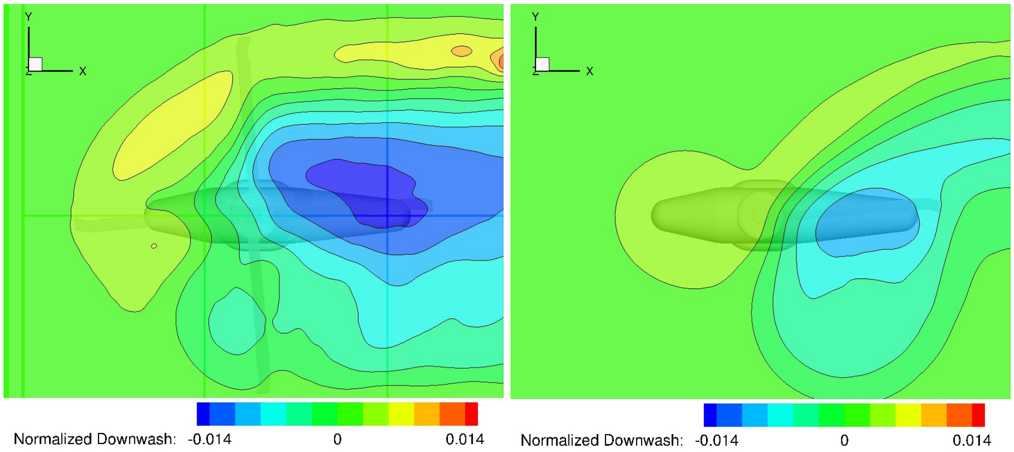

(a) Four-bladed (b) One-Bladed

Figure 6.35: Comparison between one-bladed and four-bladed downwash distributions at 25%R above the rotor plane at $\psi = 0°$. Flow is from left to right.

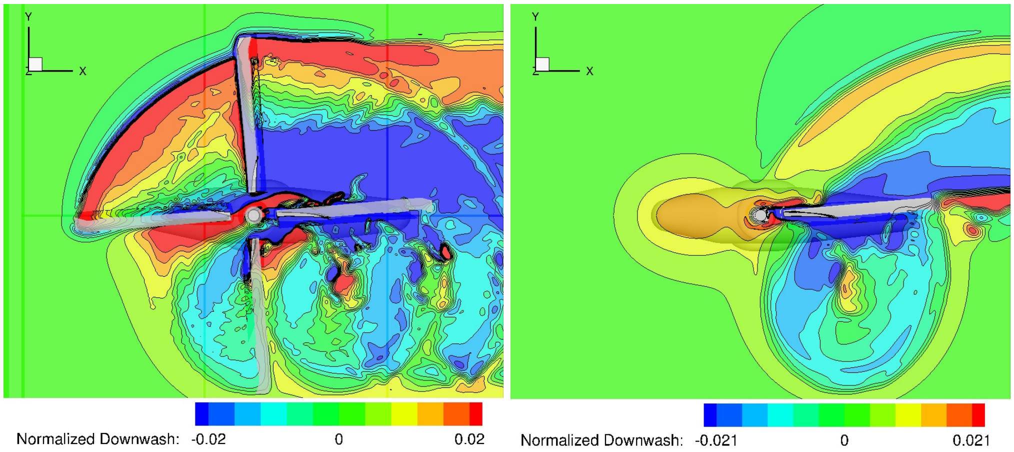

(a) Four-bladed (b) One-Bladed

Figure 6.36: Comparison between one-bladed and four-bladed downwash distributions at the rotor plane at $\psi = 0°$. Flow is from left to right.

The four-bladed and one-bladed CFD simulations capture similar trends in pitching moment (Fig. B.32). Again, the one-bladed simulation exhibits differences compared with its four-bladed counterpart between $\psi = 0°$ and $\psi = 135°$. The one-bladed rotor experiences a pitching moment peak about around $\psi = 45°$ at outboard radial stations ($r/R = 0.775$-$r/R = 0.990$) while the four-bladed experimental and CFD data encounter a loss in pitching moment. At these radial stations the blade is coincident with the vortex sheet in the four-bladed simulation while the outboard stations of the one-bladed configurations are interacting with a clean flowfield. Like normal force data showed, this further isolates blade motion from flowfield features.

Between $\psi = 90°$ and $\psi = 135°$ the four-bladed configuration begins to interact with a perpendicular trailing tip vortex from the previous blade pass (Fig. 6.37a) while the single blade is permitted to advance through a clean flowfield (Fig. 6.37b). Between $r/R = 0.675$ and $r/R = 0.865$, where the outboard blade is subject to vortex impingement, apparent BVI signatures, or the peaks and drops in airload data that are associated with BVI, appear in the four-bladed moment data but not the one-bladed data (Fig 6.37a). Where the four-bladed data (red in Fig. 6.38) show traces of BVI, the one-bladed data (blue in Fig. 6.38) is smooth, with no indication of flowfield feature interaction, verifying the impinging tip vortex has an effect on blade performance.

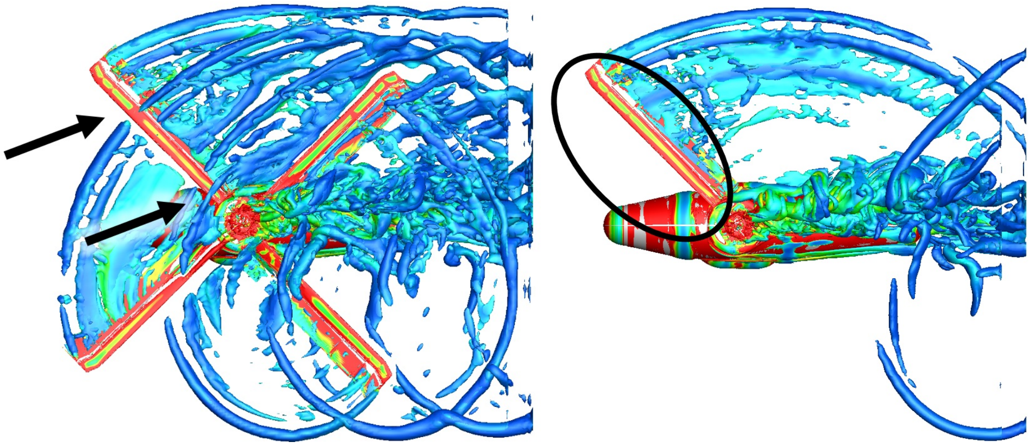

(a) Four-Bladed

(b) One-Bladed

Figure 6.37: Q-criterion isocontours for four-bladed and one-bladed configurations in light stall ($C_T/\sigma = 0.040$) at $\psi = 130°$. Flow is from left to right.

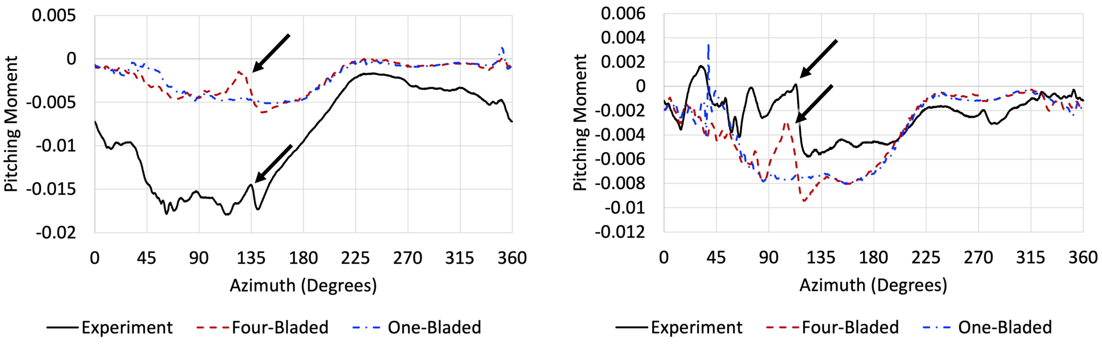

(a) $r/R = 0.675$ (b) $r/R = 0.775$

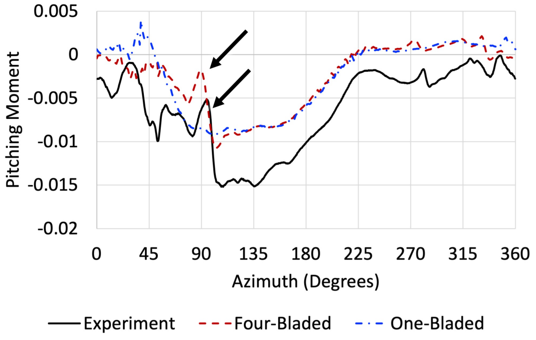

(c) $r/R = 0.865$

Figure 6.38: BVI signatures in pitching moment between $\psi = 90°$ and $\psi = 135°$

Significant differences between the predicted four-bladed and one-bladed airloads are also observed in the region bounded by $\psi = 270°$ and $\psi = 360°$ azimuth. Figure 6.39 shows Q-criterion isocontours at $\psi = 310°$. In the four-bladed configuration, the blade tip interacts with the trailing vortex from the previous blade, while the single blade outboard is permitted to retreat into a clean flowfield. Both inboard blades are subjected to an inboard vortex filament, also shown in Figure 6.39.

Figure 6.40 shows that over the outboard blade ($r/R = 0.865$-$r/R = 0.99$) the normal force for both the four-bladed configuration (red) and experiment (black) exhibit multiple sudden sharp peaks and drops, characteristics that are typical of multiple-vortex interactions. The one-bladed configuration (blue) with the same prescribed motion does not exhibit those characteristics. Similar, less pronounced, behavior is present in the pitching moment data (Fig 6.41). This indicates a BVI is present and altering blade aerodynamics.

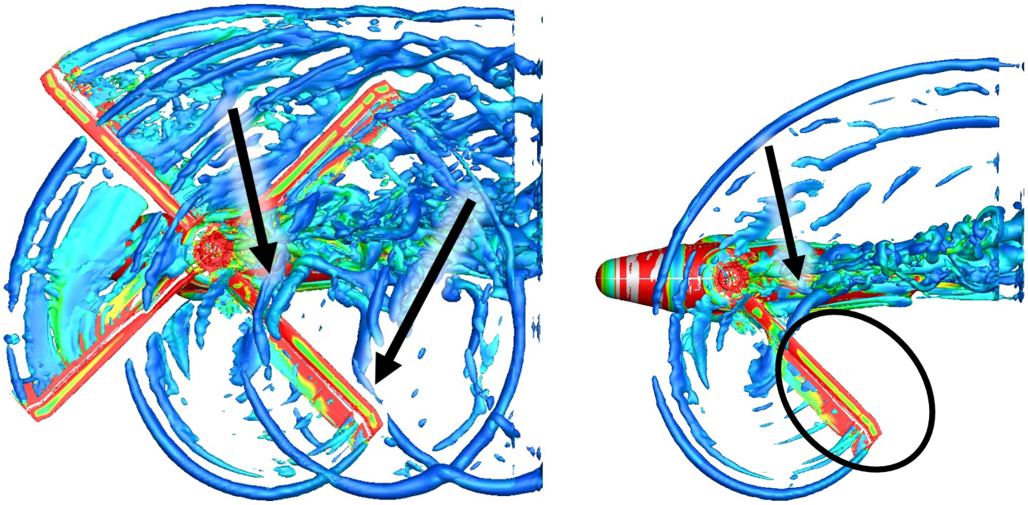
(a) Four-Bladed (b) One-Bladed

Figure 6.39: Q-criterion isocontours for four-bladed and one-bladed configurations in light stall ($C_T/\sigma = 0.040$) at $\psi = 130°$. Flow is from left to right.

Figure 6.42 illustrates the vorticity magnitude in the blade plane flowfield at $\psi = 310°$. Two inboard vortices are coincident between the one-bladed and four-bladed configuration (Fig. 6.42). The vortex filament identified in Figure 6.39 is present in both one-bladed and four-bladed flowfields, is coincident with the upper inboard vortex, and appears to be a byproduct of the hub. The lower inboard vortex is not coincident with any BVI and can be attributed to reverse flow. In addition to the two in-board vortices, the four-bladed configuration has a vortex sheet below the blade as well as a strong tip vortex. Cross-referencing with Figure 6.39 indicates that the tip vortex is shed from the previous rotor blade. The vortex sheet below the rotor blade is a by-product of agglomeration of weak vorticity shed from prior rotors, which can be seen by the differences in the vorticity outboard of the arrows in Figure 6.39. For the one-bladed configuration, the path from $\psi = 270°$ to $\psi = 360°$ is free from significant shed vorticity, indicating the lack of any blade-vortex interactions. This results in the smooth airloads data observed for the one-bladed rotor in the outboard region from $\psi = 270°$ to $\psi = 360°$.

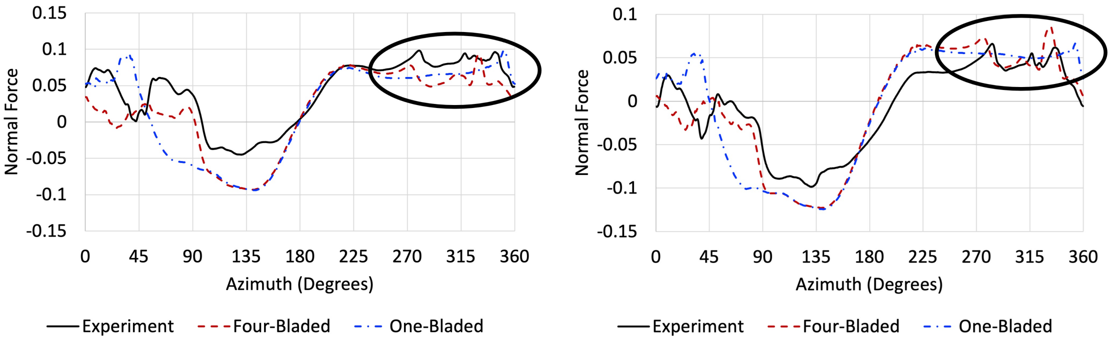

(a) $r/R = 0.865$ (b) $r/R = 0.920$

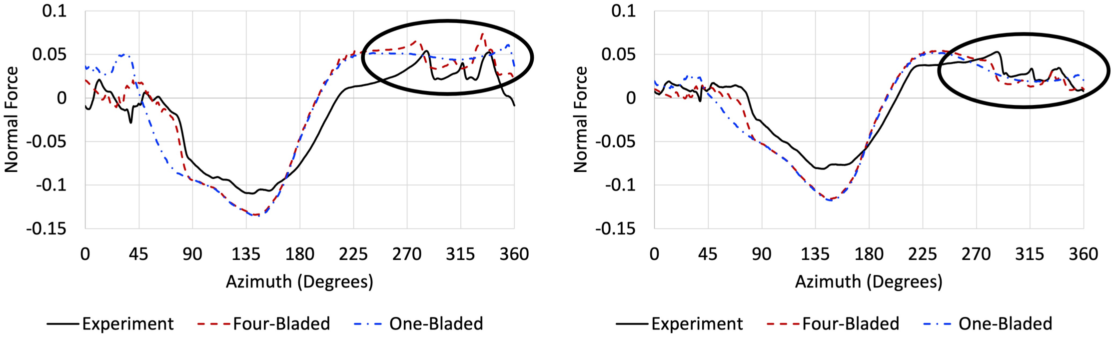

(c) $r/R = 0.965$ (d) $r/R = 0.990$

Figure 6.40: BVI signatures in normal force between $\psi = 270°$ and $\psi = 360°$

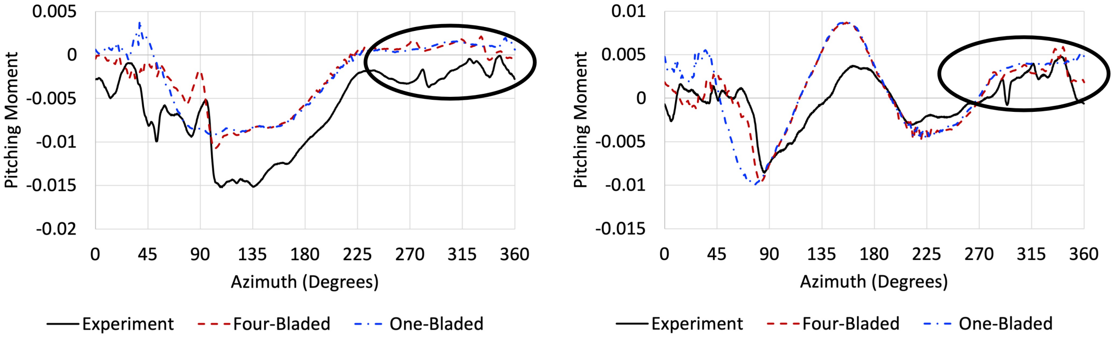

(a) $r/R = 0.865$ (b) $r/R = 0.920$

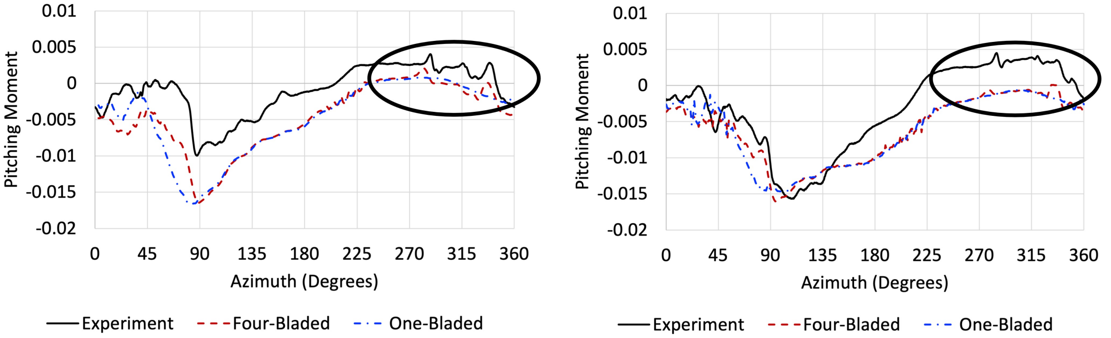

(c) $r/R = 0.965$ (d) $r/R = 0.990$

Figure 6.41: BVI signatures in pitching moment between $\psi = 270°$ and $\psi = 360°$

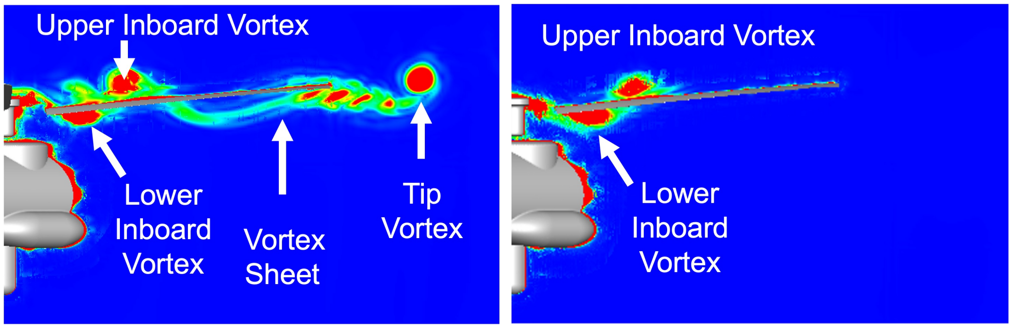

(a) Four-Bladed (b) One-Bladed

Figure 6.42: Volume slices of vorticity magnitude along blade at $\psi = 310°$ for four-bladed and one-bladed configurations in light stall ($C_T/\sigma = 0.040$)

Downwash Effects

There is some concern that one-bladed airload predictions may be inflated due to reduced rotor downwash. Significant differences in downwash could create higher induced angles of attack throughout the rotor revolution. Even in the absence of dominant flow features, the increased angles of attack could alter lift and moment data. To address these concerns, downwash and its effect on load prediction is compared between one-bladed and four-bladed simulations at various z-planes (Fig. Figure 6.43) within one rotor radius (R) of the rotor plane.

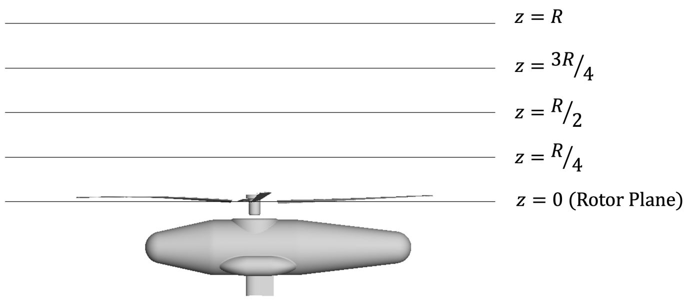

Figure 6.43: Comparison between one-bladed and four-bladed downwash distributions at various z-plane slices above the rotor plane. Flow is from left to right.

Above the rotor plane, there is a significant difference in downwash between one-bladed and four-bladed configurations for both light stall (Fig. 6.44) and deep stall (Fig. 6.45) cases. Between $\psi = 0°$ and $\psi = 90°$, the one-bladed isolation approach does not completely decouple blade motion from BVI, as shown in Figure 6.33b. However, the reduced downwash from the one-bladed rotor is not strong enough to pull the vortex sheet (Fig. 6.34) into the path of the blade. This is a positive result as it serves to further decouple blade motion from BVI, permitting classification of separated flow between $\psi = 0°$ and $\psi = 90°$.

At the rotor plane, downwash effects on airloads predictions are considered for both a light ($C_T/\sigma = 0.040$) and deep ($C_T/\sigma = 0.125$) stall case. The majority of downwash (i.e. negative velocity) for both thrust values appear between $\psi = 0°$ and $\psi = 90°$ (Fig. 6.46) where downwash effects have been shown to isolate blade motion from BVI. From $\psi = 90°$ to $\psi = 180°$, the blade on both one- and four-bladed simulations moves through a flowfield with very little downwash. Velocity in the four-bladed flowfield is dominated by the trailing tip vortex from the previous blade pass that generates positive upward velocity throughout much of the quadrant (Figs. 6.47a,6.47b). Velocity in the one-bladed flowfield is dominated by updraft off of the LRTA fuselage (Figs. 6.47c,6.47d). Any downwash differences between the configurations are negligible between $\psi = 90°$ to $\psi = 180°$, due to the presence of other, more dominant flow features.

From $\psi = 135°$ to $\psi = 225°$, normal force predictions are equivalent between the one-bladed and four-bladed rotors, as shown for four radial stations in Figure 6.48. Downwash at $\psi = 180°$, near the middle of this range, is very similar between the one- and four-bladed configurations (Fig. 6.49). The inboard and midboard is subjected to updraft from the fuselage in both configurations. The outboard in both configurations is permitted to pass through a nearly clean flowfield. Downwash above the rotor plane (Figs. 6.44,6.45) is concentrated behind the body. Based on airloads and rotor plane velocity data, rotor downwash has no effect on airloads from $\psi = 135°$ to $\psi = 225°$. Near $\psi = 225°$, normal forces between one- and four-bladed configurations begin to deviate from each other. At this same location, the four-bladed rotor encounters some velocity gradients from the previous rotor pass (Figs. 6.49a,6.49b) as it retreats towards the fourth quadrant, while the one-bladed rotor retreats through a clean flowfield (Figs. 6.49c,6.49d). As the blade continues to retreat towards $\psi = 360°$, the four-bladed configuration enters a highly nonlinear flowfield, littered with trailing tip vortices and hub and fuselage wakes (Figs.). The one-bladed configuration enters a relatively clean flowfield. Above the rotor plane, the strongest downwash is positioned over this region. However, differences between the one- and four-bladed flowfields are dominated by the highly nonlinear wake, not rotor downwash. The effect of rotor downwash can not be realized in this region due to it's highly nonlinear nature.

The downwash differential between four-bladed and one-bladed simulations does not have a direct impact on airloads predictions. The only noticeable impact occurs between $\psi = 0°$ and $\psi = 90°$, where reduced downwash serves to further isolate blade motions from flowfield interactions by preventing downward convection of the vortex sheet as demonstrated in Figure 6.34.

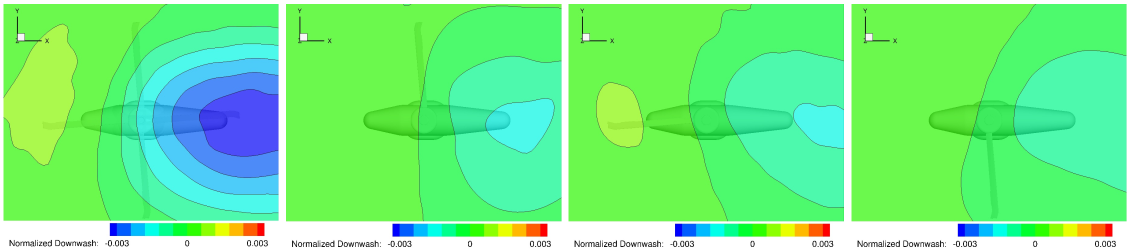

(a) Four-bladed $z = R$

(b) One-Bladed $\psi = 90°$

(c) One-Bladed $\psi = 180°$

(d) One-Bladed $\psi = 270°$

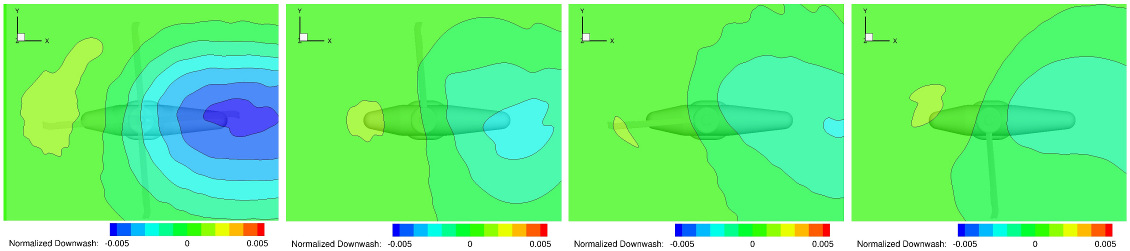

(e) Four-bladed $z = 3R/4$

(f) One-Bladed $\psi = 90°$

(g) One-Bladed $\psi = 180°$

(h) One-Bladed $\psi = 270°$

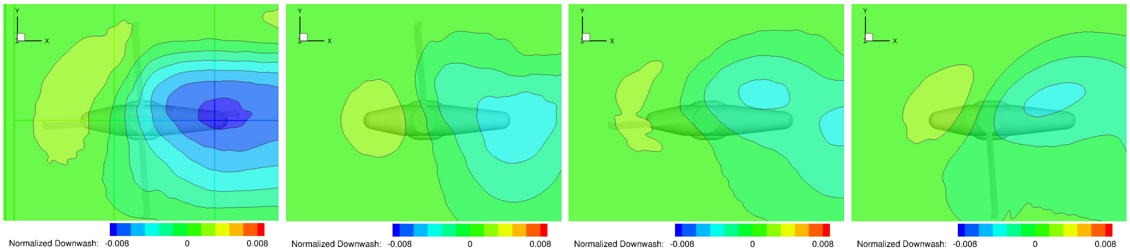

(i) Four-bladed $z = R/2$

(j) One-Bladed $\psi = 90°$

(k) One-Bladed $\psi = 180°$

(l) One-Bladed $\psi = 270°$

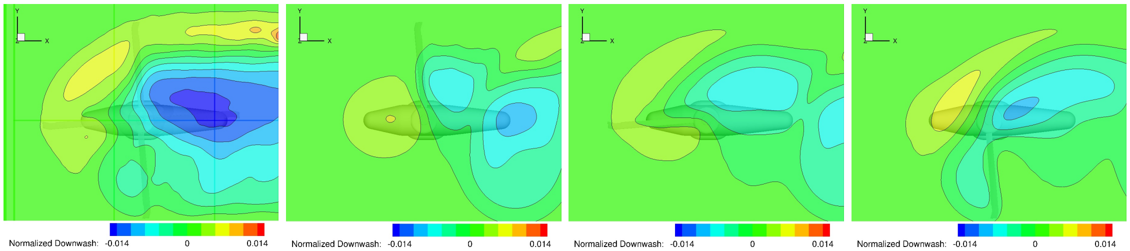

(m) Four-bladed $z = R/4$

(n) One-Bladed $\psi = 90°$

(o) One-Bladed $\psi = 180°$

(p) One-Bladed $\psi = 270°$

Figure 6.44: Comparison of downwash distributions between four-bladed and one-bladed configurations above the rotor plane at $C_T/\sigma = 0.040$. Flow is from left to right.

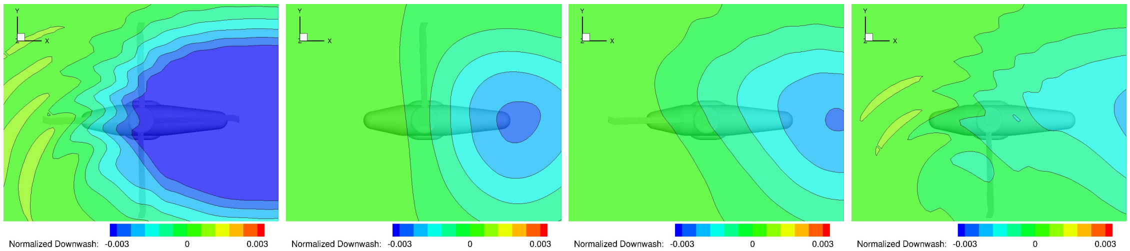

(a) Four-bladed $z = R$ (b) One-Bladed $\psi = 90°$ (c) One-Bladed $\psi = 180°$ (d) One-Bladed $\psi = 270°$

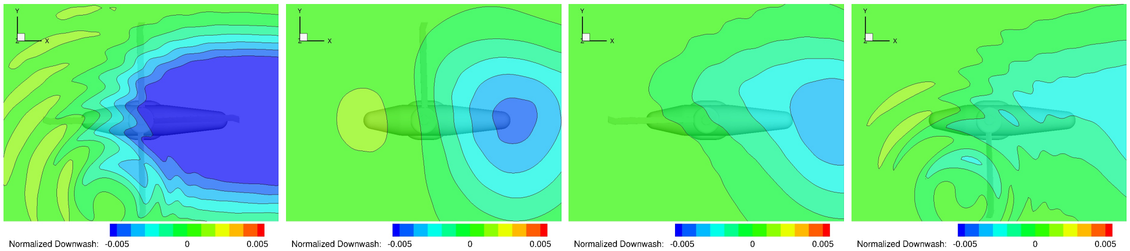

(e) Four-bladed $z = 3R/4$ (f) One-Bladed $\psi = 90°$ (g) One-Bladed $\psi = 180°$ (h) One-Bladed $\psi = 270°$

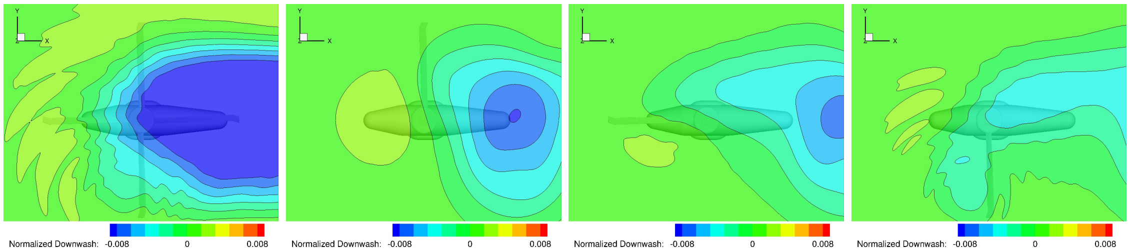

(i) Four-bladed $z = R/2$ (j) One-Bladed $\psi = 90°$ (k) One-Bladed $\psi = 180°$ (l) One-Bladed $\psi = 270°$

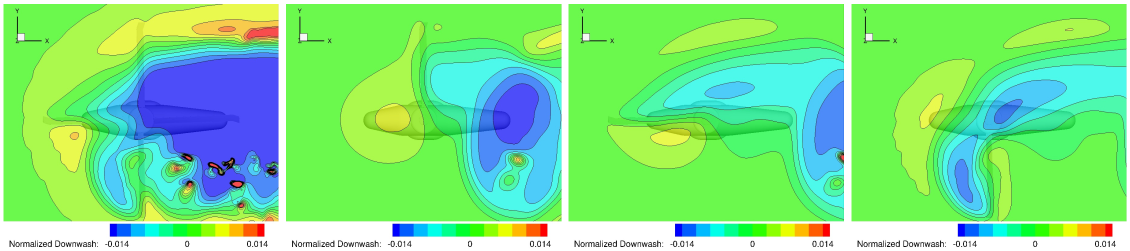

(m) Four-bladed $z = R/4$ (n) One-Bladed $\psi = 90°$ (o) One-Bladed $\psi = 180°$ (p) One-Bladed $\psi = 270°$

Figure 6.45: Comparison of downwash distributions between four-bladed and one-bladed configurations above the rotor plane at $C_T/\sigma = 0.125$. Flow is from left to right.

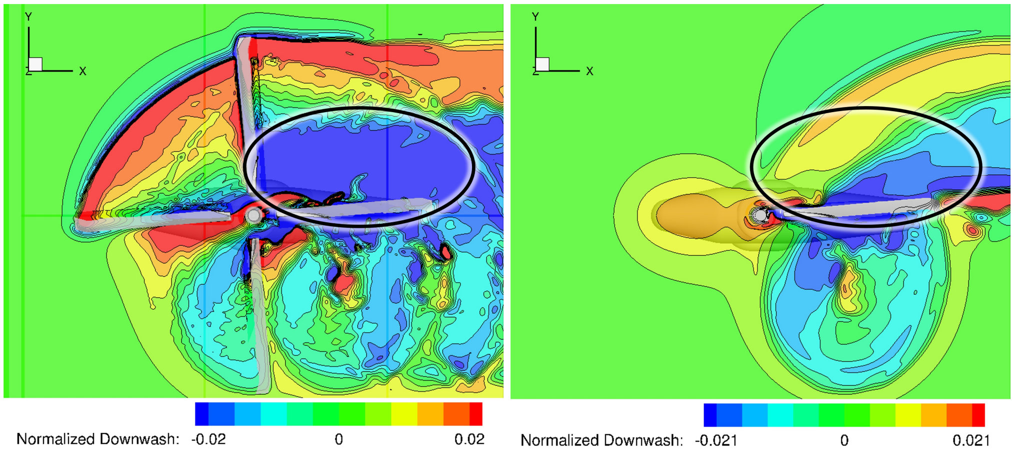

(a) Four-bladed $C_T/\sigma = 0.040$ (b) One-bladed $C_T/\sigma = 0.040$

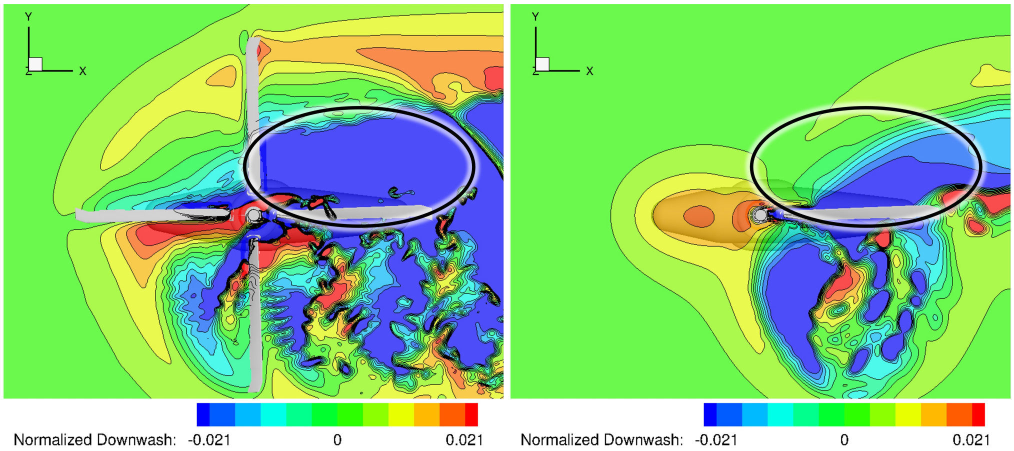

(c) Four-bladed $C_T/\sigma = 0.125$ (d) One-Bladed $C_T/\sigma = 0.125$

Figure 6.46: Downwash between $\psi = 0°$ and $\psi = 90°$ for light ($C_T/\sigma = 0.040$) and deep ($C_T/\sigma = 0.125$) stall. Flow is from left to right.

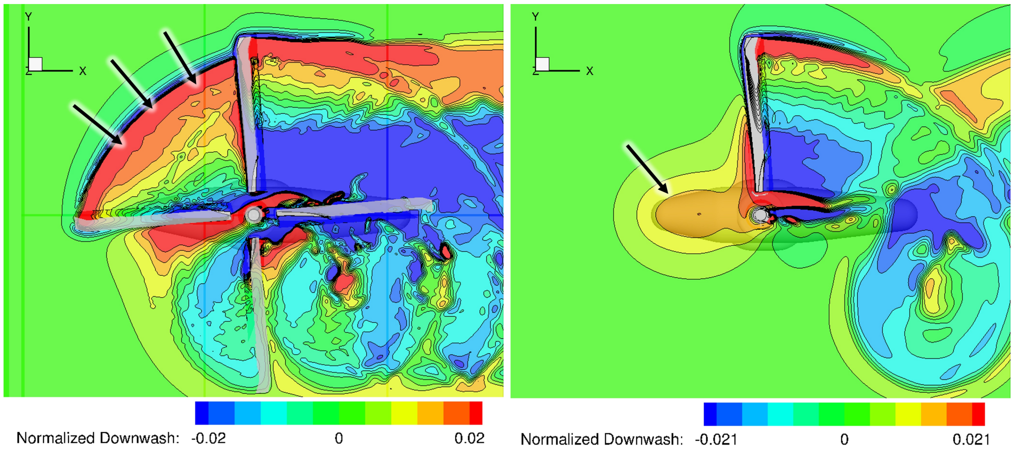

(a) Four-bladed $C_T/\sigma = 0.040$ (b) One-bladed $C_T/\sigma = 0.040$

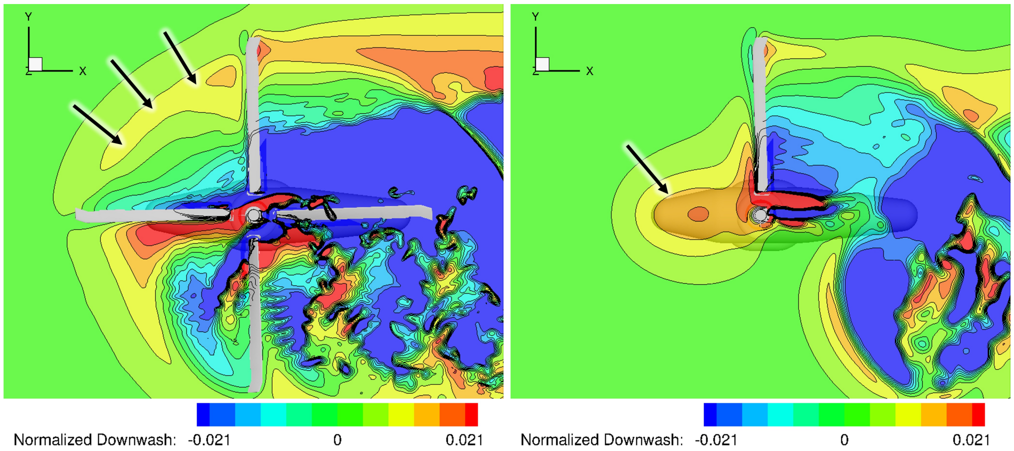

(c) Four-bladed $C_T/\sigma = 0.125$ (d) One-Bladed $C_T/\sigma = 0.125$

Figure 6.47: Downwash between $\psi = 90°$ and $\psi = 180°$ for light ($C_T/\sigma = 0.040$) and deep ($C_T/\sigma = 0.125$) stall. Flow is from left to right.

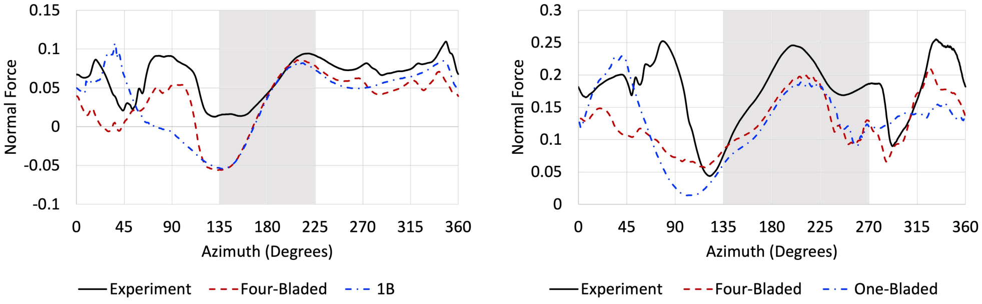

(a) $C_T/\sigma = 0.040$, $r/R = 0.775$ (b) $C_T/\sigma = 0.125$, $r/R = 0.775$

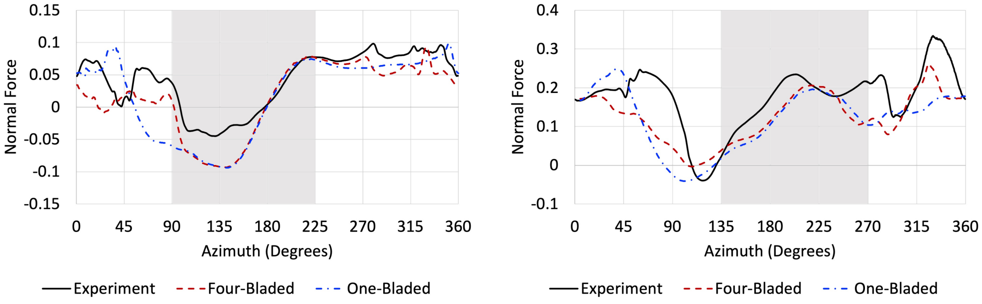

(c) $C_T/\sigma = 0.040$, $r/R = 0.865$ (d) $C_T/\sigma = 0.125$, $r/R = 0.865$

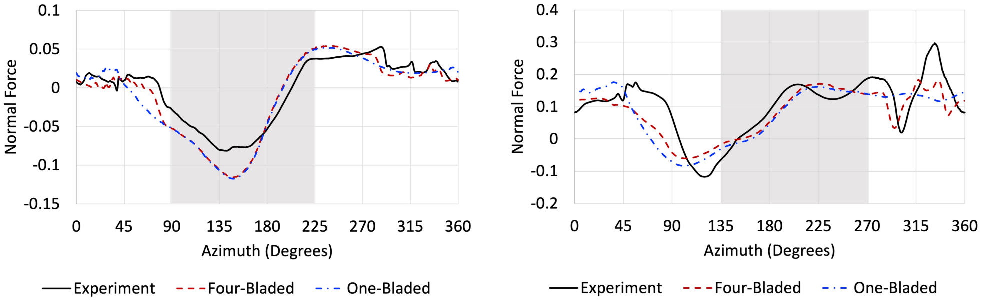

(e) $C_T/\sigma = 0.040$, $r/R = 0.965$ (f) $C_T/\sigma = 0.125$, $r/R = 0.965$

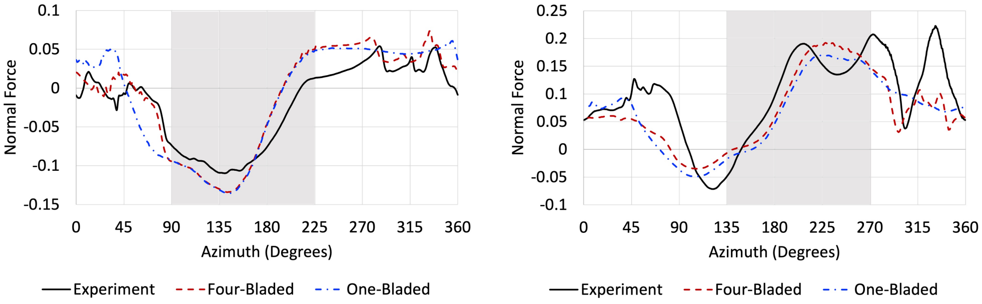

(g) $C_T/\sigma = 0.040$, $r/R = 0.990$ (h) $C_T/\sigma = 0.125$, $r/R = 0.990$

Figure 6.48: Equivalent normal force predictions between four-bladed and one-bladed configurations for light ($C_T/\sigma = 0.040$) and deep ($C_T/\sigma = 0.125$) stall cases

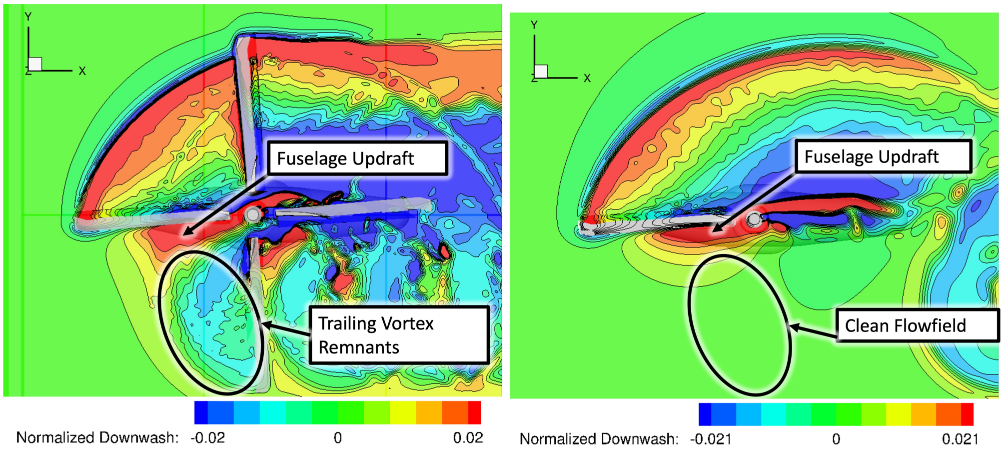

(a) Four-bladed $C_T/\sigma = 0.040$ (b) One-bladed $C_T/\sigma = 0.040$

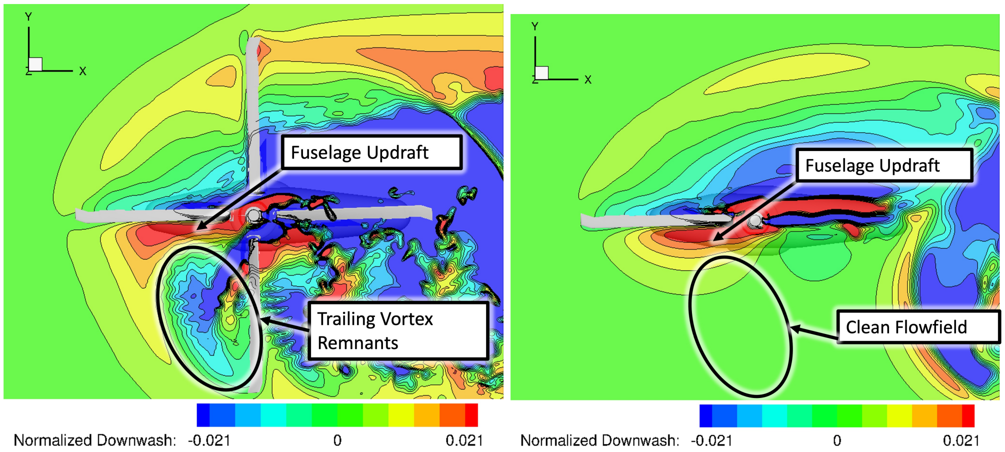

(c) Four-bladed $C_T/\sigma = 0.125$ (d) One-Bladed $C_T/\sigma = 0.125$

Figure 6.49: Downwash between $\psi = 180°$ and $\psi = 270°$ for light ($C_T/\sigma = 0.040$) and deep ($C_T/\sigma = 0.125$) stall. Flow is from left to right.

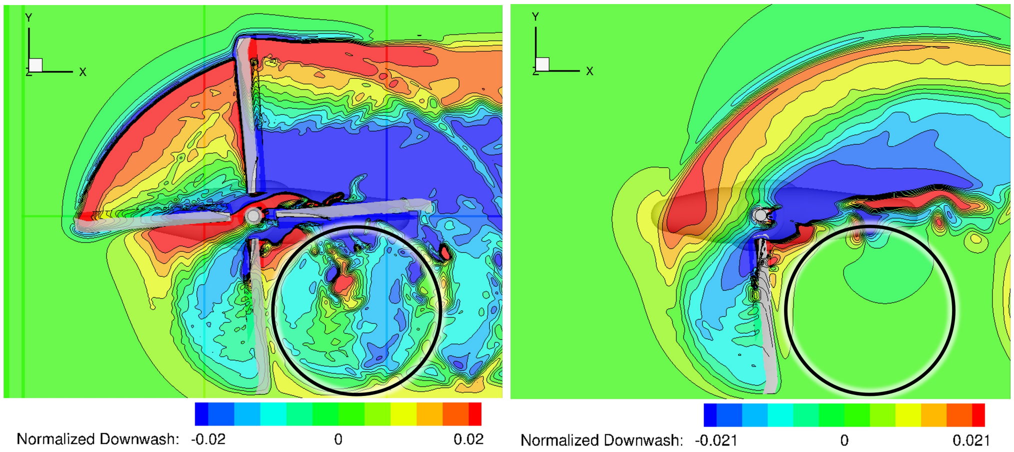

(a) Four-bladed $C_T/\sigma = 0.040$ (b) One-bladed $C_T/\sigma = 0.040$

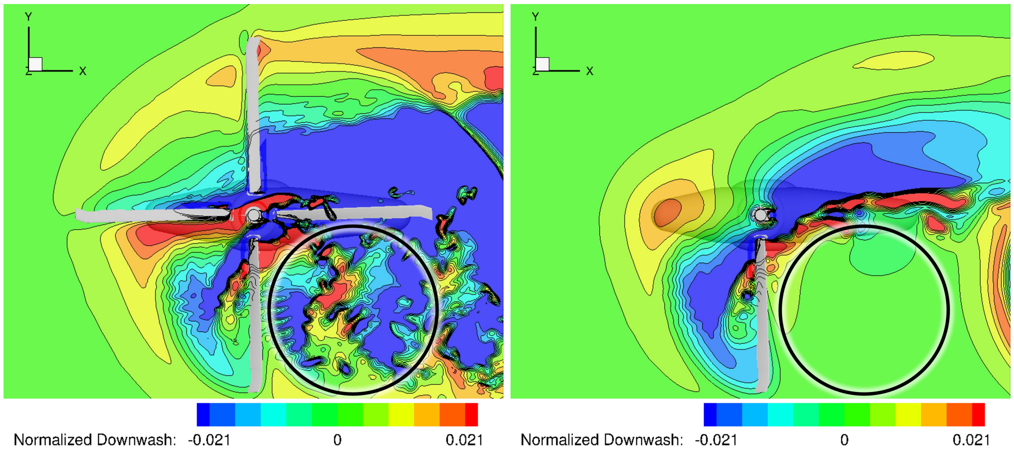

(c) Four-bladed $C_T/\sigma = 0.125$ (d) One-Bladed $C_T/\sigma = 0.125$

Figure 6.50: Downwash between $\psi = 270°$ and $\psi = 360°$ for light ($C_T/\sigma = 0.040$) and deep ($C_T/\sigma = 0.125$) stall. Flow is from left to right.

Coupled CFD-CSD

Instead of relying on motion extracted from a baseline four-bladed simulation, the loosely-coupled CFD-CSD case aimed to run independently of prescribed motion from a four-bladed simulation. The OVERFLOW CFD case was loosely-coupled with Dymore, where the one-bladed simulation is set to trim to 25% of the wind tunnel thrust conditions using Dymore's autopilot feature. The loosely-coupled simulation was performed for the UH-60A test point 4530 detailed in Section 3.2. Sectional airloads were extracted at radial stations corresponding to experimental data. The sectional normal force from the one-bladed simulation, shown in Figure 6.51, exhibits significantly different behavior at all radial stations than the sectional normal force from the four-bladed simulation, suggesting blade motions between the two simulations are fundamentally different. Blade deformation data were then extracted at eight equally spaced radial stations and compared betweeen the one-bladed and four-bladed simulations. Figures 6.53-6.55 show translational grid deformation at each azimuth position in the x, y, and z-directions. Figures 6.56-6.58 shown rotational grid deformation at each azimuth position about the x, y, and z axes. All six translational and rotational deformation quantities are significantly different between the one-bladed and four-bladed runs. This proves the two simulations are fundamentally different and that a coupled CFD-CSD simulation is not an accurate method to capture isolate blade motion from BVI.

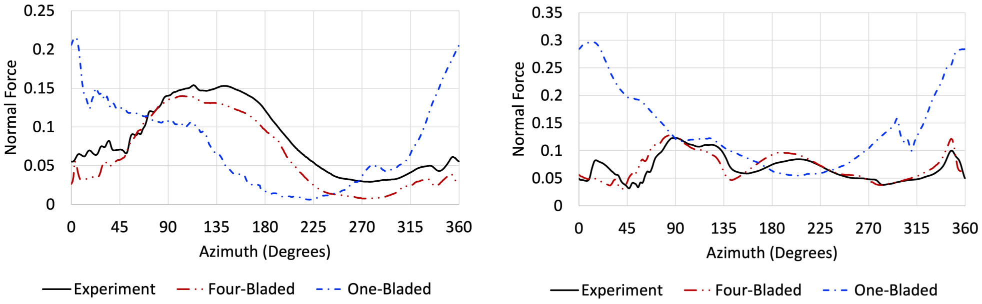

(a) r/R=0.400 (b) r/R=0.675

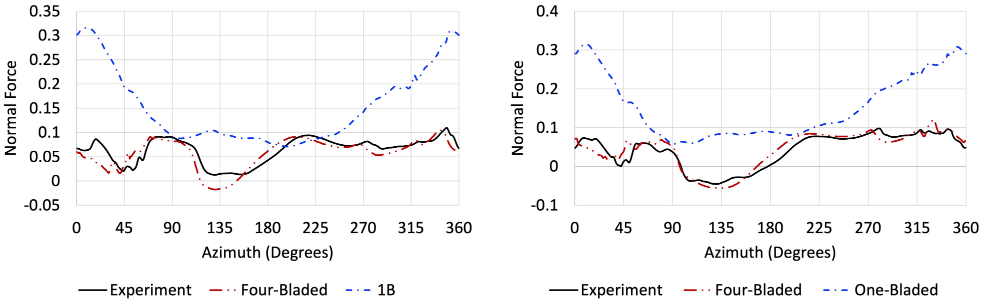

(c) r/R=0.775 (d) r/R=0.865

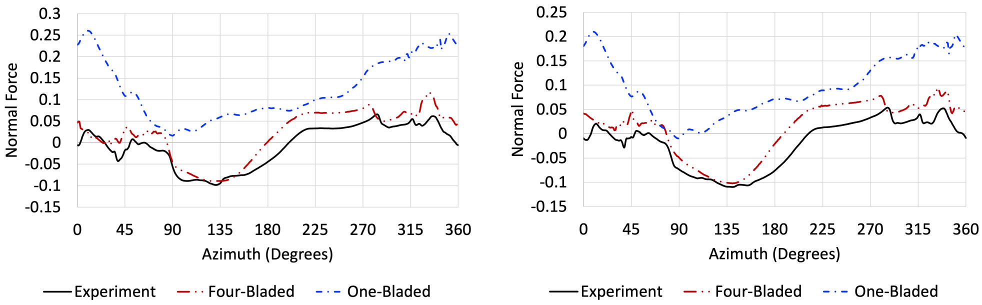

(e) r/R=0.920 (f) r/R=0.965

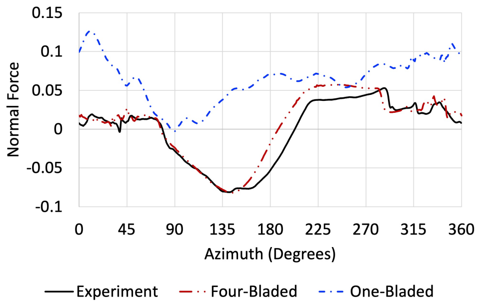

(g) r/R=0.990

Figure 6.51: UH-60A normal force at various radial stations for coupled CFD-CSD 1-bladed and 4-bladed runs

$C_T/\sigma = 0.040$

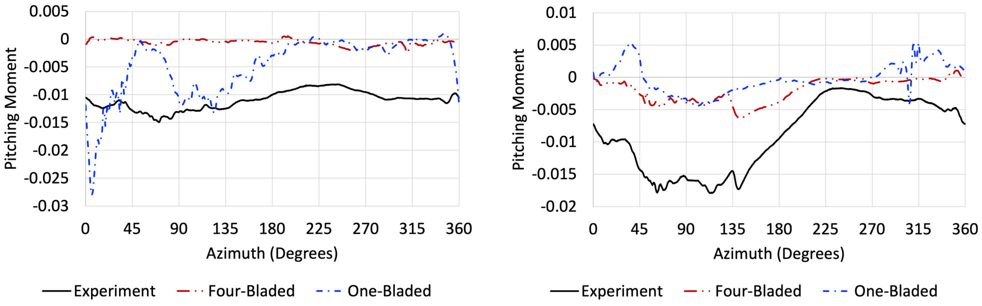

(a) r/R=0.400 (b) r/R=0.675

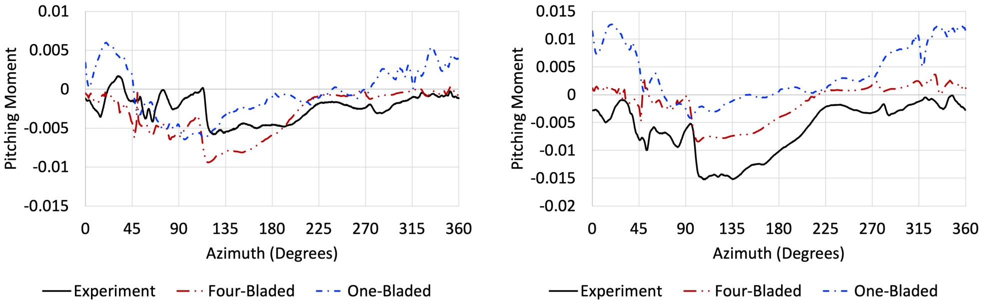

(c) r/R=0.775 (d) r/R=0.865

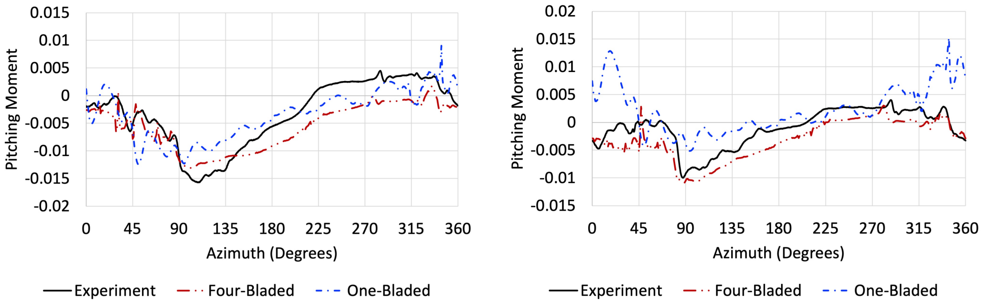

(e) r/R=0.920 (f) r/R=0.965

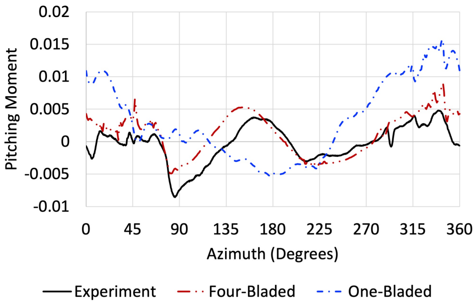

(g) r/R=0.990

Figure 6.52: UH-60A pitching moment at various radial stations for coupled CFD-CSD 1-bladed and 4-bladed runs
$C_T/\sigma = 0.040$

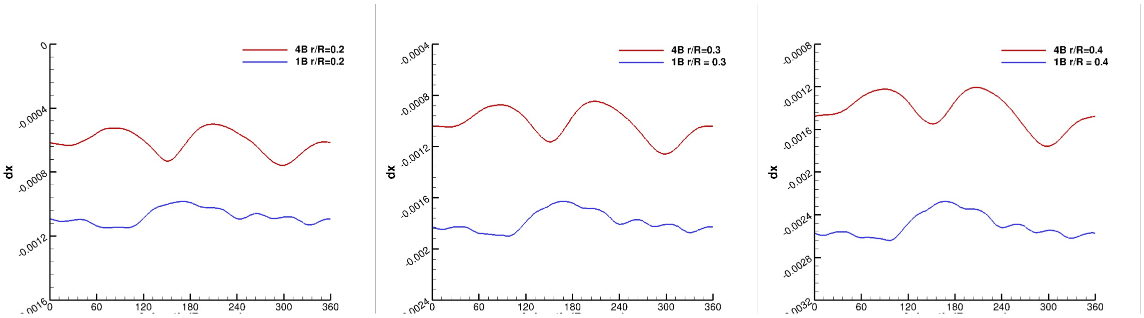

(a) r/R=0.200 (b) r/R=0.300 (c) r/R=0.400

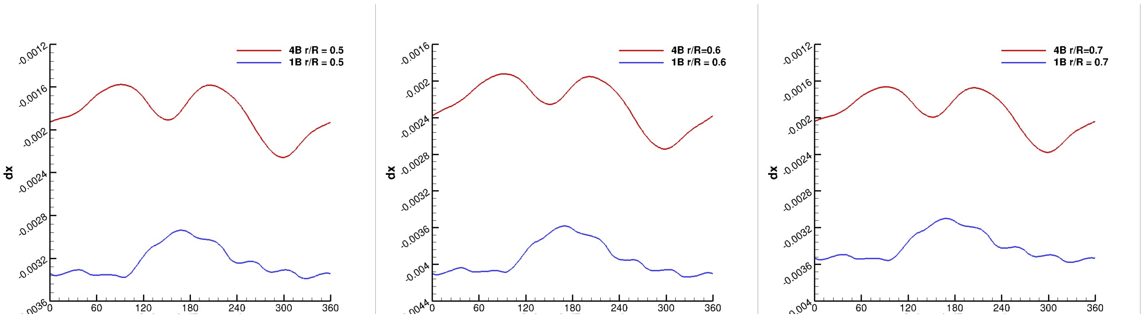

(d) r/R=0.500 (e) r/R=0.600 (f) r/R=0.700

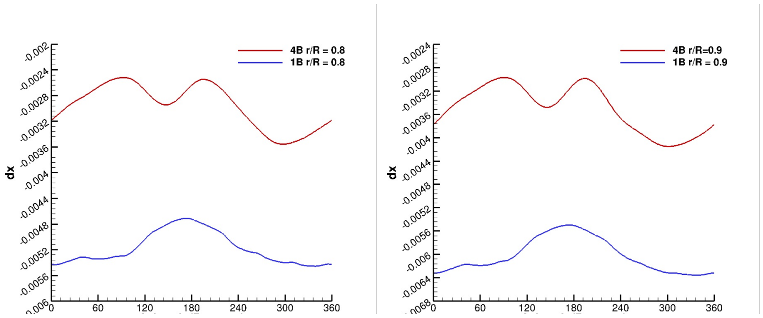

(g) r/R=0.800 (h) r/R=0.900

Figure 6.53: UH-60A x-direction blade deformation delta deflections at various radial stations for coupled CFD-CSD 1-bladed and 4-bladed runs
$C_T/\sigma = 0.040$

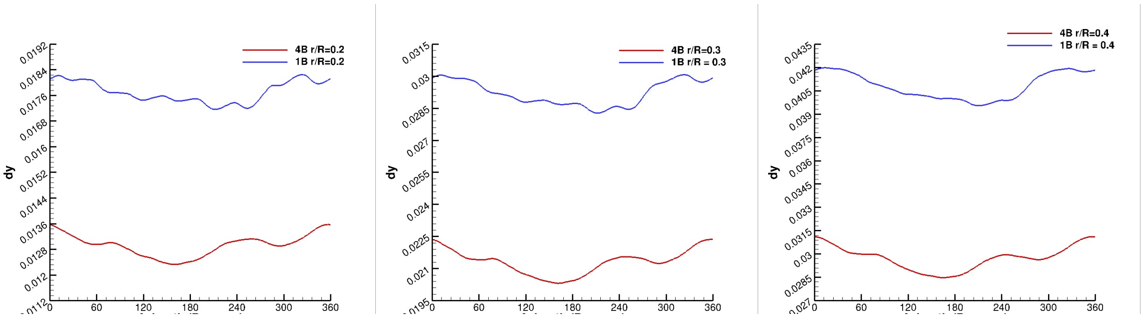

(a) r/R=0.200 (b) r/R=0.300 (c) r/R=0.400

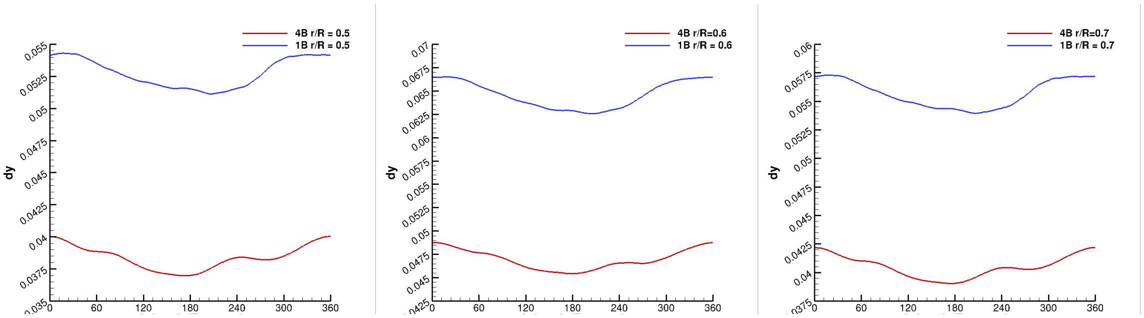

(d) r/R=0.500 (e) r/R=0.600 (f) r/R=0.700

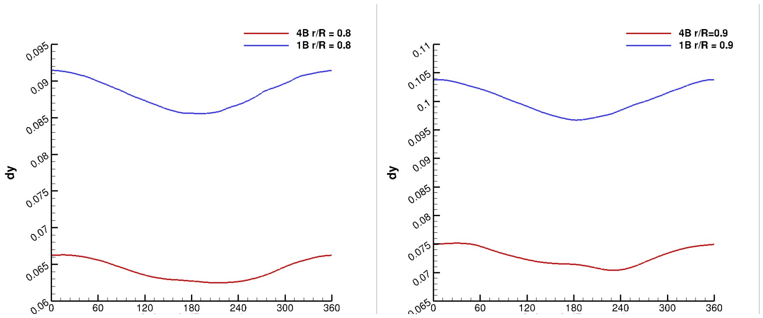

(g) r/R=0.800 (h) r/R=0.900

Figure 6.54: UH-60A y-direction blade deformation delta deflections at various radial stations for coupled CFD-CSD 1-bladed and 4-bladed runs
$C_T/\sigma = 0.040$

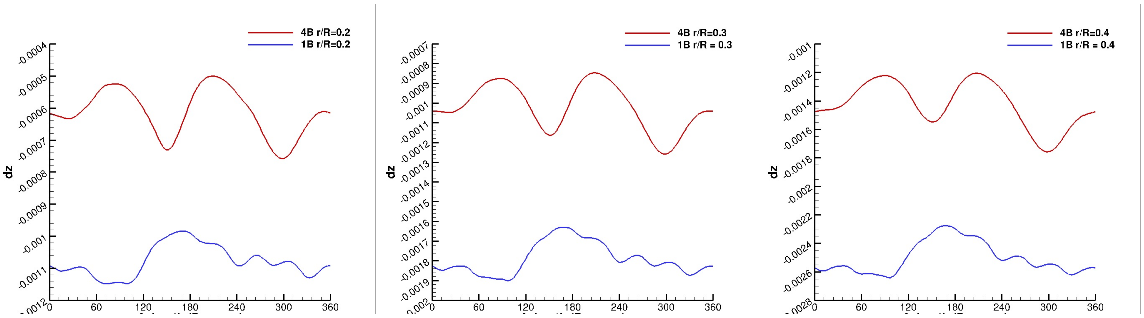

(a) r/R=0.200 (b) r/R=0.300 (c) r/R=0.400

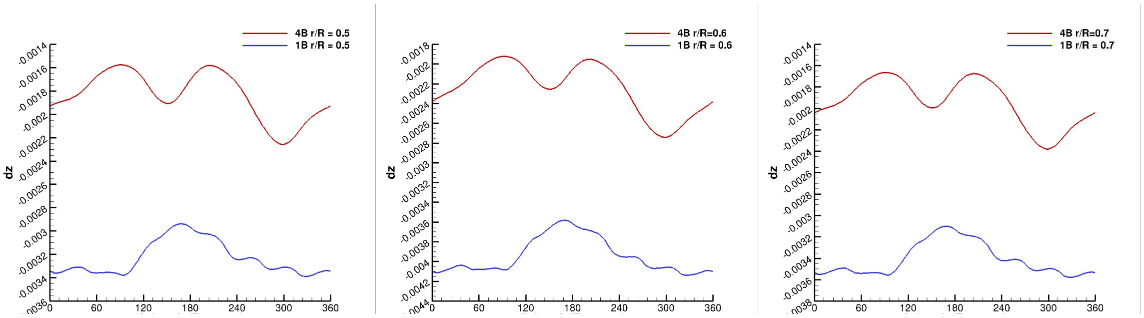

(d) r/R=0.500 (e) r/R=0.600 (f) r/R=0.700

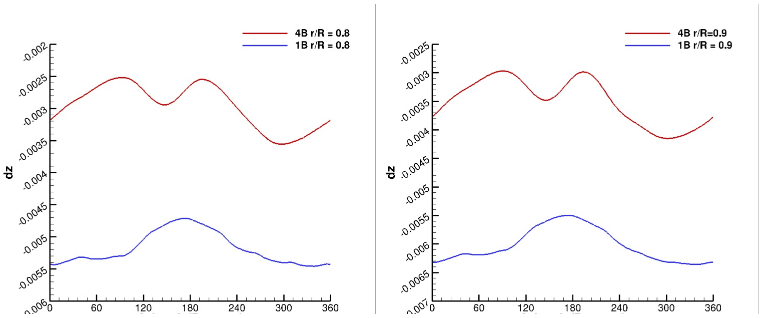

(g) r/R=0.800 (h) r/R=0.900

Figure 6.55: UH-60A z-direction blade deformation delta deflections at various radial stations for coupled CFD-CSD 1-bladed and 4-bladed runs
$C_T/\sigma = 0.040$

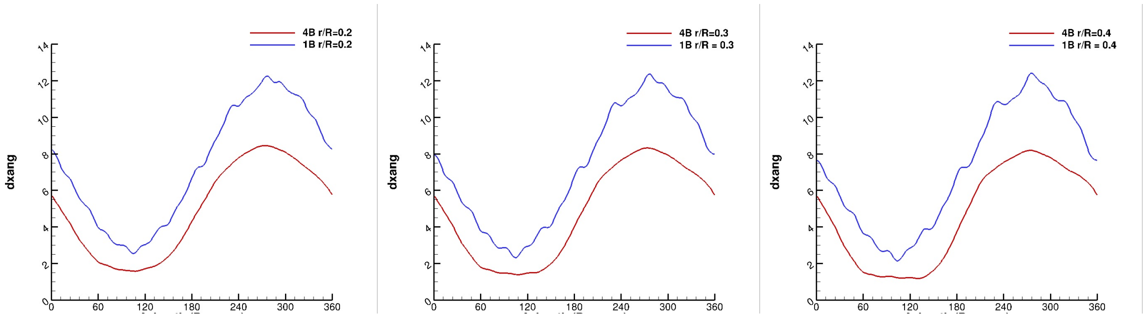

(a) r/R=0.200 (b) r/R=0.300 (c) r/R=0.400

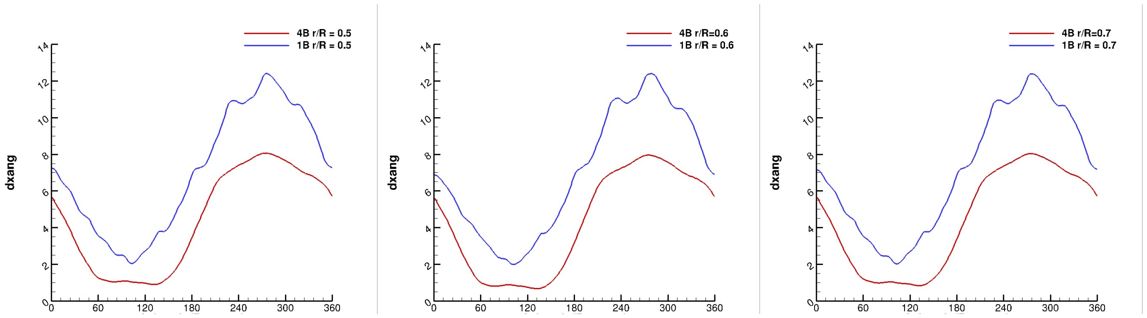

(d) r/R=0.500 (e) r/R=0.600 (f) r/R=0.700

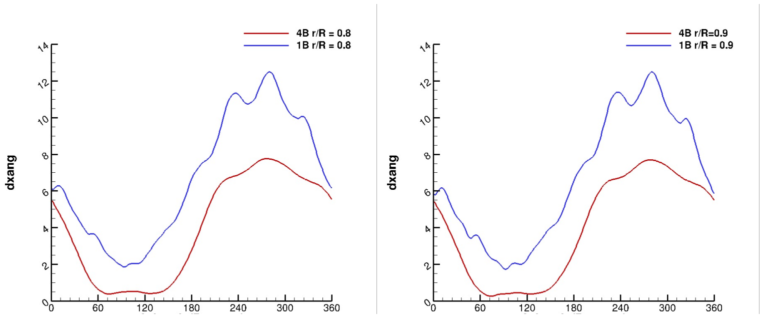

(g) r/R=0.800 (h) r/R=0.900

Figure 6.56: UH-60A x-direction blade deformation delta rotation at various radial stations for coupled CFD-CSD 1-bladed and 4-bladed runs
$C_T/\sigma = 0.060$

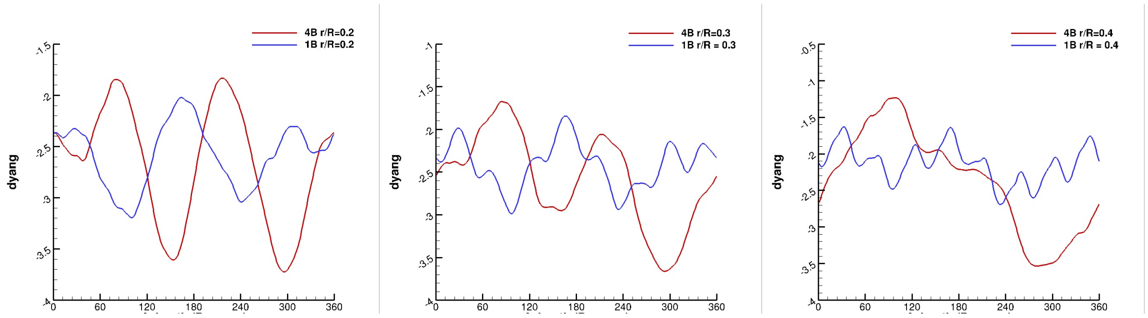

(a) r/R=0.200 (b) r/R=0.300 (c) r/R=0.400

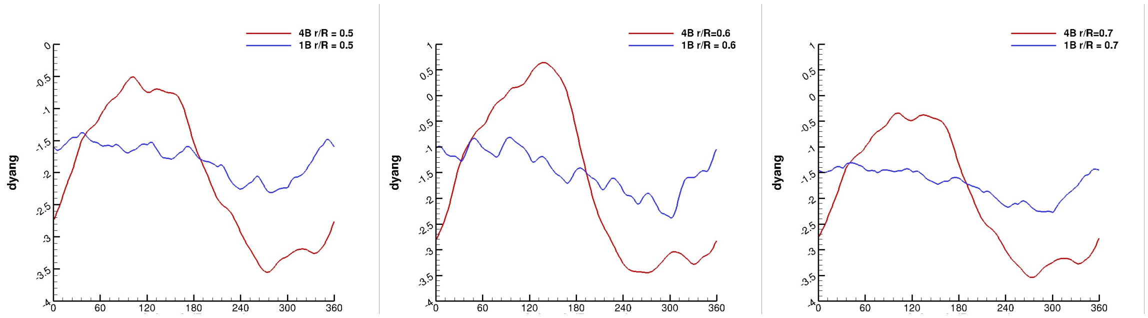

(d) r/R=0.500 (e) r/R=0.600 (f) r/R=0.700

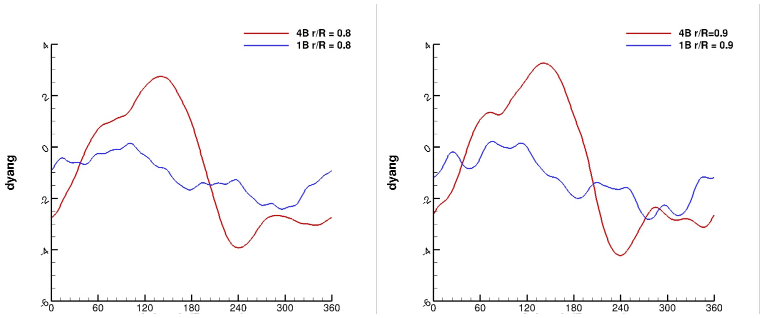

(g) r/R=0.800 (h) r/R=0.900

Figure 6.57: UH-60A y-direction blade deformation delta rotation at various radial stations for coupled CFD-CSD 1-bladed and 4-bladed runs
$C_T/\sigma = 0.040$

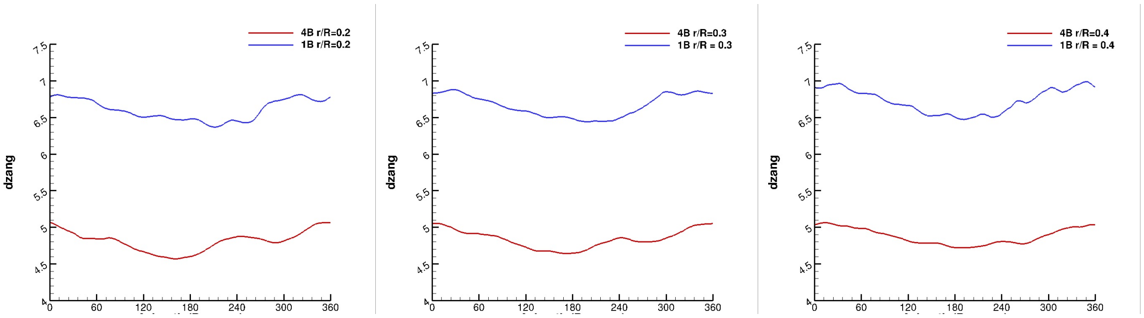

(a) r/R=0.200 (b) r/R=0.300 (c) r/R=0.400

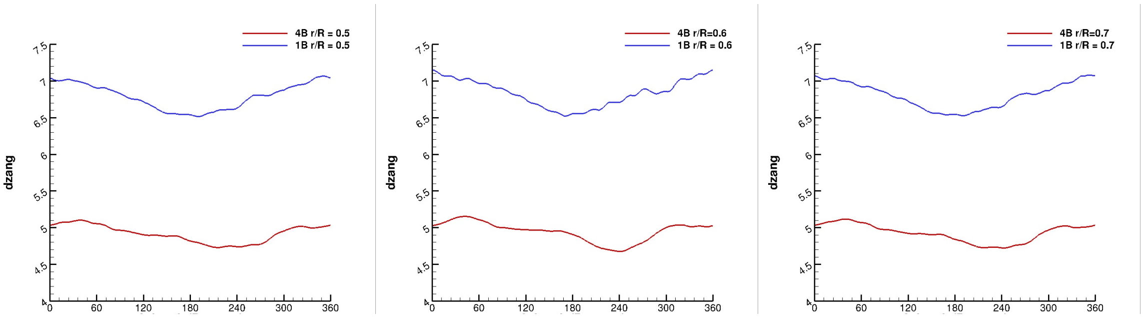

(d) r/R=0.500 (e) r/R=0.600 (f) r/R=0.700

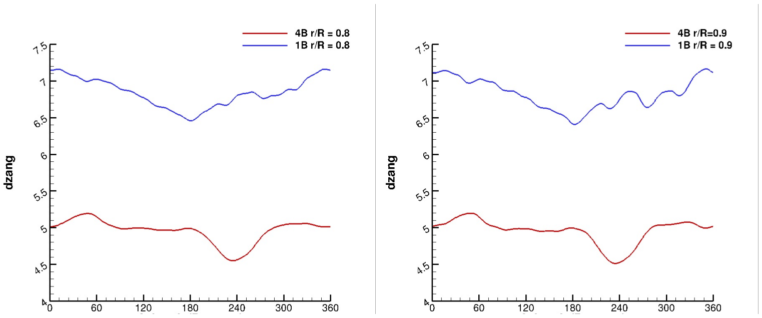

(g) r/R=0.800 (h) r/R=0.900

Figure 6.58: UH-60A z-direction blade deformation delta rotation at various radial stations for coupled CFD-CSD 1-bladed and 4-bladed runs
$C_T/\sigma = 0.040$

CHAPTER 7

THE ROLE OF BVI IN INDUCING SEPARATED FLOW IN THE ROTOR PLANE

In addition to determining the most accurate and effective method for isolating blade motion from BVI and classifying separated flow based on separation mechanism, further evaluating the physics of the entire rotor plane is an important step in advancing the state-of-the-art. In 2020 Castells et al. (Ref. [50]) studied the influence of BVI on 2D and 3D simulations of an oscillatory, pitching wing with non-uniform translation, but without rotation by introducing a vortex into the simulation via the Scully vortex model [84]. Vortex characteristics, specifically size and strength, were extrapolated from loosely-coupled CFD/CSD simulations of a full three-dimensional rotor. The influence of a vortex passing near the blade was shown to induce stall, confirming that the vortex interaction with the leading edge can produce behavior consistent with dynamic stall.

While Castells' paper investigated 3D effects, the focus was on finite-span features. Rotor effects such as rotation and downwash were not included. This investigation extends Castells work on finite wings to full three-dimensional rotor simulations that inherently include rotation and downwash. To further understand separated flow on the rotor, the Biot-Savart Law is applied to trailing tip vortices to evaluate the associated downwash at various points on the blade. The extents of vortex-induced downwash and the direct effects on the rotor plane are explored.

7.1 Biot-Savart Law

The Biot-Savart Law (Eqn. 7.2) is an inviscid, compressible flow theory that gives velocity induced at an arbitrary point P by an infinitesimal vortex filament where $\overline{dV}$ is the induced velocity, Γ is the vortex filament strength, or circulation, $\overline{dl}$ is the infinitesimal vortex filament length, and $\bar{r}$ is the distance between the infinitesimal vortex filament and point P. Integrating over the entire vortex filament gives the total induced velocity at point P (Eqn. 7.1).

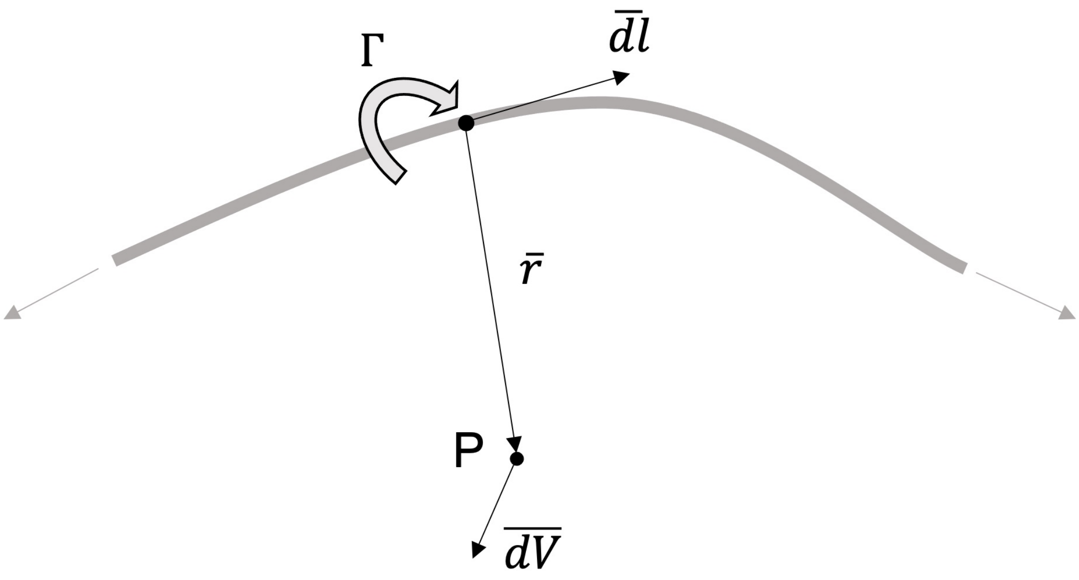

Figure 7.1: Biot-Savart Definition

$$\overline{dV} = \frac{\Gamma}{4\pi}\frac{\overline{dl} \times \bar{r}}{|\bar{r}|^3} \tag{7.1}$$

$$\overline{V}(x, y, z) = \frac{\Gamma}{4\pi}\int_{-\infty}^{\infty}\frac{\overline{dl} \times \bar{r}}{|\bar{r}|^3} \tag{7.2}$$

For any closed curve (C) in a flowfield, the circulation is defined by a line integral of the velocity vector (Eqn. 7.3). Applying Stokes Theorem, the line integral can be converted to a surface integral (Eqn. 7.4) where the integrand becomes the divergence of velocity, or vorticity vector.

$$\Gamma = -\int_C \overline{V} \cdot \overline{ds} \tag{7.3}$$

$$\Gamma = -\int\int_S \left(\boldsymbol{\nabla} \times \overline{V}\right) \cdot \overline{ds} \tag{7.4}$$

7.2 Application of Biot-Savart Law to CFD Flowfield

Application of the Biot-Savart Law to a CFD flowfield permits the study of direct vortex-induced downwash on a rotor blade for individual trailing tip vortices. Modifications are required to realistically apply the law and take into account some viscous effects. In inviscid flow theory, a vortex filament has constant circulation along its entire length. When viscous effects are included, vorticity will decay as the vortex filament in question convects through air. To take this into account the circulation is permitted to vary over the length of each trailing tip vortex filament. The modified integral with variable circulation is given in Equation 7.5, where circulation is included inside the integral calculation.

$$\overline{V}(x,y,z) = \int_{-\infty}^{\infty} \frac{\Gamma}{4\pi} \frac{\overline{dl} \times \bar{r}}{|\bar{r}|^3} \tag{7.5}$$

Consider application of the Biot-Savart Law to a point "P" on a blade at $\psi = 270°$, as shown in Figure 7.2. For a single Biot-Savart integral, circulation is calculated for the tip vortex of interest at various intervals along the vortex filament (Fig. 7.3) using Equation 7.4. To appropriately use Equation 7.4, an integration surface must be chosen to capture the majority of circulation associated with vortex. Azimuth vorticity slices, with the origin at the rotor hub, are extracted in one degree increments for calculation of a two-dimensional surface integral on each slice (Fig. 7.3). To determine the appropriate bounding curve for each slice, a circular curve with its center at the location of maximum vortex strength is chosen on each azimuth slice. The circulation integral is repeatedly calculated with increasing radius (Fig. 7.4) until the change in predicted circulation is less than one percent (Fig. 7.5). at which point, the bounding curve is frozen and deemed acceptable. For this example the change in circulation is less than one percent when integration radius is increased from 13 to 14 inches, as shown in Table 7.1.

To evaluate the integral along the length of a vortex filament, it is evaluated as a summa-

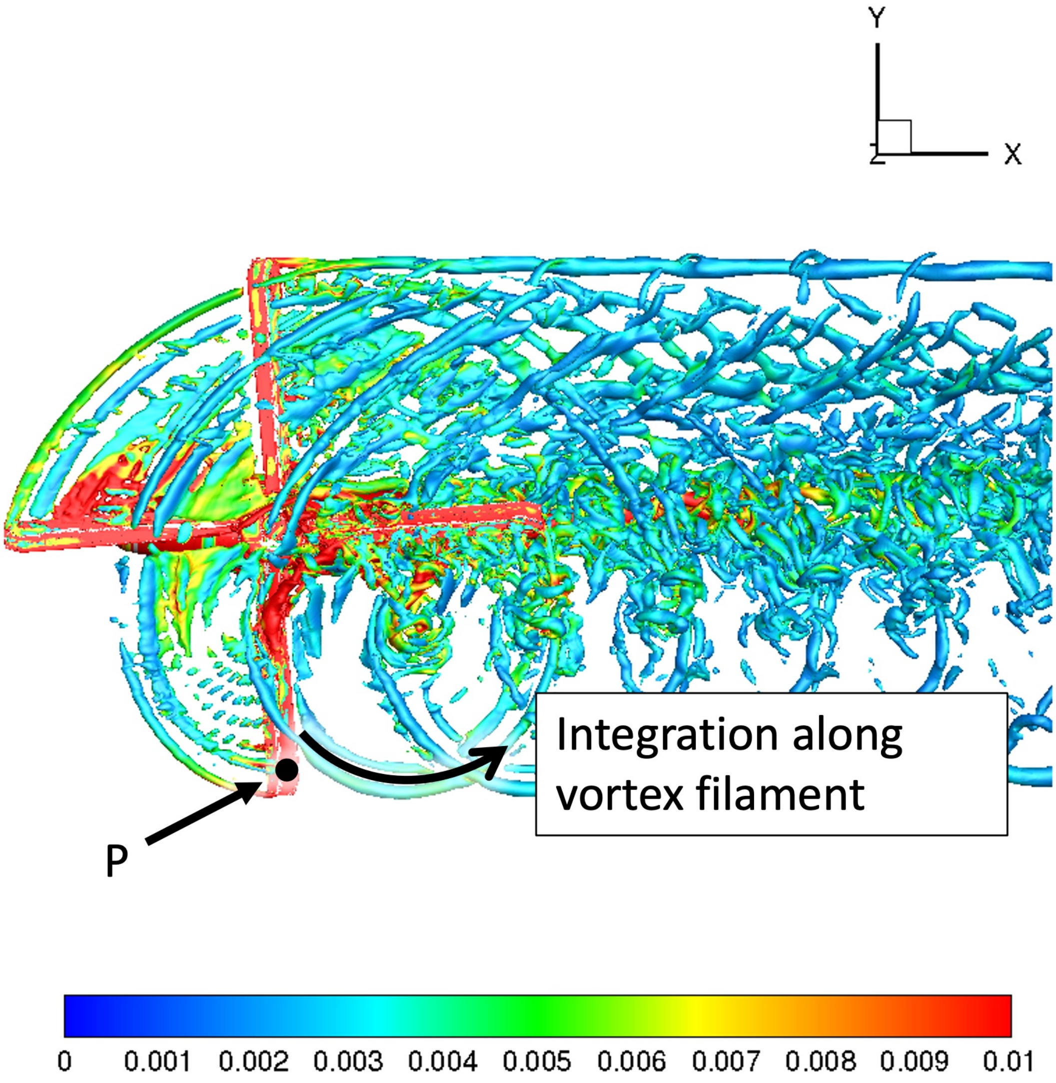

Figure 7.2: Biot-Savart application example

tion along the vortex filament with each step equal to $\psi = 1°$. (Eqn. 7.6).

$$\overline{V}(x,y,z) = \sum_{-\infty}^{\infty} \frac{\Gamma}{4\pi} \frac{\overline{l_i} \times \overline{r_i}}{|\overline{r_i}|^3} \tag{7.6}$$

This summation has lower and upper bounds that are negative and positive infinity, respectively. To realistically apply the summation, finite limits must be determined to bound the summation while still capturing the extents of the impinging vortex filament required to accurately produce downwash. The lower bound is chosen as 0 to include the effects of only current and future impinging

Table 7.1: Convergence of circulation integral values using increasingly large integration radii.

Integration radius (inches)	Circulation Value (ft^2/s)	Percent Change Magnitude
7	113.038	N/A
8	128.751	13.90%
9	140.917	9.45%
10	149.901	6.38%
11	155.969	4.05%
12	159.733	2.41%
13	161.643	1.20%
14	162.274	0.39%
15	162.062	-0.13%
16	161.481	-0.36%
17	160.807	-0.42%
18	160.257	-0.34%
19	159.897	-0.22%
20	159.747	-0.09%

vortex filament segments. To determine the appropriate upper bound, the Biot-Savart summation is repeatedly calculated with increasing upper bounds. When the change in calculated induced velocity is less than one percent for all components, the upper bound is considered acceptable. Using the example at $\psi = 270°$, the Biot-Savart summation is computed to determine induced velocity (2.28, -2.61, 1.39), a quarter-chord surface location near the blade tip (Point P in Fig. 7.2) using vortex filament segments from 1°-20° ahead of blade impingement. At each angular location the circulation is calculated using the previously described method to ensure integral convergence. Circulation calculations and induced velocity predictions are provided in, Table C.1 in Appendix C. Figure 7.6 demonstrates convergence past 18 degrees, with changes less than 1% for all three induced velocity components. Using the same method, The Biot-Savart Law can be applied at various points along the length of the blade to evaluate induced velocity distributions due to vortex impingement. Figure 7.7 exemplifies induced velocity distributions that can be calculated along the blade quarter-chord ($\psi = 270°$ in this example).

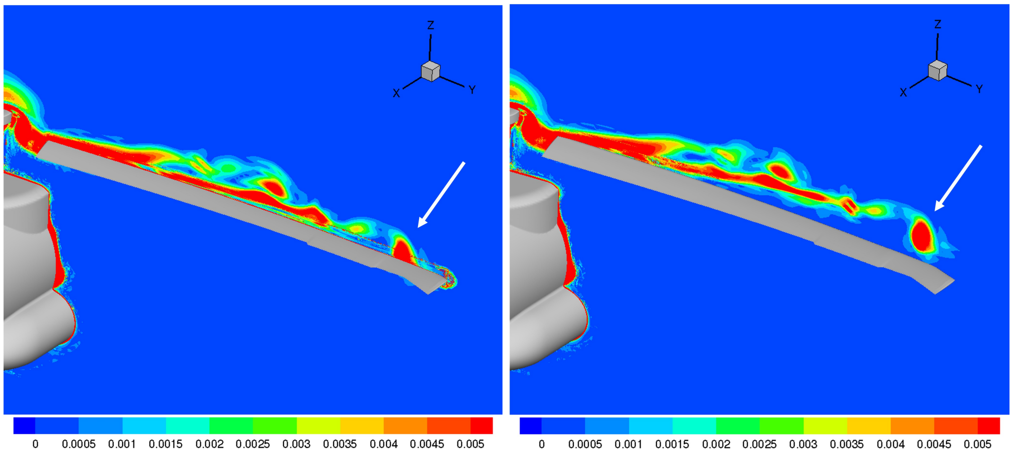

(a) $+0°$ from blade (b) $+5°$ from blade

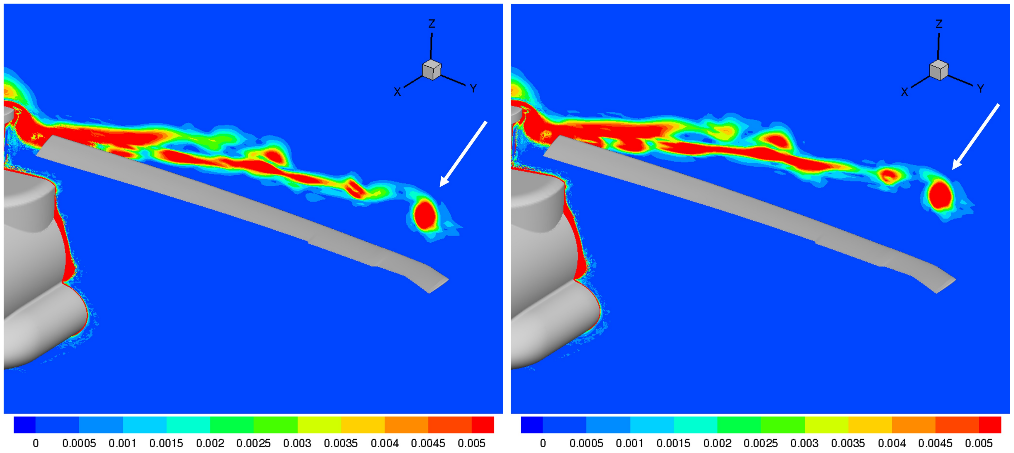

(c) $+10°$ from blade (d) $+15°$ from blade

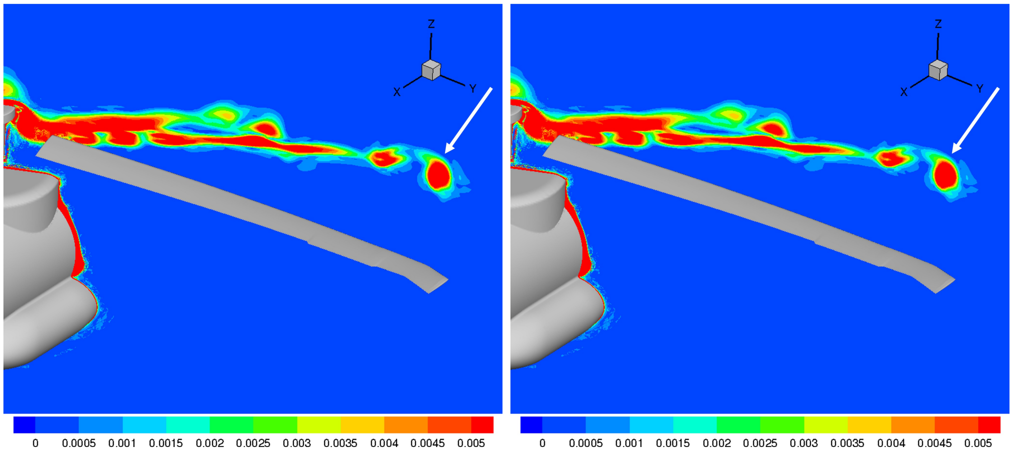

(e) $+20°$ from blade (f) $+25°$ from blade

Figure 7.3: Vorticity slices along tip vortex impinging on blade at $\psi = 270°$

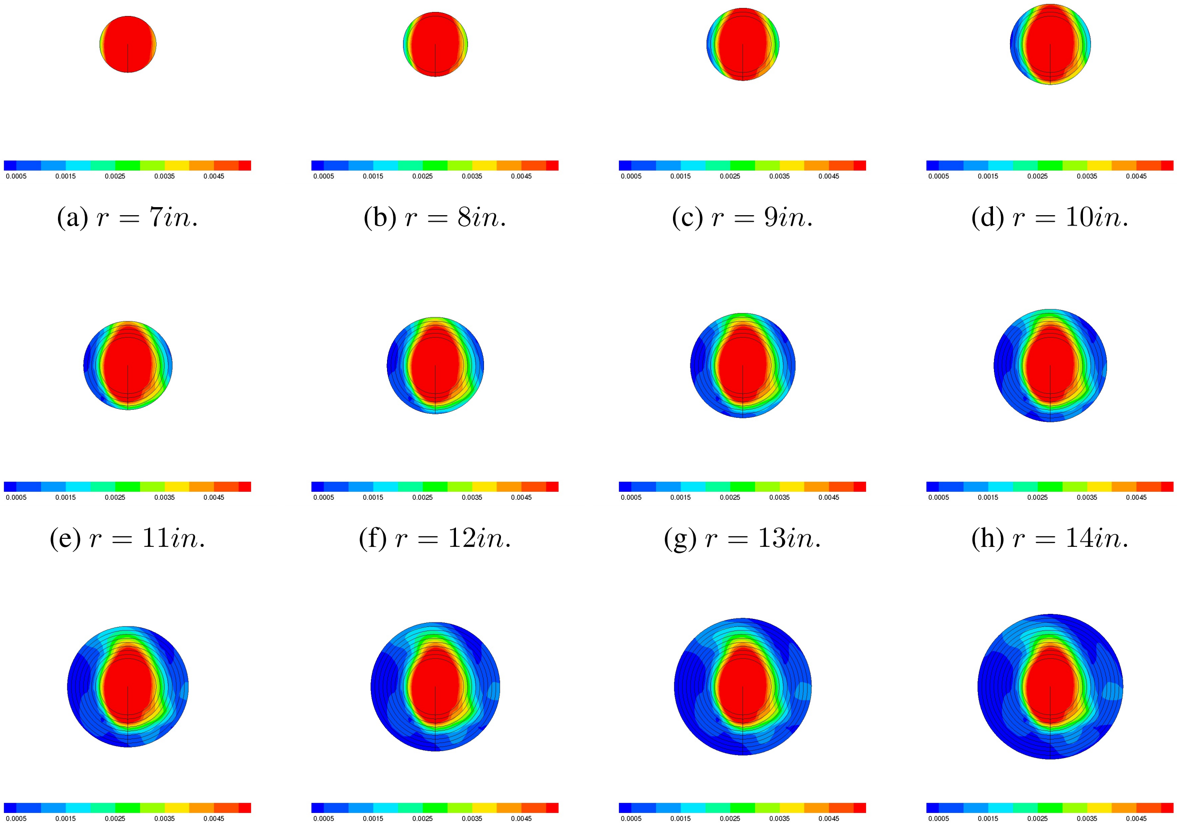

(a) $r = 7in.$ (b) $r = 8in.$ (c) $r = 9in.$ (d) $r = 10in.$

(e) $r = 11in.$ (f) $r = 12in.$ (g) $r = 13in.$ (h) $r = 14in.$

(i) $r = 15in.$ (j) $r = 16in.$ (k) $r = 17in.$ (l) $r = 18in.$

Figure 7.4: Integration surfaces used to determine the appropriate bounding curve for circulation integral.

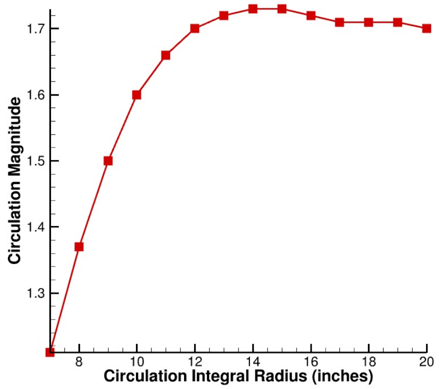

Figure 7.5: Convergence of circulation with increasingly larger integration surfaces.

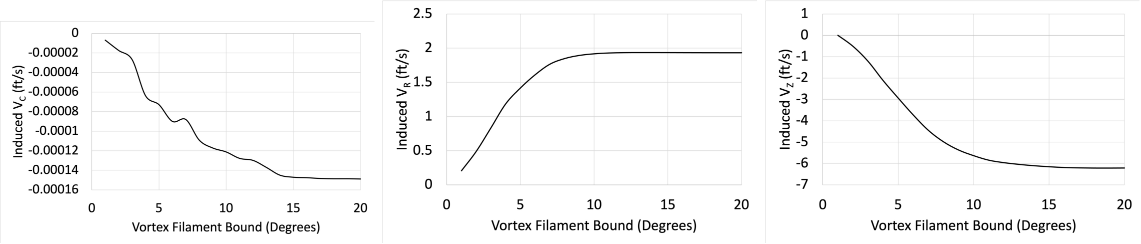

(a) Chordwise (b) Radial (c) Vertical

Figure 7.6: Convergence of induced velocity predictions with increasing Biot-Savart summation limits.

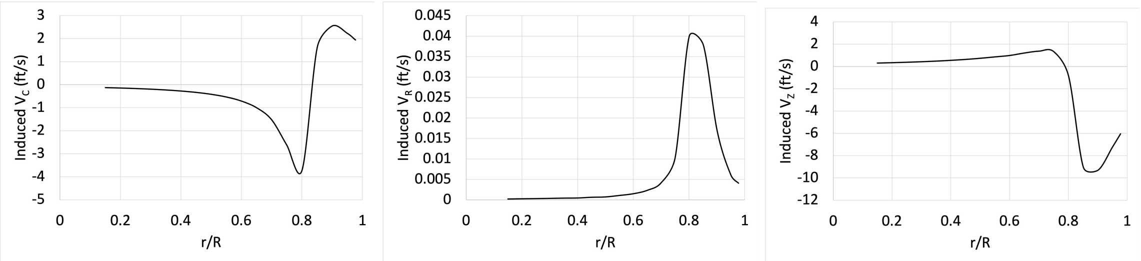

(a) Chordwise (b) Radial (c) Vertical

Figure 7.7: Induced velocity predictions at $\psi = 270°$ along the blade quarter-chord due to the vortex.

7.3 Biot-Savart and BVI Predictions

Advancing Blade

The advancing blade on the UH-60A rotor encounters two trailing tip vortices, one inboard and one outboard, for all analyzed thrust conditions as illustrated in Figure 7.8 for the light stall case. The outboard vortex originates from the blade preceding by $90°$ while the inboard vortex originates from the blade preceding by $180°$. The Biot-Savart Law was applied to understand the influence of vortex impingement on the advancing rotor blade.

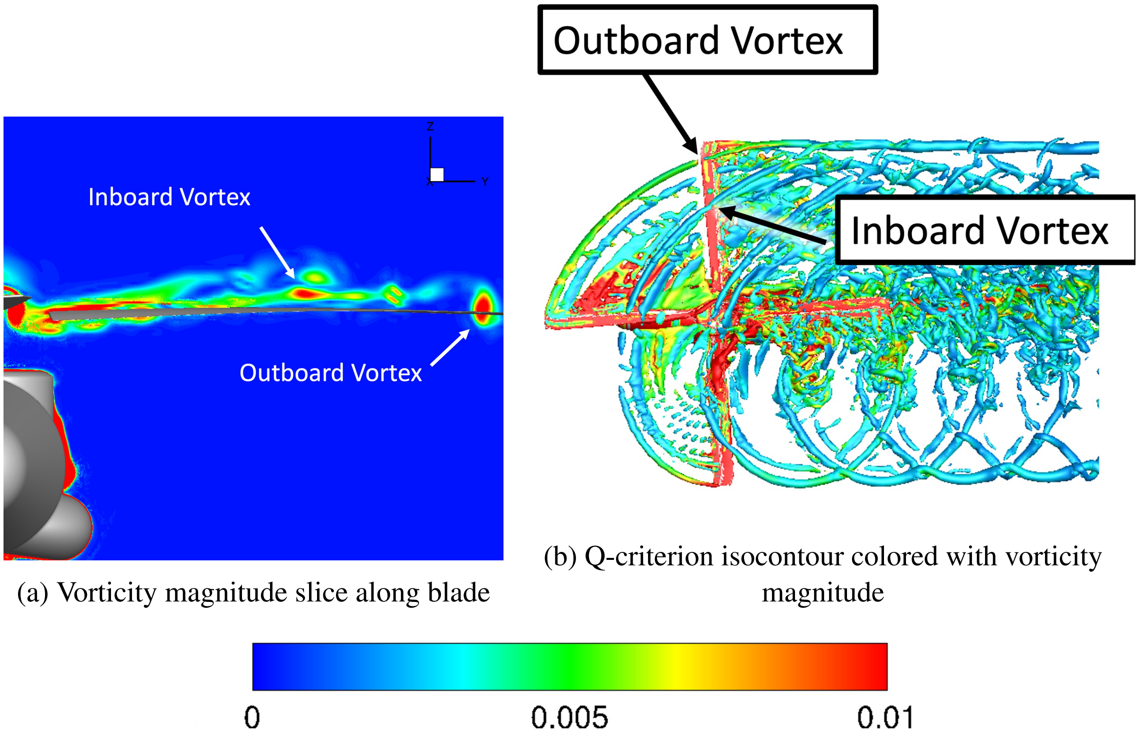

(a) Vorticity magnitude slice along blade

(b) Q-criterion isocontour colored with vorticity magnitude

Figure 7.8: Trailing tip vortex interactions at $\psi = 90°$ for light stall ($C_T/\sigma = 0.040$)

For the $C_T/\sigma = 0.040$ light stall case, BVI signatures appear between $\psi = 55°$ and $\psi = 150°$ at various radial stations on the advancing blade. Figures 7.9 highlight the peaks and drops of the BVI signatures, which are present at $r/R = 0.675$, $r/R = 0.775$, $r/R = 0.865$, and $r/R = 0.920$. The gray boxes bound the azimuth regions over which each radial station is influenced by BVI and are detailed in Table 7.2. No indication of BVI influence is present at the inboard $r/R = 0.400$ radial station or the outboard $r/R = 0.965$ and $r/R = 0.990$ radial stations.

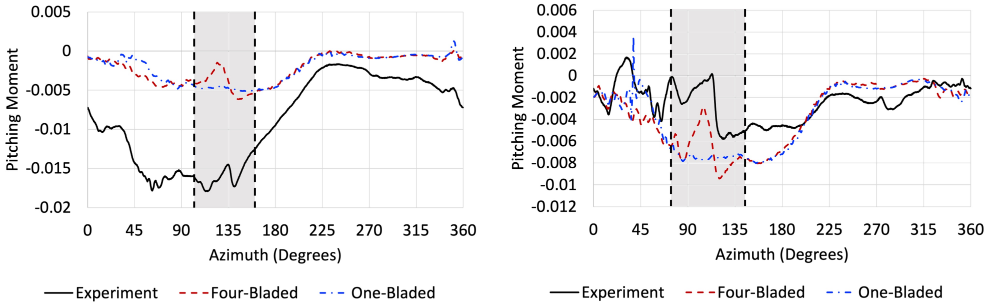

(a) $r/R = 0.675$ (b) $r/R = 0.775$

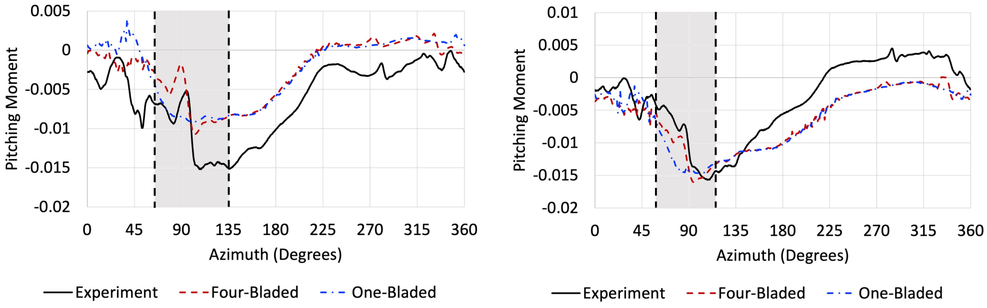

(c) $r/R = 0.865$ (d) $r/R = 0.920$

Figure 7.9: BVI signatures in pitching moment predictions at outboard stations for $C_T/\sigma = 0.040$

Table 7.2: Azimuth extents of BVI influence at various radial stations.

Radial station (r/R)	BVI influence start	BVI influence end
0.400	N/A	N/A
0.675	$\psi = 110°$	$\psi = 150°$
0.775	$\psi = 70°$	$\psi = 135°$
0.865	$\psi = 60°$	$\psi = 125°$
0.920	$\psi = 55°$	$\psi = 105°$
0.960	N/A	N/A
0.990	N/A	N/A

The Biot-Savart procedure outlined previously was used to calculate induced velocity from the outboard tip vortex along the entire blade at $\psi = 90°$ (Fig. 7.10), where the vortex was centered at $r/R = 0.88$ with a radius of 14 inches (4.3%R), as determined by circulation content. Coinciding with the vortex core are points of interest in the induced velocities, marked with a red X in the figures. The induced chordwise velocity slopes gently from $V_C \approx 0$ at the root to a minimum at $r/R \approx 0.8$. Beyond $r/R \approx 0.8$ the induced chordwise velocity rises drastically to a maximum value near the vortex core at $r/R = 0.88$. Between this location and the blade tip, the magnitude decreases slightly maintains a large value in comparison to inboard stations. The radial induced velocity (V_R) is negligible from the blade root to $r/R \approx 0.6$. At $r/R \approx 0.8$, induced radial velocity also rises drastically to a maximum near the vortex core at $r/R = 0.88$. The induced vertical velocity gently slopes upward from blade root, peaking just inboard of the vortex core at $r/R = 0.88$, and quickly dropping to negative values beyond $r/R > 0.9$. This behavior is a direct effect of the vortex rotation, which causes upwash inboard of the vortex and downwash outboard of the vortex. This can be visualized in Figure 7.11, which highlights the vortex core using vorticity magnitude contours overlaid with velocity vectors. The inboard upwash is much stronger than the outboard downwash as predicted by Biot Savart (Fig. 7.10) and indicated by the magnitude of vectors in the figure. BVI signatures, as a result, are only present at one radial station outboard of the vortex ($r/R = 0.920$) while inboard signatures are present at two inboard radial stations ($r/R = 0.775, 0.865$).

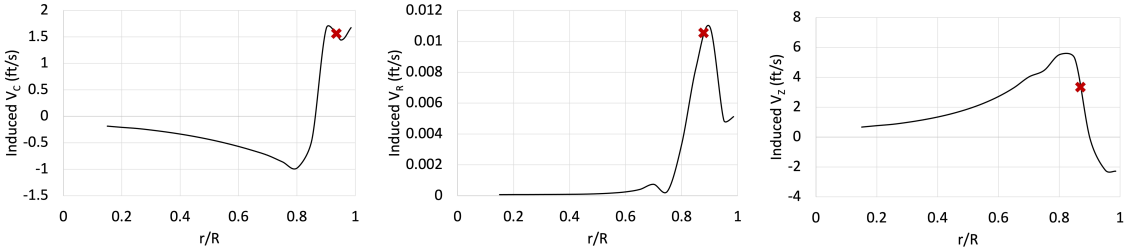

(a) Chordwise (b) Radial (c) Vertical

Figure 7.10: Induced velocities from outboard tip vortex along blade at $\psi = 90°$ for $C_T/\sigma - 0.040$

The same Biot-Savart procedure was applied from $\psi = 100°$ to $\psi = 170°$ in increments of 10 degrees, evaluating the effects of the outboard vortex. As the blade advances from $\psi = 90°$ to $\psi = 180°$, the point of vortex impingement moves inboard from the blade tip as illustrated by the isocontours in Figure 7.12 where locations of vortex impingement are identified by black circles. Exact locations of vortex impingement at each azimuth station are provided in Table 7.3.

Induced chordwise, radial, and vertical velocity distributions from vortex impingement are compared across multiple azimuth stations in Figures 7.13-7.15. The radial location of maxi-

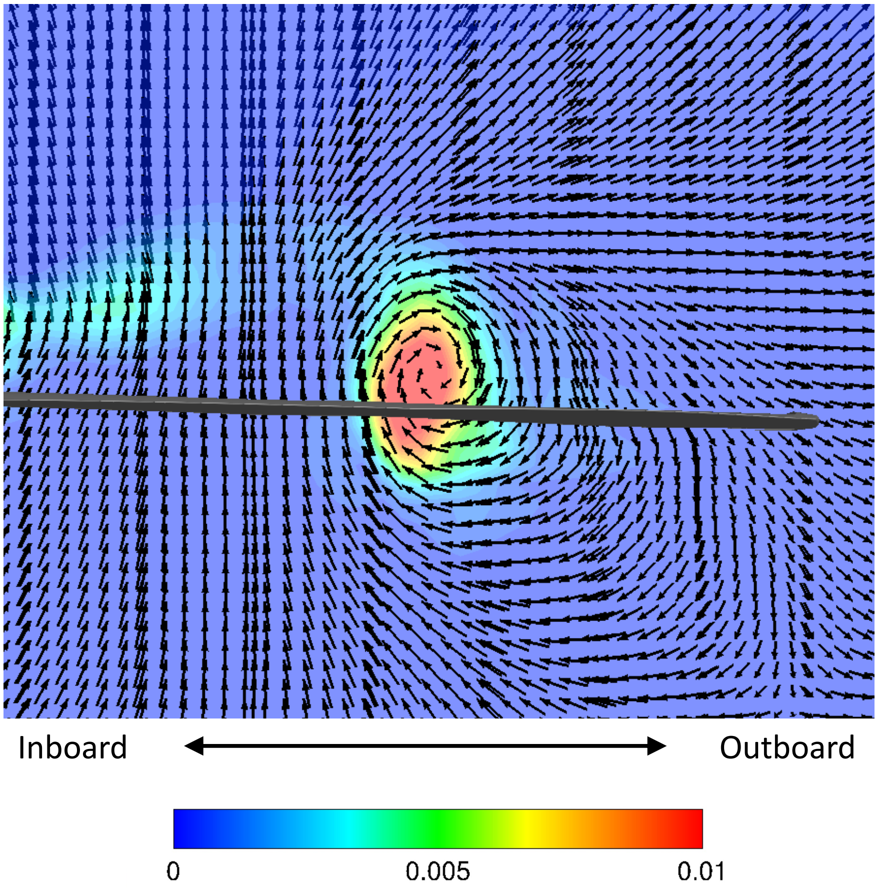

Figure 7.11: Vorticity magnitude contour overlaid with velocity vectors along plane of blade at $\psi = 90°$ for $C_T/\sigma - 0.040$

mum induced velocity moves inboard along with the location of vortex impingement as the blade advances. This behavior is responsible for the variation in BVI influence regions given in Table 7.2. At $\psi = 90°$, the vortex is centered at $r/R = 0.88R$, therefore the closest radial station at $r/R = 0.865$ is subjected to the highest induced velocities. As the vortex is nearly coincident with the $r/R = 0.865$ radial station, a BVI signature peak is present near $\psi = 90°$.

As the blade continues to advance, radial stations outboard of the vortex are farther removed from the vortex core. BVI influences vanish at earlier azimuth angles at these outboard stations, as demonstrated by the pitching moment at $r/R = 0.920$, where BVI influences extend only to $\psi = 105°$. Inboard stations will experience more BVI influence as the vortex will move closer to those radial stations as the blade advances. At $\psi = 90°$ the $r/R = 0.775$ radial station is located early within the azimuth region of BVI influence. As the blade advances from

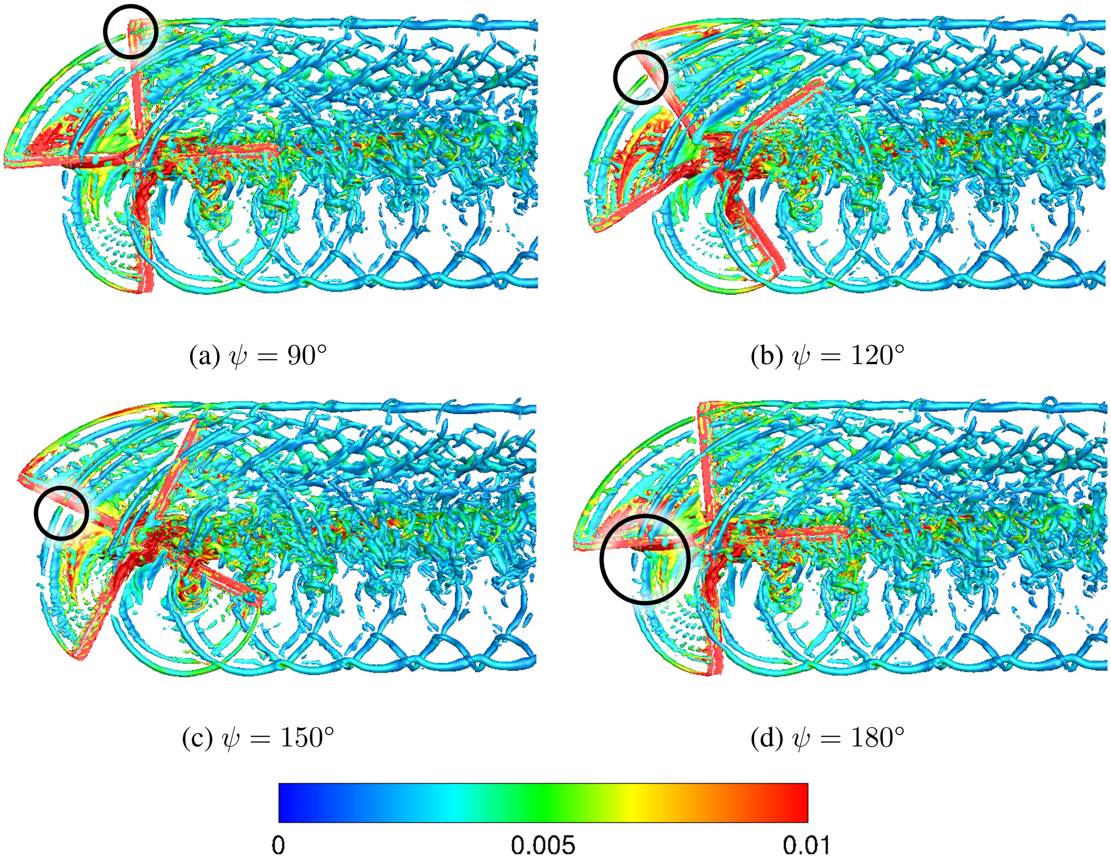

(a) $\psi = 90°$

(b) $\psi = 120°$

(c) $\psi = 150°$

(d) $\psi = 180°$

Figure 7.12: Identification of trailing tip vortex impingement on advancing blade. Flow is from left to right.

$\psi = 90°$ the induced upwash will continue to increase (Fig. 7.15), reaching a maximum value at $\psi = 110°$ where the $r/R = 0.775$ station is inboard of the vortex at $r/R = 0.790$ by 1.5%R. The $r/R = 0.675$ radial station exhibits similar behavior, with increasing upwash reaching a maximum value at $\psi = 130°$ where the vortex location was at $r/R = 0.690$ and inboard offset between maximum upwash and vortex location was once again 1.5%R.

Velocity distributions in Figures 7.13- 7.15for $\psi = 100°$-$\psi = 140°$ (left) and $\psi = 150°$-$\psi = 170°$ (right) are plotted on equivalent axes, highlighting a sharp decline in induced velocity between $\psi = 140°$ and $\psi = 150°$, continuing on through $\psi = 170°$. Figure 7.16 shows vortex circulation at the point of impingement from $\psi = 100°$-$\psi = 170°$. The decrease in circulation corresponds to the azimuth position where induced velocities decrease significantly between $\psi = 140°$ and $\psi = 150°$. Visualization of the flowfields along the blade slice from $\psi = 130°$ to

Table 7.3: Advancing blade vortex impingement locations.

Azimuth (degrees)	Radial location of vortex impingement
90	$88\%R$
100	$83\%R$
110	$79\%R$
120	$74\%R$
130	$69\%R$
140	$66\%R$
150	$62\%R$
160	$59\%R$
170	$57\%R$

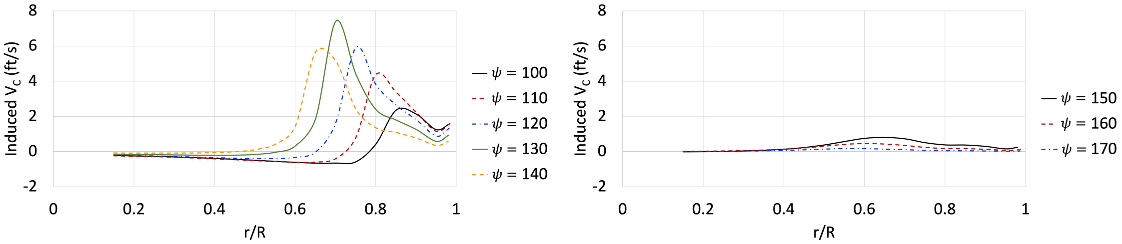

Figure 7.13: Induced chordwise velocity distributions along blade span from $\psi = 100°$ to $\psi = 170°$

$\psi = 170°$ demonstrate the diminishing effect of the vortex on the flowfield as vortex strength dissipates.

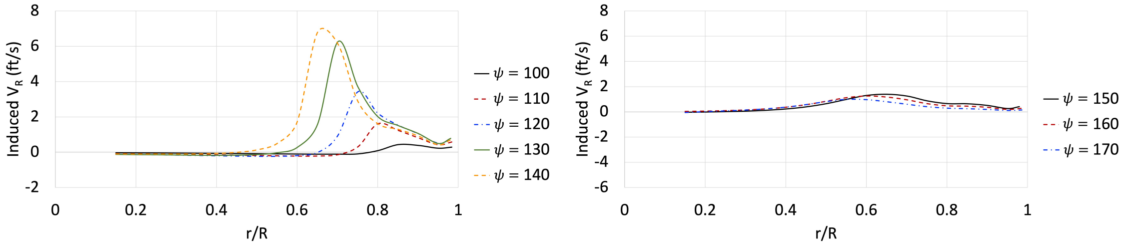

Figure 7.14: Induced radial velocity distributions along blade span from $\psi = 100°$ to $\psi = 170°$

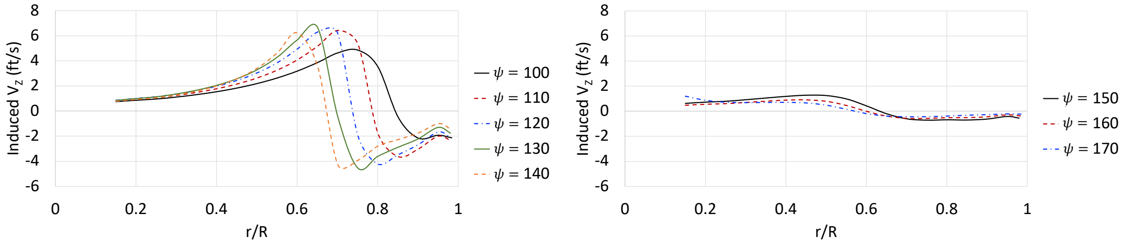

Figure 7.15: Induced vertical velocity distributions along blade span from $\psi = 100°$ to $\psi = 170°$

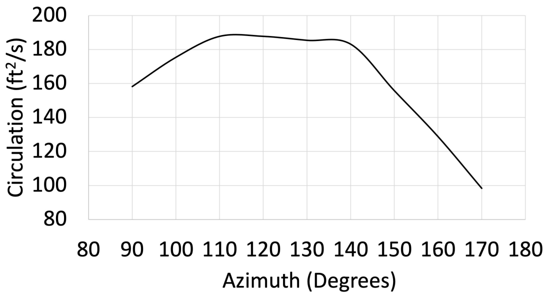

Figure 7.16: Trailing vortex circulation value point of impingement from $\psi = 100°$ to $\psi = 170°$

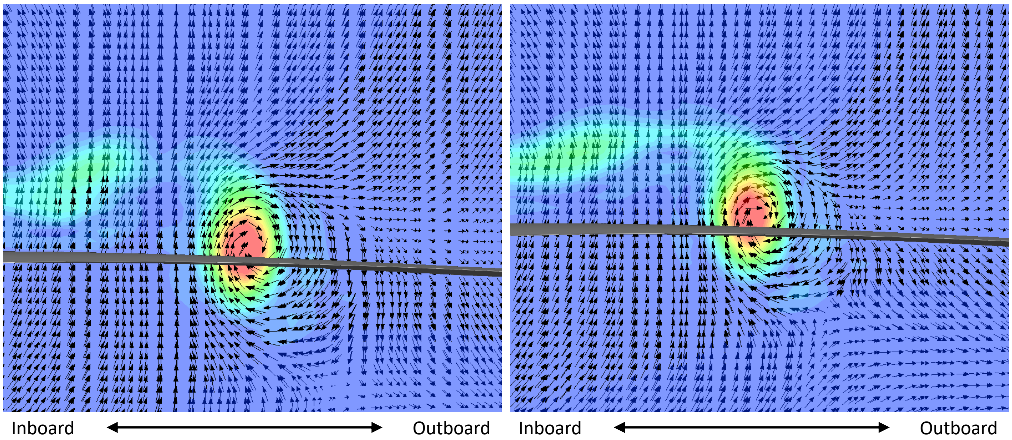

(a) $\psi = 130°$

(b) $\psi = 140°$

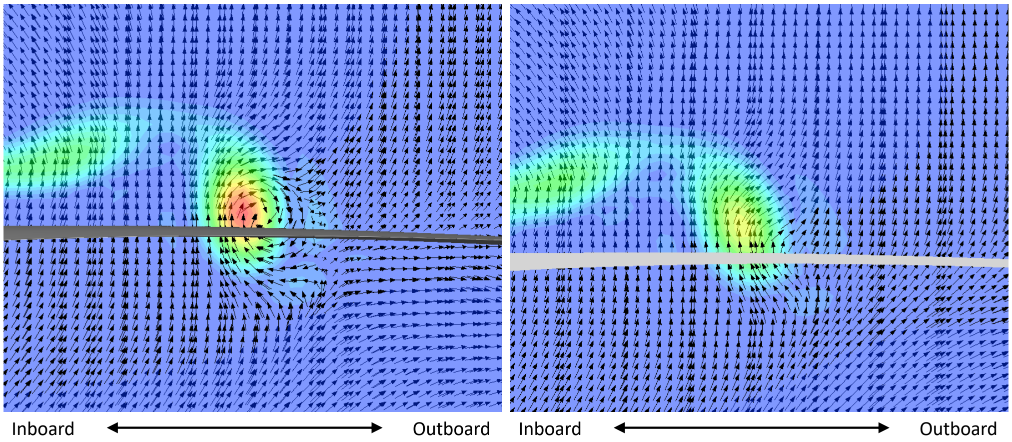

(c) $\psi = 150°$

(d) $\psi = 160°$

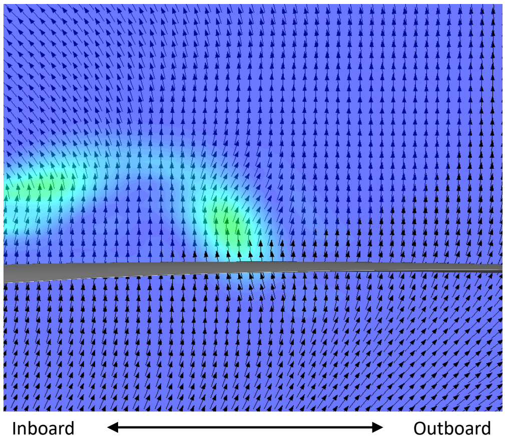

(e) $\psi = 170°$

Figure 7.17: Flowfield around impinging vector at from $\psi = 130°$ to $\psi = 140°$

Retreating Blade

On the retreating blade, the UH-60A rotor encounters one trailing tip vortex, shed from the previous blade pass as shown for several retreating blade positions in Figure 7.18 for the light stall $C_T/\sigma = 0.040$ case. As the blade retreats, the location of vortex impingement moves outward towards the tip, eventually clearing the blade tip between $\psi = 280°$ and $\psi = 290°$. The radial location of vortex impingement is provided in Table 7.4 at azimuth stations from $\psi = 250\,\mathrm{deg}$ to $\psi = 300°$.

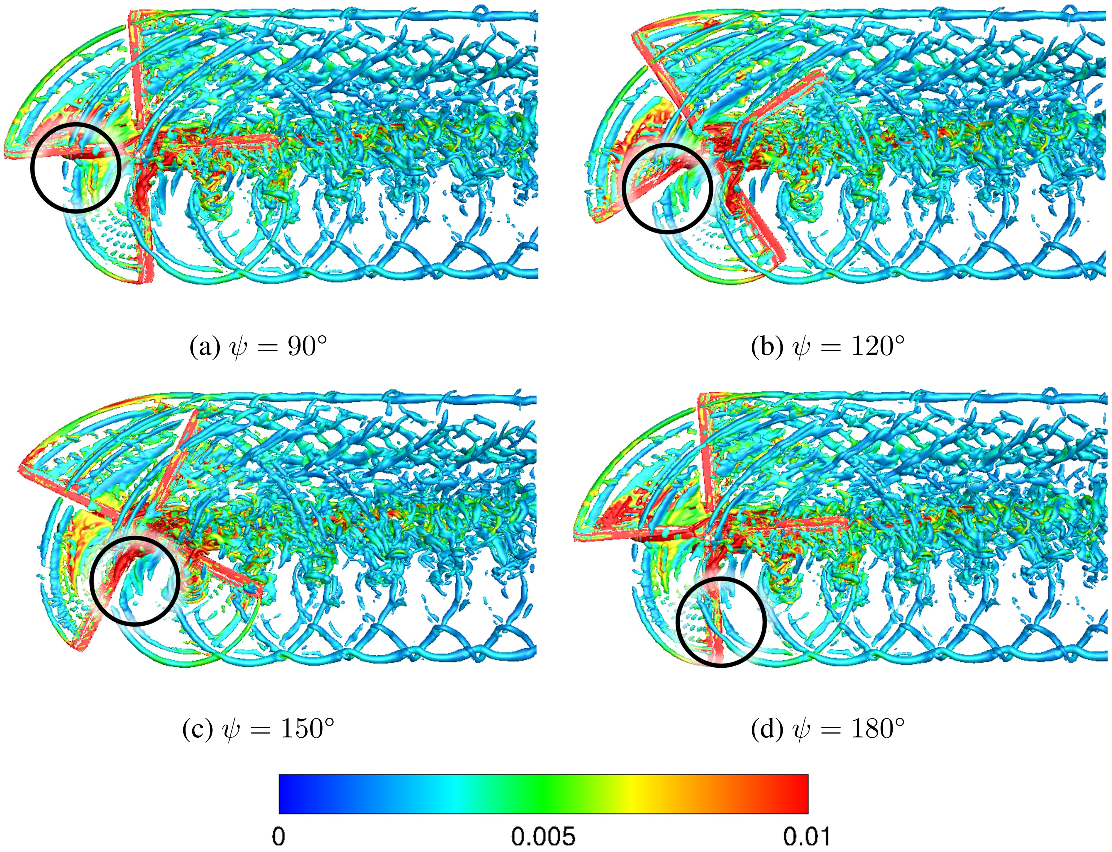
(a) $\psi = 90°$

(b) $\psi = 120°$

(c) $\psi = 150°$

(d) $\psi = 180°$

Figure 7.18: Identification of trailing tip vortex impingement on retreating blade. Flow is from left to right.

Retreating blade normal force and pitching moment data exhibit BVI signatures starting at $\psi = 250°$, as indicated by the peaks and drops highlighted in Figures 7.19 and 7.20 and extend to the end of the rotor revolution at $\psi = 360\,\mathrm{deg}$. The influence of BVI on both the normal force and

Table 7.4: Retreating blade vortex impingement locations.

Azimuth (degrees)	Radial location of vortex impingement
150	$61\%R$
260	$69\%R$
270	$80\%R$
280	$94\%R$
290	$108\%R$
300	$120\%R$

pitching moment indicates a stronger BVI interaction on the retreating blade than the advancing blade, as pitching moment is a more sensitive quantity than normal force.

The Biot-Savart Law is applied on the retreating blade from $\psi = 250°$ to $\psi = 300°$ to understand the influence of BVI on the retreating blade. Beyond $\psi = 300°$, the flowfield is comprised of hub and fuselage wake remnants along with the trailing tip vortices from previous blade passes, as exemplified in Figure 7.21 for the retreating blade at $\psi = 330°$. The trailing tip vortices are indistinguishable from other high vorticity content features making integration along the vortex filament as well, as calculation of circulation at each azimuth station, difficult and restricting application of the Biot-Savart Law to regions outside of wake.

The Biot-Savart induced downwash distribution along the blade is shown in Figure 7.22 from $\psi = 250°$ to $\psi = 300°$. From $\psi = 250°$ to $\psi = 270°$, induced downwash is significant and corresponds to azimuth angles where the trailing vortex from the previous blade pass directly impinges on the blade. Beyond $\psi = 280$ the vortex passes the outboard blade but does not directly impinge on it, resulting in the significant reduction in induced downwash illustrated in Figure 7.22. Flowfield slices along the blade highlight the vortex location and strength using vorticity magnitude contours and illustrate the effects of the vortex on the velocity field using overlaid velocity vectors (Fig. 7.23). From $\psi = 250°$-$\psi = 260°$, a weaker vortex has minimal effects on the overall flowfield and corresponds to four-bladed airloads that only differ slightly from one-bladed airloads, indicating minimal BVI influence.

Similar to the advancing blade, the highest BVI influence on the retreating blade is noticed closest to the vortex impingement location. At $\psi = 270$ the velocity vectors in Figure 7.23

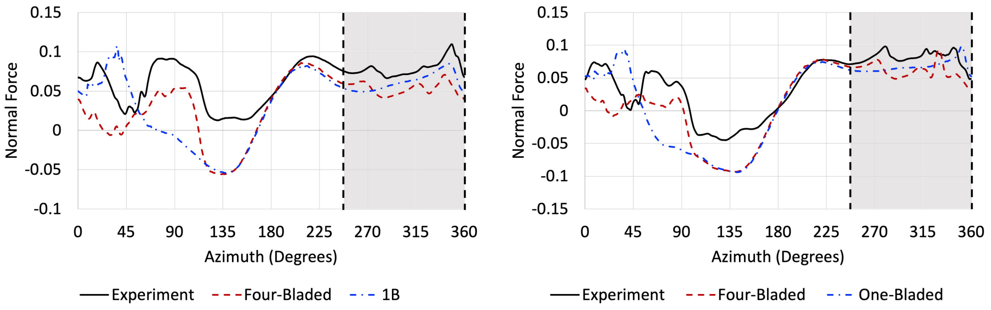

(a) $r/R = 0.775$ (b) $r/R = 0.865$

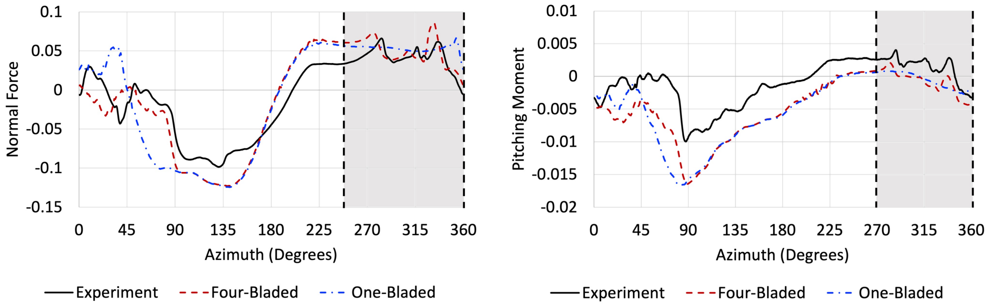

(c) $r/R = 0.920$ (d) $r/R = 0.965$

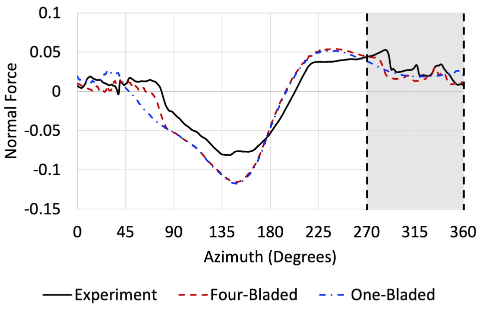

(e) $r/R = 0.990$

Figure 7.19: BVI signatures in normal force predictions on retreating blade for $C_T/\sigma = 0.040$

indicate a portion of the blade is dominated by the presence of the vortex, located at 80%R. The radial station closest to impingement at 270° ($r/R = 0.775$), experiences lift and moment peaks within the BVI signature at $\psi = 270°$ and $\psi = 267°$, respectively. As the blade advances from $\psi = 270°$ to $\psi = 280°$, the $r/R = 0.865$ station experiences lift and moment peaks at $\psi = 276°$ and $\psi = 275°$ as the vortex moves outboard with increasing azimuth. Near $\psi = 280°$ where vortex impingement is at 94%R, both $r/R = 0.920$ and $r/R = 0.960$ stations exhibit lift and moment peaks. As the blade advances past 280° and vortex impingement location moves beyond the blade tip, the $r/R = 0.990$ stations experiences lift and moment peaks at $\psi = 284°$ and $\psi = 288°$,

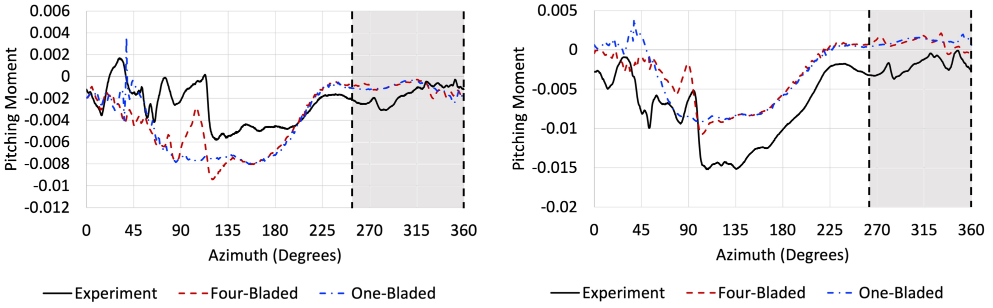

(a) $r/R = 0.775$ (b) $r/R = 0.865$

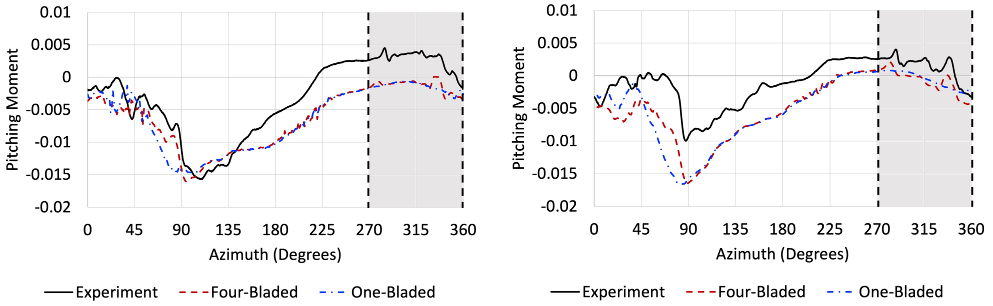

(c) $r/R = 0.920$ (d) $r/R = 0.965$

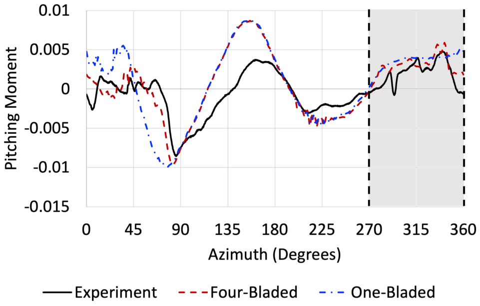

(e) $r/R = 0.990$

Figure 7.20: BVI signatures in pitching moment predictions on retreating blade for $C_T/\sigma = 0.040$

respectively.

At $\psi = 300°$, the trailing tip vortex from the previous pass has minimal influence on the retreating blade, as demonstrated by Figure 7.24. Beyond $\psi = 300°$, the trailing vortex sheet begins to dominate the flowfield as demonstrated by the flowfield along the blade at $\psi = 310°$ (Fig. 7.25).

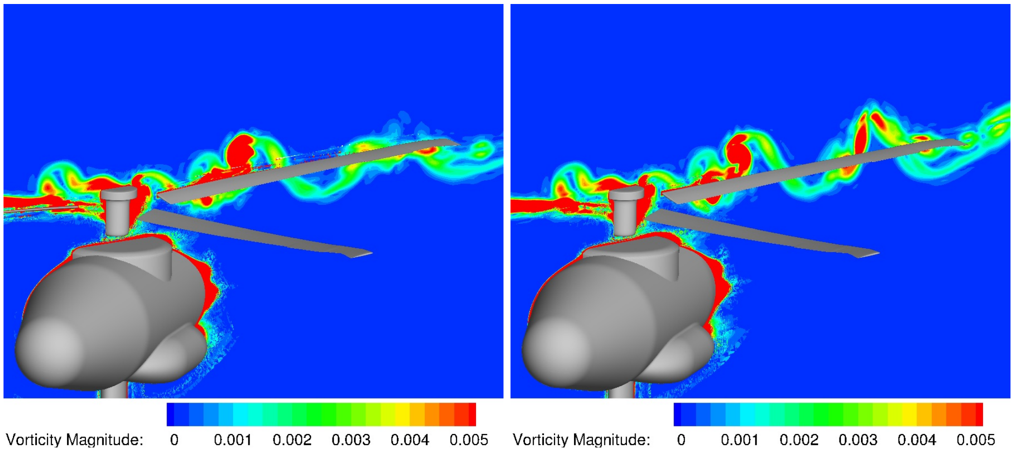

(a) $+0°$ from blade (b) $+5°$ from blade

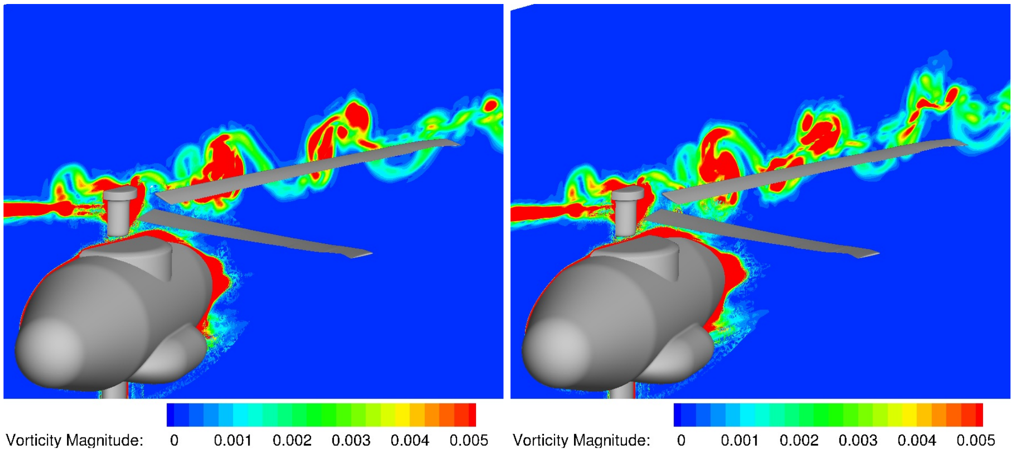

(c) $+10°$ from blade (d) $+15°$ from blade

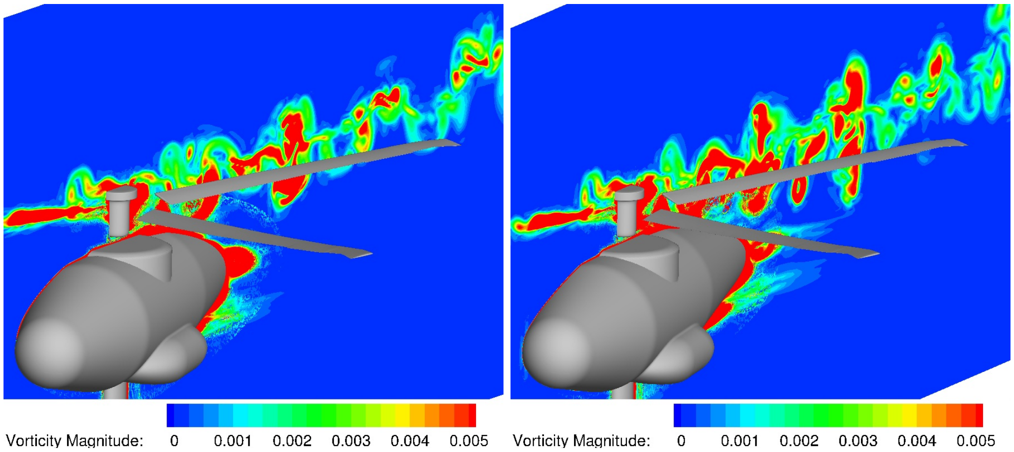

(e) $+20°$ from blade (f) $+25°$ from blade

Figure 7.21: Vorticity slices along tip vortex impinging on blade at $\psi = 300°$

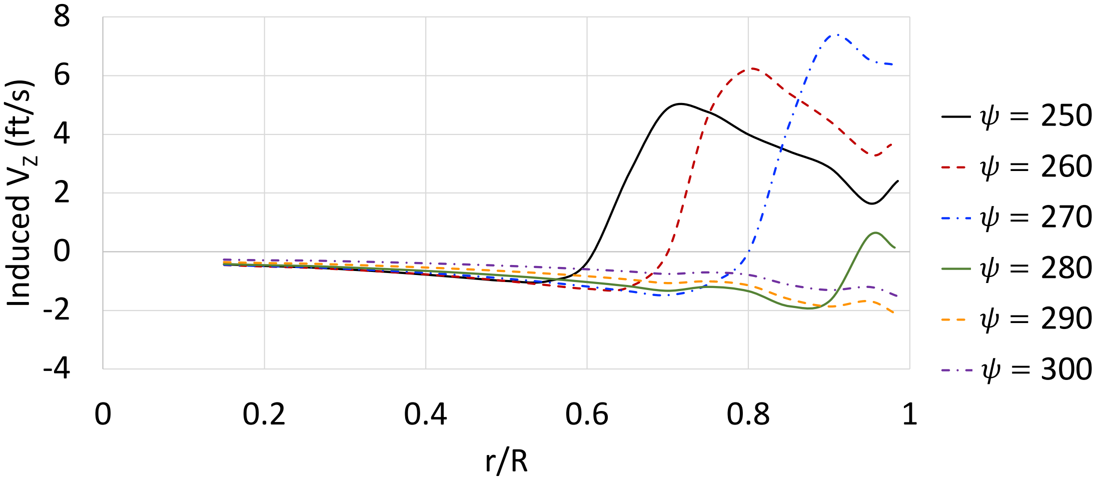

Figure 7.22: Induced vertical velocity distributions along blade span from $\psi = 250°$ to $\psi = 300°$

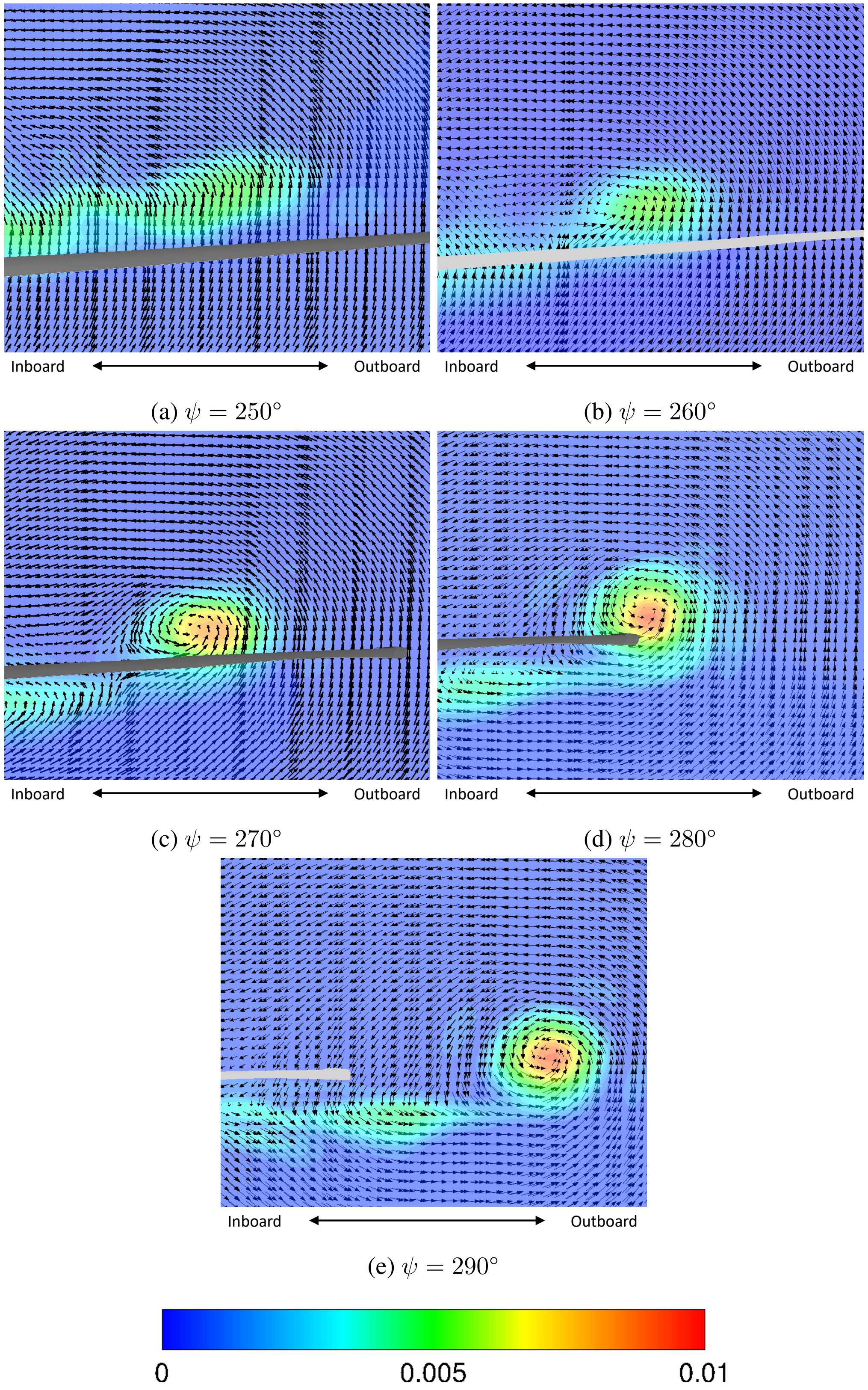

(a) $\psi = 250°$

(b) $\psi = 260°$

(c) $\psi = 270°$

(d) $\psi = 280°$

(e) $\psi = 290°$

Figure 7.23: Flowfield around impinging vector at from $\psi = 250°$ to $\psi = 290°$

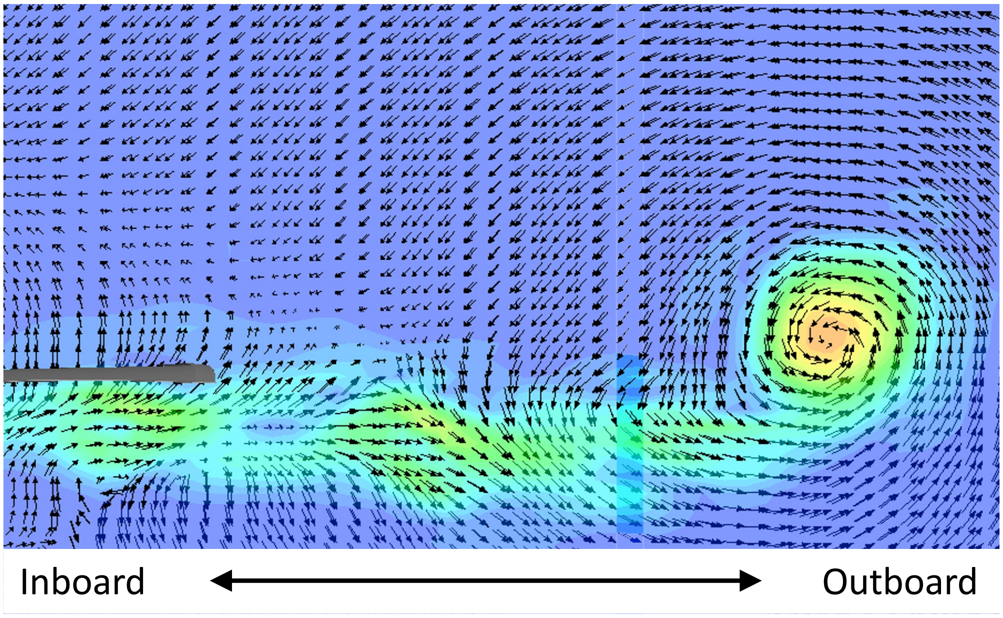

(a) $\psi = 280°$

Figure 7.24: Flowfield around impinging vector at $\psi = 300°$

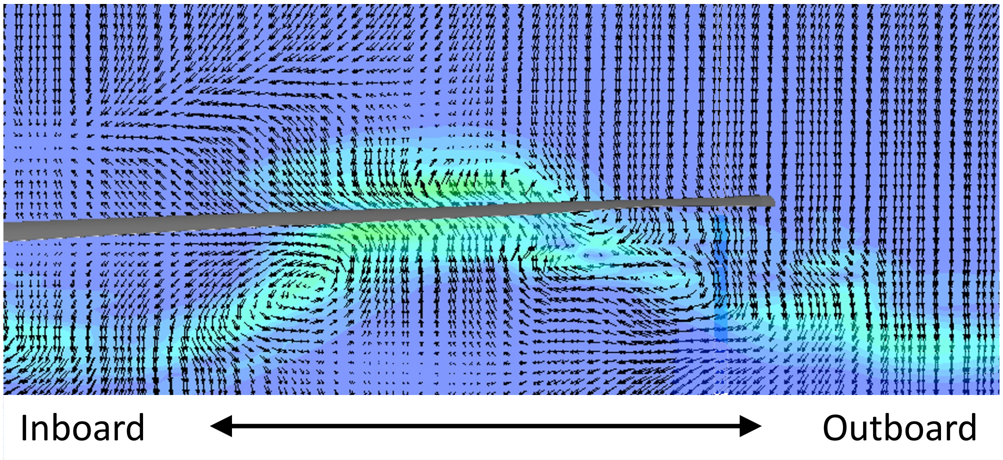

(a) $\psi = 280°$

Figure 7.25: Flowfield around impinging vector at $\psi = 310°$

CHAPTER 8

CONCLUSIONS

This dissertation advances the state-of-the-art of high-fidelity CFD applications to separated flows on three-dimensional rotors. These advances answer critical questions for future applications and are summarized here:

Thesis Goal 1: To identify and quantify capabilities and limitations of the state-of-the-art CFD modeling approach for capturing massively separated flows on three-dimensional rotors

- **Is radial grid density important in capturing separated flow?**
  Grid generation techniques for finite wing and rotating blade dynamic stall analyses have largely been based on infinite wing grid generation techniques, where spanwise or radial spacing is quite large. Improvements to grids often focused on normal and chordwise refinement without considering the effects of large aspect ratios on solution refinement and accuracy. An extensive finite wing structured grid refinement study, performed to assess the effects of both chordwise and spanwise/radial refinement, found that both chordwise and spanwise/radial spacing is important to achieve accurate separation prediction. Additionally, best results are achieved when chordwise and spanwise/radial spacing are compatible to minimize mid-chord aspect ratios as well as spanwise aspect ratio gradients. These parameters are then applied to generate an optimized rotor blade grid. Results are obtained using the optimized rotor blade grid as well as a baseline rotor blade grid, based on infinite wing grid generation techniques. The baseline grid behaves similarly to a two-dimensional simulation, where flow features causing separation on the inboard blade do not experience radial relief due to grid coarseness, resulting in stronger separation over a smaller region. When increased radial refinement is considered via the optimized grid, three-dimensional relief effects are realized and a larger, weaker separation region is predicted on the rotor

plane.

- **Can radial spacing be quantified for general use?**

  Findings from this grid study are generalized so that they can be applied to other finite wing and rotor blades geometries using general parameters and distributions. Chordwise connectors should be dimensioned to 500 points with leading and trailing edge spacings of 0.04% and 0.01% chord, respectively, with a hyperbolic distribution to achieve equivalent mesh parameters along the characteristic length. In the spanwise direction, root and tip spacing should be chosen to accurately capture the geometry. Using a hyperbolic distribution, the spanwise connector dimension should be chosen to minimize mid-chord aspect ratio at the mid-span.

- **Which popular turbulence models most accurately capture separated flows when applied within the same flow solver on the same grid?** A turbulence model study was performed on a finite wing in various pre-stall, stall, and post-stall configurations. Results from this study demonstrated that the SA DDES and $k\omega$-SST DDES models most accurately predicted airloads consistently across all three regimes. The $k\omega$-SST RANS model did not predict airload magnitudes as accurately as the hybrid URANS-LES methods at post-stall angles of attack; however, it did accurately predict the onset of separation. The SA-RANS model failed to accurately capture separated flows for stall and post stall angles of attack. Rotorcraft experience all three regimes throughout a single rotor revolution with additional complexities from BVI and rotational effects. Only the hybrid URANS-LES models and the $k\omega$-SST RANS were utilized in the rotor simulations. All three turbulence models were found to be sufficient to capture light, moderate, and deep stall on as sufficiently refined grid. Across all test points, the SA-DDES model requires on average 7760 core-hours per quarter revolution on the HPCMP SGI ICE XA Centennial machine compared to 15,600 core-hours per quarter revolution using the $k\omega$-SST models. The SA-DDES model requires approximately 50% of the computational time required by the $k\omega$-SST models. Due to cost savings without loss of accuracy, the SA-DDES model is the preferred model for analysis.

- **Are there coupled effects between grid refinement and turbulence model in separated flow regimes?** Use of a higher-fidelity turbulence model is often leveraged in hopes of achieving a more accurate solution. Finite wing analysis demonstrated that turbulence model does play an important role in prediction accuracy but only when grids were sufficiently refined. The coupled effects of grid refinement and turbulence model were studied on the UH-60A configuration. When URANS and hybrid URANS-LES models were evaluated on the baseline grid, airloads data and separation predictions were equivalent across all solvers, indicating grid refinement was not sufficient for a DDES turbulence model, causing DDES to essentially revert to a URANS solution. With the optimized grid, the DDES simulations yielded different results. This indicates that the grid has been refined sufficiently to support the smallest scales of interest in separated flow and the hybrid URANS-LES simulation is not reduced to a standard URANS model.

- **How important are aeroelastic effects in capturing separated flows?**
  Full-scale rotors are highly elastic structures subjected to intense, repeated loading. Accurate CFD analyses must consider blade motion and deformation that occurs throughout a rotor revolution to achieve accurate predictions. Two coupled CFD-CSD simulations were performed with equivalent trim parameters, one on a four-bladed rotor and one on a one-bladed rotor. Even with equivalent trim parameters, the predicted blade deformation and airloads were significantly different, highlighting the importance of accurate inclusion of aeroelastic effects.

- **What bias, if any, is introduced when prescribed motions are applied versus coupled CFD-CSD?**
  Rotor blade motion and deformation can be accounted for in two different ways for an aeroelastic rotor: prescribed motion and coupled CFD-CSD. Prescribed motion is a simpler and faster approach than coupled CFD-CSD. However, the most robust aeroelastic approach is

a coupled CFD-CSD approach using a sufficiently refined grid. The refined grid produces a flowfield that more accurately depicts the strength and location of important physical features than a coarse grid. Resolving those physical features with a refined grid permits highly accurate rotor airloads to be used when coupled with a CSD solver. The resulting blade motion and deformation values can not be achieved with a coarse grid. When motions are prescribed from a coarse grid simulation, the resulting flowfield can be accurately resolved, however blade motions are still based on a less robust flowfield. Capturing the coupling between a flowfield and blade deformations eliminates any bias that may be introduced via prescribed motions.

Thesis Goal 2: To advance the knowledge of the physics of separated flows on rotors using a combination of state-of-the-art CFD modeling and high-quality experimental data

- **How can classic dynamic stall be isolated from BVI and other mechanisms of separation on a rotating system?**

  Traditionally, the term “dynamic stall” referred only to “classic dynamic stall” where the vortex formation is a product of lifting surface kinematics. Recently, however, research has shown that some dynamic stall events may have a BVI mechanism. In order to classify the dynamic stall mechanism, it is required to decouple blade motion from BVI. Prescribed motion and coupled CFD-CSD approaches, both taking advantage of a computationally configured equivalent one-bladed rotor, are investigated. For the prescribed motion case, a baseline four-bladed loosely coupled CFD-CSD simulation is performed to match flight test conditions conducive to dynamic stall. Then the rotor is computationally configured to run with only one blade while blade motion and deformation are prescribed to match motion and deformation from the four-bladed CFD-CSD results. The result is a blade permitted to advance through a mostly clean flowfield, decoupling blade motions from BVI. For the coupled CFD-CSD case, a one-bladed simulation is performed, trimming the rotor to 25% of the total four-bladed thrust. The sectional forces and moments exhibit significantly different behavior at all radial stations than the same quantities from the four-bladed simulation, suggesting blade motions between the two simulations are fundamentally different. Blade deformation data are then examined at eight equally spaced radial stations and compared betweeen the one-bladed and four-bladed simulations. All six translational and rotational deformation quantities are significantly different between the one-bladed and four-bladed runs. This proves the two simulations model fundamentally different flight scenarios and that a coupled CFD-CSD simulation is not an accurate method to isolate blade motion from BVI.

- **Can flowfield data from CFD simulations be used to classify flow separation mechanisms on a rotating system?**

  Separated flow is identified on the rotor plane when the tangential component of skin friction is negative. Once regions of separation are identified, they can be classified using several approaches. A baseline method requires visual inspection of Q-criterion isosurfaces colored by vorticity magnitude, which highlight trailing tip vortices. As the rotor completes a revolution, the rotor blades pass through remnant vortices shed from the previous blade pass. The rotor blade can be visually tracked throughout a rotor revolution and impingement of tip vortices on the blade can be used to identify possible BVI-induced flow separation. Once potential BVI-induced separation is identified, a more robust approach is used to verify findings by isolating rotor blade motion from BVI via a prescribed motion one-bladed simulation. Differences in airloads data between the one- and four-bladed simulations with equivalent blade motions emerge as BVI signatures and permit classification of separation regions based on separation mechanism.

- **How do isolation methods affect rotor downwash, and what is effect does that have on airloads predictions?**

  There is some concern that one-bladed airload predictions may be inflated due to reduced rotor downwash. Significant differences in downwash could create higher induced angles of attack throughout the rotor revolution. Even in the absence of dominant flow features, the increased angles of attack could alter lift and moment data. To address these concerns, downwash and its effect on load prediction is compared between one-bladed and four-bladed simulations for both a light and deep stall case. Results show that the downwash differential between four-bladed and one-bladed simulations does not have a direct impact on airloads predictions. The only noticeable impact occurs between $\psi = 0°$ and $\psi = 90°$, where reduced downwash serves to further isolate blade motions from flowfield interactions by preventing downward convection of tip vortex remnants.

Thesis Goal 3: To explore the application of the Biot-Savart Law to the entire rotor plane to evaluate the effects of trailing tip vortices on the rotor plane aerodynamics

- **Can the Biot-Savart Law be applied to accurately predict induced velocities in a complex rotor plane?** The Biot-Savart Law predicts induced velocities at a point due to a vortex filament by integrating over the entire length of the filament. CFD provides entire flowfield data where vortex filaments can be identified and tracked throughout an entire rotor revolution, providing aerodynamicists with sufficient data to use the Biot-Savart Law on real data. Trailing tip vortices from a previous blade pass are tracked visually throughout the rotor plane using Q-criterion isocontours. For a single azimuth station, quantities required for the Biot-Savart integral are extracted along the vortex filament for integration. The induced velocity predictions from the Biot-Savart Law are identified in flowfield data. Due to the coalescence of trailing tip vortices with the hub and rotor wake, application of the Biot-Savart Law to the rotor plane is limited to azimuth stations between $\psi = 30°$ and $\psi = 330°$

- **What modifications, if any, are required to apply the Biot-Savart Law to a viscous flowfield?**. The Biot-Savart Law is an inviscid, compressible flow theory that gives velocity induced at an arbitrary point P by an infinitesimal vortex filament. Modifications are required to realistically apply the Biot-Savart Law to a rotor plane and take into account some viscous effects. In inviscid flow theory, a vortex filament has constant circulation along its entire length. When viscous effects are included, vorticity will decay as the vortex filament in question convects through air. Additionally, the rotor blade is constantly deforming throughout a rotor revolution, and the strength of the shed vortex changes with that deformation. To take these phenomena into account the circulation is be permitted to vary over the length of each trailing tip vortex filament, requiring circulation calculations via a surface integral at each interval within the Biot-Savart integral. To evaluate the integral along the length of a vortex filament, it is evaluated as a summation along the vortex filament with each step equal to $\psi = 1°$. To realistically apply the summation, finite limits must be determined to bound the summation while still capturing the extents of the impinging vortex filament required to accurately produce downwash. The lower bound is chosen as 0 to include the effects of only current and future impinging vortex filament segments. To determine the appropriate upper bound, the Biot-Savart summation is repeatedly calculated with increasing upper bounds. When the change in calculated induced velocity is less than one percent for all components, the upper bound is considered acceptable.

- **What are the extents of BVI influence over the advancing and retreating rotor blades?** Both advancing and retreating rotor blades encounter BVI due to trailing tip vortices from previous blade passes. The Biot-Savart Law was applied to understand the influence of vortex impingement on the advancing rotor blade. The advancing blade first encouters BVI near the blade tip. As it advances, that impingement location moves inboard along the blade, serving as a dynamic source of induced velocity on the blade. The vortex produces upwash on the inboard blade and downwash on outboard blade, with the maximum influence at 1.5% inboard of the vortex core location. BVI signatures are present in airloads data, however it does not result in separation on the advancing blade. As the blade retreats, the vortex impingement location moves outboard along the blade, inducing inboard downwash and outboard upwash. In high thrust conditions, these induced velocities can trigger stall event. Eventually, the blade retreats to the point where the there is no direct impingement. One the vortex location exceeds 110%R, induced velocity effects are negligible.

- **Can induced velocities at a point on the rotor, predicted by the Biot-Savart Law applied**

to trailing tip vortex filaments, help predict flow separation on the rotor?. Induced velocities due to the presence of an impinging vortex are the mechanism that causes separated flow on portions of the rotor. With increasing thrust, the trailing tip vortices become stronger and associated induced velocities have a more dominant effect on the flowfield. With additional data points, induced velocity distributions along the blade can be used to determined where flow is separated.

The following are suggestions for future work for continued advancement in this area:

- In this thesis, an intensive grid refinement study was performed to develop structured grid generation best-practices for application in pre-stall, stall, and post-stall conditions. Similar refinement studies should be performed on finite wings/rotor blades to develop unstructured meshing requirements for separated flows.
- Comparisons are often drawn between results from unstructured solvers using second-order spatial differencing and structured solvers using sixth-order spatial differencing. Differences in predictions are attributed to the differing numerical schemes, but those claims are typically not verified and could be due to other factors. Direct comparisons between second-order structured and second-order unstructured results are necessary to identify differences between structured and unstructured formulations, not numerical schemes. This will also serve to guide future unstructured numerical scheme development.
- Qualitative comparisons are often drawn between CFD and experimental data using normal force and pitching moment plots. When plotting, experimental data sets are typically displayed as a single line achieved by averaging airloads over many rotor revolutions. Cycle-to-cycle variations exist in those data and often that information is not expressed. Similarly, cycle-to-cycle variations occur in CFD simulations, but a single converged revolution is typically used for plotting. To further understand the root cause of differences between experimental and CFD data, which can inform future CFD development, quantification of

CFD error as well as cycle-to-cycle variations in both CFD and experiment using frequency analysis is required.

- Solution refinement was only investigated in terms of grid refinement. Time step refinement was not addressed. Finite pitching wing simulations require approximately 18,000 timesteps per pitching cycle to accurately capture dynamic stall (Ref. [25]), nearly an order of magnitude more timesteps than standard practice rotor simulations which typically set the timestep equal to $0.25°$, or 1440 timesteps per revolution. Using the newly refined grid parameters developed in this thesis, state-of-the-art timestep requirements for rotors in separated flows should be reassessed.
- Computational advancements over the past decaade have permitted evaluation of separated flows on finite wings and three-dimensional single rotors. With those evaluations complete, the next step to continue advancement in this area is to consider multi-rotor configurations.
- As separated flow in the rotor plane continues to be studied, one-bladed prescribed motion simulations should become standard practice in addition to four-bladed simulations to classify separated flow on the rotor plane. Knowledge of separation mechanism will be crucial as more advanced configurations are investigated.
- The Biot-Savart Law was applied to a single geometry over one experimental thrust sweep in this thesis to demonstrate the methodology and type of data it can produce. To develop a more robust relationship between induced velocity predictions and separated flows, the Biot-Savart Law should be applied to a range of geometries and flight conditions throughout the rotor plane.
- To apply the Biot-Savart Law across multiple geometries and flight conditions, it needs to be a more efficient automated process. Currently, the vortex is visually tracked and data is manually extracted for each integration segment. Automation of integration along the vortex filament would significantly speed up the process. Additionally, in this study the circulation

integral at each vortex filament segment was calculated 14 times with increasing radius to determine the appropriate integration bounds for completeness. Establishing best-practices for determining those circulation integration bounds could also significantly speed up the calculation process.

- Induced velocity predictions using the Biot-Savart Law, coupled with a tip vortex model, has the potential to fill a gap in current rotorcraft prediction capabilities. A reduced order model, using findings from this study, could help predict separated flow in the design phase without the use of CFD. This would permit separated flow prediction, along with any associated aeromechanics problems, early in the design phase for multiple configurations.

Appendices

APPENDIX A

FINITE WING DATA

A.1 OA-209 Lift Variation with Chordwise Refinement

Table A.1: 200 spanwise points, varying chordwise refinement, SA RANS Turbulence Model

Angle of Attack	r/R=0.5	r/R=0.8	r/R=0.95	r/R=0.99
10°	0.02%	0.01%	0.02%	0.02%
15°	0.05%	0.02%	0.04%	0.13%
20°	0.09%	0.04%	0.09%	0.18%
21°	0.59%	0.54%	0.65%	1.02%
22°	0.47%	1.25%	0.55%	0.93%

Table A.2: 400 spanwise points, varying chordwise refinement, SA RANS Turbulence Model

Angle of Attack	r/R=0.5	r/R=0.8	r/R=0.95	r/R=0.99
10°	0.03%	0.02%	0.03%	0.11%
15°	0.05%	0.03%	0.08%	0.44%
20°	0.18%	0.08%	0.18%	0.65%
21°	0.49%	0.34%	0.35%	0.84%
22°	0.59%	1.54%	0.64%	0.94%

Table A.3: 800 spanwise points, varying chordwise refinement, SA RANS Turbulence Model

Angle of Attack	r/R=0.5	r/R=0.8	r/R=0.95	r/R=0.99
10°	0.01%	0.01%	0.02%	0.12%
15°	0.02%	0.01%	0.06%	0.46%
20°	0.11%	0.05%	0.16%	0.67%
21°	0.20%	0.05%	0.04%	0.57%
22°	0.27%	0.96%	0.40%	1.02%

Table A.4: 200 spanwise points, varying chordwise refinement, SA DDES Turbulence Model

Angle of Attack	r/R=0.5	r/R=0.8	r/R=0.95	r/R=0.99
10°	0.11%	0.05%	0.05%	0.27%
15°	0.21%	0.11%	0.11%	0.92%
20°	0.06%	0.04%	0.19%	1.35%
21°	4.16%	4.37%	2.64%	3.95%
22°	4.21%	9.09%	4.48%	6.78%

Table A.5: 400 spanwise points, varying chordwise refinement, SA DDES Turbulence Model

Angle of Attack	r/R=0.5	r/R=0.8	r/R=0.95	r/R=0.99
10°	0.09%	0.05%	0.04%	0.63%
15°	0.04%	0.03%	0.07%	1.45%
20°	1.57%	0.48%	0.31%	2.55%
21°	4.00%	4.29%	2.46%	4.12%
22°	3.28%	8.41%	4.25%	6.55%

Table A.6: 800 spanwise points, varying chordwise refinement, SA DDES Turbulence Model

Angle of Attack	r/R=0.5	r/R=0.8	r/R=0.95	r/R=0.99
10°	0.25%	0.11%	0.09%	0.53%
15°	0.10%	0.06%	0.02%	1.02%
20°	15.22%	4.21%	3.63%	5.70%
21°	1.35%	0.67%	0.50%	1.87%
22°	1.58%	0.94%	0.66%	2.06%

Table A.7: 200 spanwise points, varying chordwise refinement, $k\omega$-SST RANS Turbulence Model

Angle of Attack	r/R=0.5	r/R=0.8	r/R=0.95	r/R=0.99
10°	0.03%	0.01%	0.03%	0.08%
15°	0.07%	0.03%	0.09%	0.27%
20°	1.26%	1.75%	0.90%	1.39%
21°	3.03%	2.61%	0.97%	1.57%
22°	0.26%	1.88%	0.94%	1.42%

Table A.8: 400 spanwise points, varying chordwise refinement, $k\omega$-SST RANS Turbulence Model

Angle of Attack	r/R=0.5	r/R=0.8	r/R=0.95	r/R=0.99
10°	0.05%	0.03%	0.03%	0.17%
15°	0.09%	0.06%	0.11%	0.39%
20°	1.49%	1.03%	0.81%	0.74%
21°	1.63%	1.37%	0.73%	0.42%
22°	0.34%	7.72%	3.71%	5.72%

Table A.9: 800 spanwise points, varying chordwise refinement, $k\omega$-SST RANS Turbulence Model

Angle of Attack	r/R=0.5	r/R=0.8	r/R=0.95	r/R=0.99
10°	0.03%	0.02%	0.02%	0.17%
15°	0.06%	0.04%	0.09%	0.36%
20°	1.67%	0.72%	0.18%	1.06%
21°	0.13%	1.10%	0.57%	0.04%
22°	0.16%	1.19%	0.57%	0.68%

Table A.10: 200 spanwise points, varying chordwise refinement, $k\omega$-SST DDES Turbulence Model

Angle of Attack	r/R=0.5	r/R=0.8	r/R=0.95	r/R=0.99
10°	0.62%	0.30%	0.25%	0.26%
15°	0.11%	0.06%	0.07%	0.37%
20°	8.75%	5.87%	3.76%	5.32%
21°	2.01%	3.84%	1.76%	2.41%
22°	1.27%	1.42%	0.57%	0.83%

Table A.11: 400 spanwise points, varying chordwise refinement, $k\omega$-SST DDES Turbulence Model

Angle of Attack	r/R=0.5	r/R=0.8	r/R=0.95	r/R=0.99
10°	0.41%	0.19%	0.14%	0.29%
15°	0.20%	0.10%	0.13%	0.44%
20°	2.08%	3.66%	1.35%	2.19%
21°	3.37%	10.17%	4.15%	6.50%
22°	0.89%	1.54%	0.68%	0.47%

Table A.12: 800 spanwise points, varying chordwise refinement, $k\omega$-SST DDES Turbulence Model

Angle of Attack	r/R=0.5	r/R=0.8	r/R=0.95	r/R=0.99
10°	0.13%	0.06%	0.04%	0.21%
15°	0.11%	0.07%	0.12%	0.32%
20°	1.39%	2.15%	1.02%	0.94%
21°	1.20%	4.11%	1.52%	1.53%
22°	1.34%	3.28%	1.59%	1.21%

A.2 OA-209 Moment Variation with Chordwise Refinement

Table A.13: 200 spanwise points, varying chordwise refinement, SA-RANS Turbulence Model

Angle of Attack	r/R=0.5	r/R=0.8	r/R=0.95	r/R=0.99
10°	0.11%	0.05%	0.07%	0.01%
15°	0.13%	0.06%	0.21%	0.13%
20°	0.14%	0.09%	0.36%	0.06%
21°	0.40%	11.80%	0.09%	0.78%
22°	1.09%	10.01%	1.13%	0.57%

Table A.14: 400 spanwise points, varying chordwise refinement, SA-RANS Turbulence Model

Angle of Attack	r/R=0.5	r/R=0.8	r/R=0.95	r/R=0.99
10°	0.11%	0.05%	0.21%	0.14%
15°	0.13%	0.07%	0.60%	0.60%
20°	0.12%	0.09%	1.19%	0.62%
21°	2.33%	5.55%	0.73%	0.66%
22°	2.80%	6.79%	1.00%	0.86%

Table A.15: 800 spanwise points, varying chordwise refinement, SA-RANS Turbulence Model

Angle of Attack	r/R=0.5	r/R=0.8	r/R=0.95	r/R=0.99
10°	0.07%	0.06%	0.07%	0.16%
15°	0.07%	0.08%	0.45%	0.60%
20°	0.13%	0.08%	1.09%	0.61%
21°	1.37%	1.50%	0.66%	0.37%
22°	0.47%	5.81%	0.81%	0.67%

Table A.16: 200 spanwise points, varying chordwise refinement, SA-DDES Turbulence Model

Angle of Attack	r/R=0.5	r/R=0.8	r/R=0.95	r/R=0.99
10°	0.04%	1.38%	0.13%	0.60%
15°	0.06%	1.62%	0.47%	1.79%
20°	0.10%	0.09%	1.46%	2.49%
21°	11.21%	7.93%	3.90%	4.94%
22°	13.64%	12.98%	2.38%	7.86%

Table A.17: 400 spanwise points, varying chordwise refinement, SA-DDES Turbulence Model

Angle of Attack	r/R=0.5	r/R=0.8	r/R=0.95	r/R=0.99
10°	0.04%	0.06%	0.21%	1.29%
15°	0.13%	0.10%	0.91%	2.92%
20°	0.59%	0.60%	1.91%	4.47%
21°	6.85%	5.02%	3.36%	5.27%
22°	13.04%	6.99%	2.71%	7.85%

Table A.18: 800 spanwise points, varying chordwise refinement, SA-DDES Turbulence Model

Angle of Attack	r/R=0.5	r/R=0.8	r/R=0.95	r/R=0.99
10°	0.06%	0.20%	0.20%	0.99%
15°	0.45%	0.39%	0.45%	1.93%
20°	46.04%	15.67%	4.84%	6.51%
21°	3.88%	25.88%	3.35%	1.73%
22°	0.61%	18.39%	6.53%	1.35%

Table A.19: 200 spanwise points, varying chordwise refinement, $k\omega$-SST RANS Turbulence Model

Angle of Attack	r/R=0.5	r/R=0.8	r/R=0.95	r/R=0.99
10°	0.10%	1.54%	0.14%	0.10%
15°	0.02%	1.80%	0.46%	0.41%
20°	2.97%	10.60%	1.28%	1.38%
21°	3.31%	4.38%	2.31%	1.54%
22°	0.25%	9.91%	0.52%	1.73%

Table A.20: 400 spanwise points, varying chordwise refinement, $k\omega$-SST RANS Turbulence Model

Angle of Attack	r/R=0.5	r/R=0.8	r/R=0.95	r/R=0.99
10°	0.18%	0.07%	0.25%	0.24%
15°	0.31%	0.13%	0.82%	0.52%
20°	1.82%	6.44%	1.69%	0.70%
21°	2.15%	1.64%	0.87%	0.38%
22°	1.73%	8.79%	2.50%	6.50%

Table A.21: 800 spanwise points, varying chordwise refinement, $k\omega$-SST RANS Turbulence Model

Angle of Attack	r/R=0.5	r/R=0.8	r/R=0.95	r/R=0.99
10°	0.06%	0.05%	0.10%	0.23%
15°	0.11%	0.08%	0.58%	0.41%
20°	2.76%	5.76%	1.34%	1.11%
21°	0.69%	12.01%	3.18%	0.36%
22°	0.32%	2.23%	0.67%	0.74%

Table A.22: 200 spanwise points, varying chordwise refinement
$k\omega$-SST DDES Turbulence Model

Angle of Attack	r/R=0.5	r/R=0.8	r/R=0.95	r/R=0.99
10°	0.22%	0.12%	0.35%	0.26%
15°	0.02%	0.09%	0.35%	0.56%
20°	14.02%	9.36%	4.45%	5.72%
21°	11.41%	11.34%	5.37%	4.26%
22°	4.27%	5.88%	2.74%	1.38%

Table A.23: 400 spanwise points, varying chordwise refinement
$k\omega$-SST DDES Turbulence Model

Angle of Attack	r/R=0.5	r/R=0.8	r/R=0.95	r/R=0.99
10°	0.27%	0.10%	0.25%	0.40%
15°	0.15%	0.09%	0.73%	0.64%
20°	17.81%	14.87%	4.34%	3.96%
21°	14.77%	5.30%	2.81%	7.66%
22°	2.11%	10.85%	4.47%	0.85%

Table A.24: 800 spanwise points, varying chordwise refinement
$k\omega$-SST DDES Turbulence Model

Angle of Attack	r/R=0.5	r/R=0.8	r/R=0.95	r/R=0.99
10°	0.12%	0.06%	0.07%	0.27%
15°	0.21%	0.10%	0.51%	0.39%
20°	3.13%	10.44%	2.18%	0.77%
21°	3.62%	7.67%	1.43%	1.45%
22°	2.69%	7.42%	5.18%	2.24%

A.3 OA-209 Lift Variation with Spanwise Refinement

Table A.25: 250 chordwise points, varying spanwise refinement, SA-RANS Turbulence Model

Angle of Attack	r/R=0.5	r/R=0.8	r/R=0.95	r/R=0.99
10°	0.02%	0.07%	0.45%	0.41%
15°	0.04%	0.10%	0.68%	0.87%
20°	0.08%	0.12%	0.89%	1.29%
21°	0.13%	0.08%	0.75%	0.94%
22°	0.49%	1.41%	1.38%	2.01%

Table A.26: 500 chordwise points, varying spanwise refinement, SA-RANS Turbulence Model

Angle of Attack	r/R=0.5	r/R=0.8	r/R=0.95	r/R=0.99
10°	0.03%	0.07%	0.45%	0.46%
15°	0.04%	0.10%	0.67%	1.12%
20°	0.17%	0.14%	0.90%	1.68%
21°	0.30%	0.33%	1.08%	1.31%
22°	0.33%	1.35%	1.28%	2.02%

Table A.27: 1000 chordwise points, varying spanwise refinement, SA-RANS Turbulence Model

Angle of Attack	r/R=0.5	r/R=0.8	r/R=0.95	r/R=0.99
10°	0.02%	0.06%	0.43%	0.49%
15°	0.02%	0.09%	0.65%	1.16%
20°	0.08%	0.08%	0.84%	1.71%
21°	0.48%	0.58%	1.03%	0.77%
22°	0.15%	0.53%	0.59%	1.14%

Table A.28: 250 chordwise points, varying spanwise refinement, SA-DDES Turbulence Model

Angle of Attack	r/R=0.5	r/R=0.8	r/R=0.95	r/R=0.99
10°	0.15%	0.02%	0.40%	0.38%
15°	0.20%	0.17%	0.68%	0.97%
20°	1.17%	0.51%	0.89%	1.63%
21°	2.00%	1.96%	1.12%	2.08%
22°	1.81%	4.28%	1.71%	3.14%

Table A.29: 500 chordwise points, varying spanwise refinement, SA-DDES Turbulence Model

Angle of Attack	r/R=0.5	r/R=0.8	r/R=0.95	r/R=0.99
10°	0.43%	0.16%	0.36%	0.67%
15°	0.41%	0.26%	0.70%	1.60%
20°	17.37%	4.49%	3.40%	5.67%
21°	1.61%	2.57%	1.94%	2.81%
22°	1.58%	3.13%	1.47%	3.77%

Table A.30: 1000 chordwise points, varying spanwise refinement, SA-DDES Turbulence Model

Angle of Attack	r/R=0.5	r/R=0.8	r/R=0.95	r/R=0.99
10°	0.37%	0.15%	0.39%	0.79%
15°	0.15%	0.12%	0.63%	1.69%
20°	17.78%	4.60%	3.49%	4.90%
21°	1.25%	1.93%	1.26%	1.54%
22°	1.26%	4.70%	3.07%	3.57%

Table A.31: 250 chordwise points, varying spanwise refinement
$k\omega$-SST RANS Turbulence Model

Angle of Attack	r/R=0.5	r/R=0.8	r/R=0.95	r/R=0.99
10°	0.04%	0.09%	0.55%	0.74%
15°	0.03%	0.12%	0.83%	1.38%
20°	0.32%	0.57%	1.32%	1.73%
21°	1.43%	3.93%	1.83%	2.48%
22°	0.09%	4.76%	3.36%	5.27%

Table A.32: 500 chordwise points, varying spanwise refinement
$k\omega$-SST RANS Turbulence Model

Angle of Attack	r/R=0.5	r/R=0.8	r/R=0.95	r/R=0.99
10°	0.09%	0.12%	0.56%	0.84%
15°	0.09%	0.15%	0.83%	1.52%
20°	0.58%	1.90%	0.81%	0.06%
21°	2.26%	2.23%	1.58%	1.68%
22°	0.10%	0.87%	1.27%	2.06%

Table A.33: 1000 chordwise points, varying spanwise refinement
$k\omega$-SST RANS Turbulence Model

Angle of Attack	r/R=0.5	r/R=0.8	r/R=0.95	r/R=0.99
10°	0.02%	0.08%	0.52%	0.82%
15°	0.02%	0.10%	0.78%	1.48%
20°	0.57%	0.85%	1.00%	2.11%
21°	2.33%	3.63%	1.65%	1.72%
22°	0.12%	2.87%	0.84%	0.75%

Table A.34: 250 chordwise points, varying spanwise refinement
$k\omega$-SST DDES Turbulence Model

Angle of Attack	r/R=0.5	r/R=0.8	r/R=0.95	r/R=0.99
10°	0.03%	0.07%	0.51%	0.68%
15°	0.21%	0.14%	0.72%	1.30%
20°	7.79%	3.96%	3.27%	5.32%
21°	1.86%	8.11%	2.28%	4.07%
22°	0.67%	2.85%	2.12%	3.24%

Table A.35: 500 chordwise points, varying spanwise refinement
$k\omega$-SST DDES Turbulence Model

Angle of Attack	r/R=0.5	r/R=0.8	r/R=0.95	r/R=0.99
10°	0.81%	0.47%	0.71%	1.06%
15°	0.19%	0.18%	0.75%	1.46%
20°	1.02%	1.97%	1.36%	2.51%
21°	2.61%	6.72%	3.49%	5.78%
22°	1.79%	1.54%	1.71%	2.79%

Table A.36: 1000 chordwise points, varying spanwise refinement
$k\omega$-SST DDES Turbulence Model

Angle of Attack	r/R=0.5	r/R=0.8	r/R=0.95	r/R=0.99
10°	0.19%	0.08%	0.47%	0.74%
15°	0.17%	0.02%	0.67%	1.32%
20°	2.50%	5.04%	2.46%	2.64%
21°	2.51%	7.85%	4.24%	6.37%
22°	1.61%	3.37%	2.17%	3.38%

A.4 OA-209 Moment Variation with Spanwise Refinement

Table A.37: 250 chordwise points, varying spanwise refinement, SA-RANS Turbulence Model

Angle of Attack	r/R=0.5	r/R=0.8	r/R=0.95	r/R=0.99
10°	0.01%	0.02%	0.92%	0.44%
15°	0.01%	0.04%	2.03%	0.98%
20°	0.05%	0.10%	3.27%	1.34%
21°	0.11%	2.07%	2.88%	0.92%
22°	1.86%	9.91%	3.30%	1.92%

Table A.38: 500 chordwise points, varying spanwise refinement SA-RANS Turbulence Model

Angle of Attack	r/R=0.5	r/R=0.8	r/R=0.95	r/R=0.99
10°	0.00%	0.01%	0.98%	0.56%
15°	0.00%	0.03%	2.30%	1.36%
20°	0.10%	0.09%	3.95%	1.78%
21°	1.05%	4.22%	3.37%	1.30%
22°	1.32%	5.82%	3.36%	1.87%

Table A.39: 1000 chordwise points, varying spanwise refinement, SA-RANS Turbulence Model

Angle of Attack	r/R=0.5	r/R=0.8	r/R=0.95	r/R=0.99
10°	0.12%	0.04%	1.00%	0.60%
15°	0.14%	0.06%	2.31%	1.43%
20°	0.24%	0.14%	4.01%	1.84%
21°	2.21%	12.07%	3.60%	0.79%
22°	0.85%	3.20%	2.74%	1.04%

Table A.40: 250 chordwise points, varying spanwise refinement, SA-DDES Turbulence Model

Angle of Attack	r/R=0.5	r/R=0.8	r/R=0.95	r/R=0.99
10°	0.14%	1.39%	0.91%	0.45%
15°	0.29%	1.71%	1.79%	1.16%
20°	3.62%	1.34%	2.47%	1.82%
21°	2.27%	9.47%	2.67%	2.17%
22°	1.30%	19.25%	2.90%	3.13%

Table A.41: 500 chordwise points, varying spanwise refinement, SA-DDES Turbulence Model

Angle of Attack	r/R=0.5	r/R=0.8	r/R=0.95	r/R=0.99
10°	0.05%	0.13%	0.97%	1.16%
15°	0.70%	0.54%	1.94%	2.34%
20°	47.65%	14.06%	5.32%	6.22%
21°	12.98%	25.95%	5.54%	3.30%
22°	6.66%	37.55%	10.48%	2.95%

Table A.42: 1000 chordwise points, varying spanwise refinement, SA-DDES Turbulence Model

Angle of Attack	r/R=0.5	r/R=0.8	r/R=0.95	r/R=0.99
10°	0.09%	0.13%	0.97%	1.27%
15°	0.93%	0.41%	2.13%	2.68%
20°	55.79%	12.25%	6.65%	5.18%
21°	19.23%	27.49%	7.25%	2.85%
22°	19.12%	24.02%	11.31%	5.92%

Table A.43: 250 chordwise points, varying spanwise refinement, $k\omega$-SST RANS Turbulence Model

Angle of Attack	r/R=0.5	r/R=0.8	r/R=0.95	r/R=0.99
10°	0.01%	1.53%	1.16%	1.19%
15°	0.00%	1.73%	2.71%	2.17%
20°	0.42%	2.44%	2.93%	1.93%
21°	3.07%	24.75%	3.95%	2.00%
22°	0.88%	14.15%	4.10%	5.83%

Table A.44: 500 chordwise points, varying spanwise refinement, $k\omega$-SST RANS Turbulence Model

Angle of Attack	r/R=0.5	r/R=0.8	r/R=0.95	r/R=0.99
10°	0.02%	0.06%	1.17%	1.30%
15°	0.11%	0.06%	2.86%	2.23%
20°	1.73%	12.17%	3.14%	0.50%
21°	4.90%	9.01%	1.72%	1.71%
22°	0.53%	1.30%	3.35%	2.13%

Table A.45: 1000 chordwise points, varying spanwise refinement, $k\omega$-SST RANS Turbulence Model

Angle of Attack	r/R=0.5	r/R=0.8	r/R=0.95	r/R=0.99
10°	0.14%	0.05%	1.35%	1.35%
15°	0.23%	0.18%	3.16%	2.28%
20°	1.36%	4.20%	3.30%	2.49%
21°	5.02%	11.62%	0.81%	1.65%
22°	0.98%	3.95%	1.92%	0.96%

Table A.46: 250 chordwise points, varying spanwise refinement, $k\omega$-SST DDES Turbulence Model

Angle of Attack	r/R=0.5	r/R=0.8	r/R=0.95	r/R=0.99
10°	0.03%	0.02%	0.91%	1.07%
15°	0.06%	0.07%	2.01%	1.99%
20°	4.56%	25.13%	2.48%	4.89%
21°	2.27%	3.20%	2.58%	3.73%
22°	0.71%	6.31%	3.06%	4.07%

Table A.47: 500 chordwise points, varying spanwise refinement, $k\omega$-SST DDES Turbulence Model

Angle of Attack	r/R=0.5	r/R=0.8	r/R=0.95	r/R=0.99
10°	0.39%	0.18%	0.54%	1.44%
15°	0.26%	0.15%	2.03%	2.02%
20°	10.81%	22.17%	5.22%	2.49%
21°	10.28%	16.42%	6.42%	5.10%
22°	5.22%	6.74%	5.37%	2.77%

Table A.48: 1000 chordwise points, varying spanwise refinement, $k\omega$-SST DDES Turbulence Model

Angle of Attack	r/R=0.5	r/R=0.8	r/R=0.95	r/R=0.99
10°	0.13%	0.06%	1.11%	1.17%
15°	0.26%	0.13%	2.51%	1.96%
20°	19.19%	17.87%	7.11%	4.32%
21°	18.70%	12.84%	7.39%	7.09%
22°	3.98%	10.56%	2.71%	4.61%

A.5 OA-209 Average and Maximum SDP Values

Table A.49: Maximum SDP of pre-stall sectional lift predictions with varying chordwise refinement

Turbulence Model	r/R=0.5	r/R=0.8	r/R=0.95	r/R=0.99
SA RANS	0.05%	0.03%	0.08%	0.46%
SA DDES	0.25%	0.11%	0.11%	1.45%
$k\omega$-SST RANS	0.09%	0.06%	0.11%	0.39%
$k\omega$-SST DDES	0.62%	0.30%	0.25%	0.44%

Table A.50: Average SDP of pre-stall sectional lift predictions with varying chordwise refinement

Turbulence Model	r/R=0.5	r/R=0.8	r/R=0.95	r/R=0.99
SA RANS	0.03%	0.01%	0.04%	0.21%
SA DDES	0.13%	0.07%	0.06%	0.80%
$k\omega$-SST RANS	0.05%	0.03%	0.06%	0.24%
$k\omega$-SST DDES	0.26%	0.13%	0.12%	0.31%

Table A.51: Maximum SDP of pre-stall sectional moment predictions with varying chordwise refinement.

Turbulence Model	r/R=0.5	r/R=0.8	r/R=0.95	r/R=0.99
SA RANS	0.13%	0.08%	0.60%	0.60%
SA DDES	0.45%	1.62%	0.91%	2.92%
$k\omega$-SST RANS	0.31%	1.80%	0.82%	0.52%
$k\omega$-SST DDES	0.27%	0.12%	0.73%	0.64%

Table A.52: Average SDP of pre-stall sectional moment predictions with varying chordwise refinement.

Turbulence Model	r/R=0.5	r/R=0.8	r/R=0.95	r/R=0.99
SA RANS	0.10%	0.06%	0.27%	0.28%
SA DDES	0.13%	0.62%	0.40%	1.59%
$k\omega$-SST RANS	0.13%	0.61%	0.39%	0.32%
$k\omega$-SST DDES	0.17%	0.09%	0.38%	0.42%

Table A.53: Maximum SDP of pre-stall sectional lift predictions with varying spanwise refinement

Turbulence Model	r/R=0.5	r/R=0.8	r/R=0.95	r/R=0.99
SA RANS	0.04%	0.10%	0.68%	1.16%
SA DDES	0.43%	0.26%	0.70%	1.69%
$k\omega$-SST RANS	0.09%	0.10%	0.78%	1.48%
$k\omega$-SST DDES	0.81%	0.47%	0.75%	1.46%

Table A.54: Average SDP of pre-stall sectional lift predictions with varying spanwise refinement

Turbulence Model	r/R=0.5	r/R=0.8	r/R=0.95	r/R=0.99
SA RANS	0.03%	0.08%	0.56%	0.75%
SA DDES	0.28%	0.14%	0.37%	0.99%
$k\omega$-SST RANS	0.05%	0.05%	0.26%	0.54%
$k\omega$-SST DDES	0.27%	0.16%	0.64%	1.09%

Table A.55: Maximum SDP of pre-stall sectional moment predictions with varying spanwise refinement.

Turbulence Model	r/R=0.5	r/R=0.8	r/R=0.95	r/R=0.99
SA RANS	0.14%	0.06%	2.31%	1.43%
SA DDES	0.93%	1.62%	2.08%	2.68%
$k\omega$-SST RANS	0.31%	1.80%	3.16%	2.28%
$k\omega$-SST DDES	0.39%	0.18%	2.51%	2.02%

Table A.56: Average SDP of pre-stall sectional moment predictions with varying spanwise refinement.

Turbulence Model	r/R=0.5	r/R=0.8	r/R=0.95	r/R=0.99
SA RANS	0.05%	0.03%	1.59%	0.90%
SA DDES	0.31%	0.70%	1.09%	1.64%
$k\omega$-SST RANS	0.16%	0.63%	1.03%	0.82%
$k\omega$-SST DDES	0.19%	0.10%	1.52%	1.61%

Table A.57: Maximum SDP of stall sectional lift predictions with varying chordwise refinement

Turbulence Model	r/R=0.5	r/R=0.8	r/R=0.95	r/R=0.99
SA RANS	0.18%	0.08%	0.18%	0.67%
SA DDES	15.22%	4.21%	3.63%	5.70%
$k\omega$-SST RANS	1.67%	1.75%	0.90%	1.39%
$k\omega$-SST DDES	8.75%	5.87%	3.76%	5.32%

Table A.58: Average SDP of stall sectional lift predictions with varying chordwise refinement

Turbulence Model	r/R=0.5	r/R=0.8	r/R=0.95	r/R=0.99
SA RANS	0.13%	0.06%	0.14%	0.50%
SA DDES	5.62%	1.58%	1.38%	3.20%
$k\omega$-SST RANS	1.47%	1.17%	0.63%	1.06%
$k\omega$-SST DDES	3.65%	3.48%	3.21%	7.59%

Table A.59: Maximum SDP of stall sectional moment predictions with varying chordwise refinement.

Turbulence Model	r/R=0.5	r/R=0.8	r/R=0.95	r/R=0.99
SA RANS	0.14%	0.09%	1.19%	0.62%
SA DDES	46.04%	15.67%	4.84%	6.51%
$k\omega$-SST RANS	2.97%	10.60%	1.69%	1.38%
$k\omega$-SST DDES	17.81%	14.87%	4.45%	5.72%

Table A.60: Average SDP of stall sectional moment predictions with varying chordwise refinement.

Turbulence Model	r/R=0.5	r/R=0.8	r/R=0.95	r/R=0.99
SA RANS	0.13%	0.09%	0.88%	0.43%
SA DDES	15.57%	5.45%	2.74%	4.49%
$k\omega$-SST RANS	2.52%	7.60%	1.44%	1.06%
$k\omega$-SST DDES	11.65%	11.56%	3.65%	3.48%

Table A.61: Maximum SDP of stall sectional lift predictions with varying spanwise refinement

Turbulence Model	r/R=0.5	r/R=0.8	r/R=0.95	r/R=0.99
SA RANS	0.17%	0.14%	0.90%	1.71%
SA DDES	17.78%	4.60%	3.49%	5.67%
$k\omega$-SST RANS	1.49%	1.75%	1.00%	2.11%
$k\omega$-SST DDES	7.79%	5.04%	3.27%	5.32%

Table A.62: Average SDP of stall sectional lift predictions with varying spanwise refinement

Turbulence Model	r/R=0.5	r/R=0.8	r/R=0.95	r/R=0.99
SA RANS	0.11%	0.11%	0.87%	1.56%
SA DDES	11.74%	3.04%	2.36%	3.97%
$k\omega$-SST RANS	1.11%	1.21%	0.90%	1.41%
$k\omega$-SST DDES	3.77%	3.66%	2.37%	3.49%

Table A.63: Maximum SDP of stall sectional moment predictions with varying spanwise refinement.

Turbulence Model	r/R=0.5	r/R=0.8	r/R=0.95	r/R=0.99
SA RANS	0.24%	0.14%	4.01%	1.84%
SA DDES	55.79%	14.06%	6.50%	6.22%
$k\omega$-SST RANS	2.97%	10.60%	3.30%	2.49%
$k\omega$-SST DDES	19.19%	25.13%	7.11%	4.89%

Table A.64: Average SDP of stall sectional moment predictions with varying spanwise refinement.

Turbulence Model	r/R=0.5	r/R=0.8	r/R=0.95	r/R=0.99
SA RANS	0.13%	0.11%	3.74%	1.65%
SA DDES	34.51%	8.80%	4.43%	4.63%
$k\omega$-SST RANS	2.05%	7.08%	2.09%	1.52%
$k\omega$-SST DDES	11.52%	21.72%	4.94%	3.90%

Table A.65: Average SDP of post-stall sectional lift predictions with varying chordwise refinement

Turbulence Model	r/R=0.5	r/R=0.8	r/R=0.95	r/R=0.99
SA RANS	0.59%	1.54%	0.65%	1.02%
SA DDES	4.21%	9.09%	4.48%	6.78%
$k\omega$-SST RANS	3.03%	7.72%	3.71%	5.72%
$k\omega$-SST DDES	3.37%	10.17%	4.15%	6.50%

Table A.66: Average SDP of post-stall sectional lift predictions with varying chordwise refinement

Turbulence Model	r/R=0.5	r/R=0.8	r/R=0.95	r/R=0.99
SA RANS	0.43%	0.78%	0.44%	0.89%
SA DDES	3.10%	4.63%	2.50%	4.22%
$k\omega$-SST RANS	0.92%	2.64%	1.25%	1.64%
$k\omega$-SST DDES	1.68%	4.06%	1.71%	2.16%

Table A.67: Maximum SDP of post-stall sectional moment predictions with varying chordwise refinement.

Turbulence Model	r/R=0.5	r/R=0.8	r/R=0.95	r/R=0.99
SA RANS	2.80%	11.80%	1.13%	0.86%
SA DDES	13.64%	25.88%	6.53%	7.86%
$k\omega$-SST RANS	3.31%	12.01%	3.18%	6.50%
$k\omega$-SST DDES	14.77%	11.34%	5.37%	7.66%

Table A.68: Average SDP of post-stall sectional moment predictions with varying chordwise refinement.

Turbulence Model	r/R=0.5	r/R=0.8	r/R=0.95	r/R=0.99
SA RANS	1.41%	6.91%	0.74%	0.65%
SA DDES	8.21%	12.86%	3.70%	4.84%
$k\omega$-SST RANS	1.41%	6.49%	1.68%	1.87%
$k\omega$-SST DDES	6.48%	8.08%	3.67%	2.97%

Table A.69: Maximum SDP of post-stall sectional lift predictions with varying spanwise refinement

Turbulence Model	r/R=0.5	r/R=0.8	r/R=0.95	r/R=0.99
SA RANS	0.49%	1.41%	1.38%	2.02%
SA DDES	2.00%	4.70%	3.07%	3.77%
$k\omega$-SST RANS	2.33%	4.76%	3.36%	5.27%
$k\omega$-SST DDES	2.61%	8.11%	4.24%	6.37%

Table A.70: Average SDP of post-stall sectional lift predictions with varying spanwise refinement

Turbulence Model	r/R=0.5	r/R=0.8	r/R=0.95	r/R=0.99
SA RANS	0.31%	0.71%	1.02%	1.36%
SA DDES	1.58%	3.09%	1.76%	2.82%
$k\omega$-SST RANS	1.06%	3.05%	1.75%	2.33%
$k\omega$-SST DDES	1.84%	5.07%	2.67%	4.27%

Table A.71: Maximum SDP of post-stall sectional moment predictions with varying spanwise refinement.

Turbulence Model	r/R=0.5	r/R=0.8	r/R=0.95	r/R=0.99
SA RANS	2.21%	12.07%	3.60%	1.92%
SA DDES	19.23%	37.55%	24.22%	5.92%
$k\omega$-SST RANS	5.02%	24.75%	4.10%	5.83%
$k\omega$-SST DDES	18.70%	16.42%	7.39%	7.09%

Table A.72: Average SDP of post-stall sectional moment predictions with varying spanwise refinement.

Turbulence Model	r/R=0.5	r/R=0.8	r/R=0.95	r/R=0.99
SA RANS	1.23%	6.22%	3.21%	1.31%
SA DDES	10.26%	23.32%	9.48%	3.39%
$k\omega$-SST RANS	2.56%	10.80%	2.64%	2.38%
$k\omega$-SST DDES	6.86%	9.34%	4.59%	4.56%

APPENDIX B

ROTOR AIRLOADS DATA

B.1 UH60 Coarse Grid Turbulence Comparison

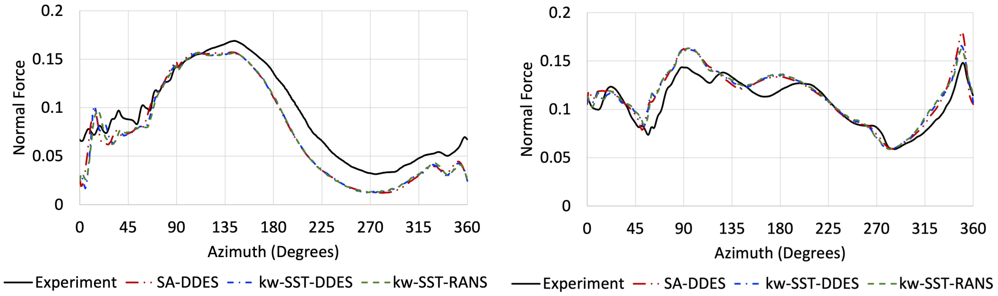

(a) r/R=0.400 (b) r/R=0.675

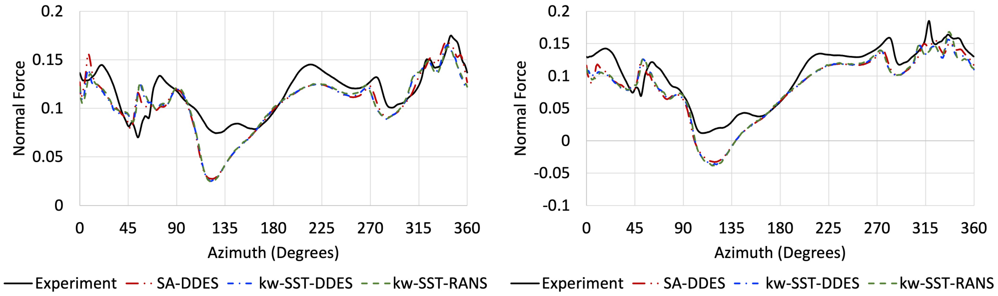

(c) r/R=0.775 (d) r/R=0.865

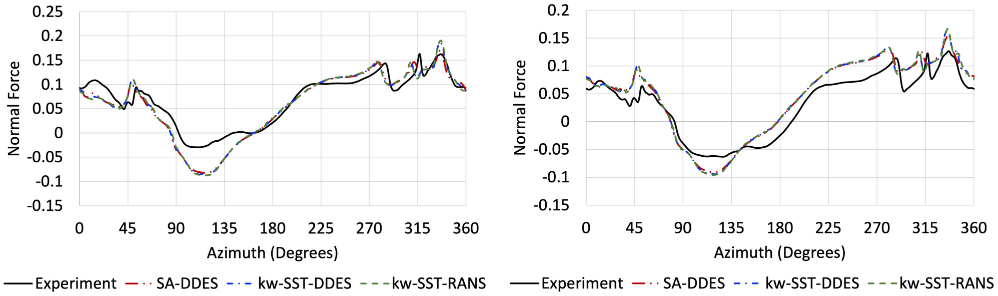

(e) r/R=0.920 (f) r/R=0.965

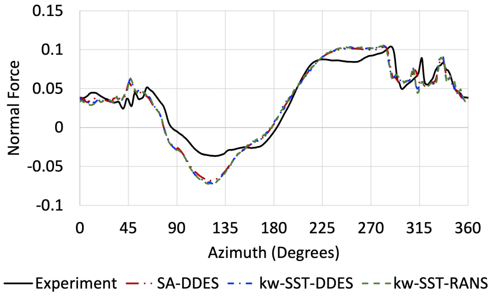

(g) r/R=0.990

Figure B.1: UH-60A normal force at various radial stations for various turbulence models
Test point 4533 ($C_T/\sigma = 0.040$)
Coarse Grid

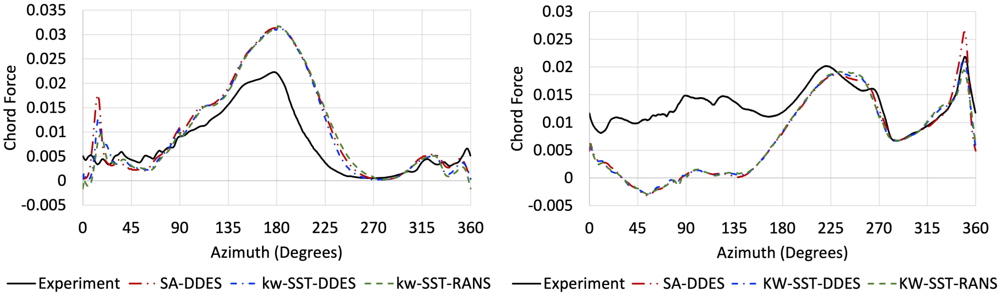

(a) r/R=0.400

(b) r/R=0.675

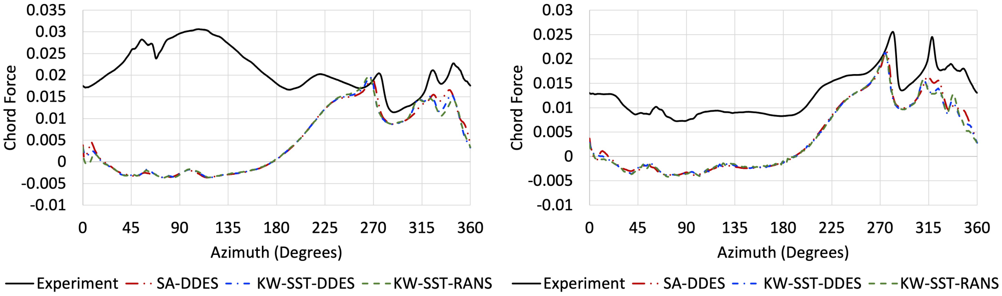

(c) r/R=0.775

(d) r/R=0.865

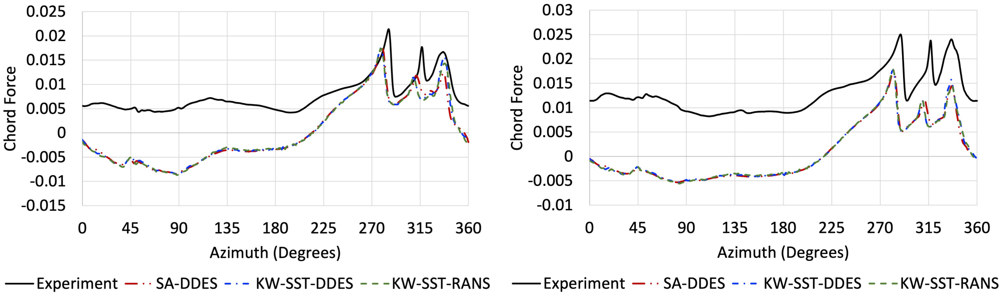

(e) r/R=0.920

(f) r/R=0.965

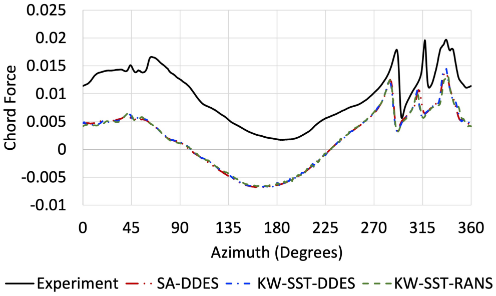

(g) r/R=0.990

Figure B.2: UH-60A chord force at various radial stations for various turbulence models
Test point 4533 ($C_T/\sigma = 0.040$
Coarse Grid

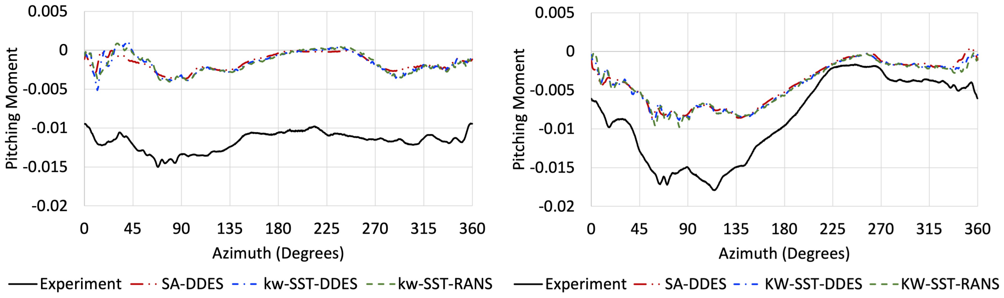

(a) r/R=0.400 (b) r/R=0.675

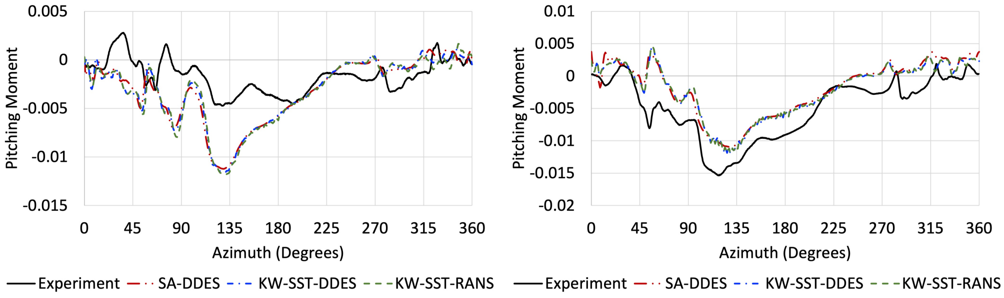

(c) r/R=0.775 (d) r/R=0.865

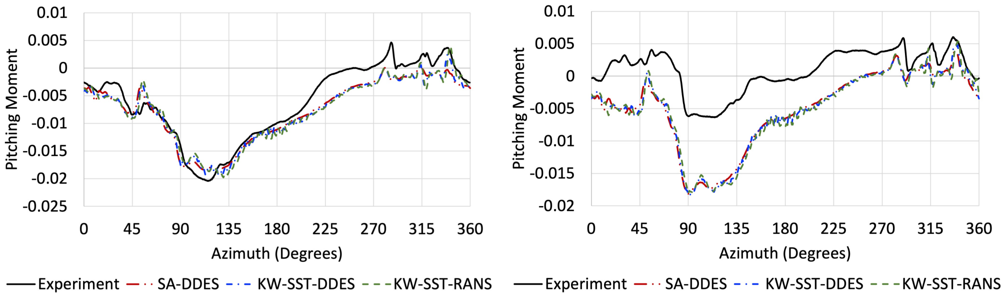

(e) r/R=0.920 (f) r/R=0.965

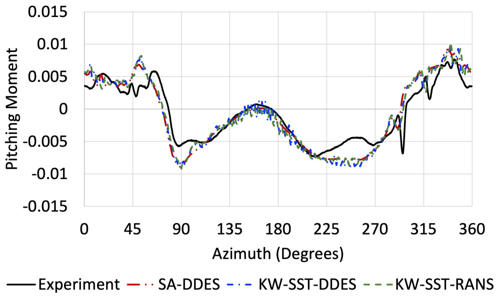

(g) r/R=0.990

Figure B.3: UH-60A pitching moment at various radial stations for various turbulence models
Test point 4533 ($C_T/\sigma = 0.040$
Coarse Grid

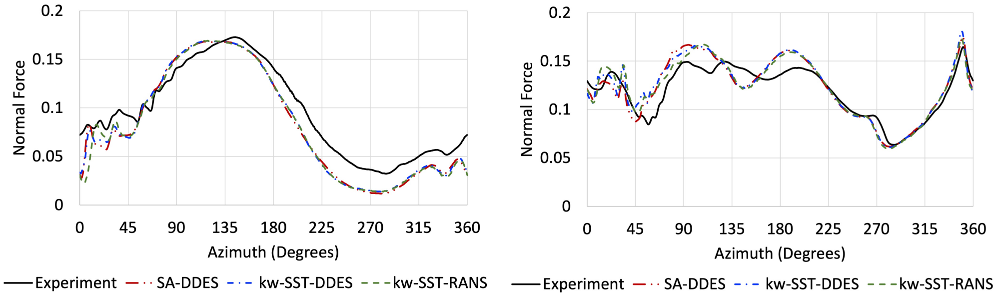

(a) r/R=0.400 (b) r/R=0.675

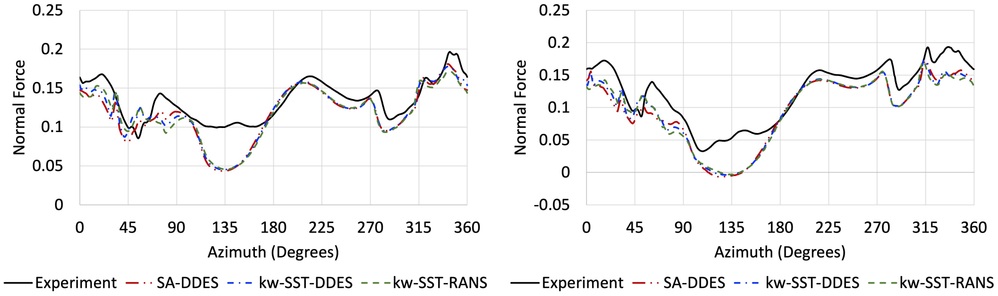

(c) r/R=0.775 (d) r/R=0.865

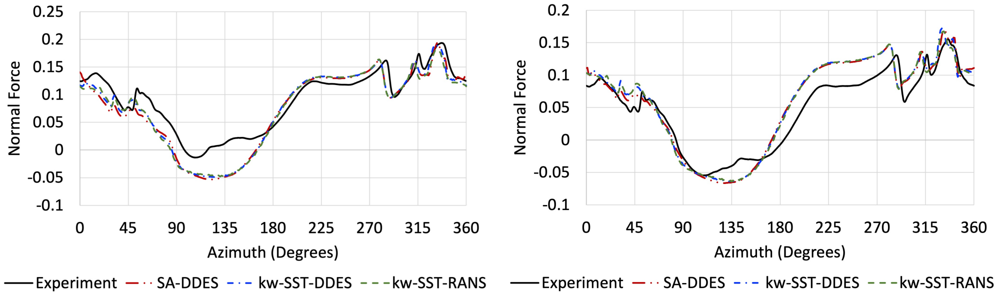

(e) r/R=0.920 (f) r/R=0.965

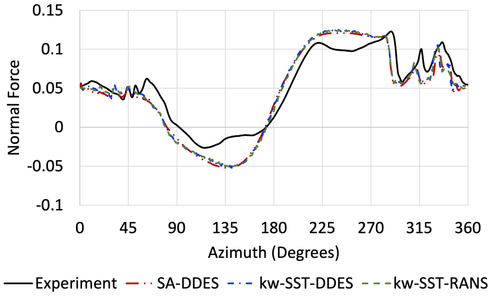

(g) r/R=0.990

Figure B.4: UH-60A normal force at various radial stations for various turbulence models
Test point 4534 ($C_T/\sigma =$
Coarse Grid

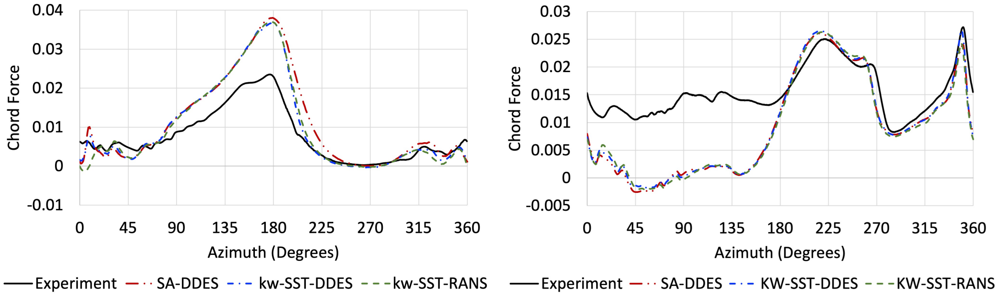

(a) r/R=0.400 (b) r/R=0.675

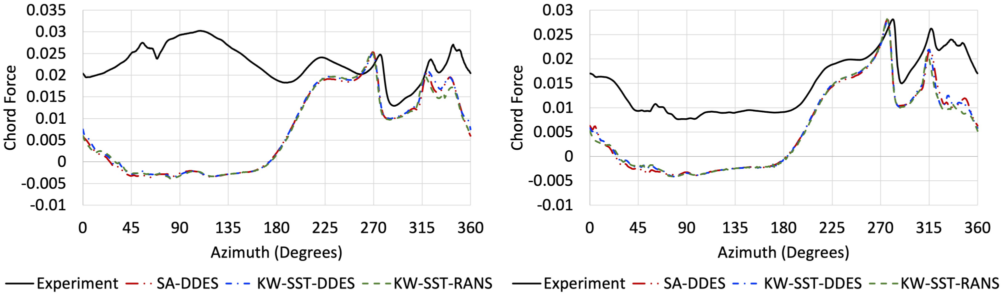

(c) r/R=0.775 (d) r/R=0.865

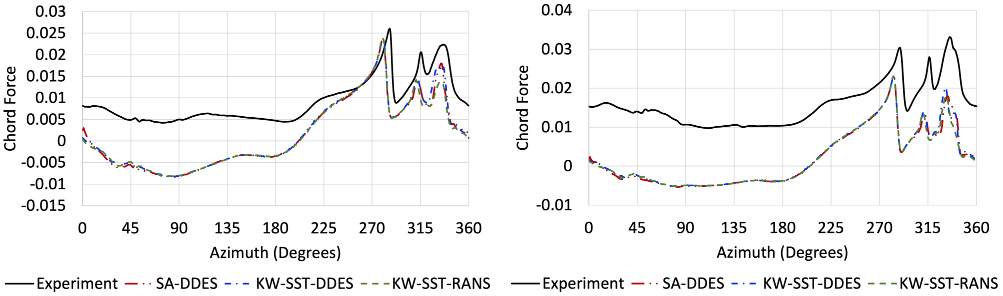

(e) r/R=0.920 (f) r/R=0.965

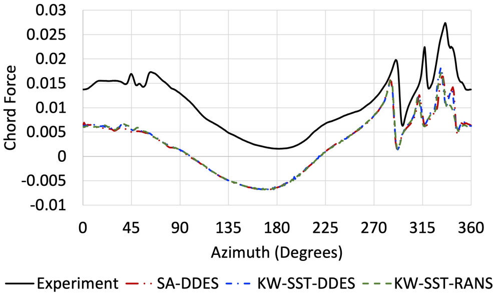

(g) r/R=0.990

Figure B.5: UH-60A chord force at various radial stations for various turbulence models
Test point 4534 ($C_T/\sigma =$
Coarse Grid

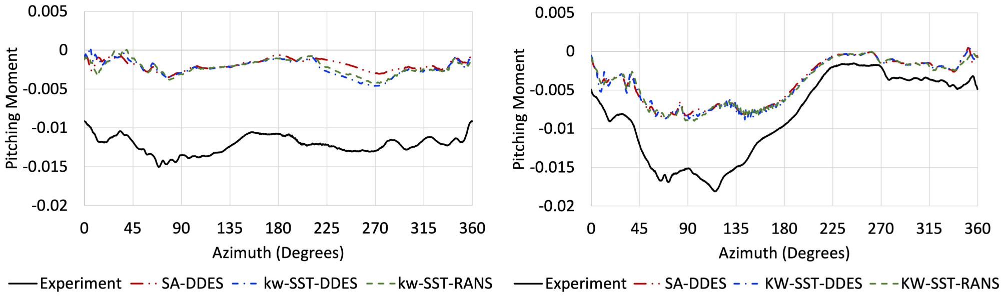

(a) r/R=0.400 (b) r/R=0.675

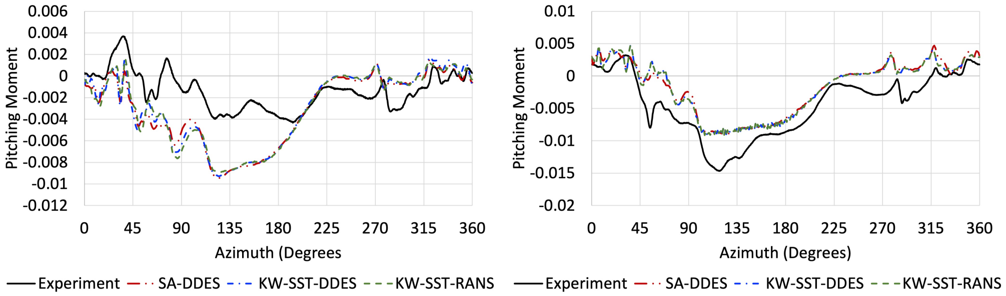

(c) r/R=0.775 (d) r/R=0.865

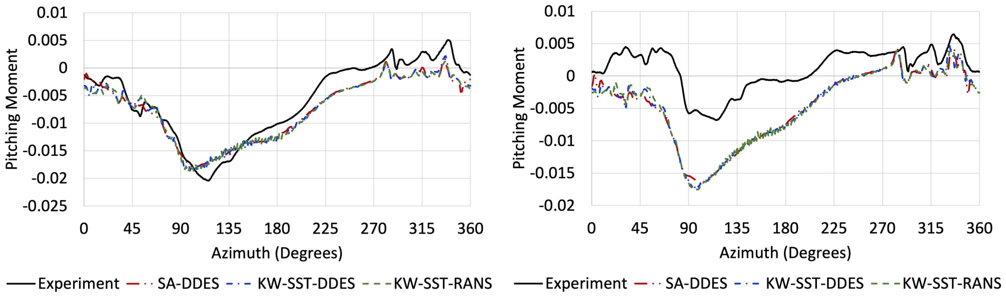

(e) r/R=0.920 (f) r/R=0.965

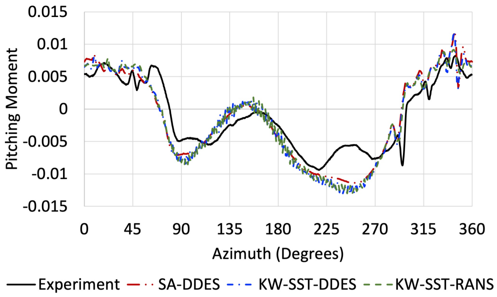

(g) r/R=0.990

Figure B.6: UH-60A pitching moment at various radial stations for various turbulence models Test point 4534 ($C_T/\sigma =$
Coarse Grid

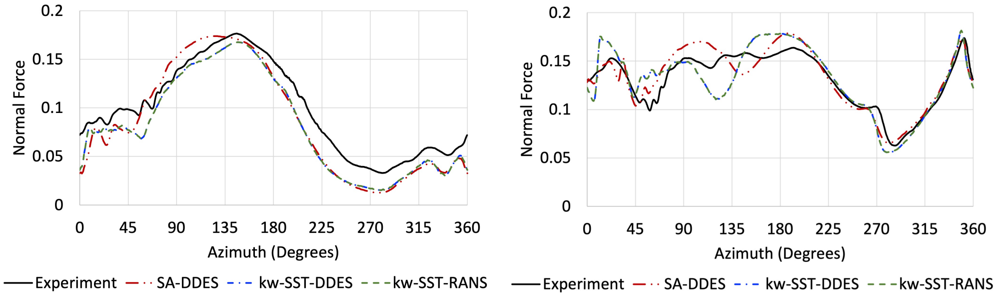

(a) r/R=0.400 (b) r/R=0.675

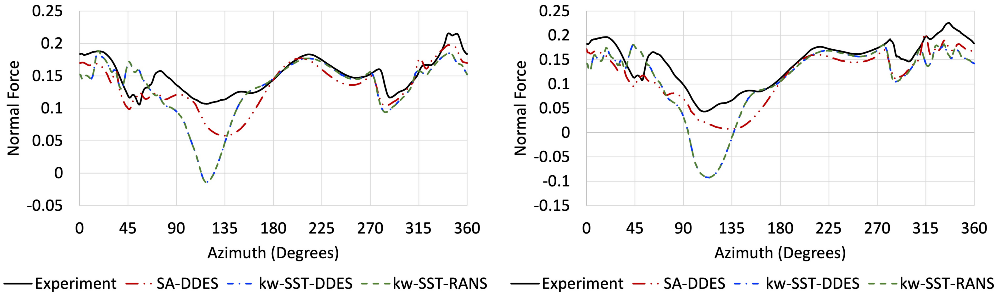

(c) r/R=0.775 (d) r/R=0.865

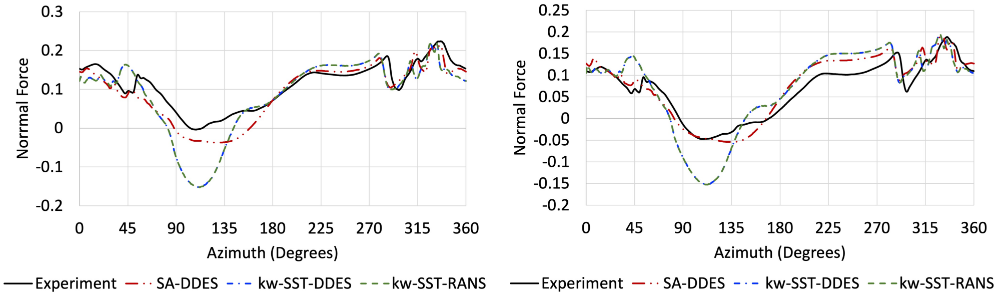

(e) r/R=0.920 (f) r/R=0.965

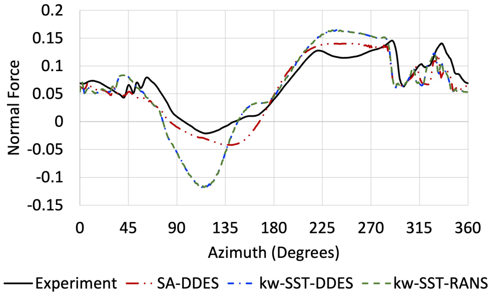

(g) r/R=0.990

Figure B.7: UH-60A normal force at various radial stations for various turbulence models Test point 4535 ($C_T/\sigma =$ Coarse Grid

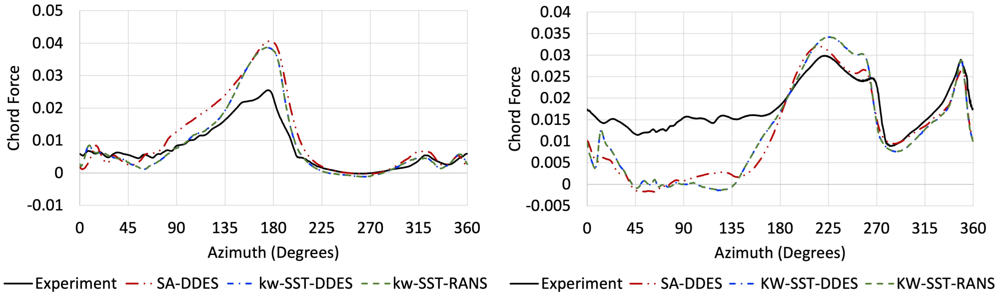

(a) r/R=0.400 (b) r/R=0.675

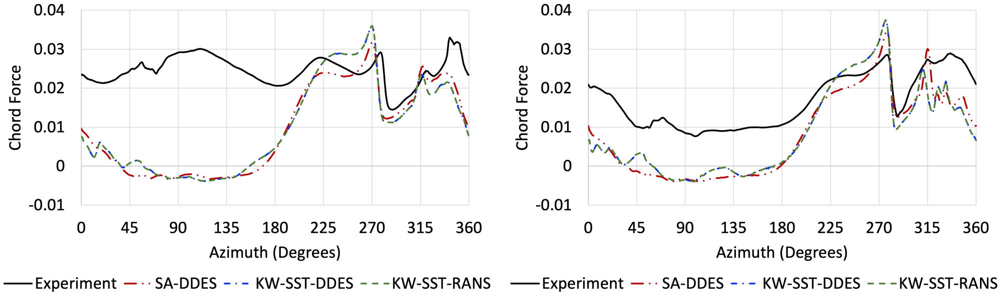

(c) r/R=0.775 (d) r/R=0.865

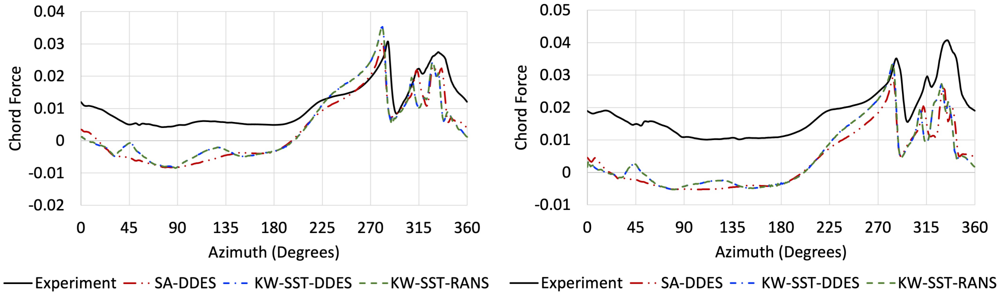

(e) r/R=0.920 (f) r/R=0.965

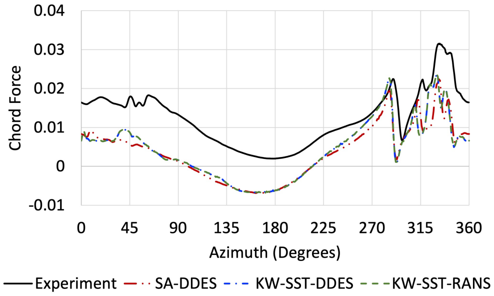

(g) r/R=0.990

Figure B.8: UH-60A chord force at various radial stations for various turbulence models
Test point 4535 ($C_T/\sigma =$
Coarse Grid

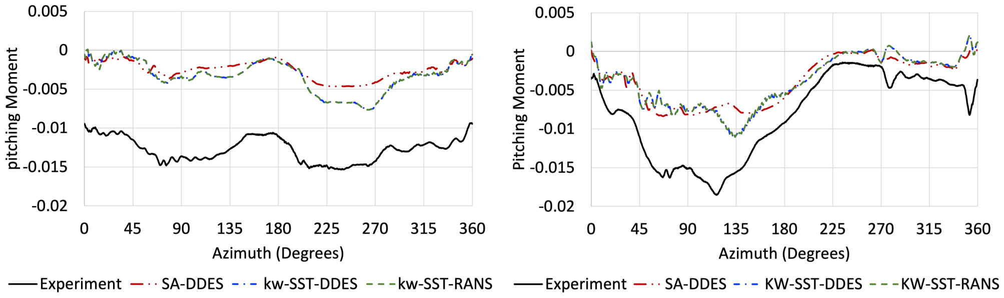

(a) r/R=0.400

(b) r/R=0.675

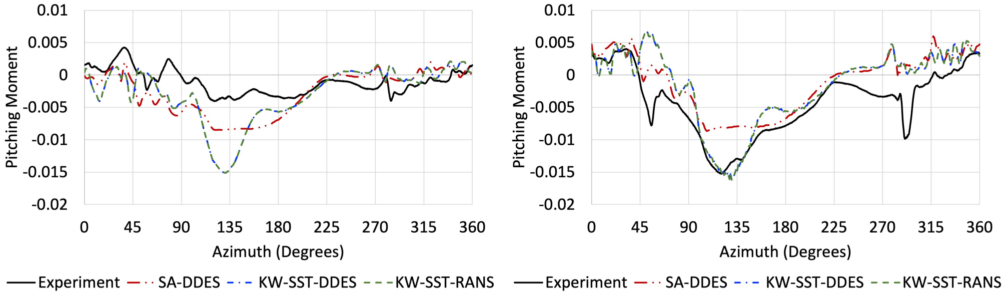

(c) r/R=0.775

(d) r/R=0.865

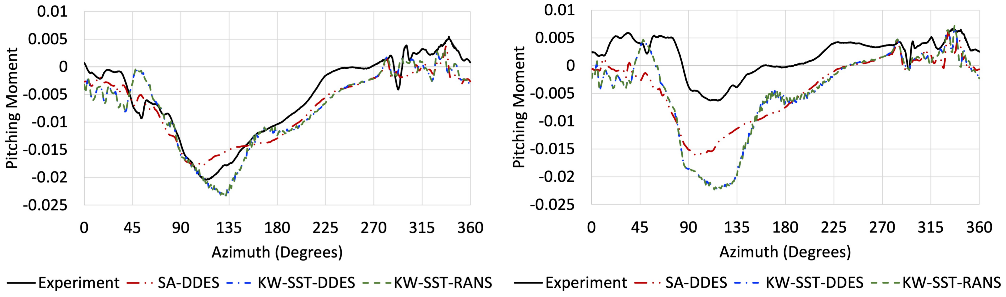

(e) r/R=0.920

(f) r/R=0.965

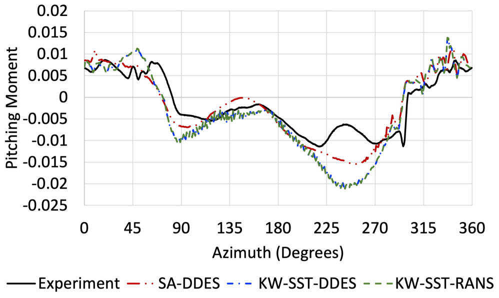

(g) r/R=0.990

Figure B.9: UH-60A pitching moment at various radial stations for various turbulence models
Test point 4535 ($C_T/\sigma =$
Coarse Grid

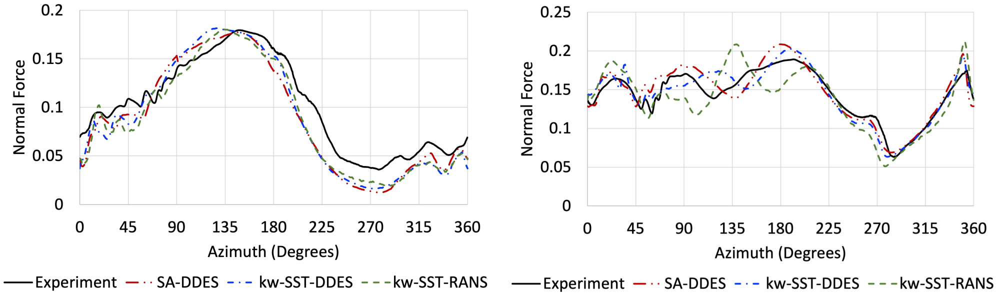

(a) r/R=0.400 (b) r/R=0.675

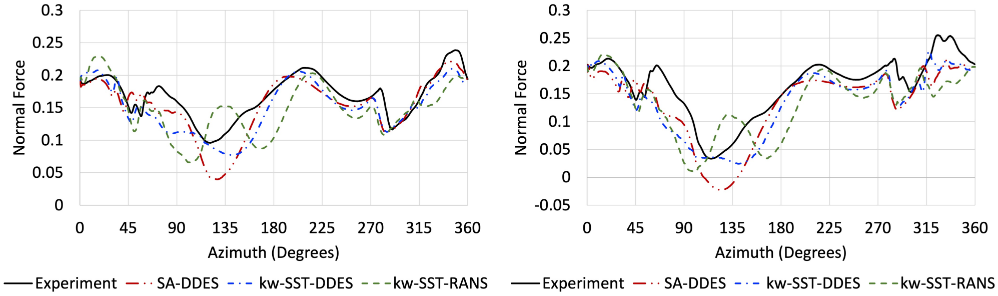

(c) r/R=0.775 (d) r/R=0.865

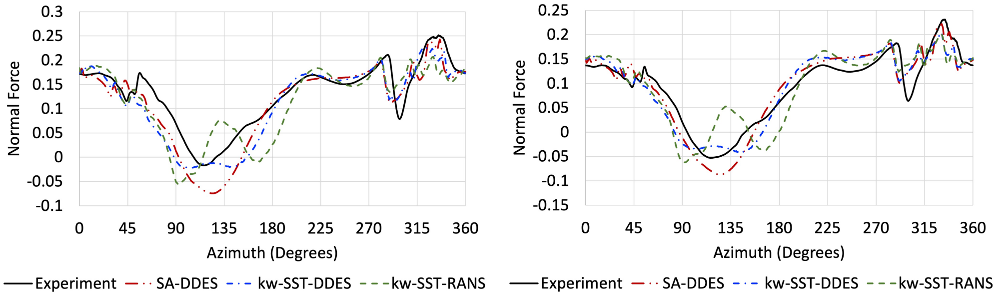

(e) r/R=0.920 (f) r/R=0.965

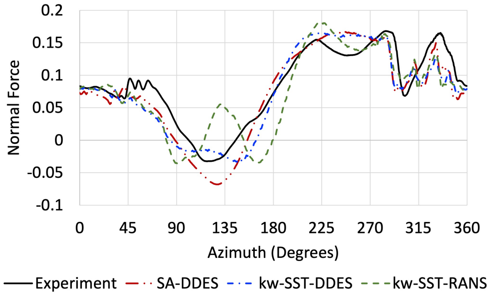

(g) r/R=0.990

Figure B.10: UH-60A normal force at various radial stations for various turbulence models
Test point 4536 ($C_T/\sigma =$
Coarse Grid

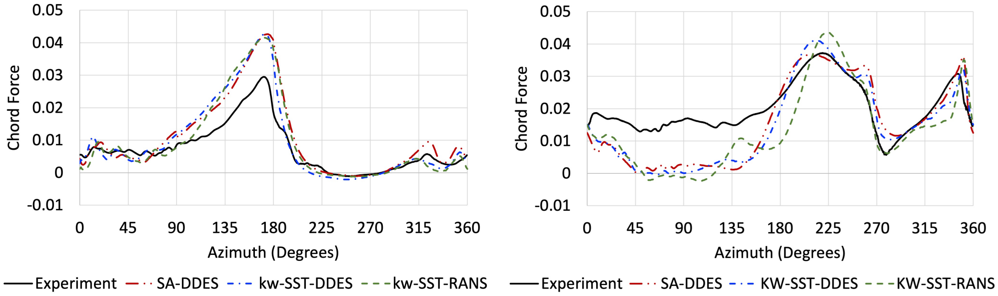

(a) r/R=0.400

(b) r/R=0.675

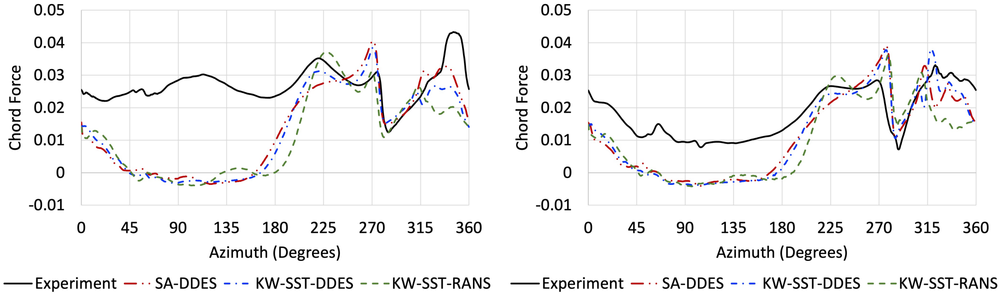

(c) r/R=0.775

(d) r/R=0.865

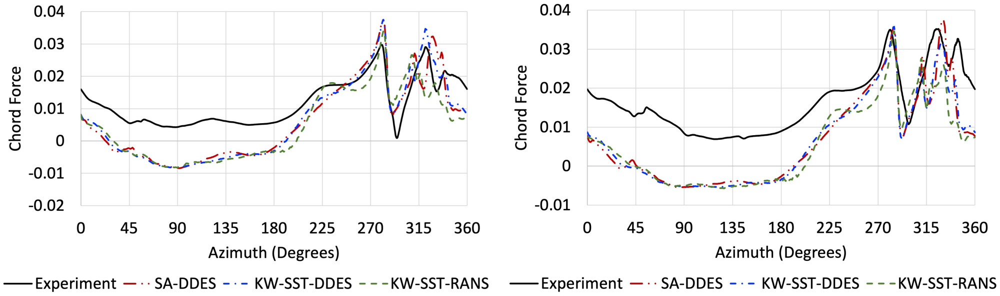

(e) r/R=0.920

(f) r/R=0.965

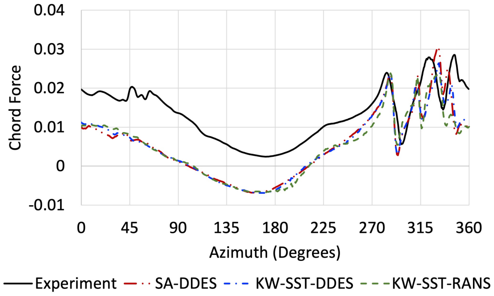

(g) r/R=0.990

Figure B.11: UH-60A chord force at various radial stations for various turbulence models
Test point 4536 ($C_T/\sigma =$
Coarse Grid

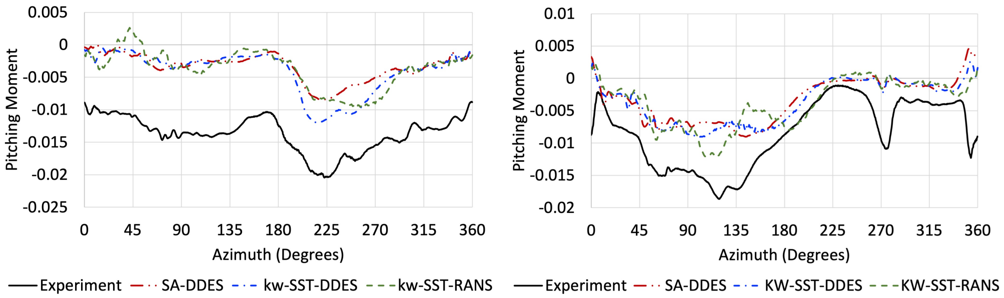

(a) r/R=0.400 (b) r/R=0.675

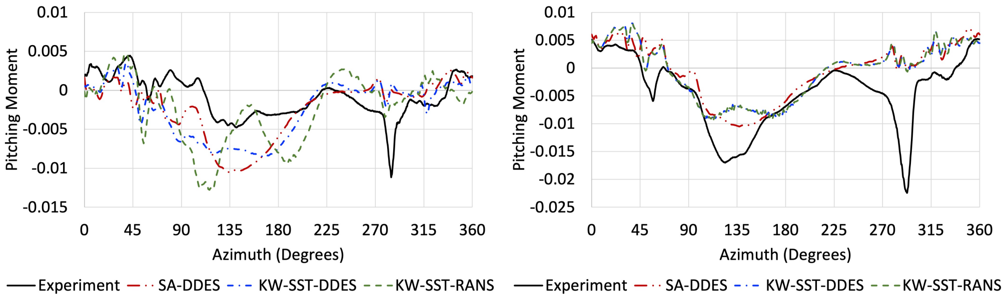

(c) r/R=0.775 (d) r/R=0.865

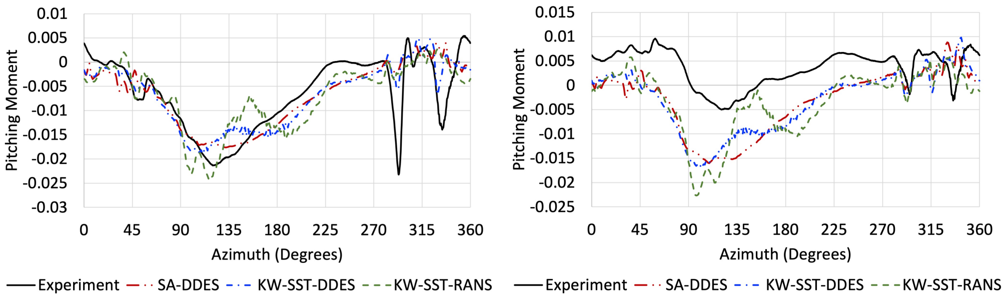

(e) r/R=0.920 (f) r/R=0.965

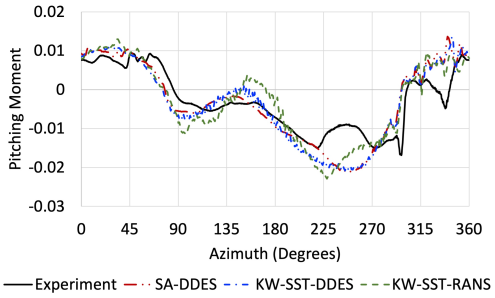

(g) r/R=0.990

Figure B.12: UH-60A pitching moment at various radial stations for various turbulence models
Test point 4536 ($C_T/\sigma =$
Coarse Grid

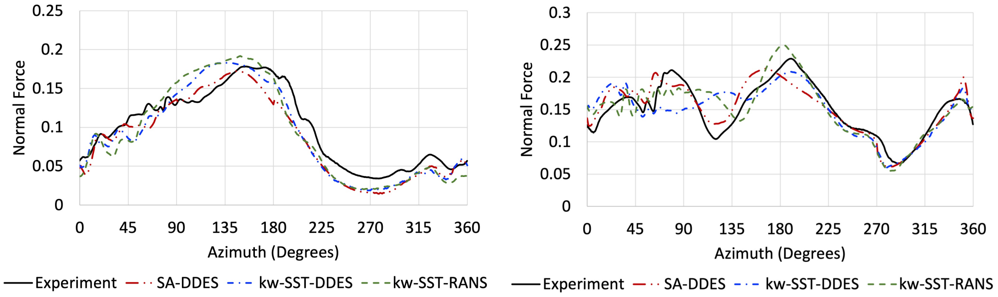

(a) r/R=0.400 (b) r/R=0.675

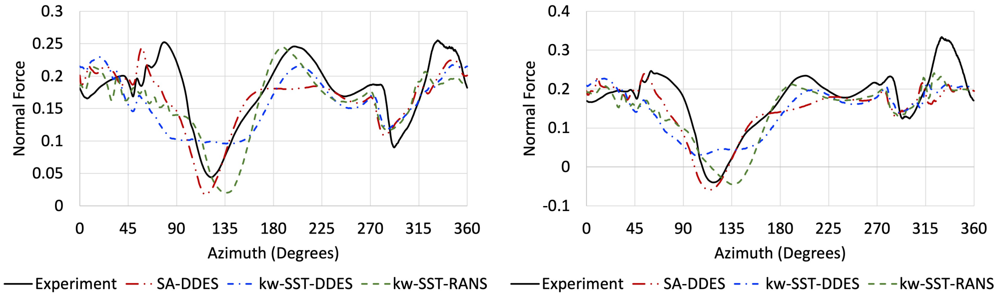

(c) r/R=0.775 (d) r/R=0.865

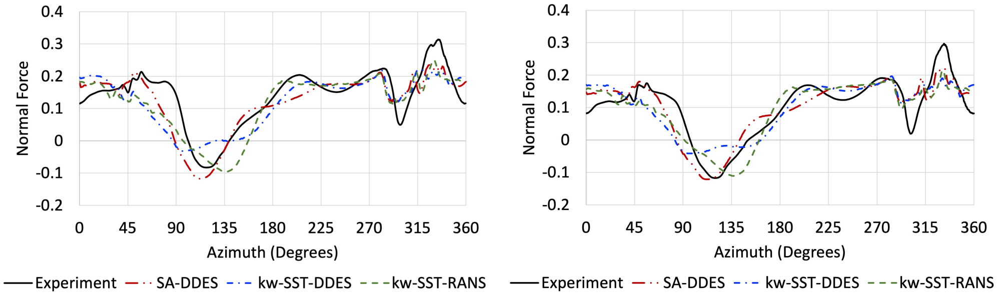

(e) r/R=0.920 (f) r/R=0.965

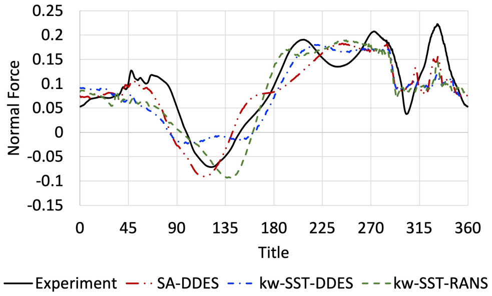

(g) r/R=0.990

Figure B.13: UH-60A normal force at various radial stations for various turbulence models
Test point 4537 ($C_T/\sigma =$
Coarse Grid

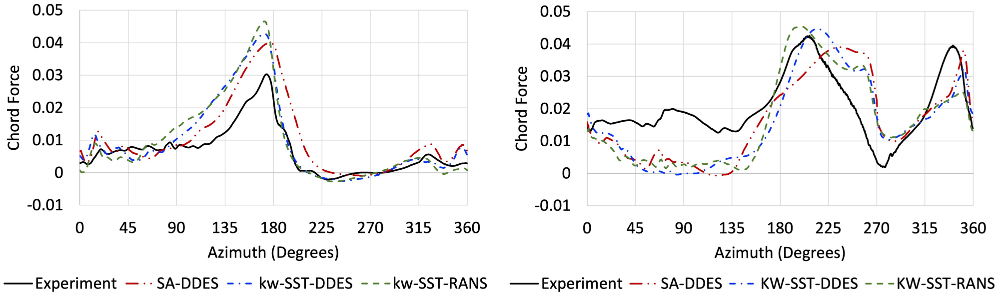

(a) r/R=0.400 (b) r/R=0.675

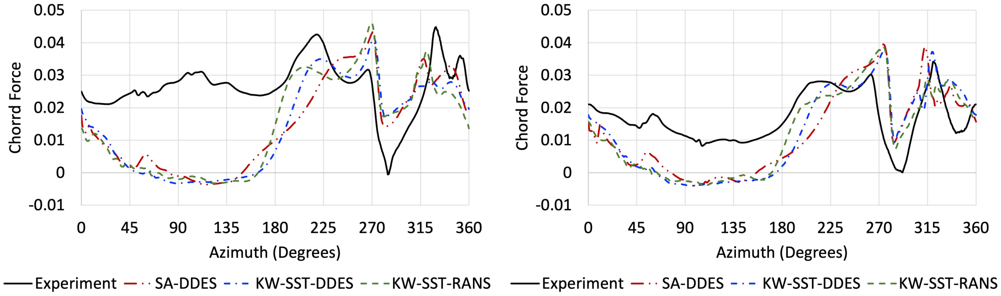

(c) r/R=0.775 (d) r/R=0.865

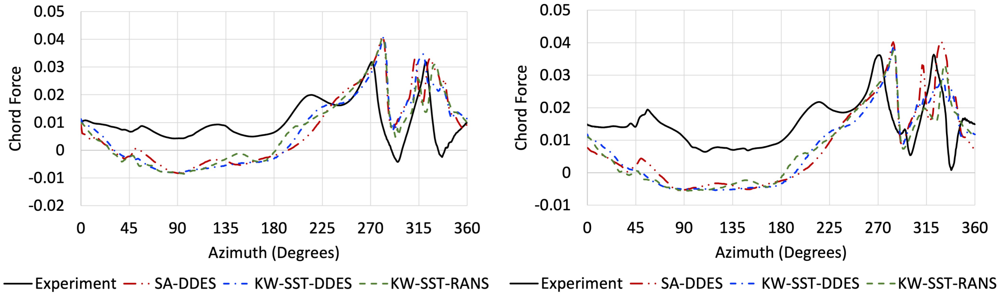

(e) r/R=0.920 (f) r/R=0.965

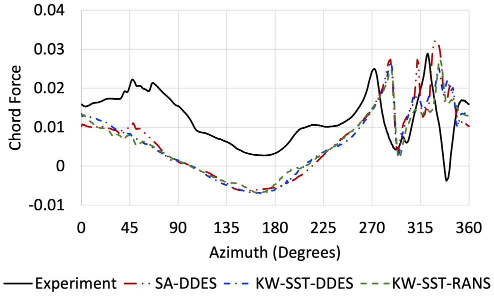

(g) r/R=0.990

Figure B.14: UH-60A chord force at various radial stations for various turbulence models
Test point 4537 ($C_T/\sigma =$
Coarse Grid

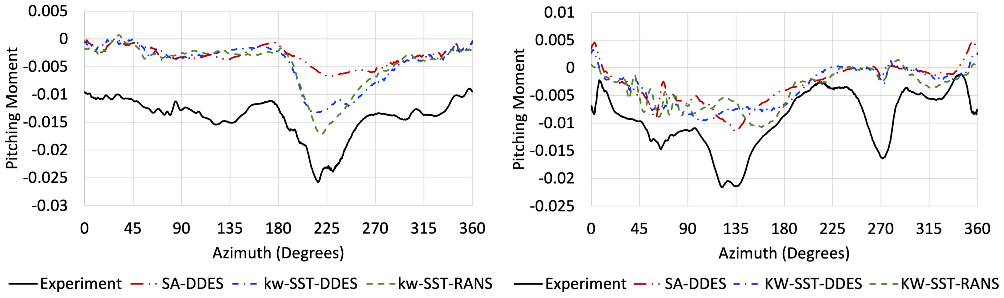

(a) r/R=0.400 (b) r/R=0.675

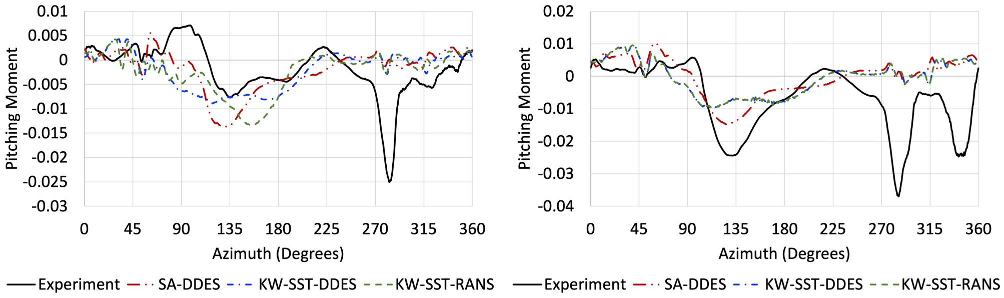

(c) r/R=0.775 (d) r/R=0.865

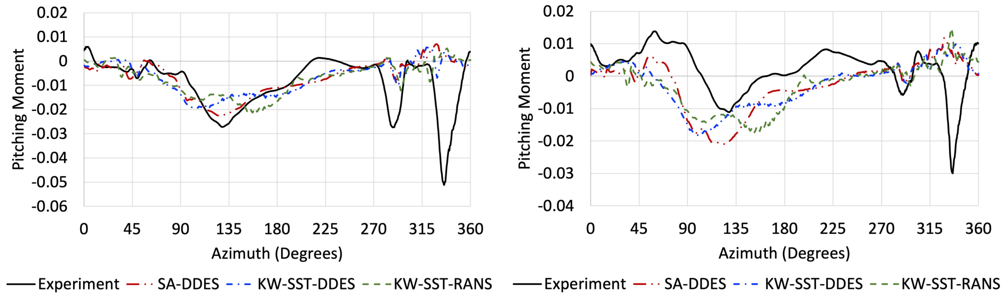

(e) r/R=0.920 (f) r/R=0.965

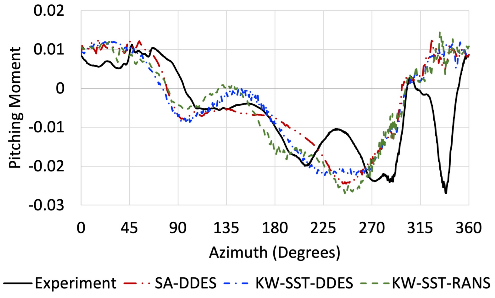

(g) r/R=0.990

Figure B.15: UH-60A pitching moment at various radial stations for various turbulence models
Test point 4537 ($C_T/\sigma =$
Coarse Grid

B.2 UH60 Fine Grid Turbulence Comparison

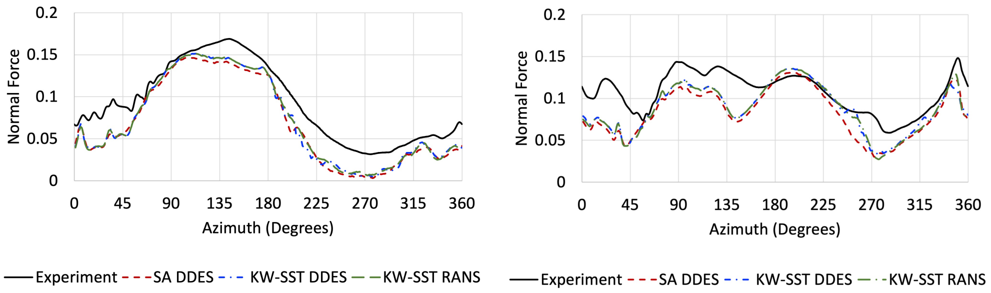

(a) r/R=0.400 (b) r/R=0.675

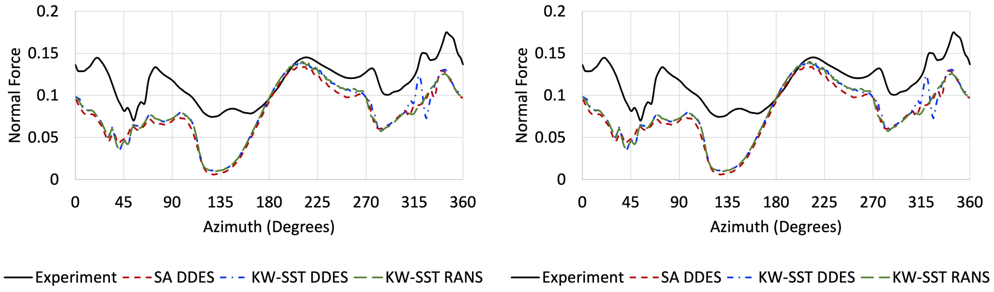

(c) r/R=0.775 (d) r/R=0.865

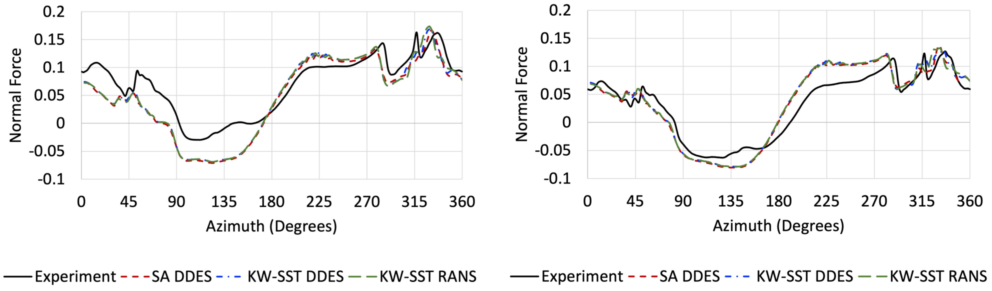

(e) r/R=0.920 (f) r/R=0.965

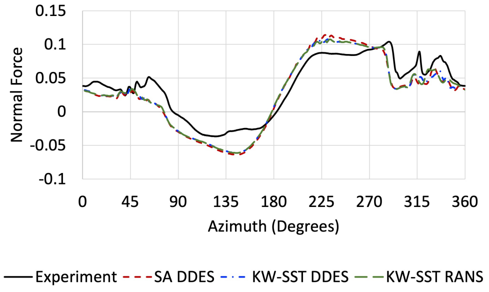

(g) r/R=0.990

Figure B.16: UH-60A normal force at various radial stations for various turbulence models
Test point 4533 ($C_T/\sigma = 0.040$)
Fine Grid

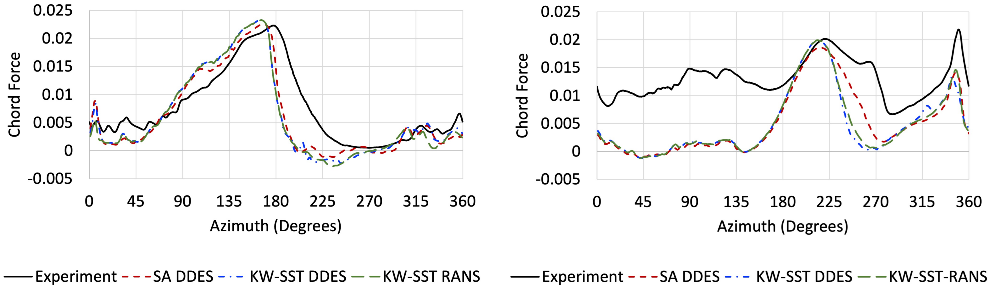

(a) r/R=0.400 (b) r/R=0.675

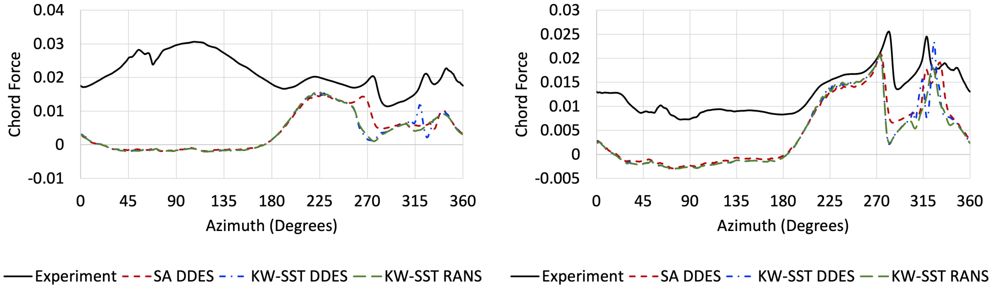

(c) r/R=0.775 (d) r/R=0.865

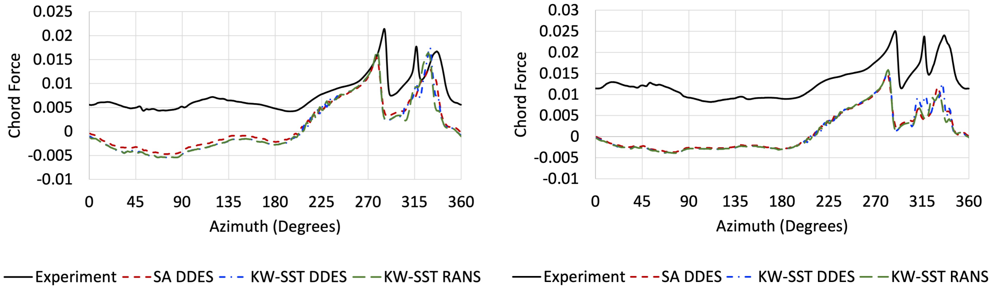

(e) r/R=0.920 (f) r/R=0.965

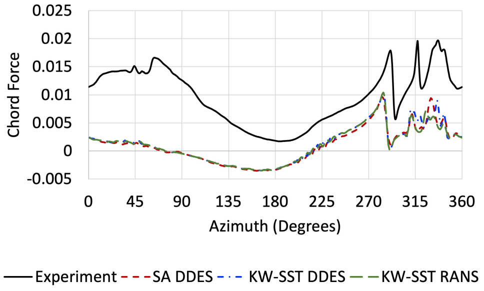

(g) r/R=0.990

Figure B.17: UH-60A chord force at various radial stations for various turbulence models
Test point 4533 ($C_T/\sigma = 0.040$
Fine Grid

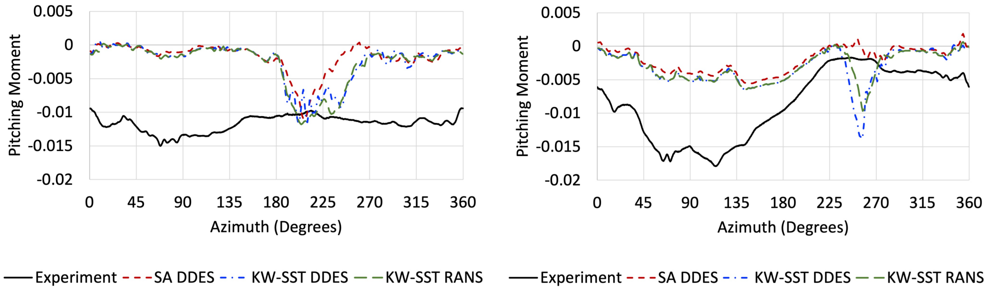

(a) r/R=0.400

(b) r/R=0.675

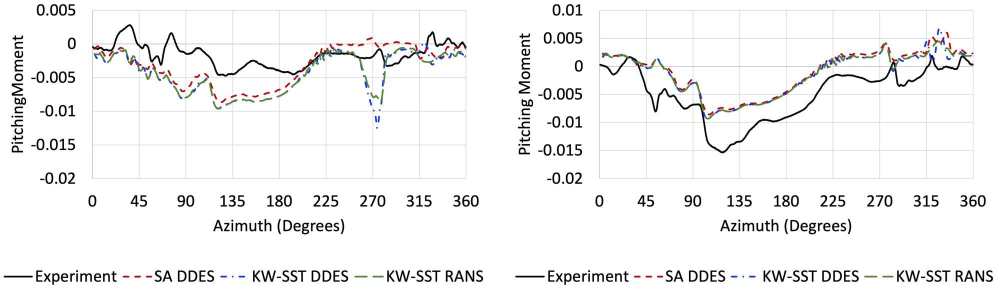

(c) r/R=0.775

(d) r/R=0.865

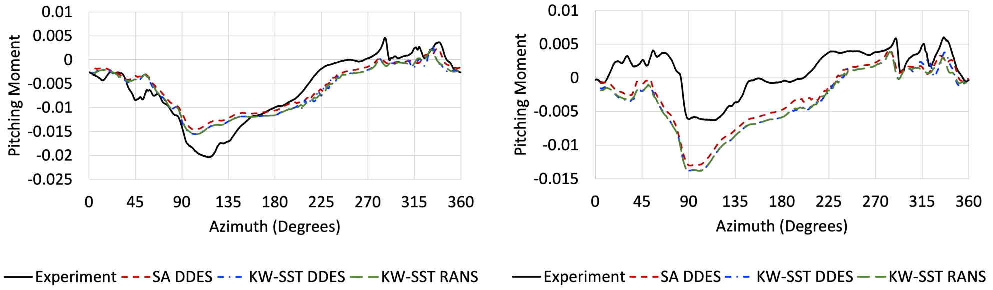

(e) r/R=0.920

(f) r/R=0.965

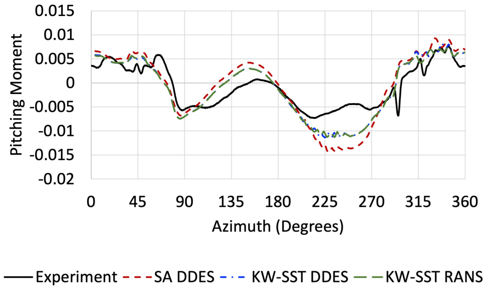

(g) r/R=0.990

Figure B.18: UH-60A pitching moment at various radial stations for various turbulence models
Test point 4533 ($C_T/\sigma = 0.040$
Fine Grid

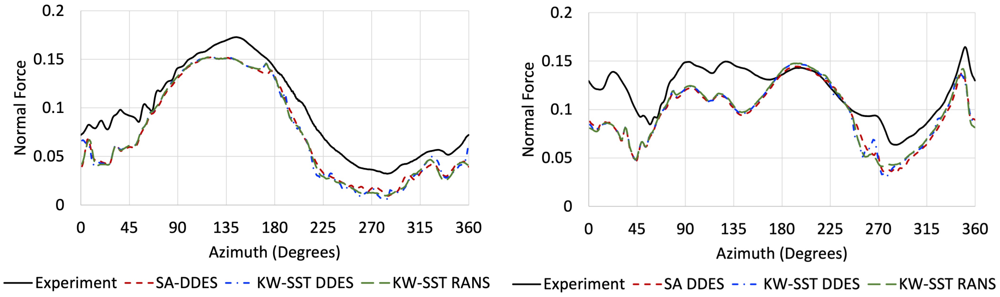

(a) r/R=0.400

(b) r/R=0.675

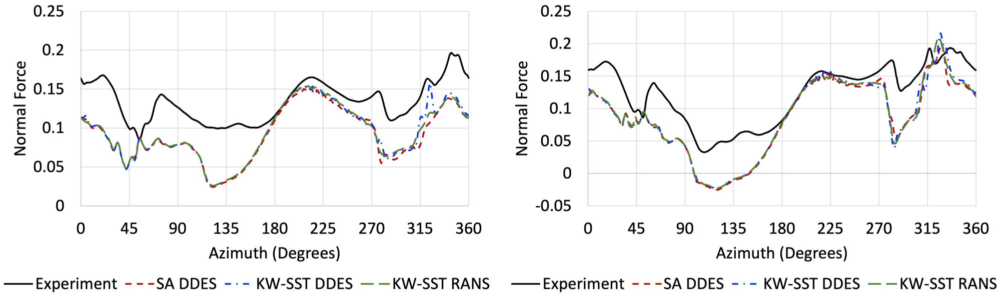

(c) r/R=0.775

(d) r/R=0.865

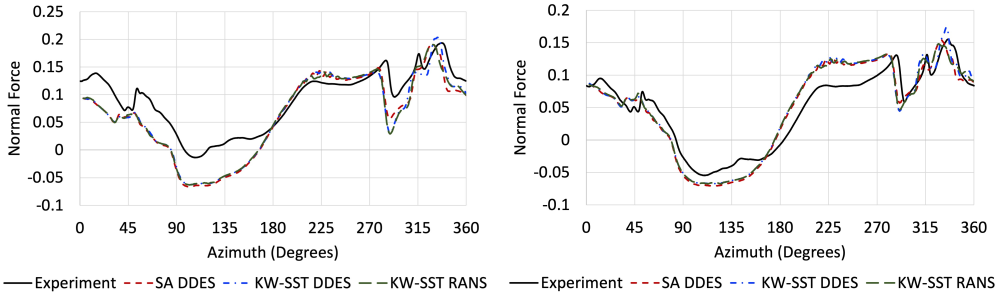

(e) r/R=0.920

(f) r/R=0.965

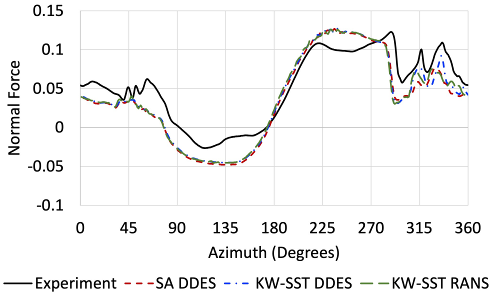

(g) r/R=0.990

Figure B.19: UH-60A normal force at various radial stations for various turbulence models
Test point 4534 ($C_T/\sigma =$
Fine Grid

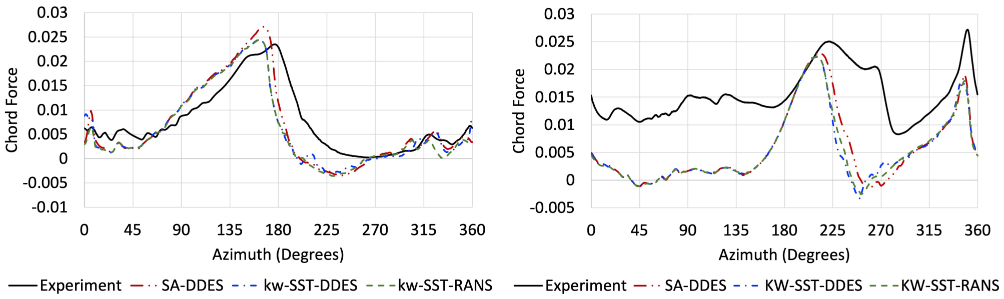

(a) r/R=0.400

(b) r/R=0.675

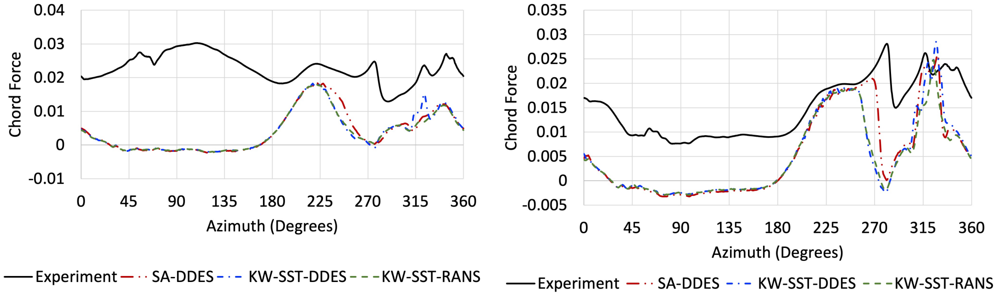

(c) r/R=0.775

(d) r/R=0.865

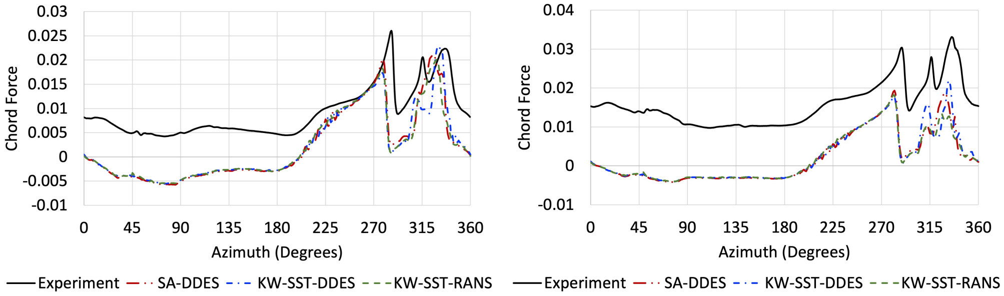

(e) r/R=0.920

(f) r/R=0.965

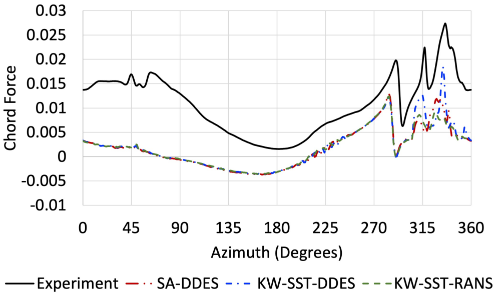

(g) r/R=0.990

Figure B.20: UH-60A chord force at various radial stations for various turbulence models
Test point 4534 ($C_T/\sigma =$
Fine Grid

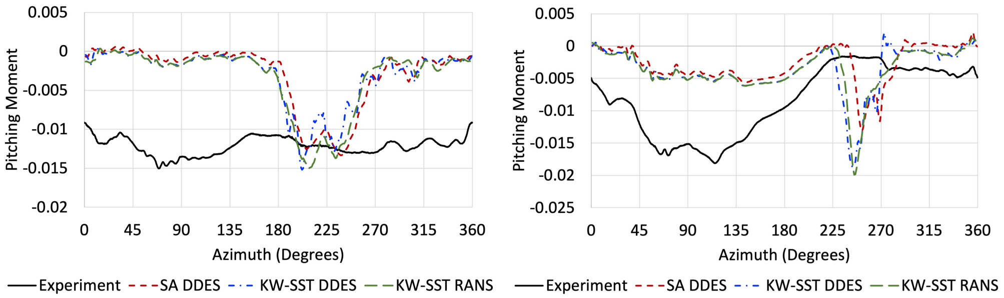

(a) r/R=0.400 (b) r/R=0.675

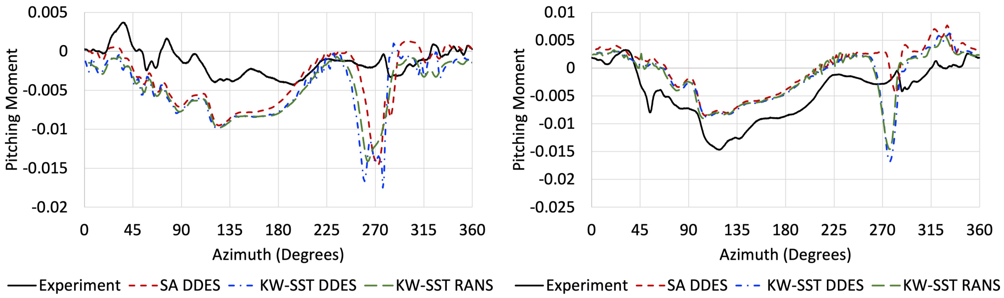

(c) r/R=0.775 (d) r/R=0.865

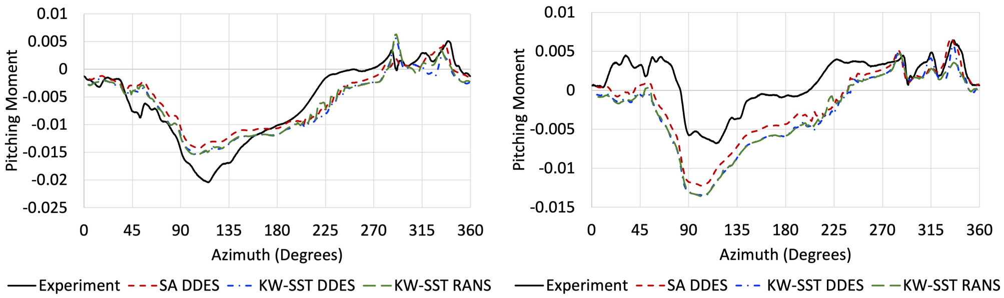

(e) r/R=0.920 (f) r/R=0.965

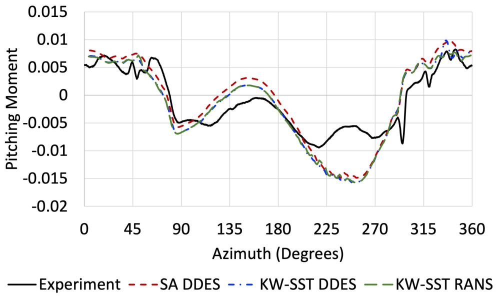

(g) r/R=0.990

Figure B.21: UH-60A pitching moment at various radial stations for various turbulence models
Test point 4534 ($C_T/\sigma =$
Fine Grid

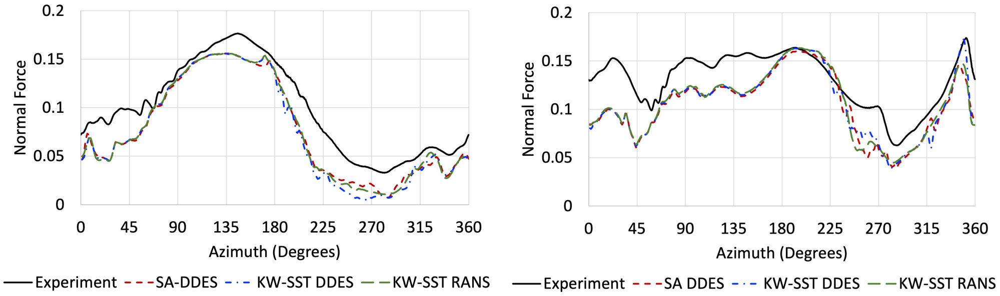

(a) r/R=0.400 (b) r/R=0.675

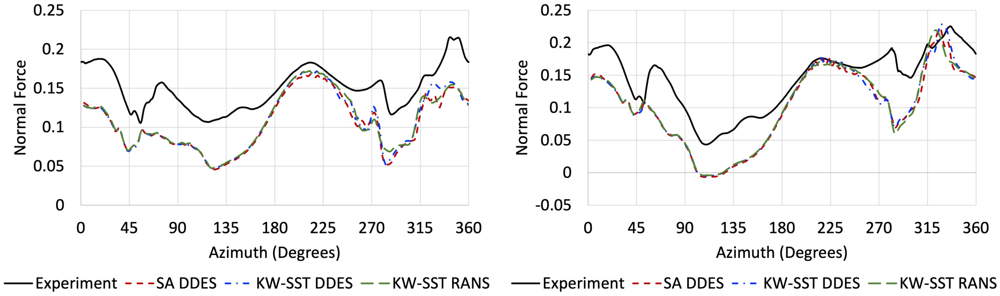

(c) r/R=0.775 (d) r/R=0.865

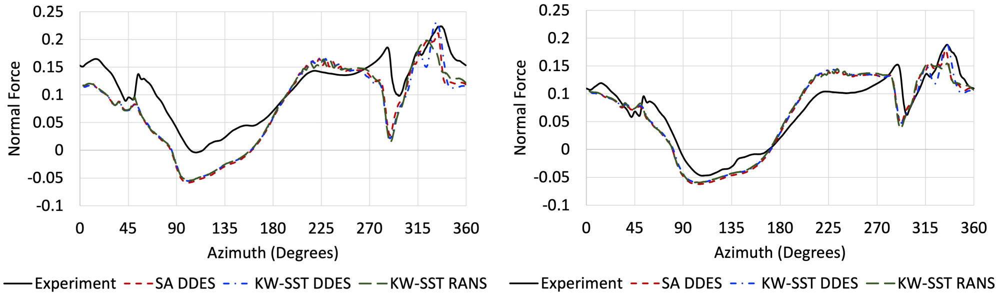

(e) r/R=0.920 (f) r/R=0.965

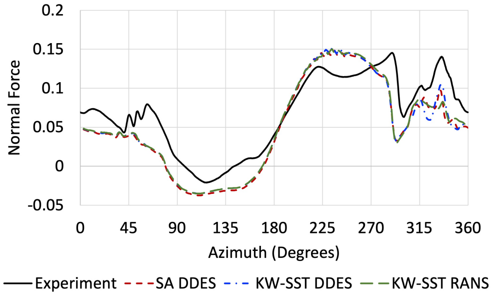

(g) r/R=0.990

Figure B.22: UH-60A normal force at various radial stations for various turbulence models
Test point 4535 ($C_T/\sigma =$
Fine Grid

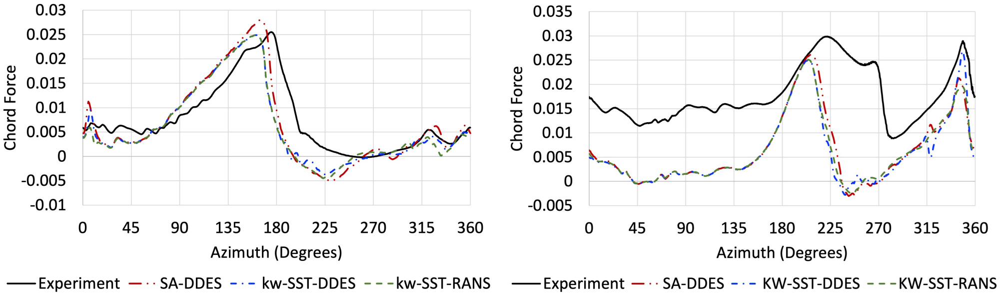

(a) r/R=0.400 (b) r/R=0.675

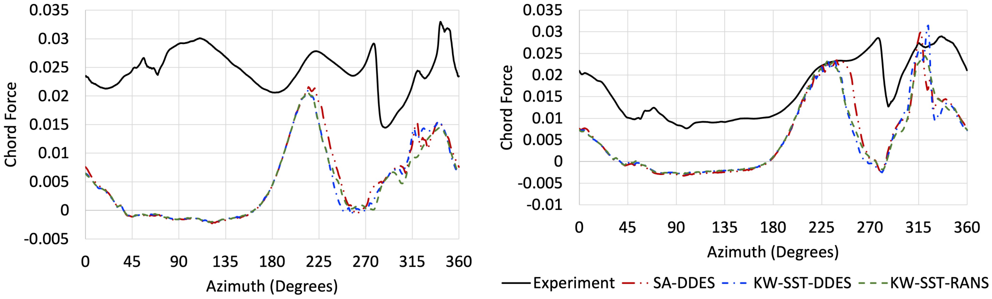

(c) r/R=0.775 (d) r/R=0.865

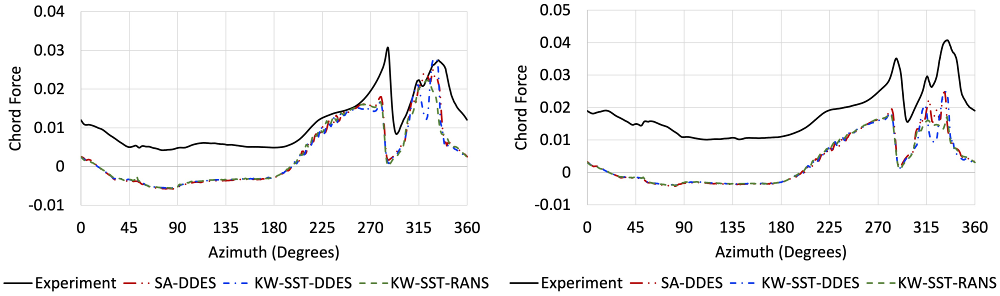

(e) r/R=0.920 (f) r/R=0.965

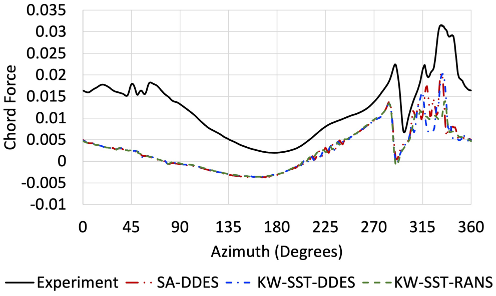

(g) r/R=0.990

Figure B.23: UH-60A chord force at various radial stations for various turbulence models
Test point 4535 ($C_T/\sigma =$
Fine Grid

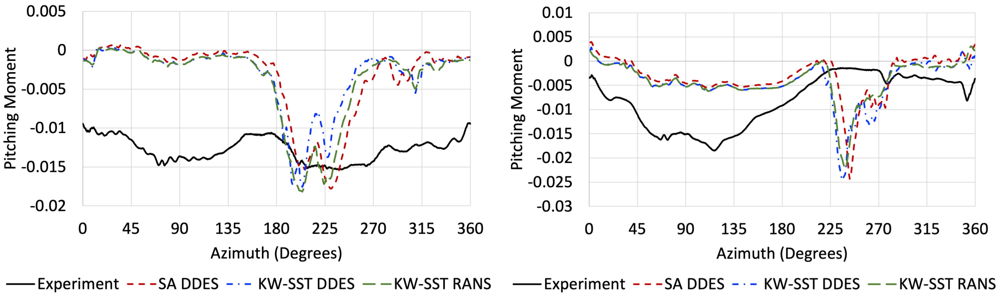

(a) r/R=0.400 (b) r/R=0.675

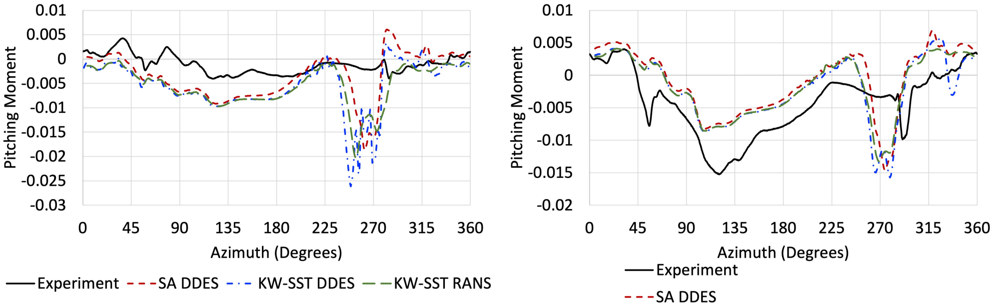

(c) r/R=0.775 (d) r/R=0.865

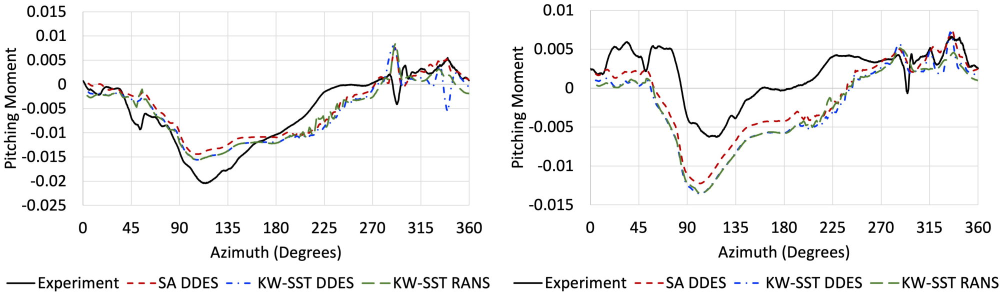

(e) r/R=0.920 (f) r/R=0.965

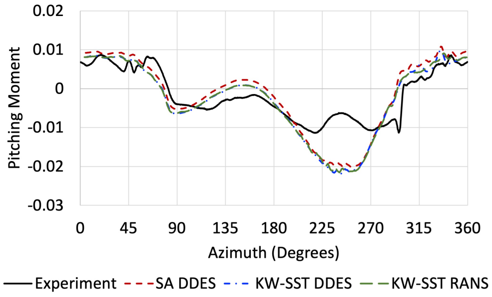

(g) r/R=0.990

Figure B.24: UH-60A pitching moment at various radial stations for various turbulence models
Test point 4535 ($C_T/\sigma =$
Fine Grid

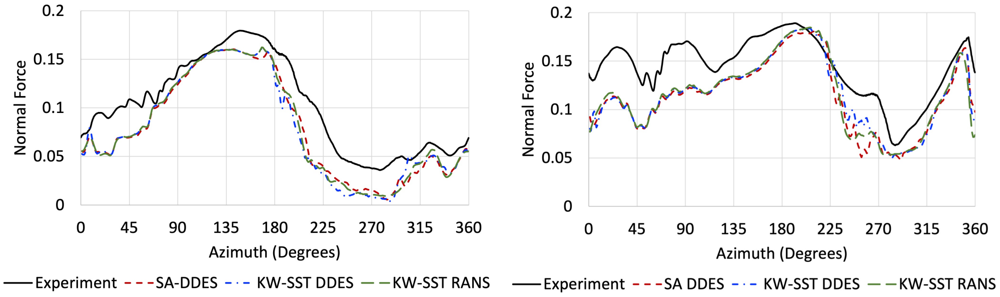

(a) r/R=0.400

(b) r/R=0.675

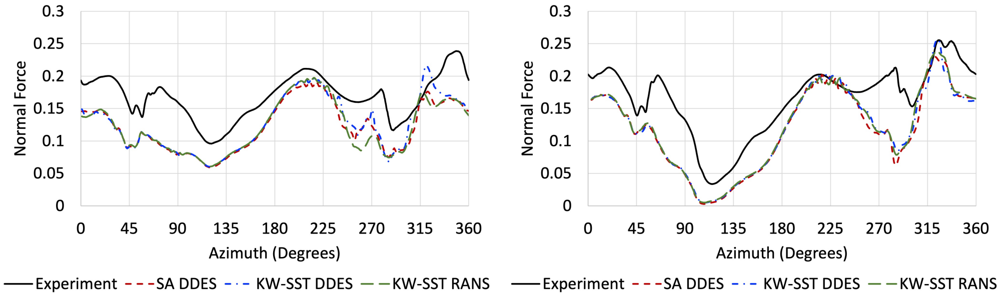

(c) r/R=0.775

(d) r/R=0.865

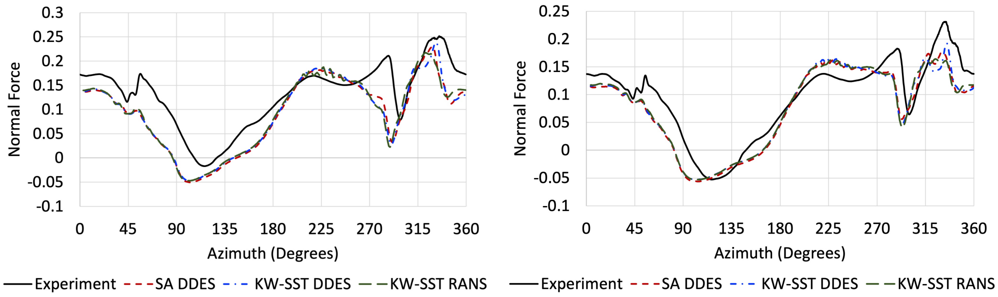

(e) r/R=0.920

(f) r/R=0.965

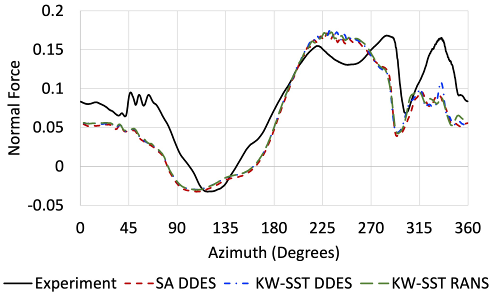

(g) r/R=0.990

Figure B.25: UH-60A normal force at various radial stations for various turbulence models
Test point 4536 ($C_T/\sigma =$
Fine Grid

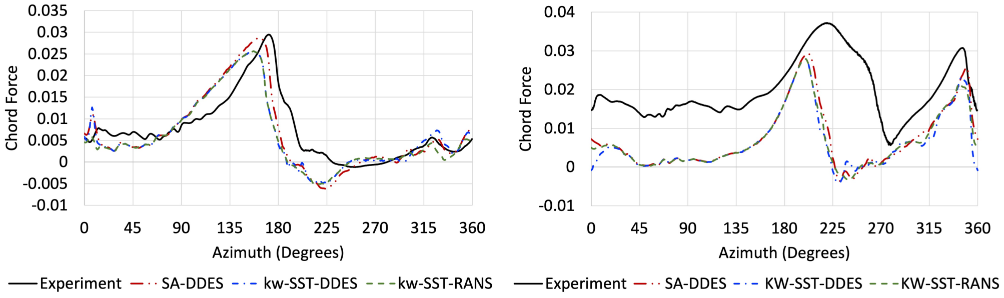

(a) r/R=0.400 (b) r/R=0.675

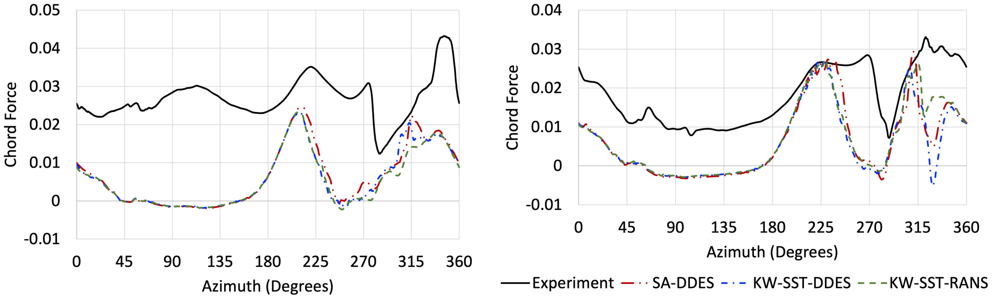

(c) r/R=0.775 (d) r/R=0.865

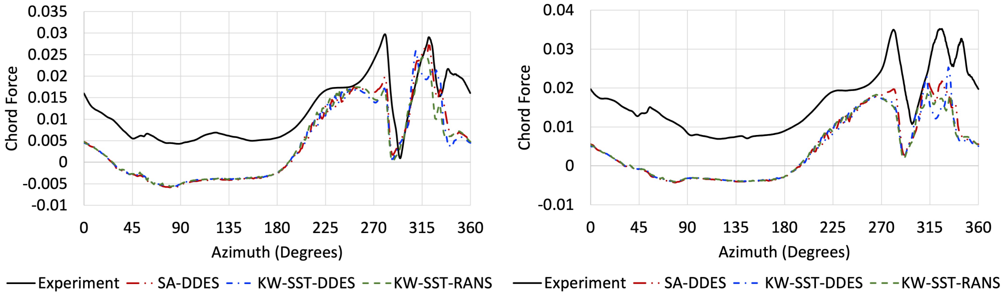

(e) r/R=0.920 (f) r/R=0.965

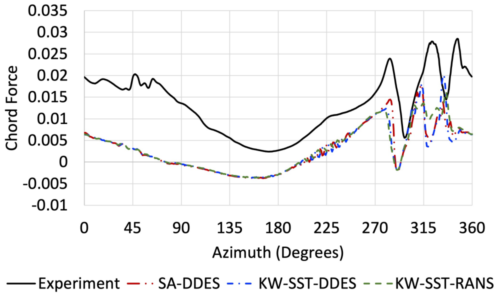

(g) r/R=0.990

Figure B.26: UH-60A chord force at various radial stations for various turbulence models
Test point 4536 ($C_T/\sigma =$
Fine Grid

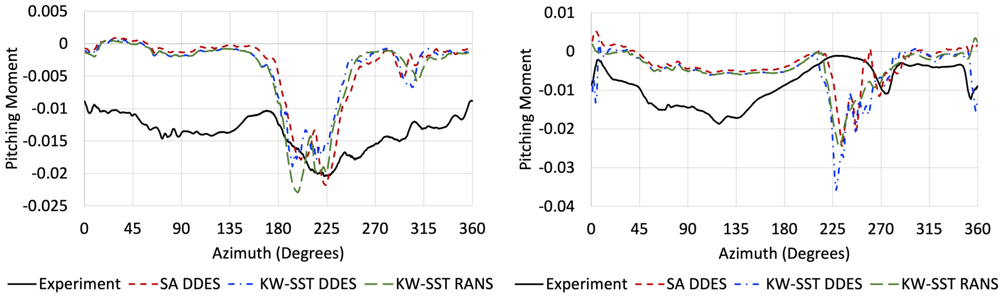

(a) r/R=0.400 (b) r/R=0.675

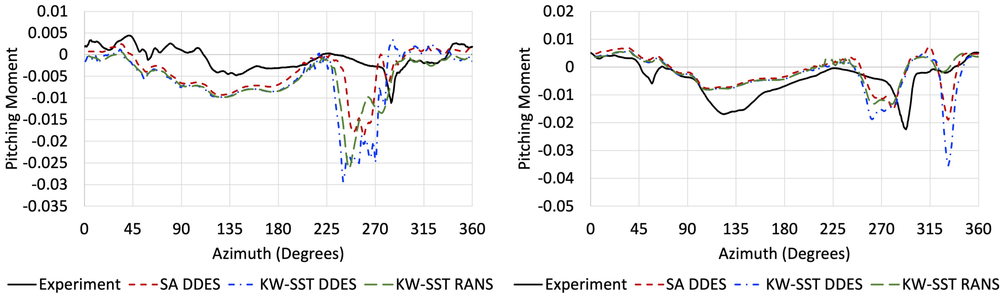

(c) r/R=0.775 (d) r/R=0.865

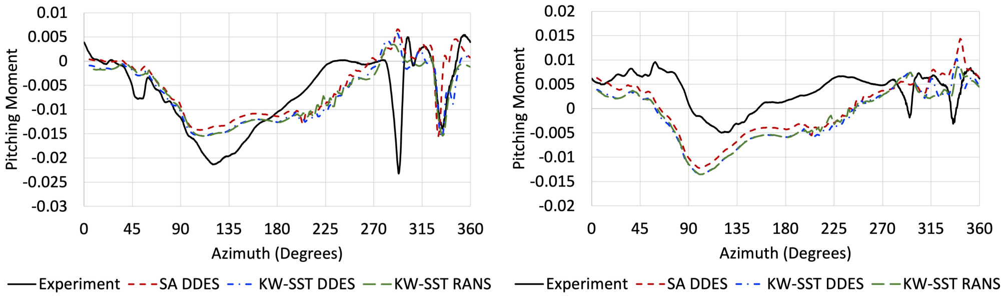

(e) r/R=0.920 (f) r/R=0.965

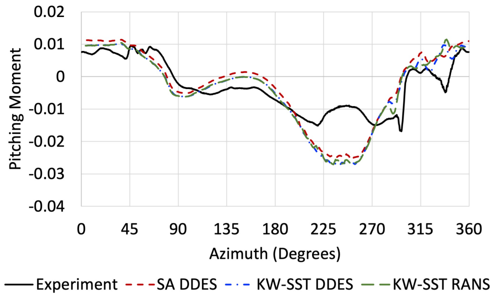

(g) r/R=0.990

Figure B.27: UH-60A pitching moment at various radial stations for various turbulence models
Test point 4536 ($C_T/\sigma =$
Fine Grid

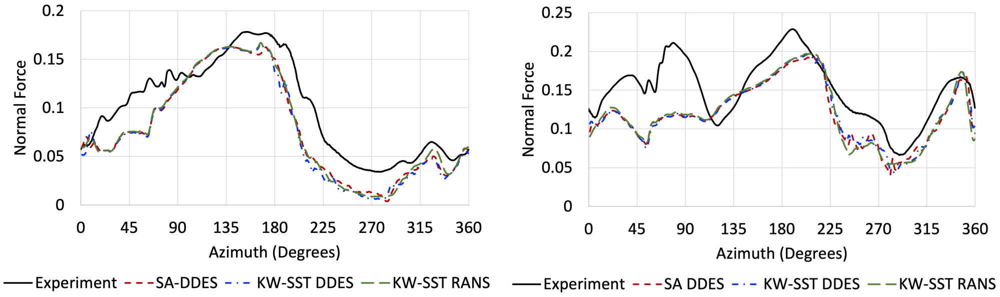

(a) r/R=0.400 (b) r/R=0.675

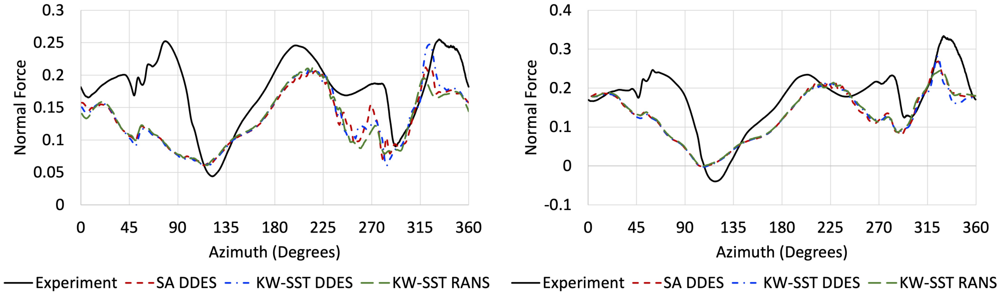

(c) r/R=0.775 (d) r/R=0.865

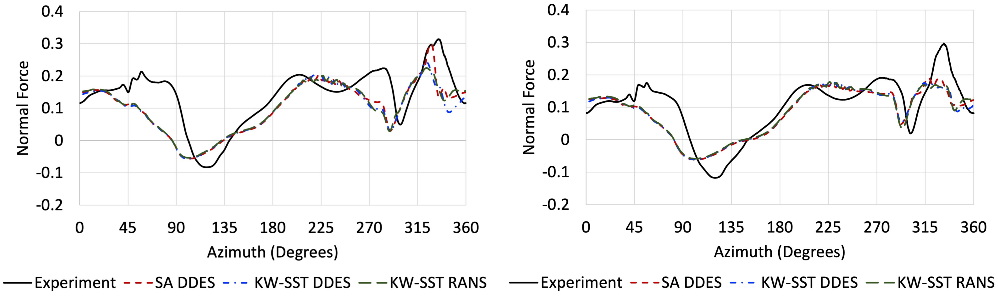

(e) r/R=0.920 (f) r/R=0.965

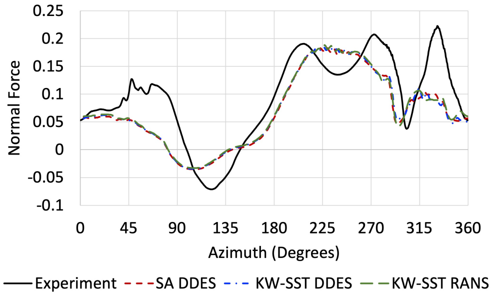

(g) r/R=0.990

Figure B.28: UH-60A normal force at various radial stations for various turbulence models
Test point 4537 ($C_T/\sigma =$
Fine Grid

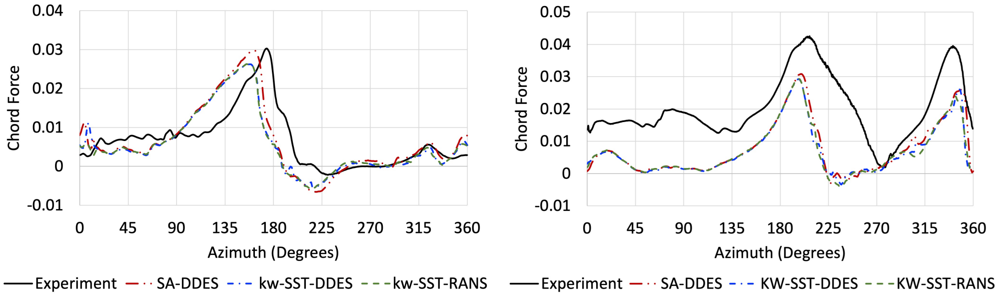

(a) r/R=0.400

(b) r/R=0.675

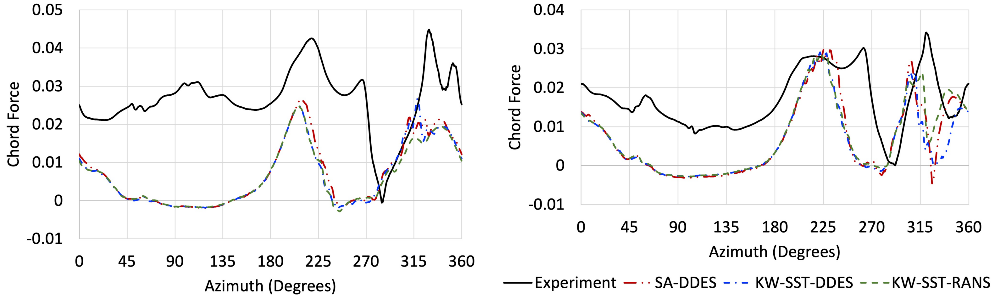

(c) r/R=0.775

(d) r/R=0.865

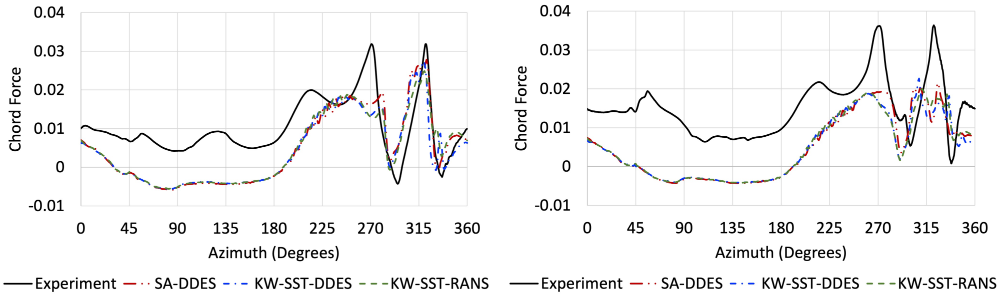

(e) r/R=0.920

(f) r/R=0.965

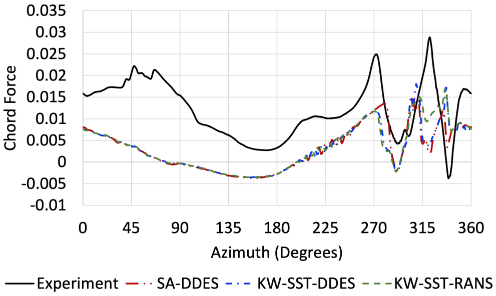

(g) r/R=0.990

Figure B.29: UH-60A chord force at various radial stations for various turbulence models
Test point 4537 ($C_T/\sigma =$
Fine Grid

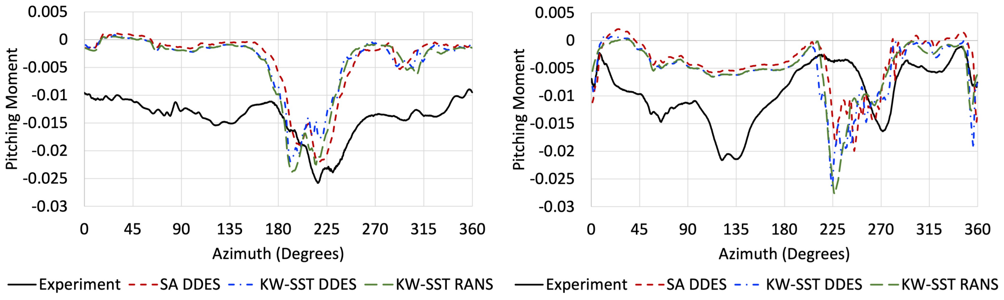

(a) r/R=0.400 (b) r/R=0.675

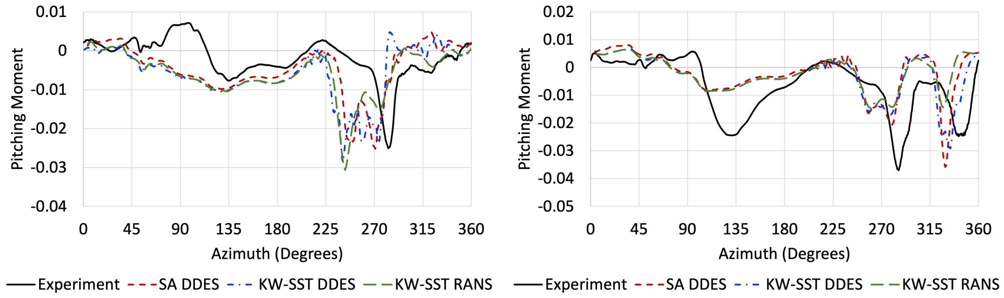

(c) r/R=0.775 (d) r/R=0.865

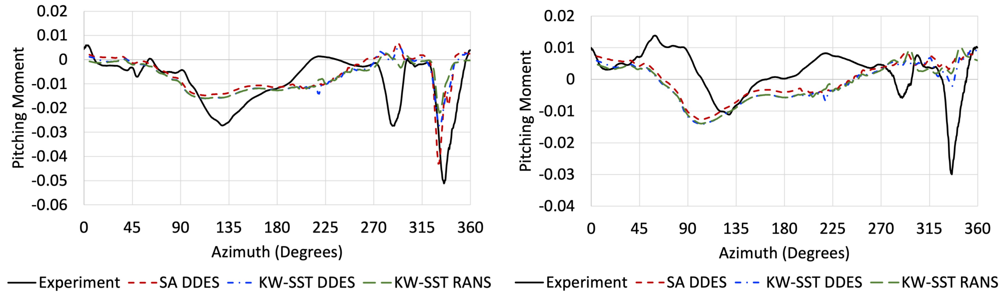

(e) r/R=0.920 (f) r/R=0.965

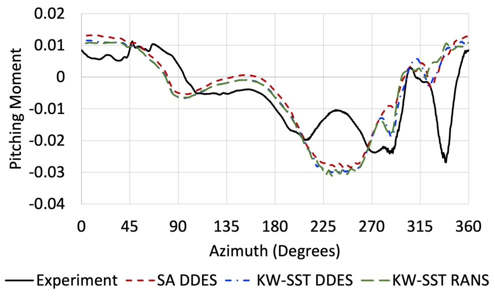

(g) r/R=0.990

Figure B.30: UH-60A pitching moment at various radial stations for various turbulence models
Test point 4537 ($C_T/\sigma =$
Fine Grid

B.3 UH-60A Airloads One-Bladed vs. Four-Bladed

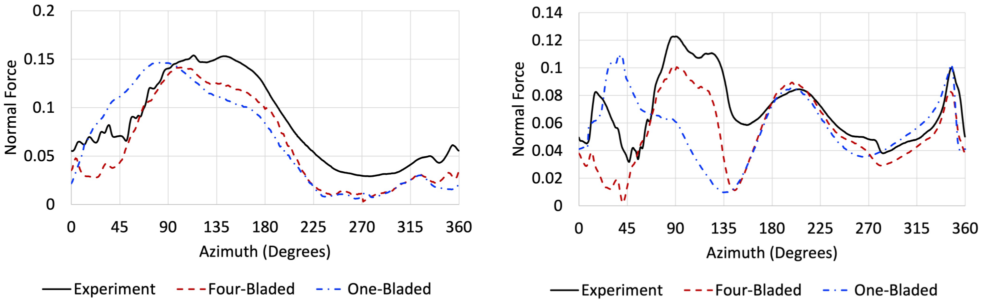

(a) r/R=0.400 (b) r/R=0.675

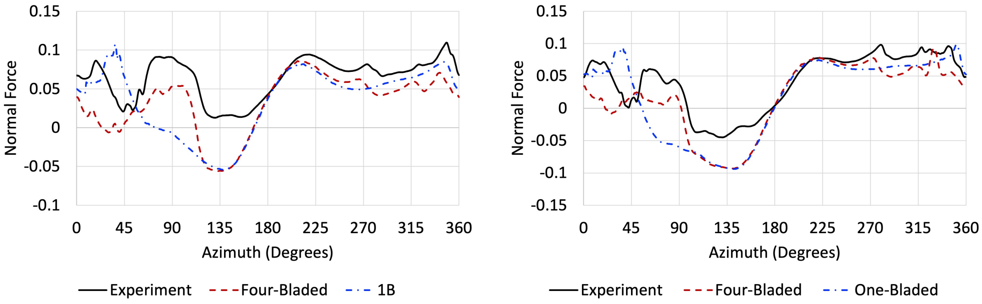

(c) r/R=0.775 (d) r/R=0.865

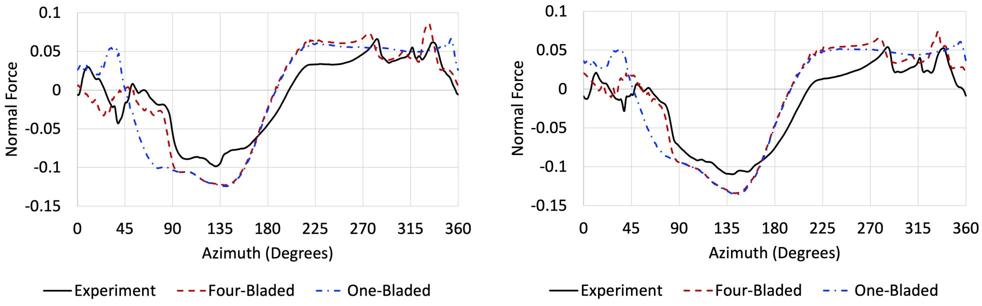

(e) r/R=0.920 (f) r/R=0.965

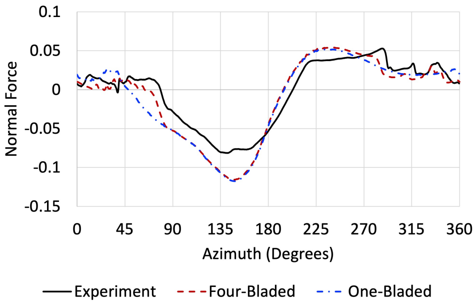

(g) r/R=0.990

Figure B.31: Comparison between one-bladed and four-bladed normal forces at various radial stations
Test point 4530 ($C_T/\sigma = 0.040$)

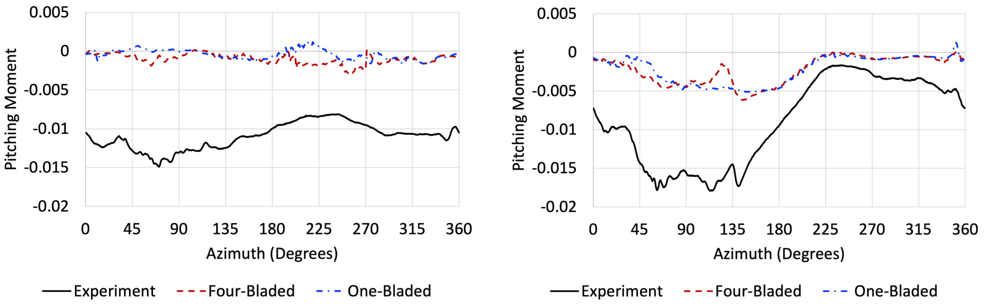

(a) r/R=0.400 (b) r/R=0.675

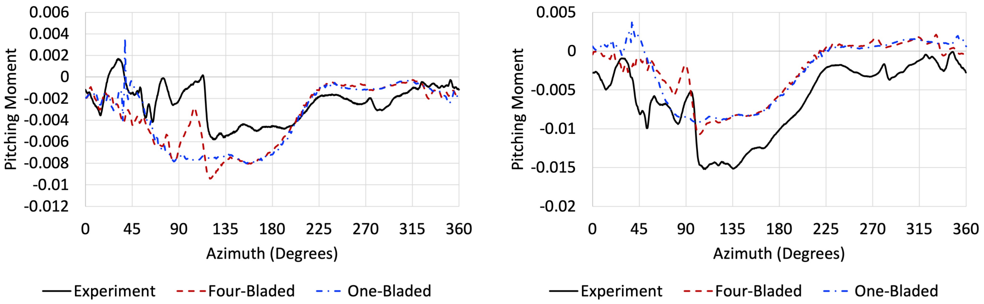

(c) r/R=0.775 (d) r/R=0.865

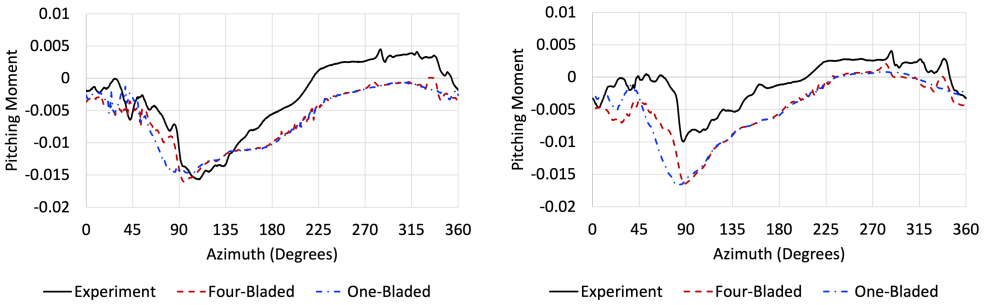

(e) r/R=0.920 (f) r/R=0.965

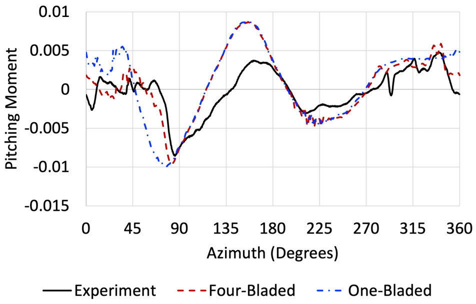

(g) r/R=0.990

Figure B.32: Comparison between one-bladed and four-bladed pitching moments at various radial stations
Test point 4530 ($C_T/\sigma = 0.040$)

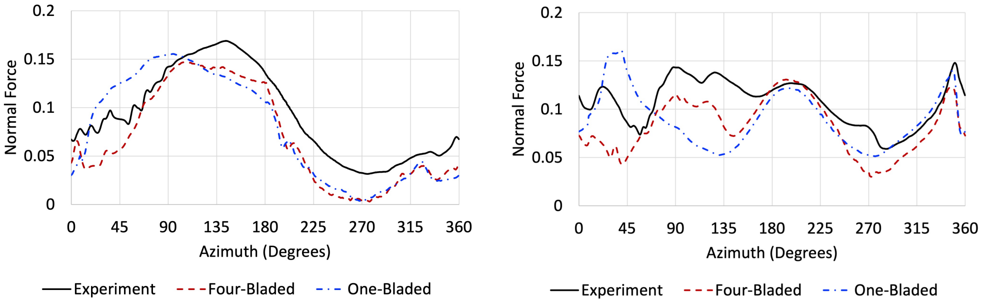

(a) r/R=0.400 (b) r/R=0.675

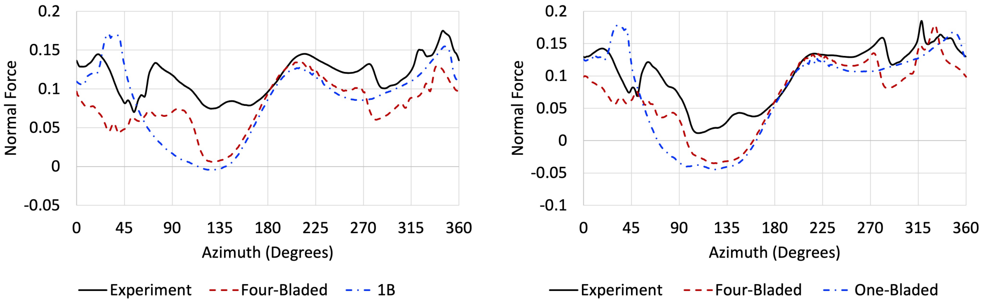

(c) r/R=0.775 (d) r/R=0.865

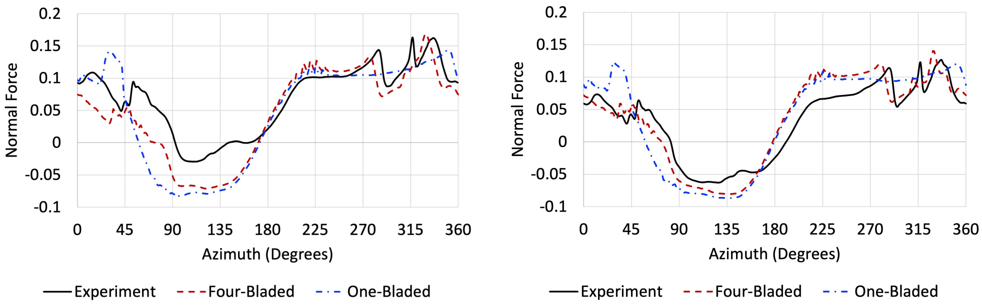

(e) r/R=0.920 (f) r/R=0.965

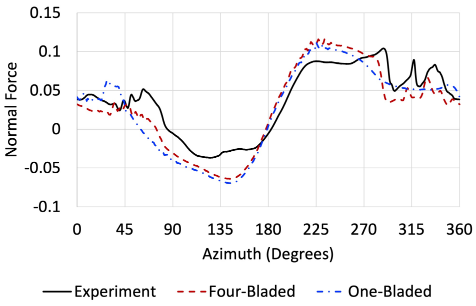

(g) r/R=0.990

Figure B.33: Comparison between one-bladed and four-bladed normal forces at various radial stations
Test point 4533 ($C_T/\sigma = 0.040$)

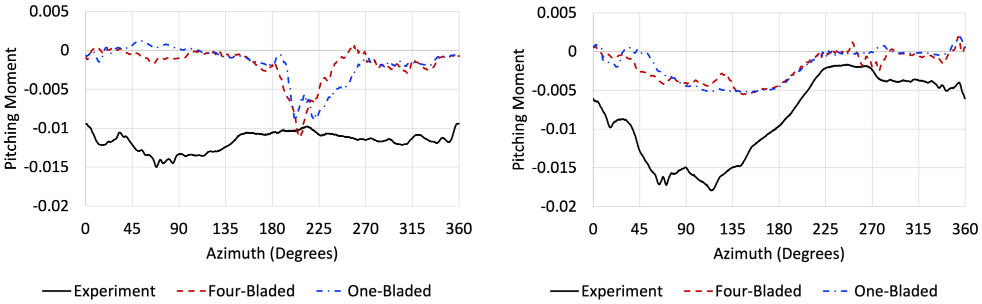

(a) r/R=0.400 (b) r/R=0.675

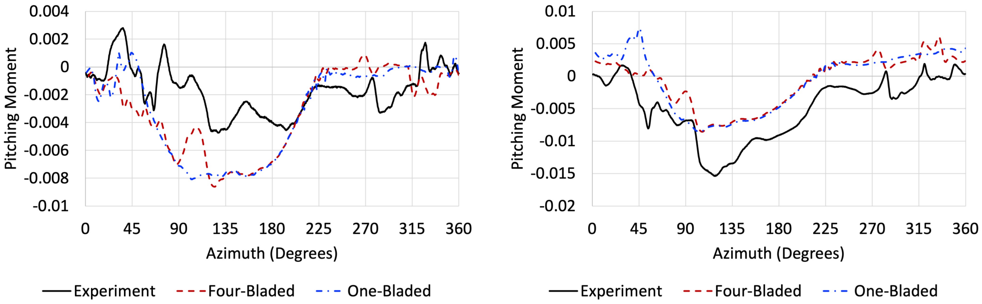

(c) r/R=0.775 (d) r/R=0.865

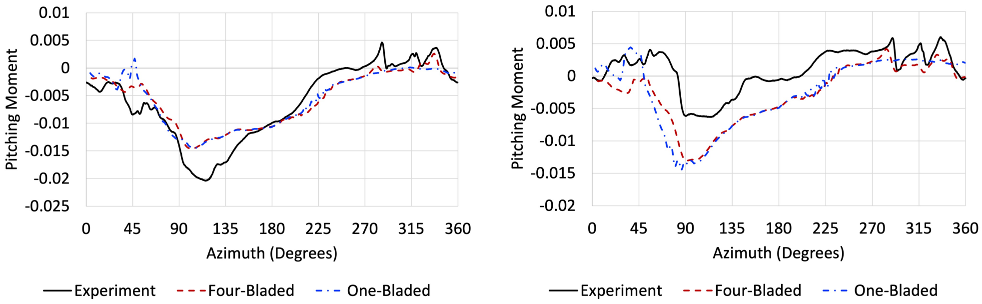

(e) r/R=0.920 (f) r/R=0.965

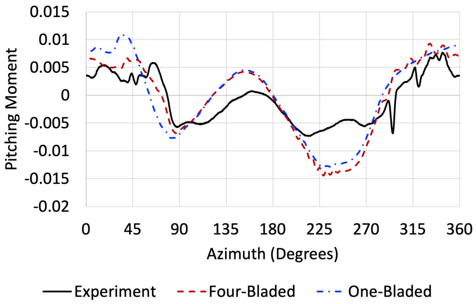

(g) r/R=0.990

Figure B.34: Comparison between one-bladed and four-bladed pitching moments at various radial stations
Test point 4533 ($C_T/\sigma = 0.040$)

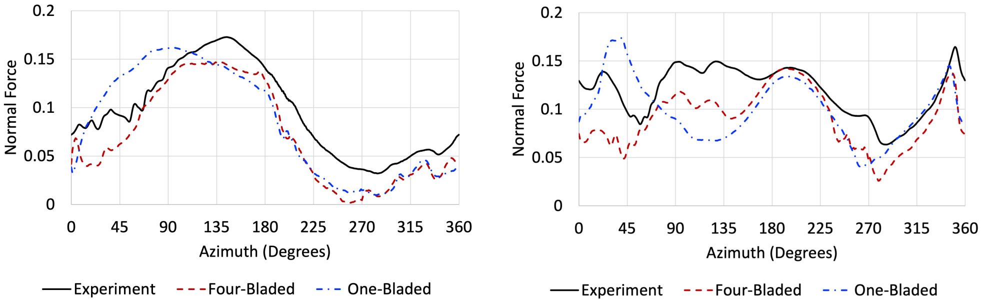

(a) r/R=0.400 (b) r/R=0.675

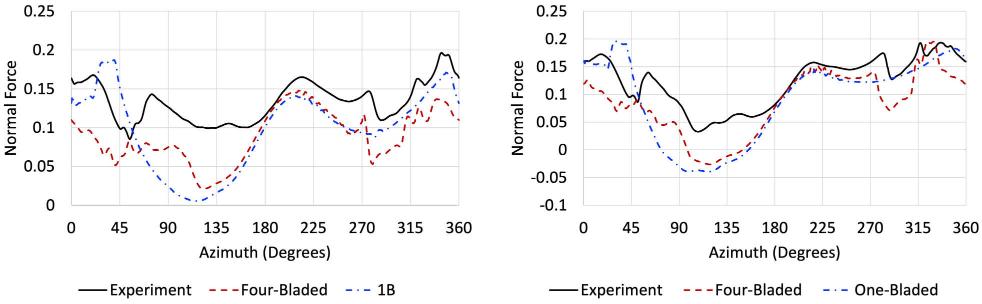

(c) r/R=0.775 (d) r/R=0.865

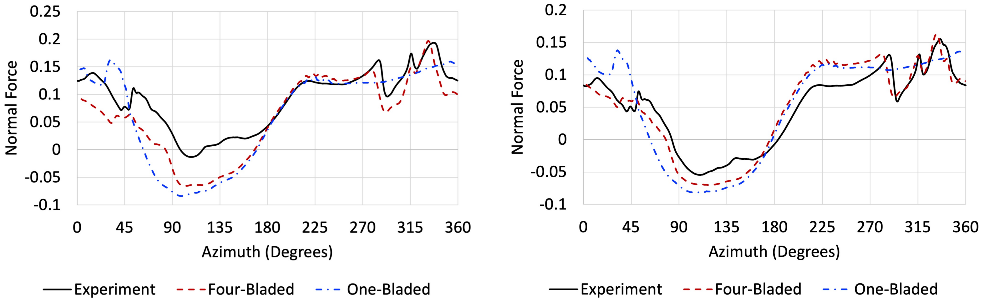

(e) r/R=0.920 (f) r/R=0.965

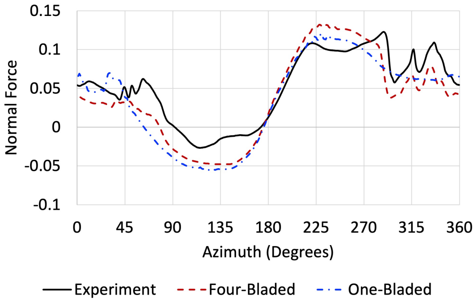

(g) r/R=0.990

Figure B.35: Comparison between one-bladed and four-bladed normal forces at various radial stations
Test point 4534 ($C_T/\sigma = 0.040$)

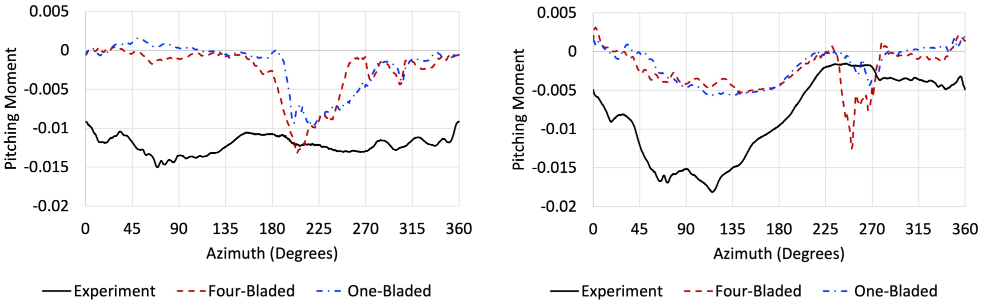

(a) r/R=0.400 (b) r/R=0.675

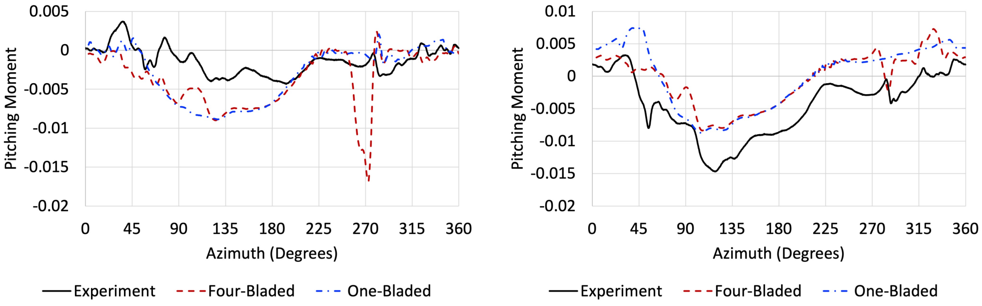

(c) r/R=0.775 (d) r/R=0.865

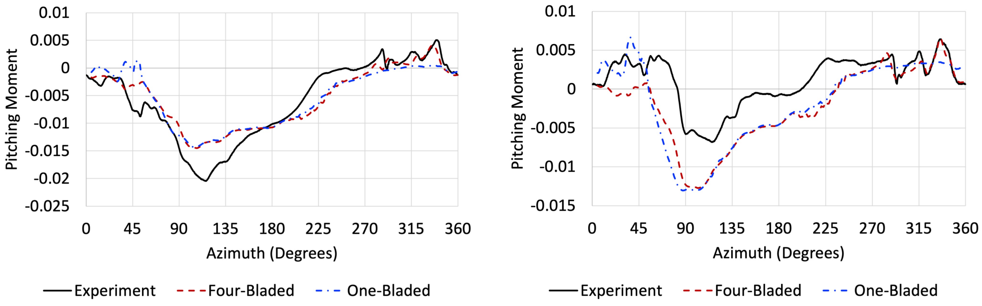

(e) r/R=0.920 (f) r/R=0.965

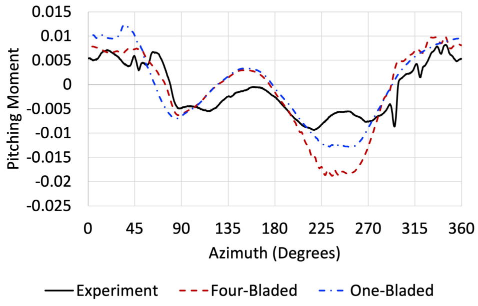

(g) r/R=0.990

Figure B.36: Comparison between one-bladed and four-bladed pitching moments at various radial stations
Test point 4534 ($C_T/\sigma = 0.040$)

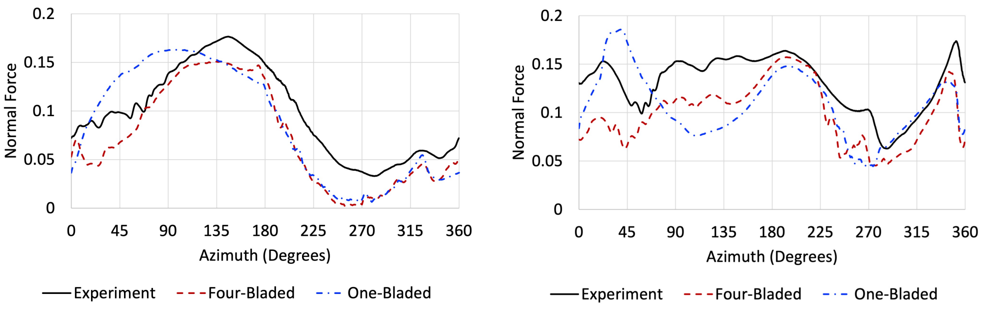

(a) r/R=0.400 (b) r/R=0.675

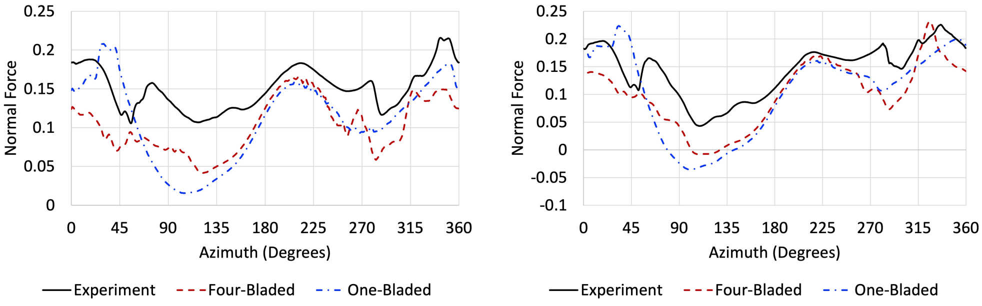

(c) r/R=0.775 (d) r/R=0.865

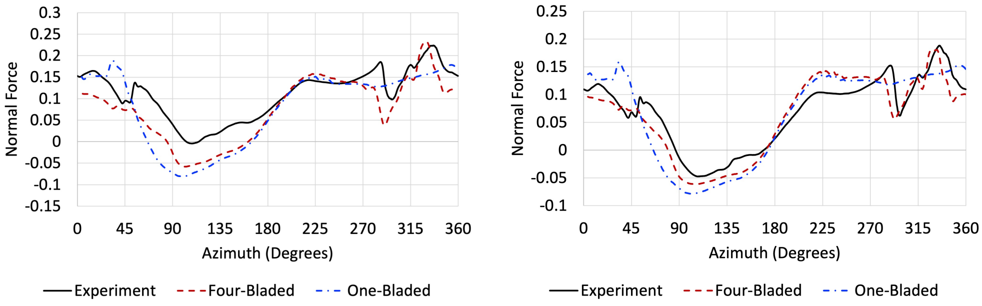

(e) r/R=0.920 (f) r/R=0.965

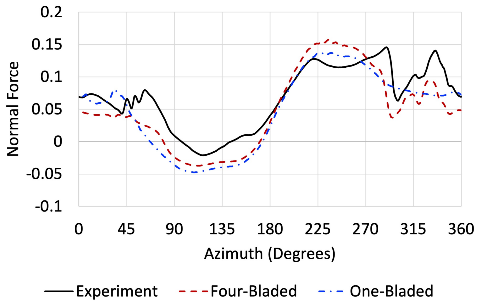

(g) r/R=0.990

Figure B.37: Comparison between one-bladed and four-bladed normal forces at various radial stations
Test point 4535 ($C_T/\sigma = 0.040$)

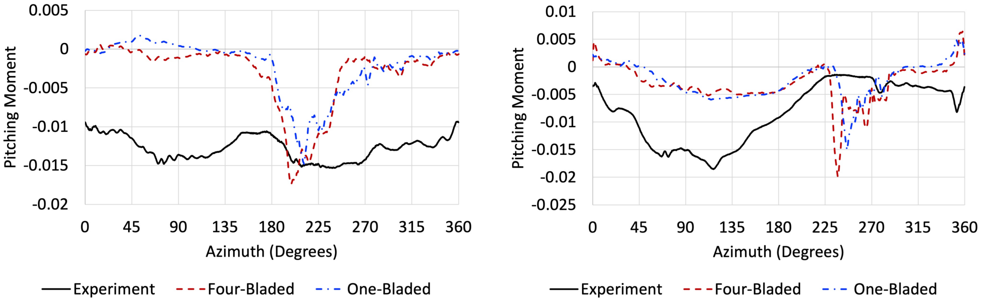

(a) r/R=0.400 (b) r/R=0.675

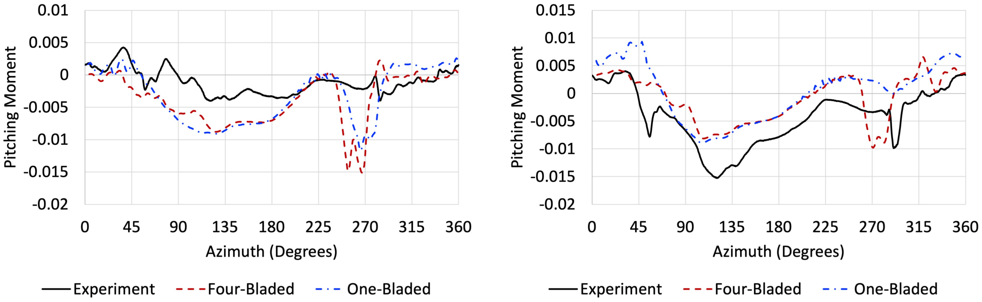

(c) r/R=0.775 (d) r/R=0.865

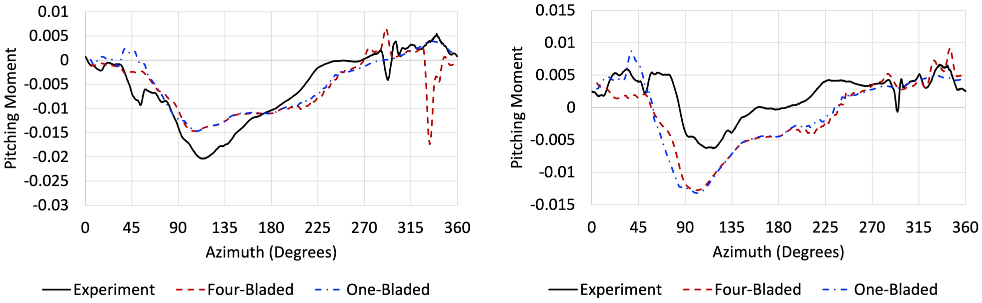

(e) r/R=0.920 (f) r/R=0.965

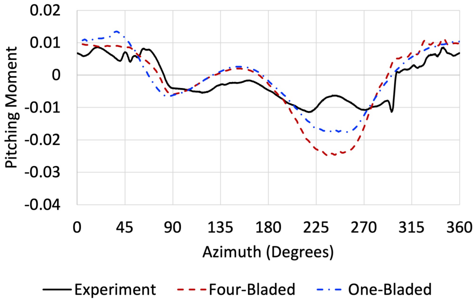

(g) r/R=0.990

Figure B.38: Comparison between one-bladed and four-bladed pitching moments at various radial stations
Test point 4535 ($C_T/\sigma = 0.040$)

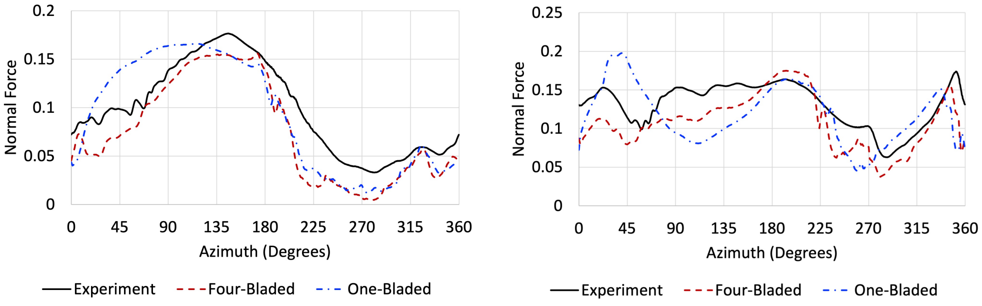

(a) r/R=0.400

(b) r/R=0.675

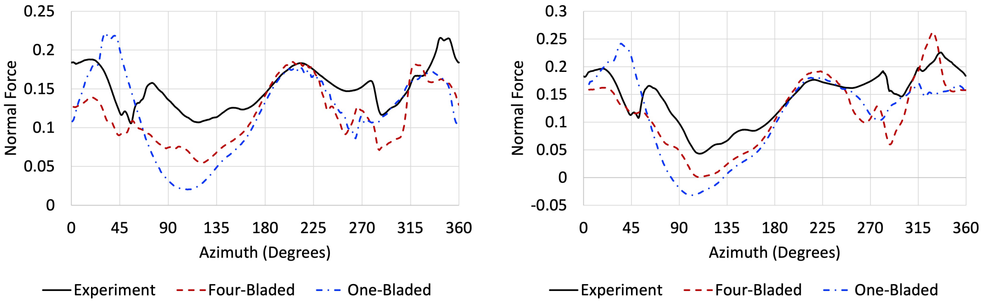

(c) r/R=0.775

(d) r/R=0.865

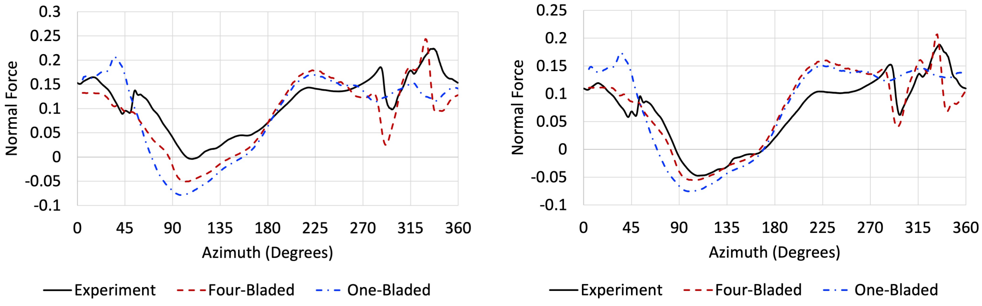

(e) r/R=0.920

(f) r/R=0.965

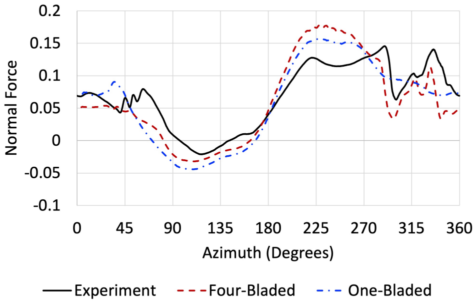

(g) r/R=0.990

Figure B.39: Comparison between one-bladed and four-bladed normal forces at various radial stations
Test point 4536 ($C_T/\sigma = 0.040$)

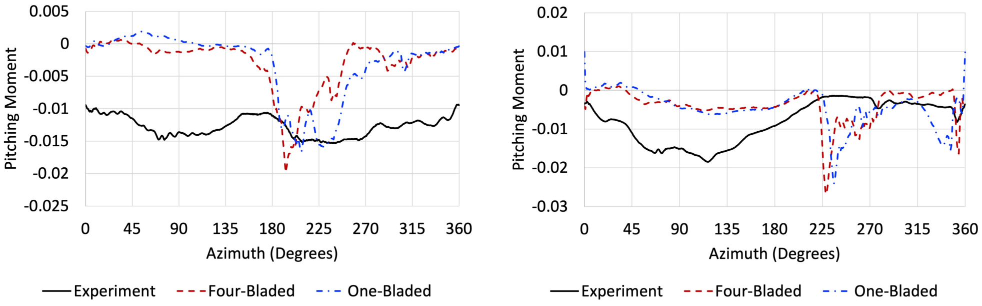

(a) r/R=0.400 (b) r/R=0.675

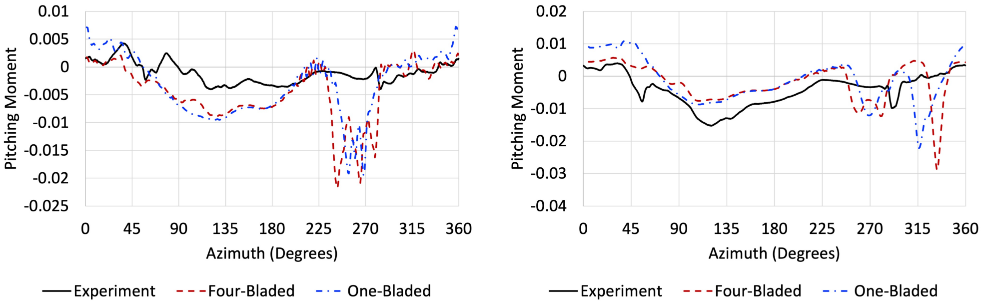

(c) r/R=0.775 (d) r/R=0.865

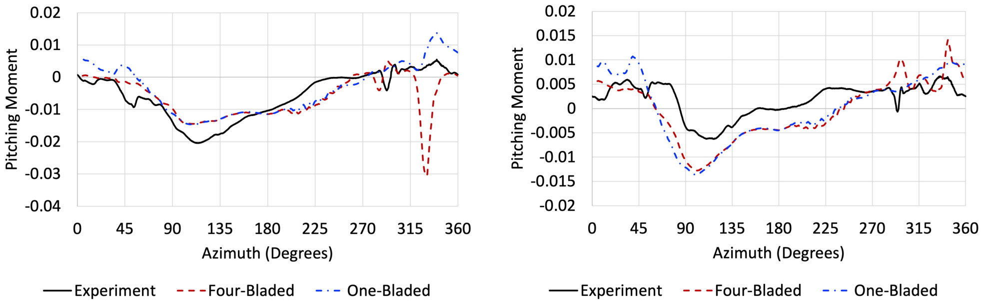

(e) r/R=0.920 (f) r/R=0.965

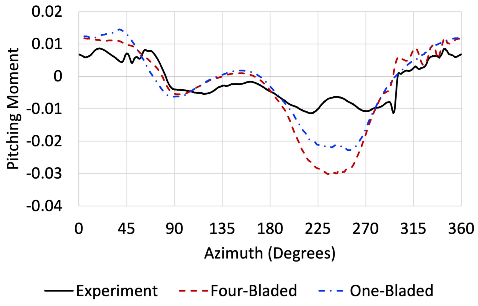

(g) r/R=0.990

Figure B.40: Comparison between one-bladed and four-bladed pitching moments at various radial stations
Test point 4536 ($C_T/\sigma = 0.040$)

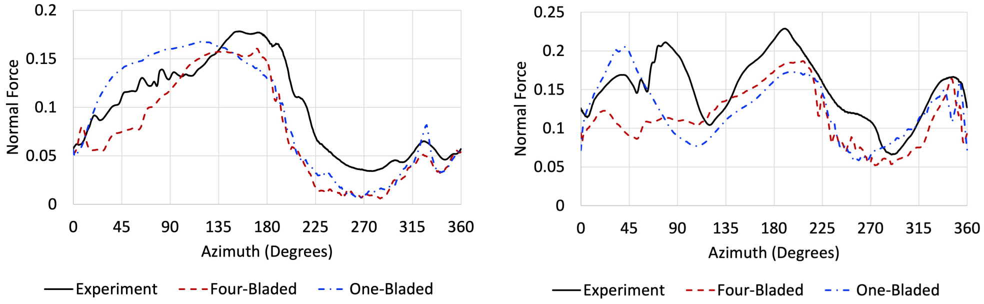

(a) r/R=0.400 (b) r/R=0.675

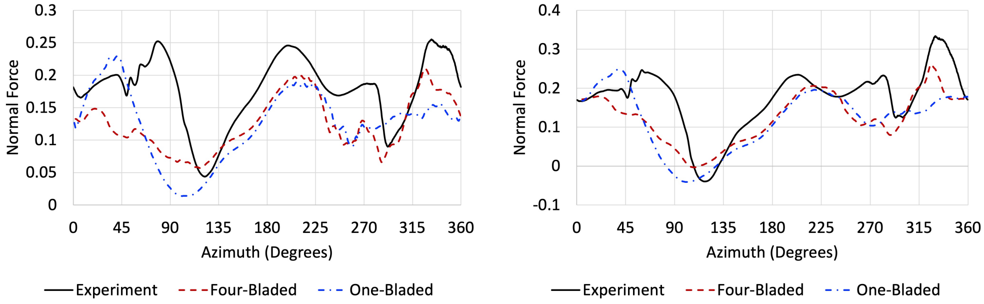

(c) r/R=0.775 (d) r/R=0.865

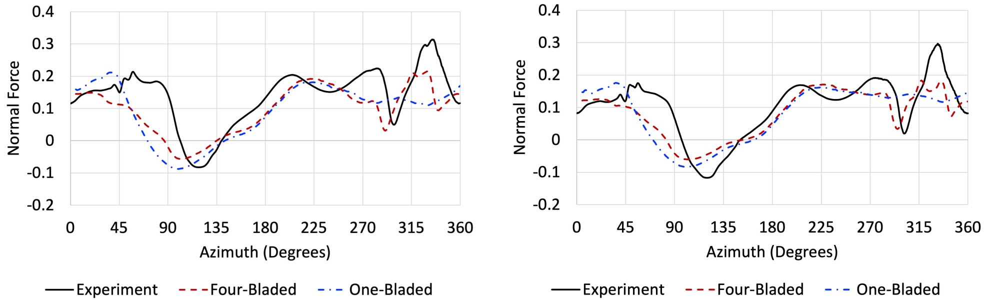

(e) r/R=0.920 (f) r/R=0.965

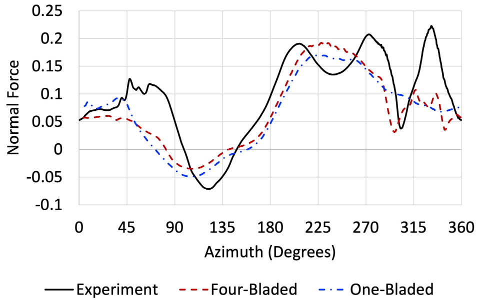

(g) r/R=0.990

Figure B.41: Comparison between one-bladed and four-bladed normal forces at various radial stations
Test point 4537 ($C_T/\sigma = 0.040$)

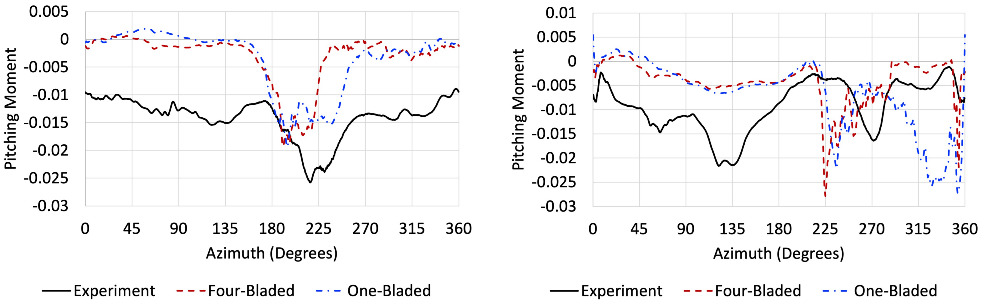

(a) r/R=0.400 (b) r/R=0.675

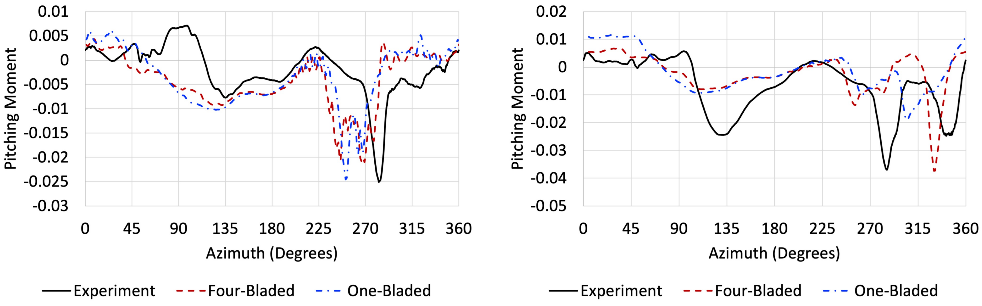

(c) r/R=0.775 (d) r/R=0.865

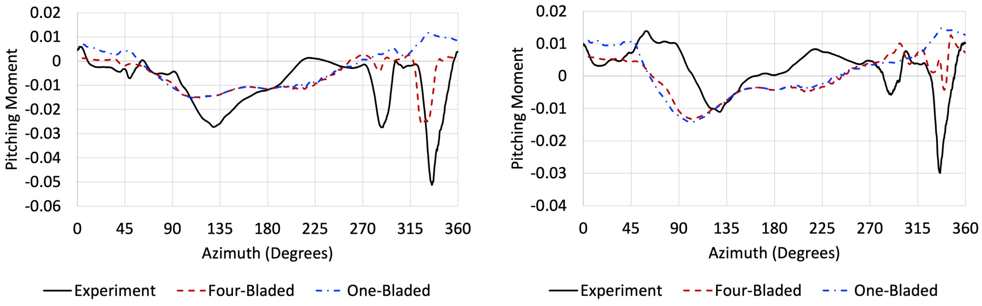

(e) r/R=0.920 (f) r/R=0.965

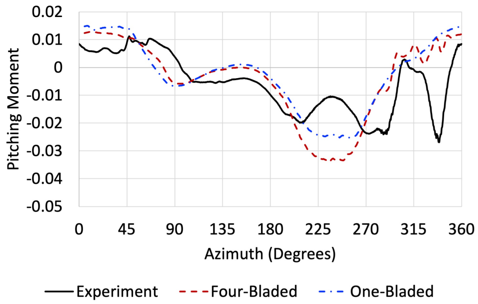

(g) r/R=0.990

Figure B.42: Comparison between one-bladed and four-bladed pitching moments at various radial stations
Test point 4537 ($C_T/\sigma = 0.040$)

APPENDIX C

BIOT-SAVART DATA

Table C.1: Convergence of induced velocity on outboard blade at (2.28, -2.61, 1.39) using the Biot-Savart summation with increasing number of vortex filament segments.

Vortex Filament Location (ft)	$\overline{R_i}(ft)$	$\overline{l_i}(ft)$	$\Gamma_i(ft^2/s)$	$V_{x_i}\ (ft/s)$	$\sum V_{x_i}\ (ft/s)$	ΔV_x	$V_{y_i}\ (ft/s)$	$\sum V_{y_i}\ (ft/s)$	ΔV_y	$V_{z_i}\ (ft/s)$	$\sum V_{z_i}\ (ft/s)$	ΔV_z
$\psi = 1^\circ$: (2.66,-21.70,1.78)	[-0.38 -4.39 -0.40]	[0.43 -0.46 -0.04]	111.94	0.21	0.21	N/A	N/A	N/A	N/A	N/A	N/A	N/A
$\psi = 2^\circ$: (3.12,-22.17,1.76)	[-0.83 -3.92 -0.37]	[0.45 -0.47 -0.03]	126.95	0.28	0.49	137%	0.00	0.00	153%	-0.51	-0.52	22583%
$\psi = 3^\circ$: (3.59,-22.66,1.81)	[-1.31 -3.43 -0.43]	[0.47 -0.49 0.06]	128.54	0.35	0.84	70%	0.00	0.00	54%	-0.70	-1.22	136%
$\psi = 4^\circ$: (4.08,-23.15,1.66)	[-1.80 -2.95 -0.28]	[0.49 -0.49 -0.15]	131.49	0.35	1.19	42%	0.00	0.00	138%	-0.90	-2.12	74%
$\psi = 5^\circ$: (4.56,-23.48,1.68)	[-2.28 -2.61 -0.30]	[0.48 -0.34 0.02]	139.38	0.23	1.42	20%	0.00	0.00	14%	-0.82	-2.94	39%
$\psi = 6^\circ$: (5.07,-23.84,1.66)	[-2.78 -2.25 -0.28]	[0.50 -0.36 -0.02]	141.50	0.19	1.61	14%	0.00	0.00	23%	-0.79	-3.73	27%
$\psi = 7^\circ$: (5.60,-24.24,1.72)	[-3.31 -1.86 -0.34]	[0.53 -0.40 0.06]	141.27	0.15	1.77	10%	0.00	0.00	-2%	-0.72	-4.45	19%
$\psi = 8^\circ$: (6.13,-24.59,1.67)	[-3.85 -1.51 -0.28]	[0.53 -0.35 -0.05]	144.55	0.08	1.85	5%	0.00	0.00	24%	-0.54	-4.98	12%
$\psi = 9^\circ$: (6.67,-24.91,1.66)	[-4.39 -1.19 -0.28]	[0.54 -0.32 -0.01]	146.64	0.05	1.90	. 2%	0.00	0.00	7%	-0.38	-5.37	8%
$\psi = 10^\circ$: (7.22,-25.18,1.67)	[-4.94 -0.92 -0.28]	[0.55 -0.27 0.01]	148.54	0.02	1.92	1%	0.00	0.00	3%	-0.26	-5.63	5%
$\psi = 11^\circ$: (7.79,-25.48,1.65)	[-5.51 -0.62 -0.26]	[0.57 -0.30 -0.02]	149.46	0.01	1.93	1%	0.00	0.00	5%	-0.21	-5.84	4%
$\psi = 12^\circ$: (8.34,-25.67,1.66)	[-6.06 -0.43 -0.27]	[0.55 -0.19. 0.01]	151.50	0.00	1.94	0%	0.00	0.00	2%	-0.12	-5.96	2%
$\psi = 13^\circ$: (8.90,-25.84,1.60)	[-6.61 -0.26 -0.21]	[0.56 -0.17 -0.05]	152.10	0.00	1.94	0%	0.00	0.00	6%	-0.08	-6.04	1%
$\psi = 14^\circ$: (9.46,-26.00,1.52)	[-7.18 -0.09 -0.13]	[0.57 -0.16 -0.08]	152.89	0.00	1.94	0%	0.00	0.00	6%	-0.06	-6.10	1%
$\psi = 15^\circ$: (10.04,-26.16,1.50)	[-7.70 0.07 -0.11]	[0.58 -0.16 -0.02]	153.52	0.00	1.94	0%	0.00	0.00	1%	-0.05	-6.15	1%
$\psi = 16^\circ$: (10.63,-26.31,1.50)	[-8.30 0.22 -0.11]	[0.59 -0.15 0.00]	154.82	0.00	1.94	0%	0.00	0.00	0%	-0.04	-6.19	1%
$\psi = 17^\circ$: (11.21,-26.40,1.49)	[-8.90 0.31 -0.10]	[0.58 -0.09 -0.01]	157.70	0.00	1.94	0%	0.00	0.00	1%	-0.02	-6.21	0%
$\psi = 18^\circ$: (11.78,-26.46,1.49)	[-9.50 0.37 -0.10]	[0.58 -0.06 0.00]	159.77	0.00	1.94	0%	0.00	0.00	0%	-0.01	-6.21	0%
$\psi = 19^\circ$: (12.35,-26.49,1.50)	[-10.07 0.40 -0.11]	[0.57 -0.03 0.01]	162.32	0.00	1.94	0%	0.00	0.00	0%	0.00	-6.21	0%
$\psi = 20^\circ$: (12.92,-26.49,1.50)	[-10.64,0.40 -0.11]	[0.57 0.00 0.00]	164.90	0.00	1.94	0%	0.00	0.00	0%	0.00	-6.21	0%

BIBLIOGRAPHY

[1] D. Bailey. *Joint Multi-Role Technology Demonstration Mission Systems Architecture Demo*. Presentation at 2016 ADD Industry Day. Mar. 2016.

[2] *Airbus reveals the next generation of CityAirbus*. Tech. rep. Airbus, Sept. 2021.

[3] G. Lighter. *Master Lecture: GoFly Technical Rules*. Aug. 2017.

[4] Federal Aviation Administration (FAA). *FAA Aerospace Forecast: Fiscal Years 2018-2038*. Tech. rep. U.S. Department of Transportation, Washington D.C., 2018.

[5] B.J. Holmes et al. *NASA Strategic Framework for On-Demand Air Mobility*. Tech. rep. National Institute of Aerospace, Jan. 2017.

[6] M. Moore and K. Goodrich. *On-Demand Mobility: Aviation's Path to High Speed Regional Mobility*. Presentation at 2015 On-Demand Mobility. July 2015.

[7] A. Wissink et al. "Improvements in the Helios Rotorcraft Simulation Code". In: *Proceedings of the American Helicopter Society 72nd Annual Forum*. West Palm Beach, Florida, May 2016.

[8] R.G. Rajagopalan et al. "RotCFD - A Tool for Aerodynamic Interference of Rotors: Validation and Capabilities". In: *Proceedings of the 2012 AHS Future Vertical Lift Aircraft Design Conference*. San Franciso, CA, Jan. 2012.

[9] K. Nguyyen and W. Johnson. "Evaluation of Dynamic Stall Models with UH-60A Airloads Flight Test Data". In: *Proceedings of the AHS 54th Annual Forum*. Washington, D.C., May 1998.

[10] W.J. McCroskey. *The Phenomenon of Dynamic Stall*. Technical Memorandum 81264. NASA, Mar. 1981.

[11] R. Jain et al. "High-resolution CFD Predictions for Static and Dynamic Stall of a Finite-span OA209 Wing". In: *72nd AHS Annual Forum*. West Palm Beach, FL, May 2016.

[12] L.W. Carr, K.W. McAlister, and W.J. McCroskey. *Analysis of the Development and of Dynamic Stall Based on Oscillating Airfoil Experiments*. Technical Note D-8382. NASA, Jan. 1977.

[13] C.P. Butterfield et al. "Wind Power Conference and Exposition". In: *Proceedings of the 2016 American Helicopter Society Technical Meeting on Aeromechanics Design for Vertical Lift*. Palm Springs, CA, Sept. 1991.

[14] D.E. Gault. *A Correlation of Low-Speed, Airfoil-Section Stalling Characteristics with Reynolds Number and Airfoil Geometry*. Technical Note 3963. NACA, Mar. 1957.

[15] M.J. Smith et al. "Evaluation of CFD to Determine Two-Dimensional Airfoil Characteristics for Rotorcraft Applications". In: *Proceedings of the American Helicopter Society 60th Annual Forum*. Baltimore, MD, June 2004.

[16] M. Ramasamay et al. "Measured Characteristics of Cycle-to-Cycle Variations in Dynamic Stall". In: *Proceedings of the 2016 American Helicopter Society Technical Meeting on Aeromechanics Design for Vertical Lift*. San Francisco, CA, Jan. 2016.

[17] A. Spentzos et al. “CFD Investigation of 2D and 3D Dynamic Stall”. In: *Proceedings of the AHS 4th Decennial Specialist’s Conference on Aeromechanics,* San Francisco, CA, Jan. 2004.

[18] M. Smith et al. “An Assessment of the State of the Art from the 2019 ARO Dynamic Stall Workshop”. In: *Proceedings of the AIAA AVIATION 2020 FORUM*. Virtual, June 2020.

[19] F. Richez. “Numerical Analysis of Dynamic Stall for Different Helicopter Rotor Flight Conditions”. In: *Proceedings of the American Helicopter Society 73rd Annual Forum*. Fort Worth, Texas, May 2017.

[20] R. Jain et al. “High-Resolution Computational Fluid Dynamics Predictions for the Static and Dynamic Stall of a Finite-Span OA209 Wing”. In: *Journal of Fluids and Structures* 78 (Apr. 2018), pp. 126–145. DOI: `10.1016/j.jfluidstructs.2017.12.012`.

[21] A. Grubb et al. “High Fidelity CFD Analyses of Dynamic Stall on a Four-Bladed Fully Articulated Rotor System”. In: *Proceedings of the 2018 AHS 74th Annual Forum*. Phoenix, AZ, May 2018.

[22] N. Chaderjian. “Navier-Stokes Simulation of a UH-60A Rotor/Wake Interaction Using Adaptive Mesh Refinement”. In: *Proceedings of the American Helicopter Society 73rd Annual Forum*. Fort Wort, Texas, May 2017.

[23] A. Le Pape et al. “Extensive Wind Tunnel Tests Measurements of Dynamic Stall Phenomenon for the OA209 Airfoil Including 3D Effects”. In: *Proceedings of the 33rd European Rotorcraft Forum*. Kazan, Russia, Sept. 2017.

[24] K. Richter et al. “Numerical Investigation of Three-Dimensional Static and Dynamic Stall on a Finite Wing”. In: *Journal of the American Helicopter Society* 60.3 (July 2015). DOI: `10.4050/JAHS.60.032004`.

[25] K. Kaufman et al. “Numerical Investigation of Three-Dimensional Static and Dynamic Stall on a Finite Wing”. In: *Journal of the American Helicopter Society* 60.3 (July 2015), pp. 1–12. DOI: `10.4050/JAHS.60.032004`.

[26] A. Goerttler et al. “Tip-Vortex Investigation on a Rotating and Pitching Rotor Blade”. In: *Proceedings of the 43rd European Rotorcraft Forum*. Milan, Italy, Sept. 2017.

[27] K. Kaufman, C.B. Merz, and A.D. Gardner. “Dynamic Stall Simulations in a Pitching Finite Wing”. In: *Journal of Aircraft* 54 (July 2017), pp. 1303–1316. DOI: `10.2514/1.C034020`.

[28] P. Beaumier, M. Costes, and R. Gaveriaux. “Comparison Between FP3D Full Potential Calculations and S1 Modane Wind Tunnel Test Results on Advanced Fully Instrumented Rotors”. In: *Proceedings of the 19th European Rotorcraft Forum*. Cernobbio, Italy, Sept. 1993.

[29] T. Schwermer, K. Richter, and M. Raffel. *Development of a Rotor Test Facility for the Investigation of Dynamic Stall*. Switzerland: Springer, 2015, pp. 663–673. DOI: `10.1007/978-3-319-27279-5-58`.

[30] T.R. Norman et al. “Full-Scale Wind Tunnel Test of the UH-60A Airloads Rotor”. In: *Proceedings of the American Helicopter Society 67th Annual Forum*. Virginia Beach, Virginia, May 2011.

[31] A. Grubb et al. “High Fidelity CFD Analyses of Dynamic Stall on a Four-Bladed Fully Articulated Rotor System”. In: *Proceedings of the American Helicopter Society 74rd Annual Forum*. Phoenix, Arizona, May 2018.

[32] T. Schwermer, A.D. Gardner, and M. Raffel. “Dynamic Stall Experiments on a Rotor with High Cyclic Setting in Axial Inflow”. In: *Proceedings of the American Helicopter Society 73rd Annual Forum*. Fort Worth, Texas, May 2017.

[33] B. Ortun et al. “Rotor Loads Prediction on the ONERA 7A Rotor Using Loose Fluid/Structure Coupling”. In: *Journal of the American Helicopter Society* 62.3 (July 2017), pp. 1–13.

[34] A. Le Pape et al. “Extensive wind tunnel measurements of dynamic stall phenomenon for the OA209 airfoil including 3D effects”. In: *Proceedings of the 33rd European Rotorcraft Forum*. Kazan, Russia, Sept. 2007.

[35] M.R. Malik and D.N. Bushnell. *Role of Computational Fluid Dynamics and Wind Tunnels in Aeronautics Research Development*. Tech. rep. TP-2012-217602. NASA, Sept. 2012.

[36] M.N. Tishchenko, V.T. Nagaraj, and I. Chopra. “Preliminary Design of Transport Helicopters”. In: *Journal of the American Helicopter Society* 48.2 (Apr. 2003), pp. 71–79. DOI: `10.4050/JAHS.48.71`.

[37] O. Rand and V. Khromov. “Helicopter Sizing by Statistics”. In: *Journal of the American Helicopter Society* 49.3 (July 2004), pp. 300–317. DOI: `10.4050/JAHS.49.300`.

[38] M. Lier. “Statistical Methods for Helicopter Preliminary Design and Sizing”. In: *Proceedings of the 37th European Rotorcraft Forum*. Vergiate and Gallarate, Italy, July 2011.

[39] G.R. Whitehouse, T.R. Quackenbush, and A.H. Boschitsch. “Variable Fidelity Preliminary Design Tools for Advanced Vertical Flight Vehicles”. In: *Proceedings of the American Helicopter Society 66th Annual Forum*. Phoenix, Arizona, May 2010.

[40] D.P. Schrage. “Technology for Rotorcraft Affordability Through Integrated Product/Process Design (IPPD)”. In: *Proceedings of the American Helicopter Society 55th Annual Forum*. Montreal, Canada, May 1999.

[41] W. Johnson and Jeffrey D. Sinsay. “Rotorcraft Conceptual Design Environment”. In: *Proceedings of the 2nd International Forum on Multidisciplinary Technology*. Seoul, South Korea, Oct. 2009.

[42] D. Worth and M. Hajek. “Probabilistic Methodology for Multi-Fidelity Model-Based Robust Preliminary Design of Rotorcraft”. In: *Proceedings of the American Helicopter Society 73rd Annual Forum*. Fort Worth, Texas, May 2017.

[43] Modarres, R. “Semi-Empirical Modeling of Two-Dimensional and Three-Dimensional Dynamic Stall”. https://openscholarship.wustl.edu. PhD thesis. St. Louis, Missouri: Washington University in St. Louis, 2016.

[44] F. Caradonna, G. Laub, and C. Tung. *An Experimental Investigation of the Parallel Blade-Vortex Interaction*. Tech. rep. NASA Ames Research Center, Nov. 1984.

[45] M. Homer et al. “Results from a Set of Low Speed Blade-Vortex Interaction Experiments”. In: *Experiments in Fluids* 14 (Apr. 1993), pp. 341–352. DOI: `10.1007/BF00189493`.

[46] M.B. Horner. “An Examination of Blade-Vortex Interaction Utilizing Pressure Measurementts and Particle Image Velocimetry”. PhD thesis. Boulder, Colorado: University of Colorado, 1994.

[47] R.C. Strawn. “New Computational Methods for the Prediction and Analysis of Helicopter Noise”. In: *Journal of Aircraft* 34.5 (Sept. 1997), pp. 665–672. DOI: `10.2514/2.2227`.

[48] M.V. Lowson. “Focusing on Helicopter BVI Noise”. In: *Journal of Sound and Vibration* 190.3 (Feb. 1996), pp. 477–484. DOI: `10.1006/jsvi.1996.0075`.

[49] B. W-C. Sim, A.R. George, and S. Yen. “Blade-Vortex Interaction Noise Studies Using Trace Mach Number”. In: *Proceedings of the American Helicopter Society Aeromechanics Specialist Conference*. Bridgeport, Connecticut, Oct. 1995.

[50] C. Castells, F. Richez, and M. Costes. “A Numerical Investigation of the Influence of the Blade Vortex Interaction on the Dynamic Stall Onset in Simplified Rotor Environment”. In: *Journal of the American Helicopter Society* 66.3 (2021), pp. 1–13. DOI: `10.4050/JAHS.66.032001`.

[51] D. Wilcox. *Turbulence Modeling for CFD*. DCW Industries, 1998.

[52] R.H. Pletcher, J.C. Tannehill, and D.A Anderson. *Computational Fluid Mechanics and Heat Transfer*. CRC Press, 2013.

[53] C. Rumsey. *NASA Turbulence Modeling Resource*. Dec. 2017. URL: `https://turbmodels.larc.nasa.gov/index.html`.

[54] P.R. Spalart and S.R Allmaras. “A One-Equation Turbulence Model for Aerodynamic Flows”. In: *Recherche Aerospatiale* (May 1994). DOI: `10.2514/6.1992-439`.

[55] M. J. Smith et al. “Evaluation of CFD to Determine Two–Dimensional Airfoil Characteristics for Rotorcraft Applications”. In: *Journal of the American Helicopter Society* 50.1 (2006), pp. 70–79.

[56] M. Strelets. “Detached Eddy Simulation of Massively Separated Flows”. In: *39th AIAA Aerospace Sciences Meeting and Exhibit*. AIAA-2001-0879. Reno, NV, Jan. 2001.

[57] F.R. Menter. “Two-Equation Eddy-Viscosity Turbulence Models for Engineering Applications”. In: *AIAA Journal* 32.8 (Aug. 1994).

[58] J. Hodara et al. “Collaborative Investigation of the Aerodynamic Behavior of Airfoils in Reverse Flow”. In: *American Helicopter Society 71st Annual Forum*. Virginia Beach, VA, May 2015.

[59] P.R. Spalart et al. “Comments on the Feasibility of LES for Wings, and on a Hybrid RANS/LES Approach”. In: *Proceedings of the First ASOSR Conference on DNS/LES*. Arlington, Texas, Aug. 1997.

[60] P.R. Spalart et al. “A New Version of Detached-Eddy Simulation, Resistant to Ambiguous Grid Densities”. In: *Theoretical and Computational Fluid Dynamics* 20 (May 2006), pp. 181–195. DOI: `10.1007/s00162-006-0015-0`.

[61] N. Liggett and M. J. Smith. “Temporal Convergence Criteria for Time-Accurate Viscous Simulations of Separated Flows”. In: *Computers & Fluids* 66.- (2012), pp. 140–156. DOI: `10.1016/j.compfluid.2012.06.010`.

[62] N.K. Burgess and R. Jain. "Effects of Numerical Methods on Static and Dynamic Stall Simulations". In: *Proceedings of the 5th Decennial AHS Aeromechanics Specialist Conference*. San Francisco, CA, Jan. 2014.

[63] A. Grubb and M. J. Smith. "Development and Application of Temporal Adaption Methods to Computationally Intensive CFD Simulations". In: *Proceedings of the 23rd AIAA Computational Fluid Dynamics Conference*. Denver, CO, June 2017.

[64] H. Yeo, M. Potsdam, and R.A. Ormiston. "Application of CFD/CSD to Rotor Aeroelastic Stability in Forward Flight". In: *Proceedings of the American Helicopter Society 66th Annual Forum*. Phoenix, AZ, May 2010.

[65] N.M Chaderjian and P.G. Buning. "High Resolution Navier-Stokes Simulation of Rotor Wakes". In: *Proceedings of 67th American Helicopter Society Forum*. Virginia Beach, Virginia, May 2011.

[66] C. "Ohrle et al. "High-Order Simulations of a Compound Helicopter Using Adaptive Mesh Refinement". In: *Proceedings of 74th American Helicopter Society Forum*. Phoenix, Arizona, May 2017.

[67] R.H. Nichols, R.W. Tramel, and P.G. Buning. "Solver and Turbulence Model Upgrades to OVERFLOW 2 for Unsteady and High-Speed Applications". In: *Proceedings of the 24th AIAA Applied Aerodynamics Conference*. San Francisco, California, June 2006. DOI: `10.2514/6.2006-2824`.

[68] T.H. Pulliam. "High Order Accurate Finite-Difference Methods: As Seen in OVERFLOW". In: *Proceedings of the 20th AIAA Computational Fluid Dynamics Conference*. Honolulu, Hawaii, June 2011.

[69] O. Bachau, C. Bottasso, and Y. Nikishkov. "Modeling Rotorcraft Dynamics with Finite Element Multibody Procedures". In: 33 (May 2001), pp. 1113–1137. DOI: `10.1016/S0895-7177(00)00303-4`.

[70] M. Potsdam, H. Yeo, and W. Johnson. "Rotor Airloads Prediction Using Loose Aerodynamic/Structural Coupling". In: *Journal of Aircraft* 43.3 (2006), pp. 732–742.

[71] J.W. Lim et al. "BVI Airloads Prediction Using CFD/CSD Loose Coupling". In: *Proceedings of the American Helicopter Society Fourth Vertical Lift Aircraft Design Conference*. San Francisco, CA, Jan. 2006.

[72] J. Morillo, M. Summers, and J.O. Bridgeman. "Implementation of Dymore (CSD)/OVERFLOW-2 (CFD) Loose Coupling Methodology at BHTI". In: *Proceedings of the American Helicopter Society 66th Annual Forum*. Phoenix, AZ, May 2010.

[73] C. Sheng et al. "A Loosely Coupled CFD/CSD Simulation of a Helicopter Rotor in Forward Flight". In: *Proceedings of the American Helicopter Society 69th Annual Forum*. Phoenix, AZ, May 2013.

[74] F. Richez et al. "Validation and Analysis of Aeroelastic Simulations of the UH-60A Rotor from Pre- to Post-stall Flight Conditions". In: *Proceedings of the 2020 AHS 76th Annual Forum*. Virtual, Oct. 2020.

[75] R.A Piziali. *2-D and 3-D Oscillating Wing Aerodynamics for a Range of Angles of Attack Including Stall*. Tech. rep. NASA Technical Memorandum 4632, Sept. 1994.

[76] J. Totah. *A Critical Assessment of UH-60 Main Rotor Blade Airfoil Data*. Tech. rep. NASA-TM-103985. NASA, Sept. 1993.

[77] L. Ahaus et al. “Assessment of CFD/CSD Analytical Tools for Improved Rotor Loads”. In: *Proceedings of the American Helicopter Society 71st Annual Forum*. Virginia Beach, Virginia, May 2015.

[78] O. Bachau and H. Liu. “On the Modeling of Hydraulic Components in Rotorcraft Systems”. In: *Journal of the American Helicopter Society* 51.2 (Apr. 2006), pp. 175–184.

[79] J. Szydlowski and M. Costes. “Simulation of Flow Around a Static and Oscillating in Pitch NACA 0015 Airfoil Using URANS and DES”. In: *Proceedings of the ASME 2004 Heat Transfer/Fluids Engineering Summer Conference*. Charlotte, NC, July 2004.

[80] M. J. Smith, N.D. Liggett, and B.C.G Koukol. “The Aerodynamics of Airfoils at High and Reverse Angles of Attack”. In: *Journal of Aircraft* 48.6 (Nov. 2011), pp. 2012–2023. DOI: `10.2514/1.C031428`.

[81] A. Zanotti et al. “Assessment of 2D/3D numerical modeling for deep dynamic stall experiments”. In: *Journal of Fluids and Structures* 51 (Jan. 2014).

[82] M. Ramasamy, R. Jain, and T.R. Norman. “Does Scatter Matter? Improved Understanding of UH-60A Wind Tunnel Rotor Measurements Using Data-Driven Clustering and CREATETM-AV Helios”. In: *Proceedings of the 2021 VFS 77th Annual Forum*. Virtual, May 2021.

[83] A. Grubb, M.J. Smith, and R. Jain. “Physics of BVI-Induced Dynamic Stall on Equivalent One-Bladed and Four-Bladed Rotors”. In: *Proceedings of the 2021 AHS 77th Annual Forum*. Virtual, May 2021.

[84] W. Kaufman. “Über die Ausbreitung kreiszylindrischer Wirbel in zähen (viskosen) Flüssigkeiten”. In: *Archive of Applied Mathmatics* 31 (1962), pp. 1–9. DOI: `10.1007/BF00538235`.